AUTOMATED QUASI-STATIC IN VITRO KNEE JOINT SIMULATOR: CONSTRUCTION AND VALIDATION

Luis Roberto Licón, B. Eng.

Thesis submitted to the Faculty of Engineering
in partial fulfillment of the requirements for the degree of
MASTER OF APPLIED SCIENCES
In Biomedical Engineering

Supervisor:
Daniel L. Benoit, PhD.

Ottawa-Carleton Institute for Biomedical Engineering

Faculty of Engineering

University of Ottawa

December 2018

Abstract

Anterior cruciate ligaments (ACL) are among the most common reported ligament injuries in athletes. This injury has been linked to changes in joint stability, neuromuscular activity and contact mechanics. In vitro simulators have proven to provide valuable insights on the potential effects of muscle activity on joint stability. The University of Ottawa Knee Simulate (UOKS) is a mechanical load driven quasi-static apparatus that provides the framework to explore pressure changes in knee compartments and the resultant kinematics in response to six individual muscle loads applied around an unconstrained joint. The main objective of the present work was to develop an automated loading mechanism for the UOKS. Furthermore, the secondary objective was to evaluate the accuracy, precision, reliability and validity of the newly automated system.

Six transmission units were designed, built and tested as part of the development of the automated mechanism adapted to the UOKS. Load cells were used to obtain real time feedback of the load created by the transmission units. A software controller was programmed using LABVIEW to control these transmissions as a graphic user interface (GUI). Each transmission was tested independently and compared to an external master load cell. Furthermore, four cadaveric knee joints were mounted and suspended inside the UOKS for experimentation. Seven different loading conditions were tested with the ACL intact and after the ACL was severed. Pressure and kinematic data were recorded to correlate the changes in these variables due to changes in loading conditions simulated by the UOKS.

The controlled loading experiment of the automated mechanism showed the accuracy of the controller to be within +/-1N, and multiple trials showed the system's capability to produce loads. Additionally, the results showed the controller to have an ICC of 0.99 between the load produced

and the target load. The comparison between feedback load cells and the master load cell displayed unique results regarding each transmission and the loads being applied. The results showed overestimations and underestimations with unique load difference trends for each transmission. Nevertheless, the relative difference measured by the master load cell was below 10% in all the transmissions.

This study demonstrated that the controller was accurate and reliable when producing loads. On the other hand, the results of the integration analysis showed the presence of losses in the system when transmitting the loads from the actuators to the front of the UOKS. These losses were different for each transmission, likely due to the independence of each pulley system. Nevertheless, the automated loading mechanism proved to be a valid replacement for the original static loading mechanism previously used by the UOKS and is capable of reliably simulating six independent loading conditions.

Acknowledgements

This work represents one of the things that I never thought I could possibly do. Without the help of many people this work would have been a lot harder and without the proper acknowledgements this would not have the same value to me. I would like to first thank my supervisor, Dr. Daniel Benoit, who took me in as a student with zero experience in research. Under his wing he taught me that I can take on any challenge and that is okay to ask for help and not knowing everything. Your constant support and encouragement could not have been any better to force me outside of my comfort zone.

To the lab (CBRU) where I found more than just lab mates: Teresa Flaxman, Brent Smale, Olivia Bayliss-Zajdman, Michael Del Bel, Olivier Miguel, Laryssa Kemp, Celine Girard and Nick Romanchuk. I found long time friends and some of the most incredible peers I could ask for. Thank you all for taking me as an outsider and making me feel like one of you. All of you contributed to this work with your constant support, feedback, review, critical thinking and admiration.

To the Orthopaedic Biomechanics Lab, where I spent countless hours working, making noise, breaking things and building things. To Hakim Louati, for whom I have nothing but admiration and respect. To Kate Culliton, thank you for your support and advice.

To my parents, thank you for your endless love and support no matter the endeavor. All my life you showed me that no matter the circumstances I should never give up and that I should always strive to better myself. Thank you for putting me through the best education a son could ask for, for all the countless sacrifices and the years of hard work. To my sister, who I have always

admired for accomplishing so many things that I could only dream of. You always showed me the way and lead me through the right path when I was overthinking. Thank you for always taking the time to give me your input and speaking up your mind when I needed it to. To my brother, who I admire for being there for me and who I will always love and appreciate. Thank you for your support.

Finally, to the most important person in my life, my best friend and my partner in crime. Karen, without you none of this would have been possible. You sacrificed so much and left everything behind to join me in this crazy cold adventure to look for a brighter future. Thank you for putting up with my constant complains, my ‘’selective ‘’ deafness, rushed decisions and for trusting me in what can only be described as a crazy ride. I will never have enough words to express all of it.

Table of Contents

List of Tables

List of Figures

Introduction

The anterior cruciate ligament (ACL) is one of the four main ligaments inside the knee joint and it is considered to play a major role in the overall joint biomechanics by maintaining joint integrity [1]–[3]. It is estimated that more than 120,000 people injure their ACL every year in the United States [4], [5] and it is considered one of the most commonly disruptive injuries that are reported. The long-term changes caused by ACL injuries are believed to be linked to the onset development of knee joint degeneration, also referred to as osteoarthritis (OA) [6]–[8]. Early symptoms of these conditions include biological changes that often lead to inflammation, and in extreme cases of OA, there are reports of bone marrow lesions, degeneration of cartilage and severe pain. The changes caused by the degeneration of the knee are reflected in a decrease in range of motion of the joint and have a negative impact in the physical activities, thus causing a decline in quality of life.

Understanding the damage and consequences of ACL injuries has been crucial in the development of clinical treatments to improve a patient's overall quality of life. One of the most generally practiced methods involves rehabilitation therapies that focus on the development of muscle strength and memory. Muscle activity provides stability and stiffness through the creation of loads and moments around the knee joint [2], [3], [9]–[16], and is believed that alterations to their functionality can also have an impact on knee stability.

Ligaments and muscles work together in complementary roles and provide passive and active mechanical constraints that result in a healthy mechanical environment for the articular cartilage Understanding the "normal conditions" in which the knee joint functions has led orthopaedic research to investigate the joint's contact mechanisms, such as contact area and contact

pressures between the two bones of the tibiofemoral joint. However, the number of studies that have explored the effects of muscle load on knee joint contact mechanics before and after ACL injuries are scarce in numbers and limited in results [14], [17]–[19].

The role of individual muscle loads, their modulation and the effects on knee joint contact mechanics have yet to be explored. Thus, there is currently a gap in the literature on how muscle loads affect the mechanism to maintain stability during various functional tasks. Therefore, understanding the contributions of muscles loads becomes of interest as it may help improve the understanding of the consequences of altering passive and active components of the knee joint. However, the simulation of these active components is not without difficulties for in vivo studies.

To overcome these obstacles, in vitro simulators are an alternative methodology to understand and expand the knowledge of knee joint contact mechanics. The possibilities of designing and building systems to simulate and control multiple conditions are valuable tools in biomechanics research. Thus, it is believed that a better understanding of the roles of muscles and contact pressure could be best investigated by implementing an in vitro simulation. The aim of this thesis was to develop an automated quasi-static loading system for the already established in vitro knee joint simulator, The University of Ottawa Knee Simulator (UOKS), by implementing custom hardware and software to simulate muscle loads. In addition, the work in this thesis addressed the validity of the new system to modulate accurate muscle loads and its application to the study of simulated joint contact pressure.

Chapter 1. Literature Review

1.1 The knee joint: Overview and Components

1.1.1 Bone Geometry

The knee is the largest joint in the human body and its functionality is determined by the complex interaction between supporting structures (soft tissue), bone geometries and neuromuscular control. The knee is formed by three bone components: the femur, tibia-fibula, and patella. The distal extremity of the femur is formed by two oblong eminences called condyles (medial and lateral) which interact with two concave opposing geometries (medial and lateral) on the tibia known as plateaus. The presence of the cartilaginous tissue on the femoral condyles (anterior, inferior and posterior surfaces) and tibial plateaus facilitates sliding motions during movements such as knee flexion. These bone structures are held together by connective tissue surrounded by a fibrous membrane known as the synovial capsule.

1.1.2 Passive components

The knee joint is held together by supportive structures known as ligaments. Ligaments are made of connective tissue with fibers that run parallel to each other, and as in any other joint, they serve the purpose of connecting bones. Additionally, ligaments play a major role in constraining relative motions between bones. Thus, it is reasonable to mention that the mechanical capabilities of the knee, to some extent, are dependent on the condition and integrity of the ligaments.

The knee joint is formed by 4 main constraining ligaments: The medial and lateral collateral ligaments (MCL and LCL), anterior cruciate ligament (ACL), posterior cruciate ligament (PCL) and

a load-bearing structures known as the menisci. The collateral ligaments are located on the sides of the knee joint, and hence the name of each ligament. These ligaments connect the epicondyles of the femur with the tibial condyles and in the lateral aspect of the joint, the LCL also attaches to the apex of the fibular head. In contrast, the ACL and PCL are located inside the knee joint and have insertion points in the surface of the tibial plateaus and on the inner surface of the intercondylar fossa of the femoral condyles. The ACL resembles a set of parallel fibers with insertion points located on the medial posterior surface of the lateral epicondyle and continues to connect with the intercondylar eminence of the tibia and with the anterior horn of the meniscus. Similarly, the PCL originates on the posterior lateral surface of the medial condyle and the intercondylar notch, then it continues to the posterior intercondylar section of the tibia.

Unlike these ligaments, the meniscus is located on the outer periphery of the tibial plateaus forming a crescent-shaped pad, which can be divided in the medial and lateral meniscus, and further subdivided into posterior and anterior horns. The form of the medial meniscus can be described to be similar; to a loop, whereas the lateral meniscus has a C shaped form. The shape of these structures helps support the contact between the femur and the tibia by increasing the contact area, reducing the stresses experienced during loading and reducing shear forces by limiting the amount of movement between bones [20]–[22].

These ligaments are capable of resisting motions in multiple planes and contribute to the overall stability of the knee by maintaining a safe range of motion [1]–[3]. For instance, internal rotations and medial to lateral translations can be affected by sectioning of the collateral ligaments, increasing the range for these motions [3]. Similarly, the ACL and PCL contribute to limit the anterior and posterior translations of the tibiofemoral joint in the sagittal plane [3], [10];

and while the ACL's primary role is to limit the anterior tibial [10], [23]–[25], this ligament can also resist internal/external and varus/valgus rotations, nevertheless it is considered a secondary resistor of these motions [26]–[28]. Moreover, the menisci serve as a load-bearing structure between condyles and tibial plateaus [20], [29], it can also serve a secondary role in maintaining anterior and external rotation stability [3].

1.1.3 Active Components

Knee joint mechanics are also influenced by muscle activity, and in the same way as ligaments, their integrity and functionality can affect the overall performance of the joint. Muscle tissue crosses the knee joint from the femur to the tibia to build an active actuation mechanism that makes the joint move. The muscles attach to the bones with an inelastic connective tissue known as tendon. The points in which the muscles attach are known as the origin and insertion points. The origin is used to describe the point where the muscle actuation is fixed, whereas the insertion is used to describe the end of the muscle and where forces are applied to create movement. For this reason, the muscles of the knee joint are considered the active components of the joint, providing a dynamic control that results in movement and/or stability of the joint during a dynamic task or in situations where external forces compromise knee integrity.

The knee joint active control system is formed by three main muscle groups: the quadriceps, hamstrings, and gastrocnemii. The activity of these muscles has been found to play an important role in joint movement by creating moments that along with ligaments contribute to the overall stability and stiffness of the joint during dynamic tasks [2], [3], [9]–[16]. Each of these muscle groups is formed by subsets of individual muscles. The quadriceps are divided into four heads: vastus lateralis (VL), vastus medialis (VM), rectus femoris (RF) and vastus intermedius, and this

muscle group is responsible for the production of extension moments. Flexion moments acting around the knee joint are created with the contraction of the individual heads of the hamstrings: the semitendinosus (ST), semimembranosus (SM) and biceps femoris (BF). Additionally, the medial and lateral heads of the gastrocnemius (MG and LG, respectively) also contribute to flexion moments of the knee joint. Together, these muscles provide the dynamic stability to the joint that is required to perform activities of daily living without overloading the passive constraints or producing non-physiological, injury inducing joint motions [12], [14].

1.1.4 Knee Kinematics

The interaction between the condyles and the plateaus attributes the knee a complex modified hinge-like mechanism allowing the knee to move in six degrees-of-freedom (DOF) [30]. The complex modified hinge mechanism of the joint is reflected in the capabilities of the knee joint to experience six different types of movements that can be described by three clinical rotations and three clinical translations.

The geometry of the femoral condyles and tibial plateaus facilitate rotational movements in the sagittal plane, known as extension-flexion rotation, which is about the axis formed by the horizontal line in the frontal plane connecting both femoral epicondyles. Extension of the joint occurs when the alignment of the two longitudinal mechanical axes of the tibia and femur in the sagittal plane is increasing towards an approximate maximum at 180 degrees of separation, while flexion of the joint is when this angle is being reduced between the two mechanical axes. This rotation is considered to encompass a full range of motion from of 160 degrees [31]. Additionally, the bone geometry of the tibiofemoral joint also allows for internal-external rotations in the transverse (horizontal) plane with the center of rotation located about the longitudinal

mechanical axis of the tibia. This rotation of the tibia is considered with respect to the femur, which is based on how the tibia rotates towards the midline (internal rotation) of the body or the opposite movement (external rotations). This motion can reach up to 30 degrees to both internal to external directions. Furthermore, a third rotation can be defined in the frontal plane and about a floating axis that is perpendicular to the mechanical axis of the tibia and the horizontal axis of the femoral epicondyles, known as varus-valgus rotation of the knee. The movement is represented as an angulation of the distal end of the femur toward the midline of the body, where the varus rotation moves the distal end away from the midline of the body and the valgus rotation being the opposite, meaning that it moves the distal end of the bone towards the midline of the body. The largest difference in the range of motion of these rotations can be obtained during full extension of the joint and can reach up to 10-15 degrees of motion[32]–[34]. This rotation has been associated with the development of OA in the knee joint, as it has been found that alterations in the angulation of the valgus position of the femur can shift the loads of the knee towards the medial compartment of the tibia [32]–[34].

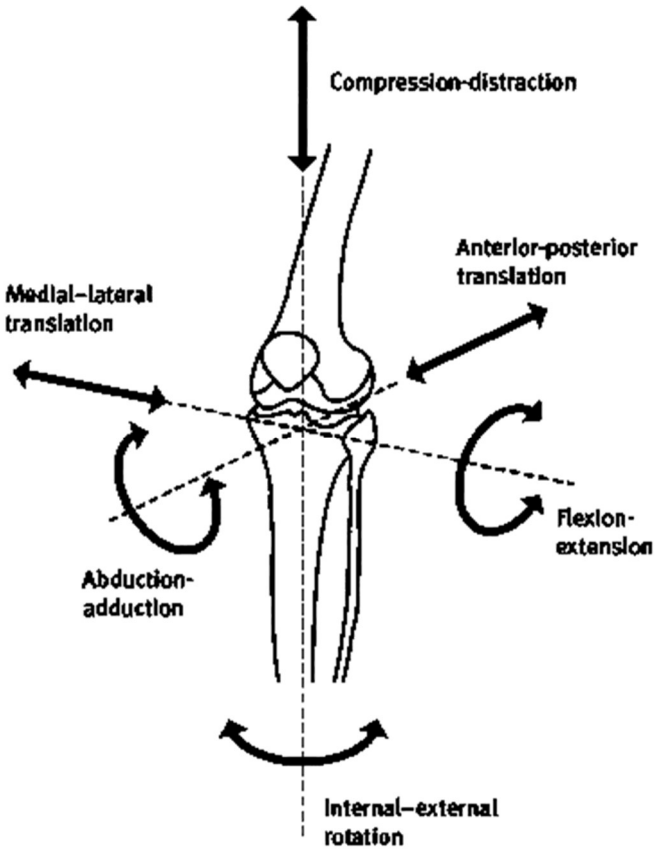

Figure 1. Degrees of freedom of the knee. The joint encompasses three rotations and three translations [31].

Knee joint kinematics can also be described with three clinical translations between the tibiofemoral bones of the joint. These translations describe the sliding motions of the femoral condyles in the anterior-posterior and medial-lateral direction on top of the tibial plateaus. The third translation of the knee is known as compression-distraction and describes the movement that increases or decreases the joint space between the femur and the tibia in a vertical upward/downward motion. In contrast to knee joint rotations, the range of motion between of

the clinical translation can vary between individuals and it is often influenced by the passive and geometrical constraints imposed by knee joint components [3], [35].

Within the scope of this document, joint stability can be defined as the range of motion of the knee joint in which it can freely move without compromising structural integrity of the components that make up the joint, and so limiting the range of motion of joint kinematics is an essential role that ensures the integrity of the knee.

Ligaments provide mechanical constraints that limit the range of motion and contact mechanics. Particularly, soft tissue and ligaments provide passive resistance to limit joint movement [10], [28], [36], [37]. For instance, disruption of the passive stability of the knee can lead to alteration of range of motion and joint loading [2], [3], [27], [28], [35], [38]–[42].

Transection of the ACL has been found to cause significant changes in anterior translations, showing an increased variability in anterior motions when compared to an intact specimen [35]. Moreover, ligaments are capable of resisting motions in more than one plane, often referred to as secondary roles, contributing to overall joint stability. The ACL is considered to resist internal tibial rotations as it can provide up to 13% of the rotational resistance when the tibia experiences internal tibial torques [43]. Similarly, a different study used MRI, dynamic stereo x-ray and in-vitro simulation to study the role of ACL during a dynamic flexion [38]. Their results showed that ACL deficiency caused an increase in anterior tibial translation and internal rotation in comparison to ACL intact conditions. Additionally, performing meniscal transections resulted in an increased knee joint laxity in varus-valgus, anterior-posterior, medial-lateral, internal-external rotation (Markolf et al., 1981). These findings indicate the importance of this ligament integrity on maintaining knee stability.

Muscle activity contributes to joint stability by providing active support and the necessary internal moments to resist external moments [2], [12], [50]–[52], [13], [18], [44]–[49]. In particular, the active components of the knee joint (muscles including the gastrocnemii, hamstrings, and quadriceps) are believed to maintain stability around the joint during dynamic and isometric activities such as weight-bearing [13]. Quadriceps muscles have higher activation when opposing pure extension during isometric knee extension and hamstrings activation is higher when opposing flexion moments during isometric knee flexion [12], [53]. Moreover, tibial internal rotations can be reduced by flexion moments created by the hamstrings [53]. Likewise, Lloyd and Buchanan (2001) reported high activation levels of the quadriceps and hamstrings during isometric tasks and attributed the prevention of large varus moments to the creation of the opposing moments by these muscles. They also suggested that the mutual activation of these muscles generated greater forces than each muscle at the individual level, equalizing the external moments. This last concept is known as co-contraction and it is a mechanism that has been suggested to produce the forces responsible to resist external forces that can compromise joint integrity. For instance, co-contraction of the gastrocnemius and quadriceps creates greater forces than each of these muscles individually and is believed to equalize flexion and extension moments and resist varus-valgus moments [12], [54].

1.1.5 Joint Loading

The knee is subjected to different loading conditions from simple, yet cyclical activities that create repetitive loads on the joint. Activities such as walking have been found to create high knee joint loads, reaching values from 2.6 up to 3 times those of the body weight (BW) [11], [51], [55] and, needless to say, dynamic activities such as running and stair climbing create even higher

loads than those during walking [56]. Furthermore, load distribution inside the joint is divided between the two compartments of the knee. For instance, the medial compartment of the joint experiences higher loads in comparison to the lateral counterpart [11], [55], [57]. Nevertheless, load distribution is not always maintained in the same ratio, as it depends on factors such as joint angles, body weight (BW) and the activity being performed [11], [55], [57], [58]. Joint angles produce different bone interactions that could lead to unloading of certain sections of the tibial plateaus. Mündermann et al. [55]found that external adduction moments unload the lateral compartment of the knee during gait cycles, thus increasing medial loads on the knee.

Joint compressive loads and muscle contraction influence loading by compressing the joint and increasing the stiffness of the knee. Unlike joint compressive loads caused by gravity and BW, the dynamic behavior of muscles allows for specific directional forces to create an active loading mechanism that results in joint stiffness [18], [19], [59]. What is more, Yack and colleagues (1994) demonstrated that the effect of combined compressive forces and muscle contractions on subjects with a previous history of ACL injuries have a significant effect on joint stiffness. Their results showed that anterior tibial translations were significantly lower when the joint experienced compression and 30% of the maximum activation value of the quadriceps when compared to an anterior drawer test with no loading. Nevertheless, the results of this study showed that the combination of compressive forces and quadriceps-hamstring co-contraction did not create a significant effect on tibial anterior translations when compared to the combination of compressive force and quadriceps activation. Similarly, the combination of joint compressive loads and quadriceps loading were found to limit tibial translations during a

simulated in-vitro study by Torzilli et al.[18]; highlighting the significant contribution of muscle contractions to increase stiffness of the joint.

1.1.6 Contact Pressure

The bones of the knee joint are in constant interaction during activities that involve the movement of the lower extremity. In a healthy knee joint, the cartilage tissue of the tibiofemoral joint is in a continuous state of stress, and thus going through constant remodeling or self-healing. Nevertheless, it is believed that disruption of the contact pressure mechanics, such as peak forces, contact area, and pressure distribution are factors linked to the onset of joint degeneration and this process is accelerated following ACL injury [60]–[62].

1.1.6.1 Contact Area and Pressure

There are differences between the contact area and pressure distribution inside the knee joints compartments. Interestingly, studies have shown the medial compartment of the knee joint to have greater contact area in comparison to that of its lateral counterpart [63]–[66]. However, the difference in contact area between the medial and lateral compartments of non-injured knees decreases as the overall compressive load experienced by the knee increases [63]. This indicates that an increase in compressive loads has an effect on the overall ratio of contact area shared between the compartments, and thus distributing the pressure. Unlike the contact area interaction between the compartments, the lateral compartment of the joint experiences higher pressure values in comparison to the medial compartment [67]. Nevertheless, the medial compartment experiences the most pressure outside of the meniscus and localized closer to the tibial spine, however the load bearing role of medial meniscus is of great importance as it experiences high pressure values on the posterior horn [67].

Alterations to contact pressure mechanics between the tibia and femur after ACL and meniscii injuries result in significant changes to contact area and pressure distribution. These differences in contact pressure mechanics have been suggested to result in high stresses that are believed influence the onset and acceleration of joint degeneration [11], [29], [74], [61], [62], [68]–[73]. These interactions between the femur and tibia are highly dependent on the condition of the meniscus, and so meniscal injuries directly affect contact area and peak pressures experienced during load bearing activities. This indicates a direct load-bearing role of the meniscus, which has been well established in the literature. The lateral compartment of the knee joint is highly dependent on the load-bearing capabilities of the lateral meniscus, as it provides a mechanism to increase the contact area of the compartment and provides support for the compressive loads of this compartment [67]. Additionally, partial or complete meniscectomies have been found to decrease contact area [42], [63], [75], [76] and to increase peak pressures in both compartments [21], [63], [77], [78]. Furthermore, ACL injuries have been found to result in changes to knee alignment, affecting the contact mechanics of the joint. For instance, patients with ACL deficient knees have shown adapted gait patterns with significant varus angle differences when compared to a non-injured population. The altered alignment patterns are believed to increase the lateral condyle lift off, thus increasing medial compartment loading [79]. Thus, the risk of developing OA was reported to increase from varus alignment, suggesting that bone position and orientation may also influence contact pressure mechanics, such as increased peak pressures in the medial compartment [33]. Similarly, a previous study investigated joint loading in different joint positions, and found increased magnitudes of contact pressure on the medial compartment with varus alignment [29].

Additionally, ruptures of the ACL have been associated with neuromuscular differences that affect the contact interactions of the knee joint [80], [81]. Muscles are the active loading components of the joint and failure to achieve proper stability could lead to OA development [82], [83]. Alkjær and colleagues [84] compared compression and shear forces between ACL-deficient and uninjured participants during walking. Their results show that ACL-deficient participants had a new muscle activation strategy and experienced less antero-posterior shear forces on the tibial plateau during the first 20% of the gait cycle. Particularly, this was suggested to be related to a decrease in peak compression forces at specific stages of the gait cycle (heel strike and toe off) and is related to less muscle activity in ACL deficient patients that produce less compressive forces and less rotations moments around the knee joint [84]. Together, these studies highlight the need to consider knee joint contact mechanics when evaluating muscular contributions to joint stability and the potential relationship between injury to the ACL and the development of knee joint OA.

1.1.7 Measurements of Contact Pressure

Currently, the accuracy and reliability of measuring physiological knee joint contact pressure are limited due to available technology and methodological capabilities, especially during in-vivo studies. Measuring contact pressure during in vivo protocols becomes difficult as there are few available instruments capable to measure contact forces. Direct measurement of the forces between the bones in vivo is not feasible as it would require the use of an invasive technique to insert sensors inside the joint space which could also alter contact pressure mechanics. Nevertheless, there have been attempts to measure in vivo forces by introducing instrumented knee implants inside of knee prosthetic replacements [55], [56]. During these studies, only a few

participants were included, thus making it hard to draw conclusions to be representative of the population. Additionally, these studies did not address the limitations surgery implantation techniques and implant design on joint biomechanics [85]–[88]. Moreover, accurate instrumentation is required to meet health and safety regulations and can be associated with high costs, as well as operational concerns, making it difficult for researchers to involve more participants in larger studies.

As an alternative, computer modeling and simulations have been developed to overcome the limitations of in vivo protocols for testing knee joint mechanics. However, a different limitation arises with these methodologies, as there is a need for input data to feed the simulation models. For instance, these methods have been used to model and estimate contact loads for each of the tibial compartments of the knee during a gait trial [11]. Their model used EMG data from in vivo protocols to feed the loading conditions at specific times of the stance gait cycle. Additionally, several parameters had to be established for the model to function, such as anatomical segment relationships and scaling of the input to the specific anatomical model. Their results showed that different contact force interactions were experienced by each of the compartments along the gait cycle and attributed specific muscle contributions to those changes in contact forces during the stance cycle. Other applications of these models have been used to estimate the biomechanical outcomes of using different tibial tubercle elevations, in particular to patellofemoral contact forces under specific loading conditions at different flexion angles [86]. This model was built as a finite element reconstruction of cadaveric knee joints and includes parameters such as mechanical properties, articular cartilage layer, and ligaments. This study found that a higher tibial tubercle elevation (2.5 cm) had a higher impact on patellofemoral

contact forces under isolated quadriceps loads. These studies indicate the potential uses and implications of the benefits of using in silico methods for the study of contact forces, nevertheless, these are not without limitations. Computer models depend on the driving equations and the inputs used feed said equations. First, these equations are the link between the physiological interactions of the system and outputs of such models, and like any other method, models must be validated before drawing conclusions from their results and this becomes difficult as these models cannot be directly validated. Additionally, these equations are often built on assumptions that facilitate their applicability. For instance, the model built by Winby et al. [11] was used to report contact forces on tibial compartments, but only considered the forces that were affected by forces parallel to the main axis of the femur.

1.1.7.1 Pressure Sensing Technology

Pressure sensitive technology is considered a standard tool in the study of contact pressure mechanics. One of the first reported studies involving the use of pressure sensitive technology provided direct measurements of contact pressure and pressure distribution inside the joint during in vitro testing [63]. This study used a pre-scale pressure sensitive film technology (Fuji Film Co.) consisting of two thin polyethylene film layers and a middle layer of microcapsules filled with red dye, which would be released when experiencing a specific pressure threshold that could break the microcapsules. The density of red color on the films is then measured with a densitometer to obtain pressure values. This technology has demonstrated to provide accurate measurements with a 10 % error, however it can only provide the highest-pressure values that occurred over time.

In recent years, Tekscan systems (Tekscan, Inc., South Boston, MA) have developed digital pressure sensitive films that address limitations of pressure films. Tekscan sensors incorporate the use of digital technology to store, process and display data in a much organized and convenient manner. This technology is based on the use of piezo resistive transducers which change electrical properties when subjected to specific loads [89]. The matrix configuration of the transducers allows Tekscan sensors to provide and record real time data of pressure and contact area. Additionally, Tekscan sensors can be sterilized and reused for in vitro testing without affecting reproducibility and accuracy, however a proper calibration is required before each use [90].

Research has shown that Tekscan sensors are reliable systems when it comes to measuring contact area, forces and pressure. Tekscan digital technology provides significantly less error when compared to Fuji films analog technology [89], [91]. The study by Bachus et al.[89] compared contact area, force and pressure measurements obtained from these technologies to known values. For the present thesis, Tekscan provides the means to record changes in contact area, pressure and peak pressure during simulated muscle loading

Tekscan sensors are well suited for the study of pressure distribution inside the knee joint. Multiple studies have demonstrated the validity and accuracy of this pressure sensitive technology [89], [91]. However, the reliability of the measurements is highly dependent on the preparation process prior to the use of the sensors [92], [93]. There are three basic operations recommended by manufacturer to prepare the sensors for a data collection: conditioning, equilibration and calibration. Conditioning the sensor helps to decrease the effects of drift and hysteresis. Tekscan recommends the users to condition all sensors with a load that is 20% greater

to the maximum expected load during cyclic load test three to five times. Additionally, it is also suggested to use a material with similar compliance to the actual material that will be use in the application of the sensor.

The calibration operation must be executed to ensure proper and accurate readings from the sensor. There are two basic calibration operations that are suggested by the manufacturer of the sensors. The first method lies in the assumption of the linear behaviour of the sensor and a pair of known loads is applied to calculate a linear interpolation. This method is suggested when the loads expected during the application of the sensor are within the range of the known applied calibration loads. The second method, known as a power calibration, uses two known loads to calculate a power law interpolation and is recommended when the loads are expected to vary between 20% and 80% of the maximum expected test loads. The accuracy and error of these two methods has been reported by Brimacombe and colleagues [93]. The results showed the average RMS Error for both calibration methods and demonstrated that the power calibration resulted in an average RMS error of less than 4%.

Chapter 2. University of Ottawa Knee Simulator

2.1 In vitro Simulators

Multiple techniques have been implemented with the intent to accurately measure and describe the interactions inside the joint, such as; radiographs and radio fluorescent contrasts [94], [95]; Magnetic Resonance Imaging (MRI) along with computer algorithms [69], [96]–[101]; instrumented knee prosthetics [55], [56], [102], [103]; silicon rubber molding [64]; pressure sensitive films [34], [104]–[111]; mathematical modeling [11], [14], [112] and digital piezo resistive transducers [20], [21], [66], [68], [78], [85], [113]–[116]. Nevertheless, these technologies are not without limitations. For instance, mathematical models assume ideal scenarios and conditions to avoid complicated and resource intensive computer iterations. Techniques based on image analysis provide detailed pictures of the interactions between bony structures, nevertheless the product of these techniques do not provide enough information to objectively quantify dynamic contact mechanics. For instance, MRI reconstructions have been found to produce reliable results when compared to standard methods [117], however image reconstruction with this method only enables the capturing of a static scenario. Additionally, cost of operation and availability of MRI scanners becomes one of the limitations of using this technology.

The use of in vitro set-ups has proven to be a valuable tool, which present an alternative to increase the knowledge and understanding of knee joint contact pressure mechanics [18], [114], [118]–[123]. The logic behind these simulators is based on the principle of applying an input that will cause a specimen to act according to its own physiological constrains. There are two main

types of in vitro simulators based on the type of input: load driven and kinematic driven, and as their names imply, these are run by either a load or kinematic profile. The output of each type of simulation depends on the motivation behind their design and construction. For instance, Torzilli et al. [18]used a mechanical load driven simulator to describe the response of anterior posterior (AP) knee stability to externally applied forces. In vitro apparatuses also have been used to simulate joint motions, as developed a machine to simulate kinematic profiles in cadaveric knee joints. Wünschel et al. [114] used an in vitro set up to simulate quadriceps loads on cadavers to measure tibiofemoral joint kinematics and patellofemoral contact pressure. Other examples of simulators are the Kansas knee simulator design by the Experimental Joint Biomechanics Research Laboratory [120], and the Tubingen knee simulator [124]. Even though these are only a few of the many reported simulators, in vitro simulators are still far from being perfect, as they have inherited limitations. For instance, load driven simulators try to leave kinematic responses unconstrained to study the relationship of loads on such responses. However, most simulators have been limited to one degree of freedom motions. Furthermore, the load profiles used to run the simulations are obtained from complex and elaborated mathematical models that do not consider a 6 DOF unconstrained motion. This introduces uncertainty towards recreating true physiological conditions, thus affecting the validity of the results [125]. Moreover, kinematic driven simulators that use robotic arms to secure the knee joint (femur and tibia) to study knee laxity and the strain of supporting structures, lack the active components of the knee joint (muscles). The lack of an active component contributing to the knee's stability raises the question of viable results, nevertheless, the results of in vitro studies have contributed to the literature by

providing input data for more elaborated simulations such as finite element models and mathematical models [14], [126].

In vitro simulators can provide an alternative method to reproduce the same conditions across specimens, ensuring that all experimental conditions are maintained between specimens and within the same experiments. Moreover, cadaver manipulation is a viable option when procedures are unethical or involve permanent alterations such as structural manipulation or permanent transection of ligaments. Additionally, the outcome from in vitro experiments can be translated into the clinical field as the similarities in mechanical properties, material properties and geometric interactions of cadaver specimens are comparable to those of live tissue [127]. Moreover, cadaver specimens can be manipulated or altered during testing for many experimental conditions to be explored and to limit inter-specimen variability.

2.2 University of Ottawa Knee Simulator

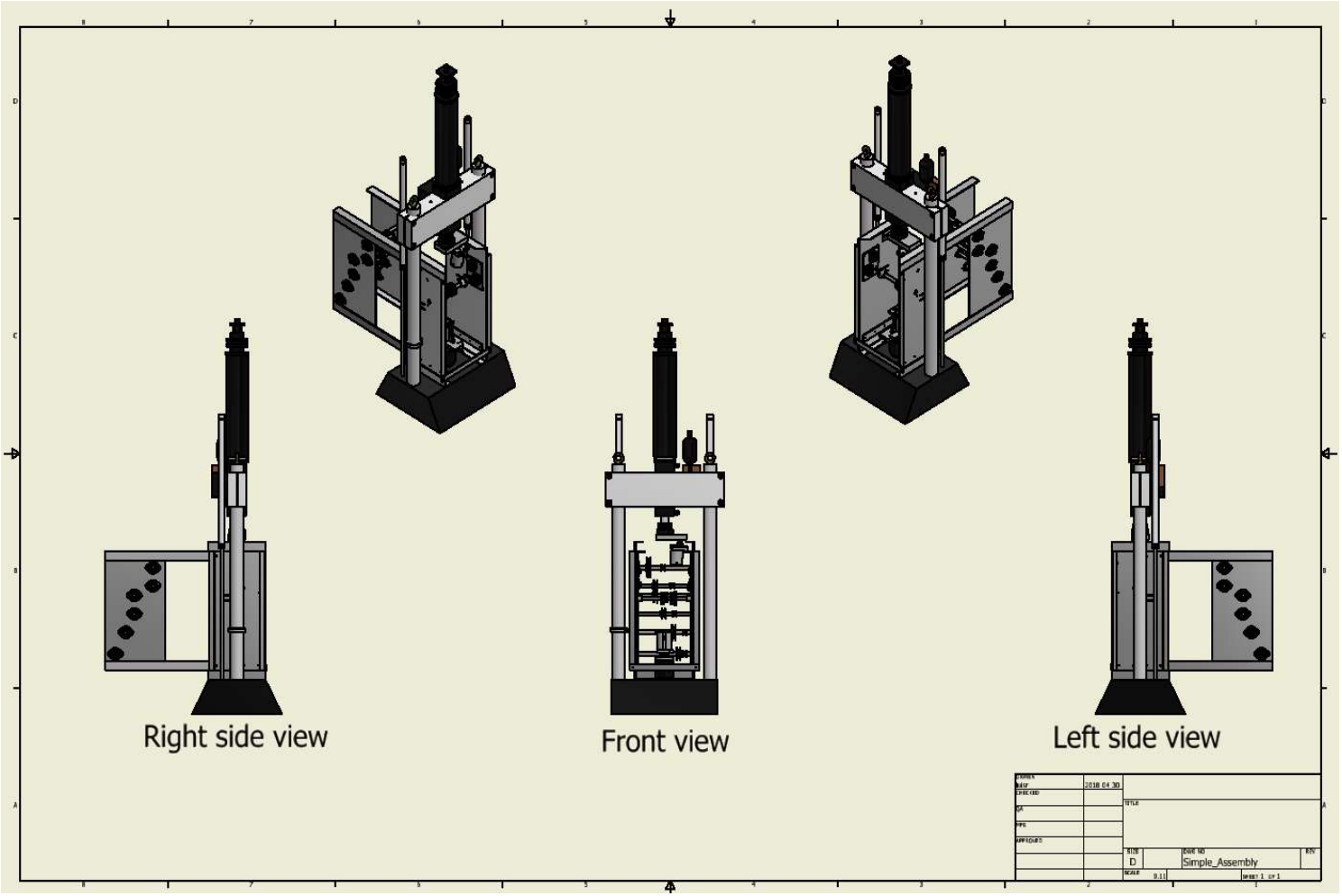

Figure 2. Previous iteration of the UOKS mounted on the MTS machine.

The development of this simulator is an on-going research project that started with the work and contributions of Dr. Andrew Speirs, the team at the Orthopaedics Biomechanics Lab and the Clinical Biomechanics Research Unit at the University of Ottawa. The UOKS was design as a quasi-static simulator capable of loading human knee joints without constraining the kinematic response. The loading mechanism was capable of simulating six independent muscle loads, Medial Quadriceps (MQ), Lateral Quadriceps (LQ), Medial Hamstrings (MH), Lateral Hamstrings (LH), Medial Gastrocnemius (MG) and Lateral Gastrocnemius (LG). The simulator applied these loads through hanging weights connected to a system of pulleys and steel wires attached to a specimen. The muscles were chosen to recreate the muscle groups believed to provide most of the forces necessary to achieve knee joint stability. In addition, the simulator has a structural frame that provides the flexibility of interfacing with a testing machine (MTS Bionix 585, MTS Systems, MN, USA) to apply accurate bodyweight forces through a 2 degrees of freedom (DOF) hydraulic actuator.

2.3 Components and configuration

2.3.1 Mechanical Frame

The UOKS is made of two sections and a set of custom-made fixtures. The main section is made of a frame that constructs the “skeleton” of the apparatus. This skeleton serves the role of structural support and assembly points for the loading chamber, the pulley system and the vertical actuator (MTS machine). The material used for most of the structural components of the simulator is aluminum, chosen due to its resistance to corrosive substances involved in the use of in vitro protocols. Additionally, the properties of this metal make it lightweight, facilitating the manipulation of simulator components before and after experiments. As seen in Figure 3, the

frame of the simulator is made of aluminum angle bars welded together to build a box like structure.

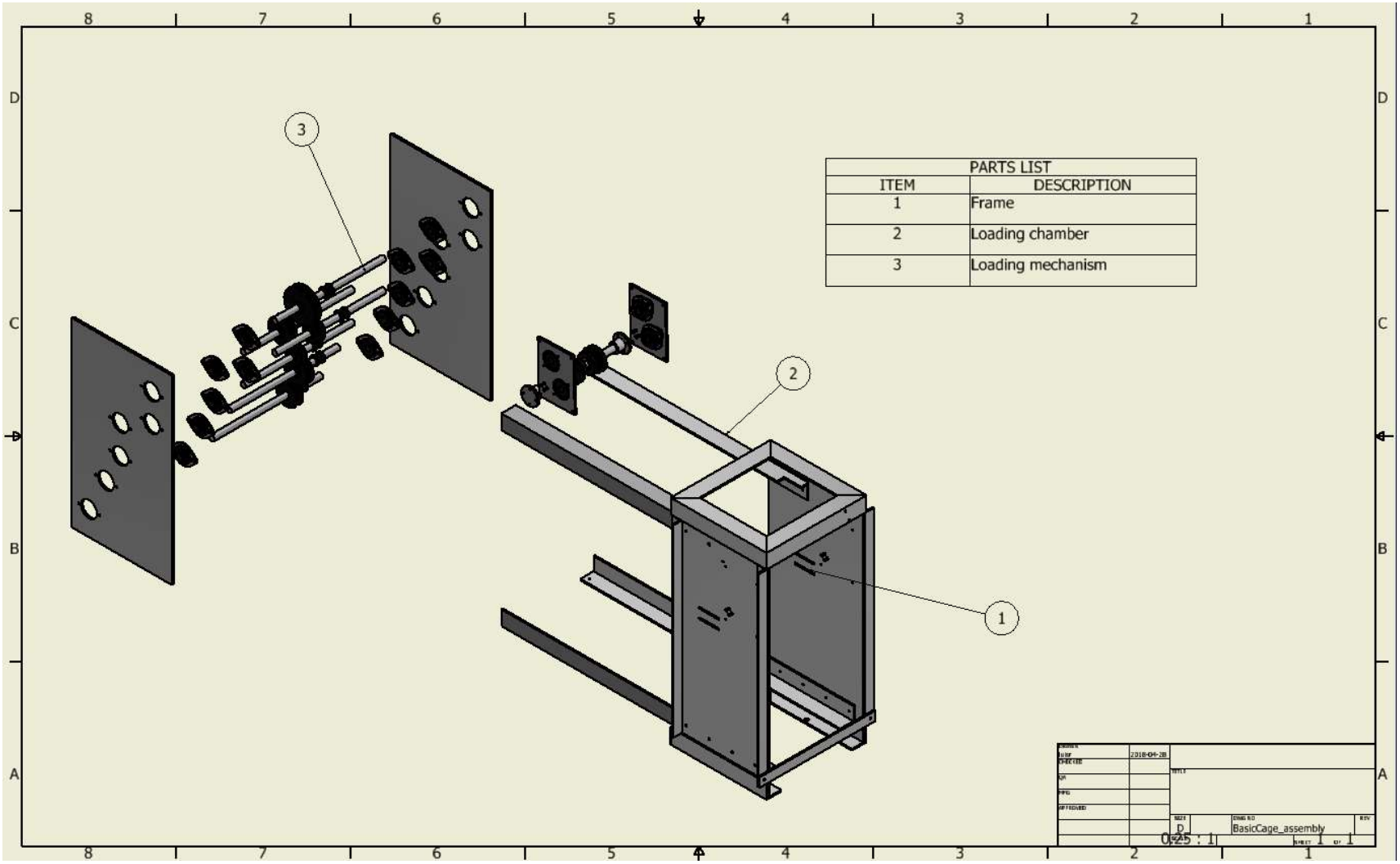

Figure 3. Exploited view of the three main components of the simulator.

The front section of the simulator houses the loading chamber, as well as the mounting holes to fix the frame to the MTS testing machine. Two ¼ inch aluminum plates are attached to the skeleton to provide support for the loading mechanisms as seen in Figure 3. These plates form the right and left walls of the apparatus. Both the top and bottom sections of the frame have two openings to accommodate the MTS components: the hydraulic actuator and a vertical load cell. Particularly, the top area of these sections has the flexibility to allow multiple spatial configurations to suspend and secure the cadaver specimen without interfering with any of the simulator's components. Additionally, the front section of the frame allows an open view of the specimen when suspended. This feature also allows the visibility of the motion tracking tools necessary to capture kinematic responses during protocol executions.

2.3.2 Loading Chamber and Loading Mechanism

The loading chamber houses a pulley system and the custom-made fixtures necessary to secure and suspend the specimen during testing. The pulley system located in this section consists of two fixed stainless steel (SS) ¾ inch shafts with two pulleys (each) and a position adjustable SS shaft with four aluminum pulleys of different dimensions (Components 9,11,12,13 in Figure 4). The fixed loading hafts are located at the most outer front part of the system and function as a load driving mechanism to load the specimen. The front shafts are used to transmit the load of the following muscles: Medial Quadriceps and Lateral Quadriceps.

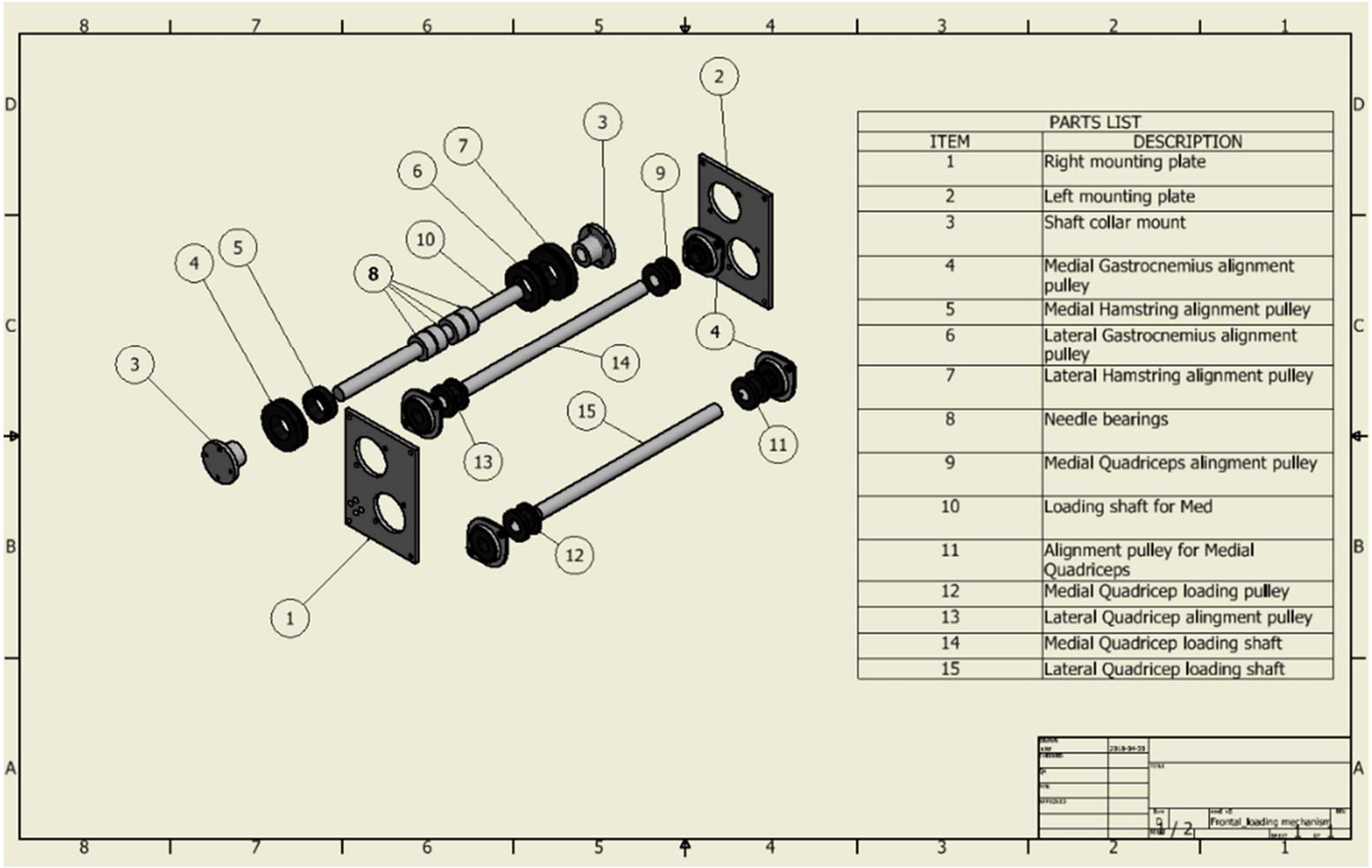

Figure 4. Exploited view of the loading shafts inside the loading chamber of the simulator.

Each of these shafts are mounted to eccentric collar locking bearings on each side. The pulleys on each of these shafts are made from 6061 aluminum and can be adjusted along the longitudinal axis of the shafts for an appropriate physiological representation of muscle line of action. Additionally, the pulleys and the shafts have a keyed joint to lock them in position and securely transmit the load generated through the loading mechanism components at the back of the simulator. For ease of manipulation the front shafts and the bearings are mounted into two ¼ inch aluminum plates. This modular design provides a quick way to detach the plates from the loading chamber frame and properly position and suspend the specimen into the loading chamber if needed.

The other shaft is used to route the loads for the following muscles: medial hamstrings, lateral hamstrings, medial gastrocnemius and lateral gastrocnemius. The shaft is found separately from the quadriceps loading module and it can only be adjusted horizontally in one axis (front to back). This posterior shaft is mounted directly into the frame of the simulator, which has horizontal slots that allow the adjustment. In contrast to the quadriceps module, the pulleys have needle bearings and a guiding pulley that allow for independent motions that are dictated by the respective muscle load being routed through them.

This loading mechanism consists primarily of two aluminum 6061 walls welded to the side of the UOKS and six independent loading units mounted in between these two walls (Components 1&2 in Figure 5). Each loading unit has the following components: a loading pulley, a driving shaft, an alignment pulley and two block bearings with mounting brackets (eccentric collar locking type). To ensure torque transmission, the pulleys and shafts interact through a keyed joint and a set screw lock. Each loading unit used a set of free hanging weight plates that caused the driving

pulley to transmit a torque to the shaft and subsequently the driven pulley would follow the same motion. As seen in Figure 5, the driving pulleys for each unit are different in size to reduce the necessary number of weight plates to achieve a specific load. To connect the hanging weights to the loading pulleys, a 1/16” galvanized aircraft cable was loop around the plates. Galvanized aircraft cable was chosen due to its high strength to weight ratio, low maintenance, corrosion resistance and cost efficiency.

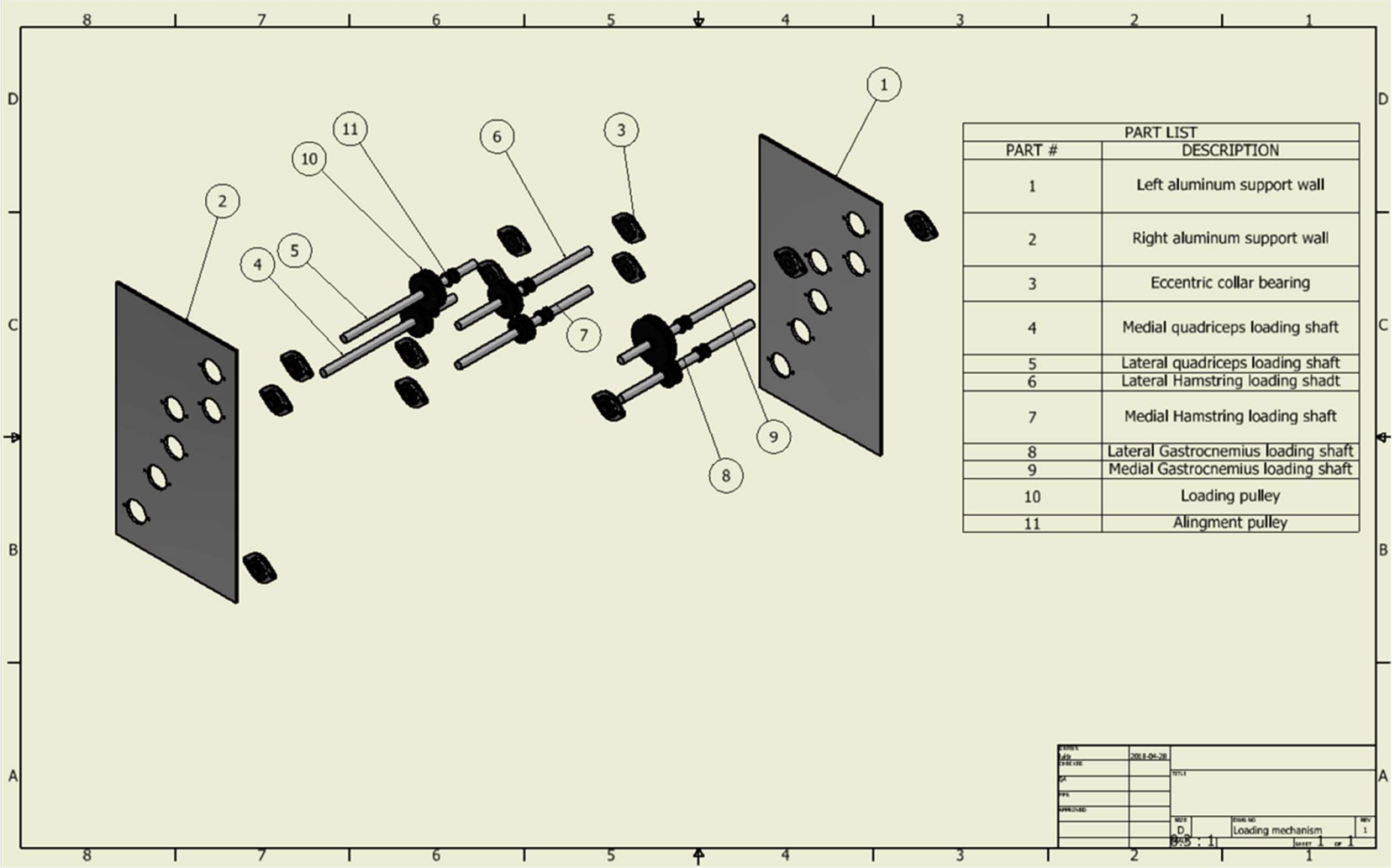

Figure 5. Exploited view of the loading mechanism. These components are located in the back of the simulator.

2.3.3 Fixtures

Inside the loading chamber two external fixators are used to secure the specimen during testing. Each external fixator consists of an assembly of multiple components to suspend the bones of the specimen. As seen in Figure 6 and Figure 7, the femoral fixator ball joint interacts with a socket to create a spherical joint to simulate hip joint motions, whereas the tibial fixators semi spherical head connects to a concave plate allowing free ankle joint movement.

The design of this fixation cup provides the simulator with flexibility to mimic two phases of gait cycle, toe off and heel strike. An attachment plate with a concave socket is used to align and support the ankle joint. Furthermore, the tibia-fibula fixation cup provides anchor points to simulate medial and lateral gastrocnemius loading that unlike the quadriceps and hamstrings are not directly attached to the specimen. Overall, the fixation cup mechanism provides a secure and standard method to fix the specimen during testing, as well as granting unconstrained kinematic responses in six DOF when loading the joint.

2.3.3.1 Femoral Fixation Cup

The femoral fixator assembly (Figure 6) incorporates a socket plate that screws into the vertical actuator of the MTS and a sub assembly between a femoral potting cup and the spherical head of the simulated hip joint. The base of the potting cup and the base of the spherical head are joined facing each other and firmly attached with screws. The spherical joint used on this fixator is a polyethylene on polyethylene spherical joint, whereas the rest of the components are made of aluminum. The socket plate is attached to the vertical actuator's head with a set of

screws and gives an offset from the actuator's axis of rotation and the ball socket. This offset allows for the positioning of the hip joint and the specimen prior testing.

The fixation cup's assembly can be modified for testing right and left specimens. The orientation of the ball joint's position with respect to the potting cup provides a physiological representation of the hip joint orientation for right and left specimens. Additionally, the socket plate can be rotated and adjusted to fit both specimen alignments. This design provides the flexibility of fitting specimens without compromising the physiological load transmission from the hip to the knee for right and left specimens.

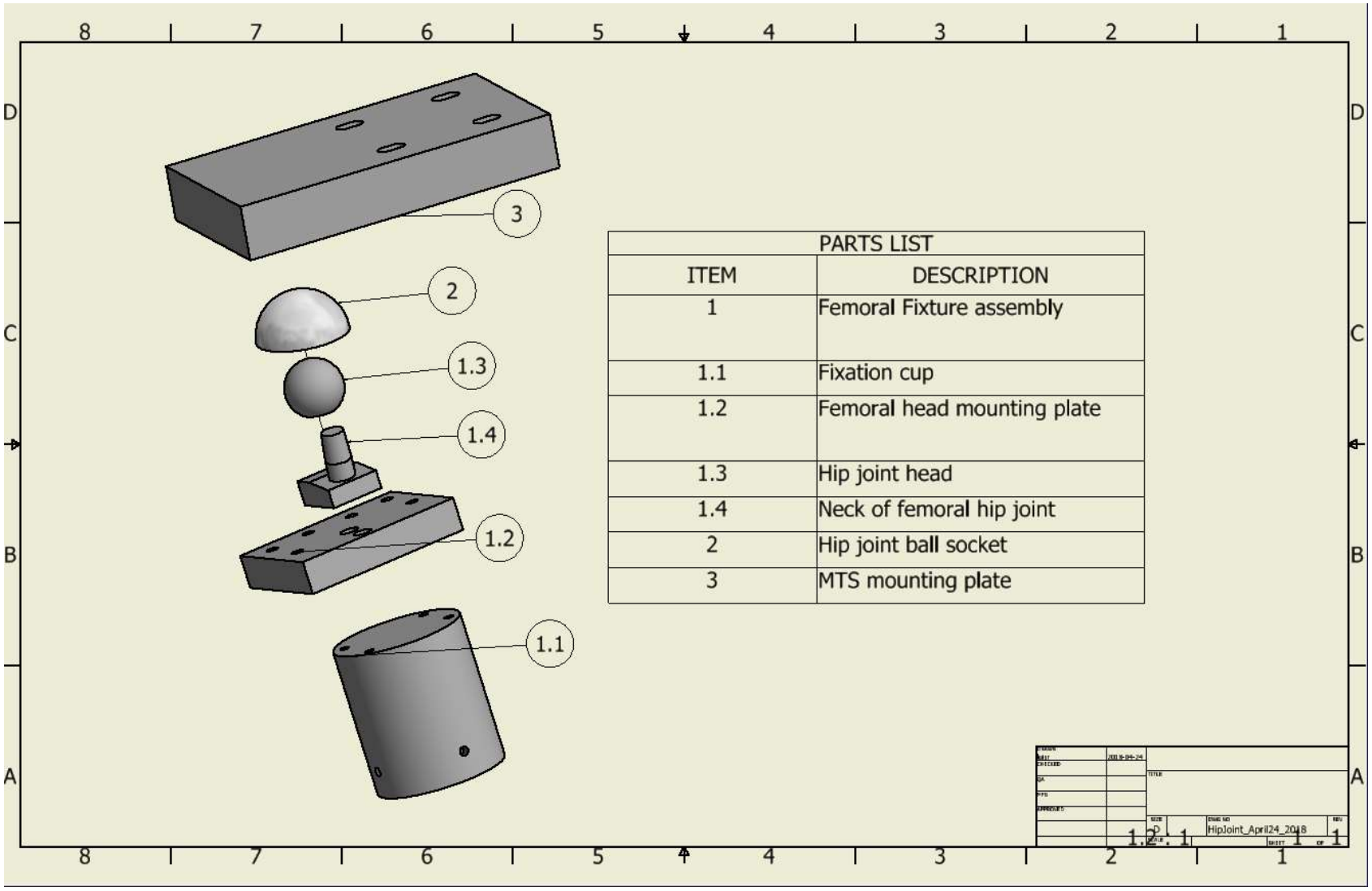

Figure 6. Exploited view of the femoral fixture assembly

2.3.3.2 Tibial Fixation Cup

The second external fixator, referred to as the tibial fixator, is an assembly that consists of a potting cup, a muscle insertion anchor plate, a foot plate, semi spherical head and a concave plate (Figure 7). The potting cup is used to secure and suspend the distal bones of the cadaver specimen. Unlike the femoral fixator, the tibial counterpart has a "U" shaped anchor plate where two threaded eyelets are inserted to provide anchor points for the simulated medial and lateral gastrocnemii loads. This design was incorporated because of the necessary alterations required to properly secure left and right specimen inside the loading chamber. Furthermore, the potting cup and anchor plate are secured to a foot plate. The addition of the foot plate grants the possibility to adjust the semi spherical ball joint in a heel strike and toe-off position by moving the semi spherical joint from the back to the front of the foot plate. Finally, the concave plate is secure down to the MTS load cell. This part is important as it is part of the instrumentation used by the UOKS to measure the vertical ground reaction forces applied by the hydraulic actuator of the MTS machine. Similarly, to its femoral counterpart, most of the parts used for the assembly of the tibial fixator are made of aluminum, except for the semi spherical joint and concave plate which are made of brass. Aluminum was once again chosen as the material for most of the parts of these two external components, because it has good corrosion resistance capabilities, and is a soft metal easy to machine and customize.

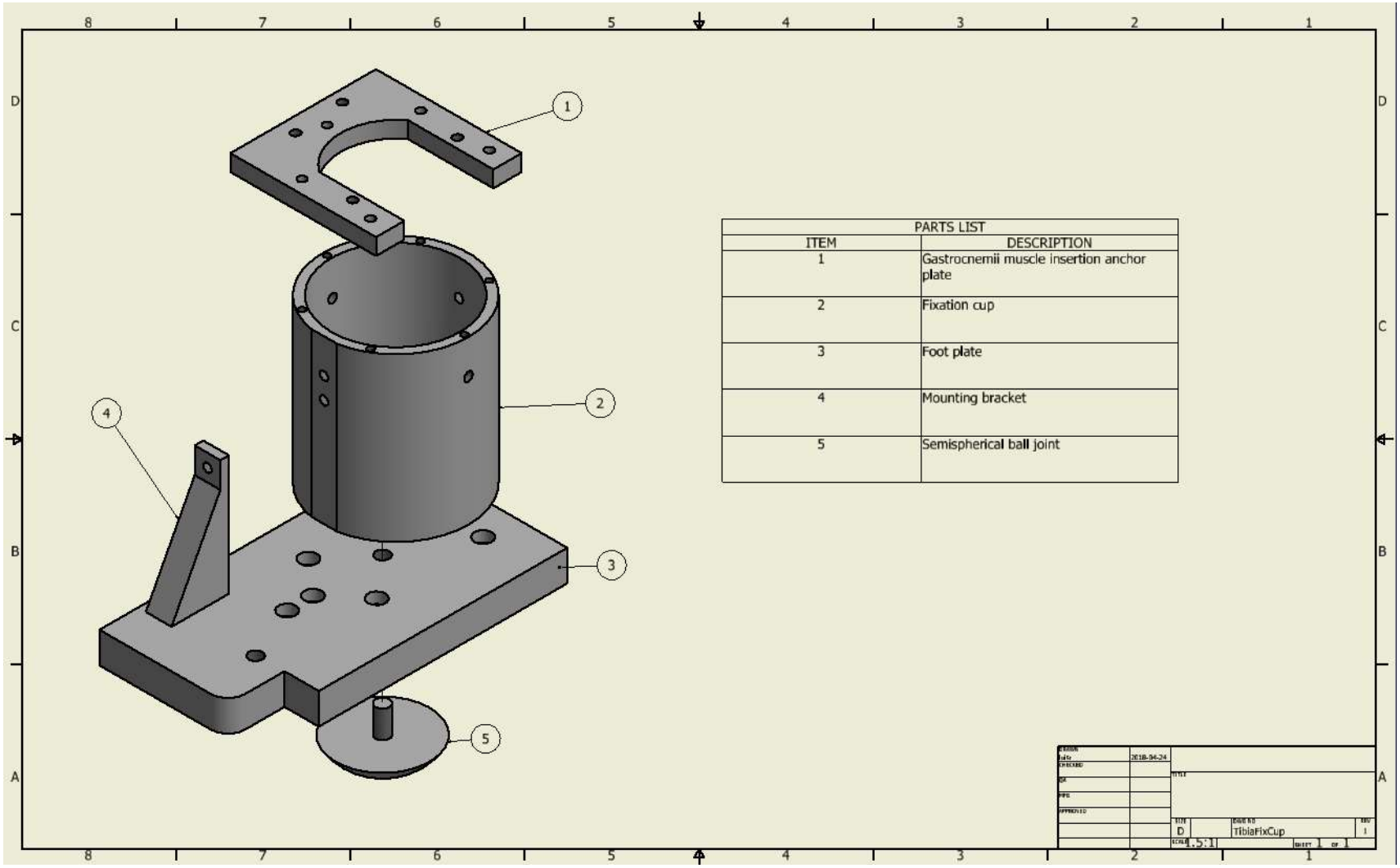

Figure 7.Exploited view of the tibial fixture assembly

Chapter 3. Automated Loading Mechanism: Design and Build

The previous iteration of the UOKS used hanging weights as means of creating the loads for a simulation. This mechanism had to be used with precaution to avoid loads to be applied in a in hasty manner resulting in abrupt failure or damage to the specimen. During the process of loading a knee joint, the operator needed to apply the loads for the simulation in incremental values to avoid sudden high loads that could potentially damage the specimen. Using weight plates limited the amount of load that could be achieved because of the set value of each plate and the combinations that can be used to reach a certain load. The issues related to this mechanism also exposed the users to dangerous situations, this task demanded a physical toll and risked the operator to be exposed to injuries. Finally, the space needed to accommodate large sets of weight plates during a simulation was very limited. For these reasons, it was decided to implement a new loading mechanism for the UOKS.

3.1 Development and Design objectives

The new loading mechanism for the UOKS includes the addition of hardware components (Figure 8) and the implementation of a user interface to control the driving parameters of the simulation. The design criteria for the development of the updated UOKS were selected to solve the limitations found on previous iterations. The new loading mechanism was designed with the following objectives in consideration:

- The first objective sought to replace the weight loading mechanism with an actuator capable to achieve the same range of forces without compromising the autonomy of each muscle load simulated. Additionally, the mechanisms needed to be compatible

with the system of pulleys to avoid modifying any components of the original framework of the UOKS and thus, maintaining the same performance. This was expected to result in a loading mechanism capable of reliable performance and repeatable loading inputs.

- The second objective focused in providing a user interface to control the loading simulation. This intended to reduce testing time and to reduce user interaction with heavy loads during testing. It was also sought to provide real time data of the loading conditions being simulated. Real time data was sought to provide the capability to digitize and store load profiles for analysis.
- The third objective was to evaluate the integration of these modifications to the UOKS by assessing the accuracy and reliability of the loading system
- The fourth objective was to test these additions during an in vitro simulation to assess the validity of these new components

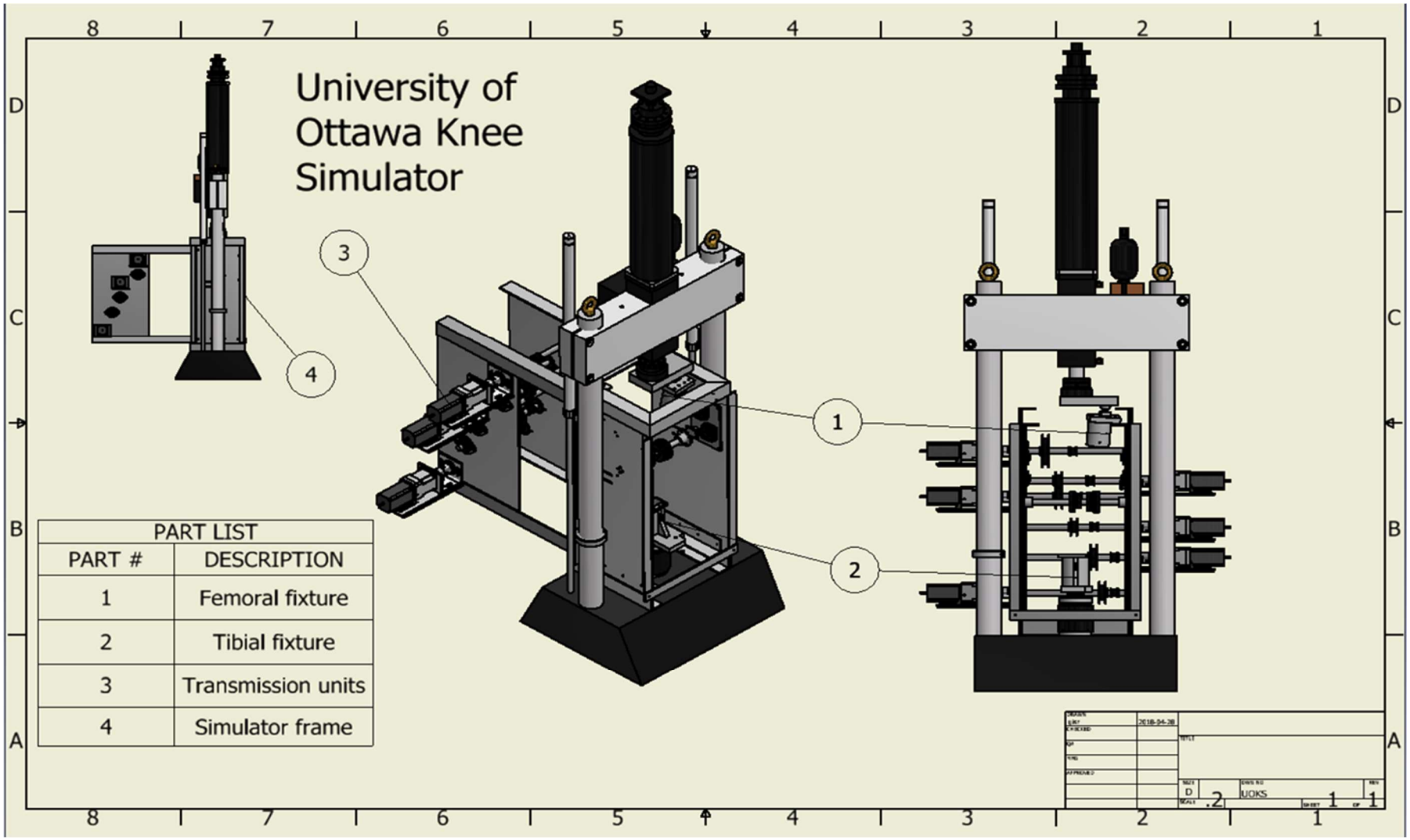

Figure 8. New UOKS assembly with the transmission units mounted to the sides.

3.2 Transmission System

This section reviews the options of actuators capable of being integrated to loading devices, as well as their advantages and disadvantages

3.2.1 Actuators

Actuators are viable solutions to overcome the difficulties of complex loading sequences and can provide accurate control of magnitude, speed, acceleration and direction of their motion through instrumented feedback [128]. This section reviews the options of actuators capable of being integrated to loading devices, as well as their advantages and disadvantages.

Selecting the type of actuator for in vitro loading devices depend on factors such as drive, performance, complexity and cost [129] . These components can be classified by the source of energy used to drive the motion, such as electric current, hydraulic pressure and pneumatic pressure. Other differences between these actuators lie on performance. For instance, pneumatic and hydraulic actuators are well known for producing high force and high speed motions at low cost (per unit size) with a relatively simple control mechanism. However, the precision of motions that can be achieved is limited and the cost of operation/maintenance are factors that influence the selection process. The operation of pneumatic and hydraulic actuators also involves the use of compressors and pumps, respectively, increasing initial cost.

Unlike pneumatic and hydraulic actuators, the motions created with electrical actuators are low force when compared to the other types of actuators; not to mention that high force electric actuators can be expensive. As an alternative, low force electric actuators can increase their force output with different types of gear systems, but using such components decreases the speed of the actuation depending on the turning ratios of the gear systems. Thus, electric actuators are

an alternative to replace pneumatic and hydraulic systems when low cost, precision and small packaging are within the established parameters of the project.

Based on the objectives established for the new loading mechanism, six high torque NEMA23 stepper motors were selected for the loading mechanism. These stepper motors were chosen to replace the hanging weight loading system used on the UOKS due to their high precision capabilities. It is important to mention that when using these actuators for loading applications, steps can be skipped if the output torque is not enough to overcome the load and for this reason, each stepper motor in the new loading mechanism was connected to a planetary gearbox with a 20:1 gear ratio with a D-shaft to increase torque production.

Planetary gearboxes are systems composed of gears mounted in an epicyclical gear train arrangement and are considered more complex system in geometry and part count. These systems are an alternative to the common pinion-gear reducers. The internal topology of planetary gearboxes consist of a sun gear, planetary gears, ring gear and a ring carrier. This systems allow to obtain a high transmission ratio in a compact design, suitable for transmissions of parallel axes [130]. Planetary gears are used in many torque transmission applications due to the load distribution between the sun gear and the multiple planet gears (Figure 9), as well as the many speed manipulation capabilities of them depending on the ratios between the gears [131][132] planetary gearboxes were chosen for their high load capacity and their ability to share load between the planet gears and limiting the speed of the loading mechanism to ensure torque transmission.

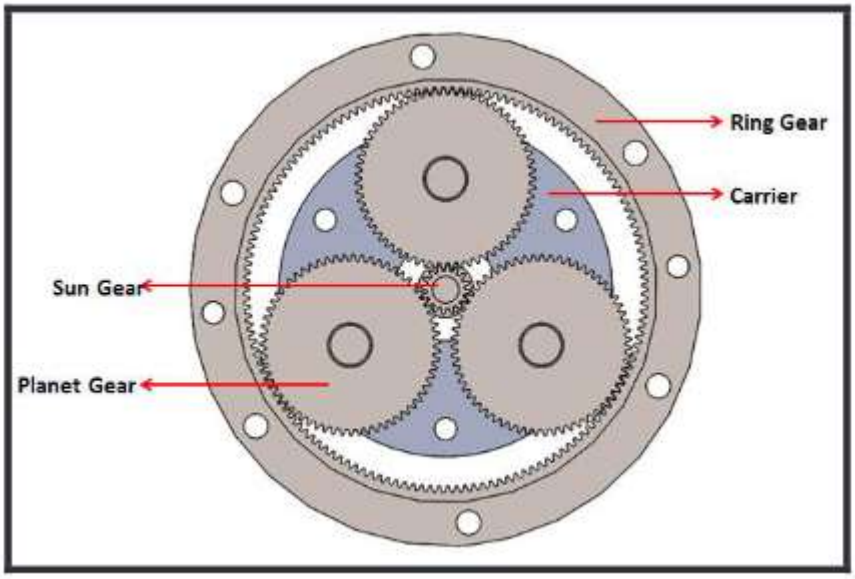

Figure 9. Planetary gear representation

The proposed controller for the loading mechanism used 2 MID-7604 industrial grade power amplifiers and one PCI-7350 motion controller system interface compatible with LabVIEW (National Instruments Austin, Texas, USA). These controllers were chosen due to their capabilities to power and control the six stepper motors simultaneously.

3.2.2 Mechanism Assembly

The new loading mechanism was made by 6 transmission assemblies mounted to the frame of the UOKS. The previous version operated with fixed shafts (driven shaft), eccentric collar bearings and two pulleys for each one of the 6 muscles. Actuators were mounted with brackets and couplers to position the motor-gearbox (transmission) driving shaft with each of the fixed driven shafts. Each transmission was assembled and mounted with two mounting brackets, one support bracket, one mounting plate and two shaft couplings (1/2” to 3/4”). Full assembly shown in Figure 10

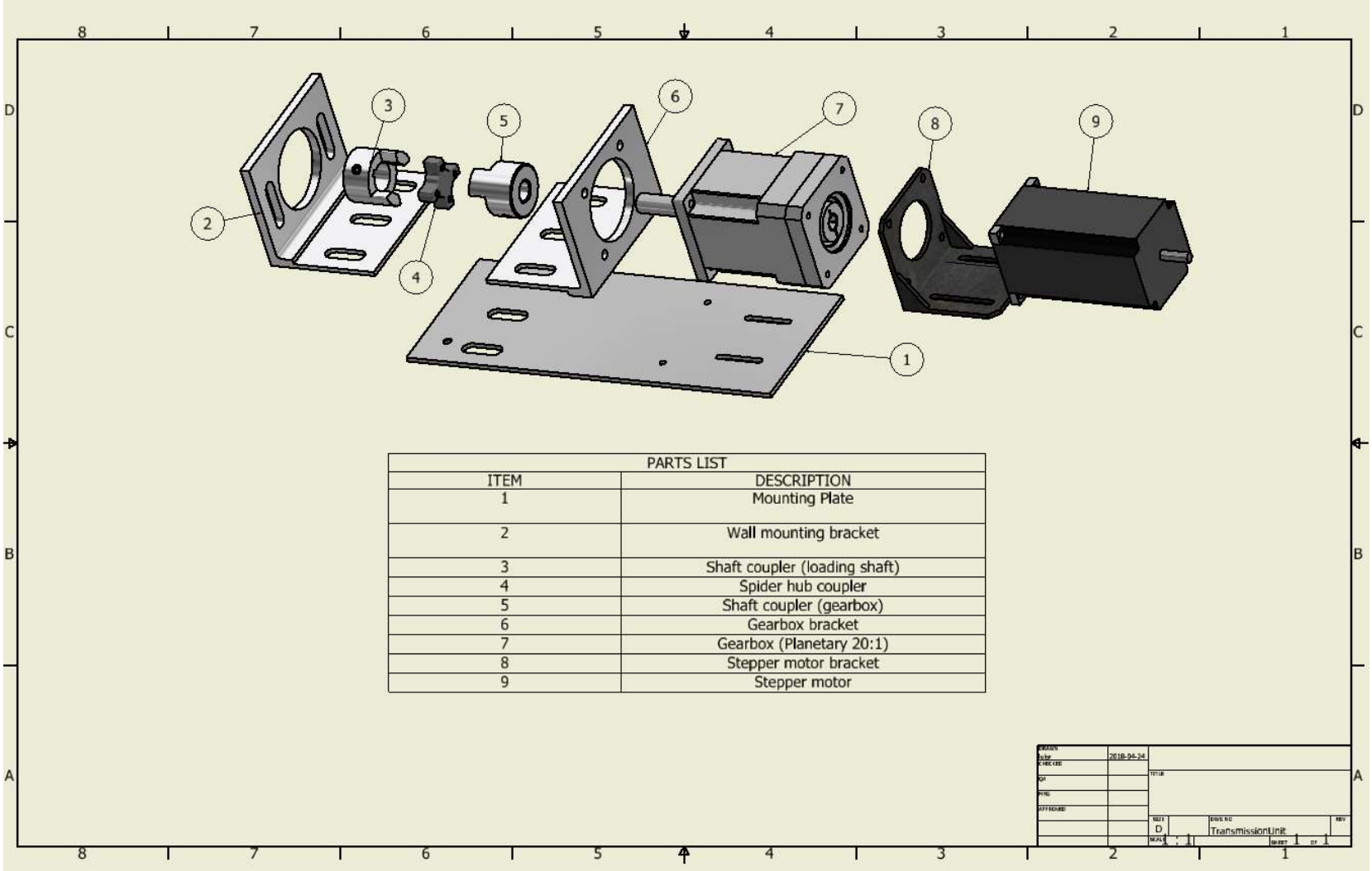

PARTS LIST	
ITEM	DESCRIPTION
1	Mounting Plate
2	Wall mounting bracket
3	Shaft coupler (loading shaft)
4	Spider hub coupler
5	Shaft coupler (gearbox)
6	Gearbox bracket
7	Gearbox (Planetary 20:1)
8	Stepper motor bracket
9	Stepper motor

Figure 10. Transmission unit assembly. the image shows an exploited view of the components of the assembly.

The stepper bracket supports the connection between the gearbox and the stepper motor. This support bracket is a steel coated commercial off-the-shelf part design to support and mount NEMA23 stepper motors. It is position between the motor and the gearbox and fixed to the faceplate mount with M4 x 16mm screws and washers. The bracket has two slots on the base and allow for alignment of the motor subassembly in one plane.

The mounting brackets are used to position the transmission to the UOKS and facilitate the connection with the pulley system. The brackets were designed using aluminum 6061 right angle extrusions and manufactured at the University of Ottawa's Manufacturing Centre. One of the mounting brackets (Gearbox Bracket, GB) was designed to match the front faceplate mounting holes of the gearbox. The design was custom made to resemble that of the support bracket (90-degree angle bracket) and to maintain the axis of actuation leveled with that of the loading shafts for each muscle. The second mounting bracket (MB) was designed to mate with the outer face of the wall that supports the driven shafts of the UOKS. This bracket has two slots on the mounting face to allow vertical alignment and mounting of the transmission assembly. The base of the mounting brackets and gearbox bracket overlap on top of each other to align the transmission and the loading shaft. The base of both mounting brackets has three slots that adjust the proximity towards and away from the wall of the UOKS. Additionally, these slots help mount the brackets and the transmission subassembly to the aluminum mounting plate, along with the two rows of holes for the base of the stepper motor support bracket. The mounting plate helps position the assembly in a transverse plane and supports part of the weight of the assembly.

Two shaft couplings connect the transmission and the loading shaft to enable torque transmission. The design of the coupling components was based on off-the-shelf components and was manufactured at the University of Ottawa's Manufacturing Centre. The parts were made from aluminum 6061 due to their mechanical properties and chemical properties to resist rust formation in humid environments. This is particularly important, as in vitro testing requires to spray specimens constantly with saline solution to maintain the mechanical properties of soft tissue. The coupling's design also allows for centre misalignment using a rubber spider between the couplings. The coupling connects the D shaft of the gearbox (1/2"inner diameter coupling) to secure torque transmission with a set screw. Similarly, torque transmission to the loading shaft is assured with a 3/4"inner diameter coupling uses a keyed joint and a set screw.

A total of six transmissions were assembled and grouped in two sets of three to connect with the loading shafts of the medial and lateral muscles. The transmissions were grouped and distributed to the sides of the simulator to maintain a balance of the new added weight of the UOKS. Each transmission system was mounted to a respective "muscle" mechanism by manually adjusting the alignment on the vertical and horizontal axis, as well as their proximity towards the side walls. Subsequently, each of the transmissions underwent a loading test. The testing consisted in attaching a set of weights to one of the loading mechanisms at a time. The transmission units were then commanded to spin in both directions to lift and descend the weights for 10 to 15 minutes without interruptions. Afterwards, the weight would be increased in random intervals until 100 Kg. Additionally, once the weight reached 100 Kg, the mechanism was left hanging for 5 minutes with the transmission stalling the load.

3.2.3 Instrumentation

Electrical load cells are versatile instruments that can be used in a wide range of conditions and loads. Load cells with an electrical output can then be digitized and monitored through computers with accuracy ranging from 0.03% to 1% depending on the weight range, application and manufacturer

Strain gauge are one of the basic functional units use to manufacture load cells. As the name implies, strain gauges are used to transform the physical deformation to an electrical potential, and their operation is based on the response of electrical conductivity of a material when exposed to stresses that deforms it. However, strain gauges require of a protective case to prevent any damage while loading and output signals are susceptible to high frequency and power line noise due to their low level signal [133].

Accuracy and reliability of strain gauge measurements (output signal) are affected by the testing conditions, as well as internal configuration. Strain gauge configuration refers to the number of active strain gauges and the spatial orientation with respect to the loading axis. The number of active strain gauges increases the sensitivity of the system, meaning that when one, two or four strain gauges are combined into a Wheatstone bridge configuration (Figure 1). These configurations represent the output signal as a relative change from the resting/baseline state of the system, usually within the μV range.

Accuracy and reliability of strain gauge measurements (output signal) are affected by the testing conditions, as well as internal configuration. Strain gauge configuration refers to the number of active strain gauges and the spatial orientation with respect to the loading axis. The number of active strain gauges increases the sensitivity of the system, meaning that when one,

two or four strain gauges are combined into a Wheatstone bridge configuration (Figure 11). These configurations represent the output signal as a relative change from the resting/baseline state of the system, usually within the μV range.

Moreover, spatial arrangement of strain gauges can also minimise noise caused by thermal effects, such as thermal expansion and Poisson's deformations. Spatial configuration of strain gauges can also increase the sensitivity to directional loading, meaning that certain arrangements provide higher sensitivity to bending, tensile or compressive (Figure 12).

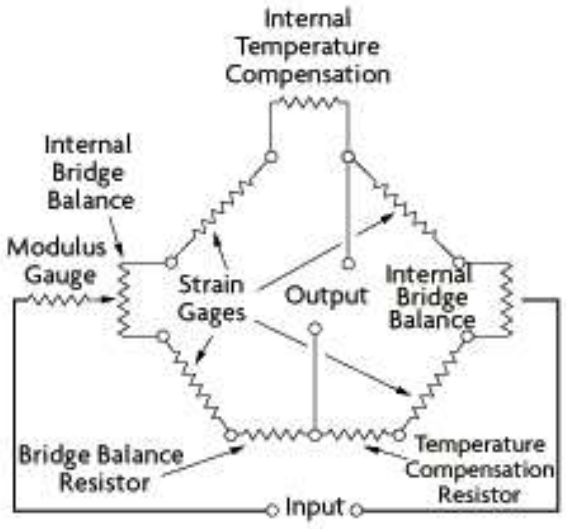

Figure 11. Wheatstone bridge in a four strain gauge configuration. Image retrieved online from https://www.omega.ca/prodinfo/loadcells.html#learn

Considering what is mentioned above, the characteristics of a loading test performed by the UOKS loading device are the decisive factors considered in selecting an adequate load cell. These factors are the behavior of the load over time, the type of load, the range of target loads and the environment. The load cells selected were S-beam, off-the-shelf from OMEGA (LC-101 OMEGA engineering Stamford, Connecticut, US) rated for static tension and compression forces between 0 and 500 lbs of force. This range is ideal for the application of forces below 2000N, which within the expected testing loads (maximum expected load 1200N). Moreover, this load cell design comes with two threaded holes at each end. These holes allow the use of lifting end rods along the tension loading axis for proper tension measurements. The stainless steel frame provides a design suitable for low and high capacities and an operation range in temperatures from 17 to 71 °C. This allows the use of the load cells during in vitro experiments, where substances such as biological substances and saline solutions could come in contact with them.

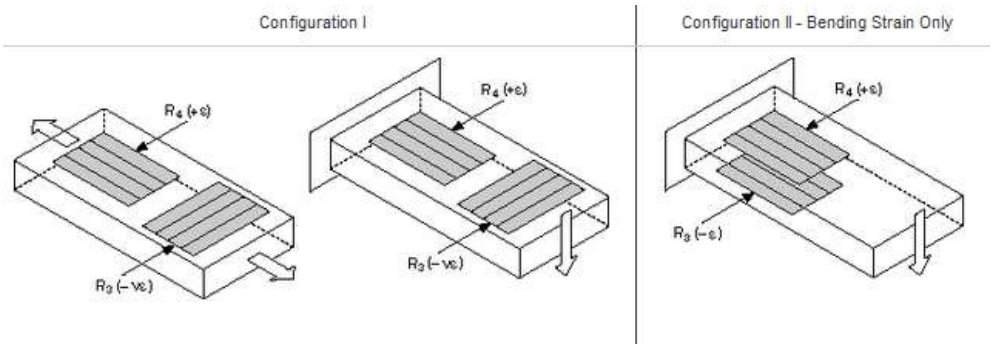

Figure 12. Strain gage half bridge configuration. Spatial configuration of the strain gages increases sensitivity of forces. Configuration I provide higher sensitivity to tensile strain (left) or bending strain (middle) with Poisson's effect compensation. Configuration II measures bending strain. https://www.hbm.com/en/2973/how-doas-a-bending-beam-load-cell-work/

3.2.4 Integration

Ensuring steady power supply to a load cell is critical for reliable measurements since the output signal of a load cell is a fraction of the excitation potential used to power the bridge, thus variation in the power supplied of the bridge can affect the absolute value obtained from strain measurements. This was ensured by using a DC benchtop power supply to power an in-line multichannel signal amplifier with step down converter (Multichannel amplifier 9235/36, Burster, Gernsbach, Germany) that guarantee a steady power supply of 5V along with a low-pass noise filtering to the load cells.

The quality of the signal is also dependent on external factors that surround the testing setup. Low amplitude signals are susceptible to ambient noise attributed to power lines and electromagnetic sources. To ensure the quality of such signals, power line and electromagnetic noise can be prevented with the use of both hardware and software implementation. Hardware implementation to reduce noise can be achieved by implementing proper protective cable shielding and proper grounding techniques to mitigate the effect of electrical fields caused by power lines. Additionally, it is recommended to avoid placement of load cells and other related signal carrier near devices or machinery with a high voltage supply to prevent any exposure to the electromagnetic fields (National Instruments, 2016). Moreover, high frequency noise can be eliminated with the implementation of amplification stages and frequency noise filters. This process is part of a conditioning process to ensure that a proper signal is being obtained by a measurement device. It is recommended to amplify the low amplitude signals before the use of filtering techniques; however, this often increases both the signal and the noise being carried. Subsequently, adequate filtering techniques can be used to remove noise outside of the useful

spectrum, this is often achieved with band eliminating filters and/or lowpass filters. For this project, the load cells signals were conditioned using the same Burster signal amplifier (multichannel amplifier 9235/36). The amplifiers were used to condition three load cells each one (medial and lateral) and placed at least 45 cm away from any power line and power outlet to minimise the effect of power line noise. Additionally, all signals were transmitted through shielded cables to reduce the influence of electromagnetic interference. The multichannel amplifiers condition the signal with an amplification stage and a low-pass filter below 1KHz of frequency.

Finally, the quality of the signal can also be preserved by recording the signals with specialized hardware capable of saving the signal over a long period of time. Devices capable of recording and storing such data are known as data acquisition instruments. Data acquisition equipment can take a wide range of input potentials depending on the application such as TTL logic levels (3.3 to 5 V) used on digital systems or industrial grade equipment with voltages ranging from low to high levels (PLC). These are also classified based on the resolution and sampling frequency in which the signal can be acquired. Resolution in this context refers to the ratio between the maximum value of the signal and the smallest part in which the signal can be fragmented, whereas sampling frequency refers to the number of points capable of being recorded in a second. These factors play a critical role in obtaining accurate and reliable information from sensors, as small changes in the signal would not be perceived by the devices with characteristics not suitable for the application.

For this reason, an analog to digital converter (ADC) integrated to the stepper driver module was used to digitize the signal of all six load cells. The ADC can measure analog inputs

from -10 to +10V with a 16 bit resolution, giving an approximate of 300μV of resolution to detect small changes coming from the load cell. The signals coming from the multichannel amplifier (after signal conditioning stage) were transmitted through shielded wire to avoid electromagnetic interference. Additionally, all readings from the ADC were converted from digital values to analog values by using Equation 1.

$$\frac{Resolution\ of\ ADC\ (dec)}{System\ voltage\ (V)} = \frac{ADC\ reading}{Analog\ voltage\ measured}$$

$$\therefore \quad Analog\ voltage\ measured = \frac{System\ Voltage * ADC\ reading}{Resolution\ of\ ADC}$$

Equation 1. Digital to analog conversion formula. This relationship was used to obtain the analog voltage measurement from the multichannel amplifier.

All load cells were added to a corresponding motor assembly prior to calibration. Each load cell was suspended between the driven pulley connected to the transmission and the pulley system of each muscle using threaded eyebolts and threaded studs. Two threaded studs were used for the quadriceps muscles and the rest of the load cells had a lifting eyebolt and a threaded stud attached to them. The combination of these components created a load cell subassembly. Using two eyebolts on each load cell was ideal, but the subassembly's length exceeded that of the space available between the pulleys and load cells could not obtain accurate readings. For this reason, the studs were added to the hamstrings and gastrocnemius muscles so that load cell subassemblies could be suspended without bumping into components when being loaded. Steel cable wires were used to connect each side of the load cell subassemblies to the corresponding

shaft. Steel wires were crimped around the eyebolts and stud holes using two aluminum crimp sleeves on each end.

3.3 Loading Controller

The controller for the UOKS combined the control for all transmission units and real time force measurement display graphic user interface (GUI). The objective of programming a custom controller was to minimise user involvement in controlling the motors, as well as providing real time data of the loading conditions being simulated.

The controller has two main functional blocks that perform all the necessary operations with a back end program and displays information through a GUI. The custom controller was programmed using LabVIEW (LabVIEW 2015, National Instruments, USA) with the motion control (2015) assistant toolbox from National Instruments. Using LabVIEW for the development of the loading controller facilitated the integration of the transmission control, data acquisition, data management and data display with minimal user involvement.

3.3.1 Graphic User Interface

The Graphic User interface (GUI) is the part of the controller responsible for connecting the user with the complex task of controlling the transmissions. It is the frontend of the controller, and handles the commands selected by the user and sends them to the back end to operate the UOKS loading sequences. This interface is linked to the back end controller through functions that displays data that has been processed on the backend. The GUI was designed to facilitate transmission control and to limit the involvement of user actions during testing.

The frontend provides the option to control transmissions with load feedback or absolute number of step/directions if needed to. The difference between these control methods is on the application. For instance, selecting a load feedback mechanism allows the application of any load with real time information to be displayed. Additionally, with this control method the user can select any number of transmissions to be activated at the same time and the load value to be applied by each one. On the other hand, an absolute number of steps would only command the stepper to spin without any feedback or target load. This control method was used to calibrate load cells and the former was used to control the transmissions when load was applied.

3.3.2 Backend Controller

The backend block of the controller was programmed with routines to handle the loading sequences (Appendix C: Front Panel and Block Diagram of the UOKS Controller).

The controller took load measurements from all load cells at a 5Hz sampling frequency. Motor control was based on the difference between the current load measurements and target loads, and if the difference fell within +/- 1N from the target load, the motor stopped spinning. Once all target loads were reached, the controller was put on idle state to maintain the load by continuously doing load measurements and fine tune the motor steps if necessary, to keep the load at a set value. If any perturbation was experienced in the system, the controller could provide rough and fine tuning to adjust the load on all muscles by adjusting the number of steps per command. The summary of the steps performed by the controller are shown in Figure 12.

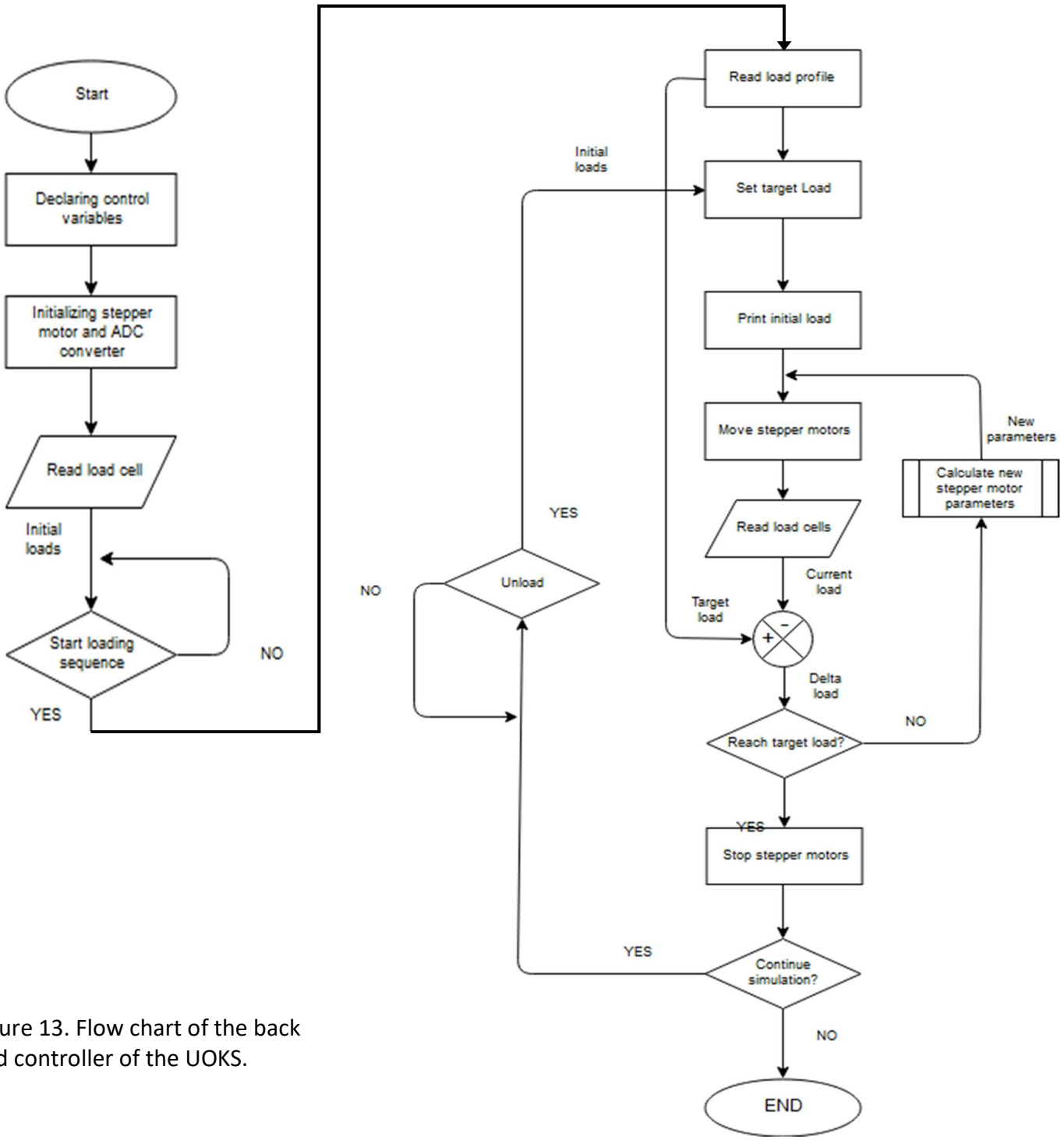

Figure 13. Flow chart of the back end controller of the UOKS.

Chapter 4. Evaluation

4.1 Load Cell Calibration

Load cells were subjected to a calibration test before full integration with the UOKS. Each assembly was used to hang a set of weightlifting plates to obtain the characteristic equation to interpret load cell readings. Before any weighing, load cells and amplifiers were subjected to a zero load ten-minute session to warm up the system's temperature to a stable state as recommended by manufacturer and force measurement guidelines. The calibration test was divided into two tasks on one instrument at the time. The first task consisted in a pre-loading cycle of ten minutes, subjecting the load cell to tension and relaxation with a total of 108.8kg (warm up weight). During this task the force producing capabilities of the transmission assembly were also tested by connecting the load cells with the warm-up weight resting on the floor. The transmissions were programmed to lift the weights from the floor, then the weights were suspended for five seconds and the transmission would put down the weights. The pre-loading routine is highly recommended for a force measuring system as it decreases the effect of hysteresis in the system [95], [96].

Based on the American Standard for Testing and Materials (ASTM) recommendations for force verifications of testing machines [136]. A randomized ten-point scale load calibration was performed to ensure the calibration loads were well distributed over the desired range of loads: 0Kg, 0.5 Kg, 1Kg, 3Kg, 8Kg, 13 Kg, 21.4Kg, 41.8Kg, 62.2Kg, 78.09Kg and 108.49Kg. The procedure used for the warm up was used for each calibration weight and was repeated five times. For each trial, weights were stacked together on a weight hanger and connected to a transmission. The transmissions were programmed to lift, suspend the calibration weight for five seconds record a

measurement and put down the weight. This sequence was repeated five consecutive times for each calibration weight.

After all calibration points were obtained for all load cells, the data was processed using MATLAB (R2017b, MathWorks, MA, USA). Data points were grouped by load cell and fed to a linear best fit model (equations shown below) to obtain the characteristic curve that best described their individual response. This regression model was chosen due to the linearity response of the load cell when subjected to loading conditions.

$$y = a + bx$$

$$a = \frac{(\sum y)(\sum x^2) - (\sum x)(\sum xy)}{n(\sum x^2) - (\sum x)^2}$$

$$b = \frac{n(\sum xy) - (\sum x)(\sum y)}{n(\sum x^2) - (\sum x)^2}$$

Where *Y* is the output obtained from the load cell in terms of Voltage (dependent variable)

a is the value of the Y interception

b is the slope of the line

X is the load that caused a change in the load cell voltage output.

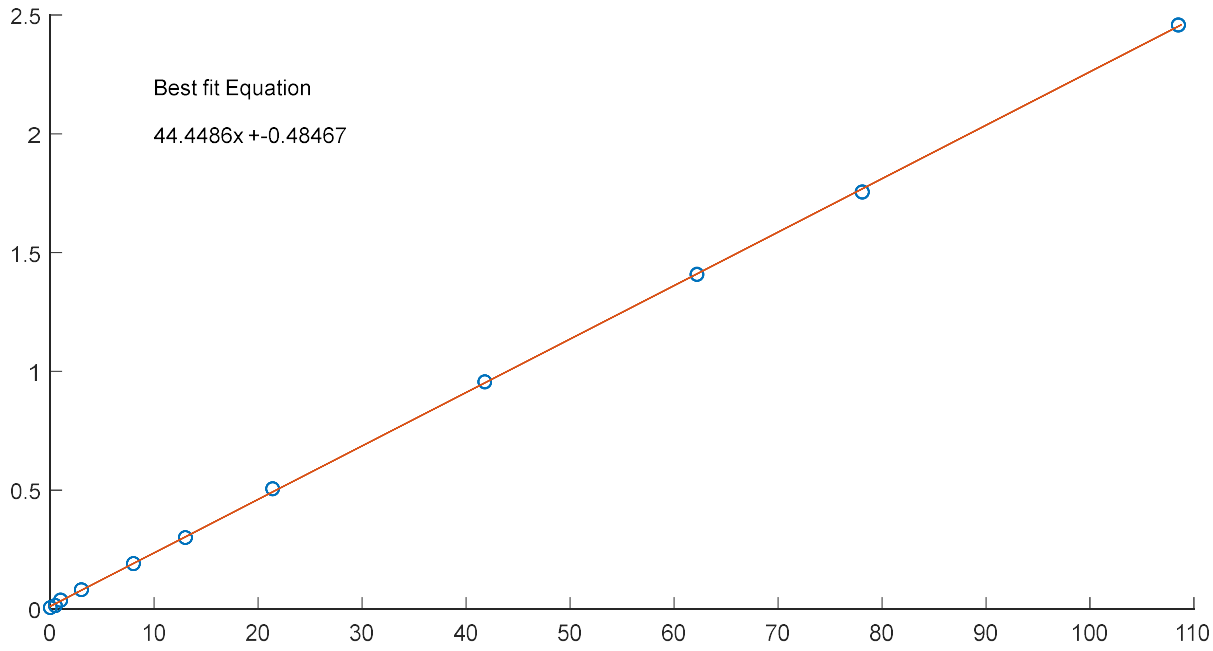

Figure 14. Distribution of data points used for the calibration of the load cell used for the transmission of the medial quadriceps (Load cell 1). The red line shows the line of best fit that describes the relationship between weight and voltage of the load cell. Blue points represent the distribution of the datapoints.

Table 1. Calculated results from the load cell calibration. These equations were used to convert the voltage output (mV) of the load cells to load units (N).

Transmission	Best fit coefficients
Medial quadriceps	44.4486*X – 0.4847
Medial hamstrings	40.354*X – 2.5865
Medial gastrocnemius	43.9620*X – 0.8555
Lateral quadriceps	43.5806*X + 0.0564
Lateral hamstrings	43.9129*X – 0.2852
Lateral gastrocnemius	44.1507*X – 0.3410

4.2 Controller Testing

The response of the controller was crucial to the performance and accuracy of the UOKS loading device for reliable simulations. The performance of each transmission was tested individually and compared to an external load measurement instrument. The main objective of this test was to demonstrate the performance of the controllers during a loading simulation. The accuracy and repeatability of the transmissions under the command of the controller were the main performance variables of interest in this stage of the project.

The UOKS was mounted on the MTS testing machine to test the loading mechanisms of each muscle. Each transmission was connected to its corresponding pulley system, allowing the transmission of load from the actuators to the loading chamber of the UOKS. Additionally, the external load cell was added to the controller to provide real time data of the measurements during the test. Steel wire was looped around a threaded stud to anchor the external load cell to a custom-made fixture hold in place with screws to the bottom of the loading chamber of the UOKS. The other end of the load cell was connected to the pulley system of its corresponding muscle. This configuration allowed the external load cell to adjust its position to the loading axis of the muscle being tested and to measure load transmission.

Before any testing was performed, the load cells (testing and external load cell) underwent a ten-minute cyclical loading 'warmup' routine to minimise the effect of hysteresis on the measurements. This also allowed for load cell pre-conditioning and amplifier stabilization. The testing sequence consisted of ten randomly selected loads from 0N to 1050N simulated in a randomized order. The testing load range was selected based on the expected simulation profiles previously tested by Gauthier & Benoit [137] . Moreover, due to the nature of the analysis that

was used it was important to select a set of loading conditions with high variance for better representation of reliability results. The following loading conditions were used: 53 N, 269 N, 299 N, 415 N, 422 N, 546 N, 737 N, 921 N, 938 N, 1050N. Each of the selected loads was tested five times, for a total of 50 trials, with a waiting period in between trials to allow both load cells to go back to a stable state, thus discarding any creep from the frame and strain gauges. After all trials were completed for each testing load cell, a resting period of ten minutes allowed for evaluation of the setup and recovery of the external load cell.

4.3 In vitro Simulation

4.3.1 Protocol Design

The in vitro simulations were used to test the response of cadaveric knee joints under loading conditions. A test-retest experiment was used to quantify the degree of agreement between trials under two different conditions. A total of seven loading sequences was used with six independent loads applied at the same time and one vertical load. The independent loads represent the actuation of six of the major muscle groups that act around the knee joint: Medial Quadriceps (MQ), Lateral Quadriceps (LQ), Medial Hamstrings (MH), Lateral Hamstrings (LH), Medial Gastrocnemius (MG) and Lateral Gastrocnemius (LG). Additionally, the subsequent vertical load was used to stabilize the specimen and to represent the effect of BW load on the knee joint. The independent loads were believed to potentially create differences in tibio-femoral contact mechanics and knee kinematics when altered [83], [138], [139]. Thus, the loading sequences were altered during the in vitro simulations expecting changes in contact pressure mechanics. The load values used during the loading sequences were obtained from an electromyography (EMG) driven model from a stair ascending task [140]. Additionally, the

specimen was tested under two *physiological* conditions, ''intact'' and ''ACL-deficient''. For the latter condition, the ACL was transected, and all conditions were re-tested in a randomized order.

A Tekscan pressure sensitive transducer (K-Scan 4011, Tekscan Boston, MA, USA) was used to record and digitize contact responses of the joint. Likewise, an Optotrak infrared camera (Northern Digital, Waterloo, ON, Canada) was used to track knee joint kinematics as result of simulated loads. The variables of interest were: contact area, contact pressure and peak contact pressure of both the medial and lateral compartment and the three rotations of the knee joint. This experimental design was created to answer the following questions:

- Can a quasi-static muscle load simulation produce repeatable kinematic and contact pressure responses during a test-retest experiment?
- Does transecting the ACL change the repeatability of contact pressure and kinematics?

4.3.2 Specimen Preparation

The use of cadaveric human knees (specimens) with the protocol presented in this document was approved by The Ottawa Hospital Research Ethics Board (protocol #20170423). Specimens were provided by the Division of Clinical and Functional Anatomy of the University of Ottawa. Specimen storage, preparation and testing took place at The Orthopaedic Biomechanics Laboratory (OBL) located at the University of Ottawa Skills and Simulation Centre.

A total of four specimens were tested following the same protocol. All specimens underwent the same preparation method based on common practices of the OBL, as well as reported methodologies on previous work [93]. Special considerations were taken to store and maintain

all specimens at an average temperature of -20°C. Prior to preparations, specimens were thawed for a period of 24 hours. All soft tissue including blood vessels, skin, nerves, muscles, tendons and adipose tissue was removed from specimens to provide access to the tibiofemoral joint. The knee ligaments were left intact to avoid compromising the results of this study. The patellar bone was left intact and used as an anchor point for muscle insertions of the medial and lateral quadriceps. After all tissue were removed, access to the tibiofemoral joint was achieved through the frontal joint capsule with two separate horizontal incisions to the posterior capsule. This provided access for the Tekscan sensor tabs to come out and be glued to the back of the knee joint. Previously documented in vitro tests on the UOKS recommend cutting the segments of the specimen at 26 cm of distance from joint line in both proximal and distal directions to maintain the desired conditions and avoid interference with frame components [137].

After the specimen was prepared, bones were placed inside the fixation cups and secured with screws making at the center of the fixation cup. Bones were potted to each of the cups with a bismuth/lead alloy. This alloy was chosen due to its low melting point, rigidity and flexibility to be melted allowing the fixtures to be reused after the experiments. Bismuth was taken to melting point and subsequently poured inside the fixation cups were the specimen had been pre-aligned and secured in position with screws.

Muscle anchors points were simulated with bone plates and bicortical bone screws. The anchor point for the quadriceps was a single plate attached to the front of the patella. The bone plates for the hamstrings used two separate plates fixed on the posterior side of the tibia, below the intercondylar area and on the soleal line. Gastrocnemius insertion points were attached to the ‘’U’’ shaped tibial fixation cup.

After specimen dissection and preparation, a manual cyclic preconditioning was performed to ensure a consistent soft tissue mechanical behaviour. The importance of the precondition in biological viscoelastic materials has been established in the literature [141], [142], however there are no specific guidelines to ensure consistent behavior of soft tissue. The conditioning routine adopted for this protocol consisted of two minutes of repeated cycles of manual flexion-extension motions to ensure consistent mechanical behaviour from soft tissue [143]. A serrated wire was looped around the ACL after preconditioning to facilitate access to the ligament between intact and transected conditions. The insertion of the wire after preconditioning helped to avoid dismantling the steel cables from the specimen and compromising the results by switching the position of the cadaver on the loading chamber [93].

The specimen was then placed in the loading chamber, properly securing the femoral and tibial fixtures on the MTS machines and the steel cables on the mounted bone plates. Steel cables were then attached to the pulleys. Subsequently, pulleys were adjusted by identifying the mechanical axis of the femur as a reference and aligning the angles of the steel cables with help of a goniometer according to the values described by Masouros et al.[144]. Finally, using the controller the muscles were loaded with 20 N to reach an initial ''stability position'' to keep the specimen in place. Additionally, an initial vertical force was applied to secure the specimen.

4.3.3 Tekscan Calibration

Two K-scan 4011 Tekscan sensors (Figure 15) were calibrated for each specimen tested using the Tekscan software wizard and the MTS machine in manual load control. The MTS machine was used due to its precise control and closed loop feedback mechanism that provided

accurate readings of vertical forces. The sensor was placed between two aluminum plates and two pieces of cork mounted on the load cell of the MTS and the MTS actuator.

Figure 15. Tekscan K-scan 4011 sensor.

A total of two equilibration tests were performed for each sensor with the same conditions. Each test applied a load to the sensor, ensuring contact in all sensing cells of the sensor and after 30 seconds of load the sensor was unloaded. Tests were done consecutively with a resting period of one minute in between. Subsequently, the sensor was given a five-minute resting period to relax and stabilize before the calibration test took place. The calibration process also used the MTS to apply the loads necessary to calibrate the sensor. The sensor was placed

between two aluminum plates to ensure an even distribution of the force and two cork pieces to resemble a more compliant material. This is recommended by the manufacturer and it is a common practice among Tekscan users to resemble the environment in which the sensor will be used. Tekscan recommendations suggest calibrating with higher loads than expected, as this could potentially affect the results in case measurements with error are above the 100% range set on the calibration. A power calibration was used with two loads at 2000N and 600N applied to the sensor for a duration of ten seconds, as recommended by the manufacturer for best performance without compromising the physical integrity and capabilities of the sensor. Subsequently, the calibration process was repeated following the same steps with a different sensitivity setting. This last step is suggested as it could provide a way of analysing the data with a different sensitivity in case the environment does not require a highly sensitive response.

4.3.4 Motion Capture Static Calibration

Motion capture was used to track the motion of the tibia and femur of the specimens during the in vitro loading simulations in six degrees of freedom. Each segment of the knee joint was tracked with the help of reflective tool. The tools are referred to as the “Y-Tool” and “T-Tool”, due to their marker configuration (Figure 16). A tool was fixed to each segment by drilling two threaded bone pins from end to end across the diameter of the bone. Each tool was position ensuring clearance inside the loading chamber. Each bone pin stuck out away from the segment and outside of the loading chamber to provide a clear view of the markers for the Optotrak infrared camera (Northern Digital, Waterloo, ON, Canada) to properly track each tool.

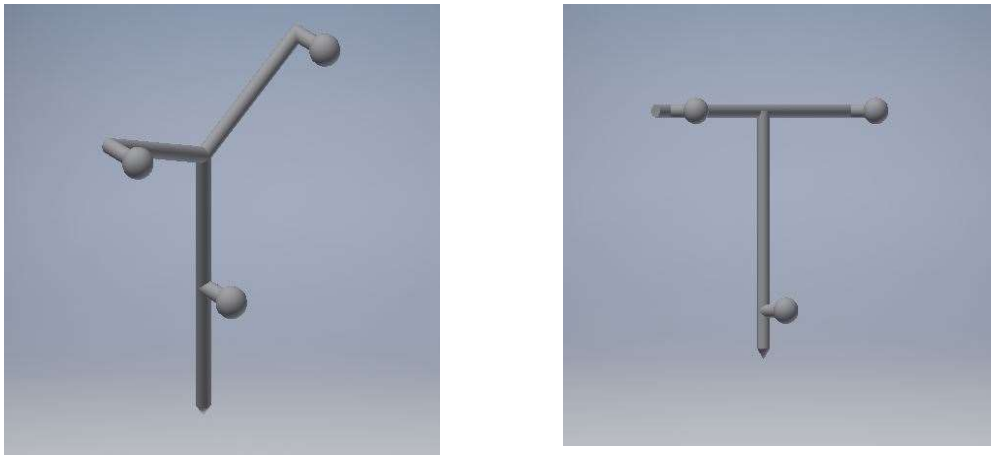

Figure 16. Markers used by the Polaris hybrid system to capture the motion and trajectories of rigid bodies. Each tool has a unique geometry. The picture to the left, the Y tools and the right pictures shows the T tool.

Prior to simulating the loading conditions, the specimen's bony landmarks including the lateral malleolus, medial malleolus, lateral tibial condyle, medial tibial condyle, lateral femoral epicondyle, medial femoral epicondyle and hip joint center were identified. These landmarks were obtained following ISB guidelines [145] and the calculation of local coordinate system of knee joint motion as reported by Grood and Suntay [146]. A detailed explanation on how the joint coordinate systems were created and calculated can be found in the data analysis section of this document. A third reflective tool was used to digitize the position of these landmarks with respect to the tools and the global coordinate system of the motion capture camera. Static calibration trials were recorded for each one of these landmarks, while the specimen remained still in all of them.

4.3.5 Loading Protocol

The loading protocol included the simulation of seven different loading conditions (Table 2) believed to demonstrate the sensitivity of the mechanical response from knee joint specimens. The loading profiles selected for the simulation represent a muscle load base line and a 20% alteration value below and above this reference based on the findings of Flaxman et al. [44]. The muscle load alterations were simulated to prove the reliability of the system to measure responses of knee joint specimens.

Table 2. Load profiles obtained from Manal et al. [140] and modulation range for each muscle

	Condition 1	Condition 2	Condition 3	Condition 4	Condition 5	Condition 6	Condition 7
Medial Quadriceps	203	243.6	162.4	203	203	203	203
Lateral Quadriceps	504	604.8	403.2	504	504	504	504
Medial Hamstrings	128.5	128.5	128.5	154.2	102.8	128.5	128.5
Lateral Hamstrings	77	77	77	92.4	61.6	77	77
Medial Gastrocnemius	78.5	78.5	78.5	78.5	78.5	94.2	62.8
Lateral Gastrocnemius	34.25	34.25	34.25	34.25	34.25	41.2	27.4
Total Load	1025.25	1166.65	883.85	1066.35	984.15	1047.9	1002.7

With the cadaver in place inside the loading chamber and connected to the transmission units through steel cables, a muscle loading condition was randomly selected and applied to the

specimen by slowly increasing the load from each simulated muscle. Previous in vitro testing with knee joint specimens demonstrated that slow increments of load is necessary to maintain specimen integrity. Subsequently, the MTS actuator applied a compressive load into the specimen slowly increasing the load until reaching 500 N. Once all loads were applied, the MTS was unloaded, followed by unloading of the muscles until the loads returned to their initial state or ''stability position''. Measurements of contact pressure and kinematic responses of the specimen were recorded from beginning to end of the loading simulation trial. A total of five trials were tested for each muscle loading condition. Trials that had issues with the MTS, Tekscan or Polaris readings were classified as failed and repeated (Figure 17).

Figure 17. UOKS with specimen suspended. Bone pins were used to fix the Polaris tracking tools to each segment. Tekscan sensor inserted inside the knee joint.

Once all loading conditions were tested on the specimen, the ACL was transected using the serrated wire looped around the ACL and all muscle load conditions were repeated and tested in a different randomized order until five successful trials were simulated. The serrated wire was removed before testing resumed. Specimens were consistently sprayed with a saline solution throughout testing for preservation of mechanical properties and moisture levels. A flowchart summary of a single trial is shown in Figure 18.

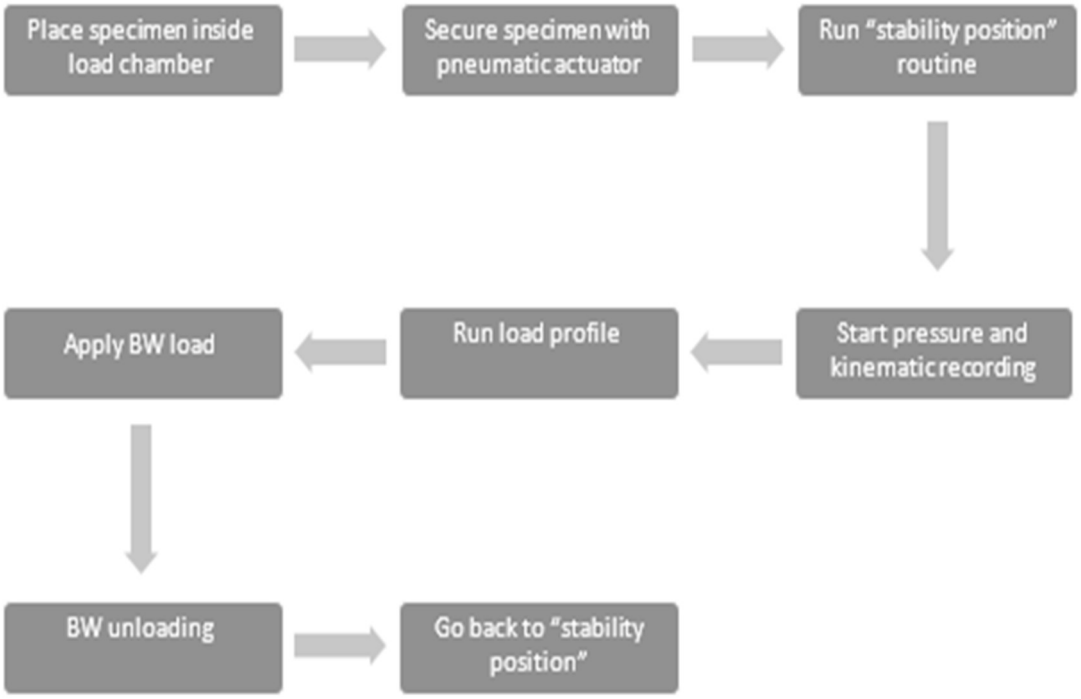

Figure 18. Flow chart of the protocol that will be followed for the pilot in vitro testing

4.4 Data Analysis

4.4.1 Pressure Data

Pressure data obtained from the trials was analyzed with the I-scan software built in analytical tools that allow the extraction of information through different methods. The information extracted were peak pressures, contact area, mean pressures and force from each of the compartments of the knee.

4.4.2 Kinematic Data.

All kinematic data were processed and analyzed with a custom MATLAB script. Kinematic data analyses were split into two parts: static and dynamic data. The static calibration was calculated to find the relationship between the digitized landmarks and the tools. These relationships were then used to construct two coordinate systems from the simulation trials. These result in the calculation of the joint kinematics as a result of the simulated loading conditions.

The Polaris software system recorded four quaternion units and three translation vectors to describe the orientation of rotation of each tracking tools (*Qo, Qx, Qy* and *Qz*). The translation vectors described the position of the centroid of the tools with respect to the origin of the global reference system in a three-dimensional reference system. All quaternions were transformed to Euler angles to facilitate interpretation using the following formula:

$$R = \begin{bmatrix} 1 - 2Qx^2 - 2Qz^2 & 2QxQy - 2QzQo & 2QxQz - 2QyQo \\ 2QxQy - 2QzQo & 1 - 2Qx^2 - 2Qz^2 & 2QyQz - 2QxQo \\ 2QxQz - 2QyQo & 2QyQz - 2QxQo & 1 - 2Qx^2 - 2Qy^2 \end{bmatrix}$$

Where *Qo, Qx, Qy* and *Qz* are the quaternion units found on the files that are created after a recording of a kinematic trial.

As previously stated, the static calibration was required as the operator can only track the tools attached to the rigid bodies. The data obtained with this calibration was used to calculate the fixed distances between the centroid of the tools and the digitized landmarks. All tools' parameters from the static trials were compared as a way of evaluating if the tool moved during the static trials. Subsequently, once the inspection proved if the data was good, the seven parameters that described the tools orientation and locations were averaged. The general process followed to construct these local reference systems described the location of the bony landmarks with respect to the corresponding tool's centroid and transformed from the global reference system to the tool's reference system. This means the landmarks of the femur were transformed to the system of the tool that was mounted on the femur, and tibial landmarks were transformed to the system of the tool mounted on the tibia. Once the fixed distances between landmarks and tools were obtained and stored, the reconstruction of landmarks based on tool location was obtained by transforming the landmarks back to the global coordinate system. The transformation from tool's coordinate system to the global coordinate system was calculated with the following transformation equation:

$$P_L^G = R_L^G P_L + T_G$$

Where P_L^G is the point in the global coordinate system

R_L^G is the rotation matrix to transform from the local to the global reference system

P_L is the vector that describes the landmark in terms of the local coordinate system, and

T_G is vector that describes the position of the tool with respect to the global coordinate system.

4.4.2.1 Femoral Coordinate system

The creation of the joint coordinate system for the femur followed the steps from the standards recommended by the International Society of Biomechanics (ISB) and Grood and Suntay [146]. This joint coordinate system was created by using the digitized points of the static calibration.

This joint coordinate system was created by using the digitized points of the static calibration.

The first axis was calculated by obtaining a line from the medial femoral epicondyle (*MFEpi*) to the lateral femoral epicondyle (*LFEpi*), forming the X axis (*Fx*). This vector was considered a fixed axis and was assumed to be perpendicular to the sagittal plane of the femur. The next axis was defined accordingly to the mechanical axis of the femur by using the hip joint center as a reference point. This axis was defined by creating a line that connects the point located at mid distance between the femoral epicondyles (previously used to calculate *Fx*) to the hip joint center (*HJC*). This new axis was named Fz and was used to represents the Z axis of this segment. Finally, the remaining axis, *Fy* was defined to be the cross product of vectors *Fz* and *Fx*. The origin of the femoral coordinate system (*Fo*) was located at mid distance between the femoral epicondyles. All vectors were then normalized to unit vectors.

$$Fo = \frac{LFEpi - MFEpi}{2}$$

$$Fx = \frac{LFEpi - MFEpi}{\left|\left|LFEpi - MFEpi\right|\right|}$$

$$Fz = \frac{HJC - \frac{LFEpi - MFEpi}{2}}{\left|\left|HJC - \frac{LFEpi - MFEpi}{2}\right|\right|}$$

$$Fy = \frac{Fz\ X\ Fx}{||Fz\ X\ Fx||}$$

4.4.2.2 Tibial Coordinate system

Similarly, a coordinate system for the tibial was created by following the recommendations of the ISB and the work of Grood and Suntay [146]. The axes that were created for the tibial segment and defined in a similar fashion, where the X axis was perpendicular to the sagittal plane of the bone. The axis was defined by the vector created from the medial tibial epicondyles (*MTEpi*) to the lateral tibial epicondyle (*LTEpi*) and referred to as *Tx*. The mechanical longitudinal axis of the tibia (*Tz*) was defined as the vector joining the ankle joint center (*AJC*) and the point located at mid distance between the two tibial epicondyles. The *AJC* was defined as the mid distance point between the malleoli. The Y axis of the tibial coordinate system was defined as the cross product of the *Tz* and *Tx* axes.

$$To = \frac{LTEpi - MTEpi}{2}$$

$$Tx = \frac{LTEpi - MTEpi}{||LTEpi - MTEpi||}$$

$$Tz = \frac{AJC - \frac{LTEpi - MTEpi}{2}}{\left|\left|AJC - \frac{LTEpi - MTEpi}{2}\right|\right|}$$

Where $AJC = \frac{LatMal - MedMal}{2}$

$$Ty = \frac{Tz\ X\ Tx}{||Tz\ X\ Tx||}$$

4.4.2.3 Angle Calculations

Once the two coordinate systems were calibrated to the specific segment, the spatial configuration of the joint was calculated. As previously stated, once the spatial location of the tool's centroid is known, the fixed distances from landmarks to the tool could be applied for the trial being processed. The construction of the coordinate systems was applied for all frames of each trial. To calculate the spatial orientation of the joint, an instantaneous floating axis (IFA) was defined as the instantaneous cross product of Tz and Fx and tracked for each frame on the trial. This model was proposed by Grood and Suntay [146] and described a simple approach to obtaining knee joint rotations independently from the order of the movement. The floating axis was used as a reference to calculate all three knee joint rotations by defining trigonometric relationships between the floating axis and the rest of the previously defined axes. All three rotation angles were found using the following equations:

$$Flexion = \alpha\ (+\text{ve}) = \cos(\alpha) = Fy \bullet \text{IFA}\ \ (\text{Magnitude of rotation})$$

$$\cos\left(\frac{\pi}{2} + \alpha\right) = -\sin(\alpha)\ \ (direction)$$

$$Adduction = \frac{\pi}{2} + \beta \ \text{for right knee}$$

$$and\ \ \frac{\pi}{2} - \beta \ \text{for left knee}$$

$$\cos(\beta) = Fx \bullet \text{Tz (Magnitude of rotation)}$$

$$\beta - \frac{\pi}{2}\ for\ right\ knee\ (direction)$$

$$\beta + \frac{\pi}{2}\ for\ right\ knee (direction)$$

$$External\ Rotation = \gamma\ (+ve) = \cos(\gamma) = Ty \bullet \text{IFA (Magnitude of rotation)}$$

$$\cos\left(\frac{\pi}{2}+\gamma\right) = -\sin(\gamma) \quad for\ right\ knee(direction)$$

$$\cos\left(\frac{\pi}{2}-\gamma\right) = \sin(\gamma)\ for\ left\ knee\ (direction)$$

Where α, β and γ are the angles designated to represent the three rotations as explained above. Each of the rotations is assigned a reference sign for differentiating the direction of the rotation. The set of equations will be used and solve for α, β and γ to obtain both magnitude and direction of the movement.

4.5 Statistical Analysis

4.5.1 Accuracy, Precision and Validity of the Load Controller

The accuracy, precision, validity, and reliability of transmission units were analyzed by comparing the load measurements from the transmission units and the external load cell. The data obtained from this experiment was used to test the reliability and validity of the controller used to modulate the loading conditions.

The reliability of the controller was analyzed by comparing the feedback measurement used by the controller to modulate and control the output of the actuators to the respective target load. The difference between these two paired loads was then calculated and descriptive statistics were calculated, such as means and standard deviations. Additionally, the data were compared and plotted using a Bland & Altman method of agreement to display the distribution and relationship between the difference of the paired loads and the target load. This method used the descriptive statistics to calculate two limits of agreement at +/- 1.96 times the standard deviation from the mean difference of these paired loads. The differences of these two paired loads was transformed to a percentage difference with respect to the target load and limits of

agreement were obtained with the mean percentage difference and the percentage standard deviation. Finally, the intraclass correlation (ICC) coefficients were calculated with a two-way mixed effect (3,1) model for single measurements. High correlations were defined to be any value over 0.75.

4.5.2 Reliability Analysis of Loading Mechanism

The second analysis for the load cell data consisted in comparing the load measurements from the feedback measurements and the measurements from the external load cell. A correlation plot was used to display the distribution of the data points to inspect the deviation between the slopes made by these points when comparing the measurements of the external load cell and the feedback measurement. The descriptive statistics were then calculated for the differences between these measurements and plotted using the Bland & Altman method of agreement. Additionally, the percentage difference was calculated and plotted using Bland & Altman method. Both Bland & Altman plots show the mean difference and the limits of agreement calculated. ICC coefficients were calculated using a two-way mixed effects model for single measurements. Furthermore, a high correlation was defined to be any value over 0.75.

4.5.3 In vitro Simulations

In vitro simulation data from 15 trials was analysed using a custom Matlab script (R2017b, Mathworks, Inc.). Tekscan variable (load, pressure, peak pressures and contact area) were plotted and included the respective curves for 15 trials. The sum of muscle loading profiles for all trials condition were also plotted in a single plot for comparison. The slopes for all load curves (Tekscan and muscle loads) were calculated from the start of the trial to the 30th second of the trial. The period in time was chosen based on visual inspection of the profiles, which showed the

loading profiles were fully applied and stable in all conditions. Load measurements from individual trials that were obtained with Tekscan were compared against the corresponding sum of muscle loads for that trial. The load value from the 30th second of the trial were extracted for both paired variables (Tekscan and sum of muscle loads) and plotted to analyze its distribution. Moreover, the difference between these paired measurements at the 30th second of the trial was extracted and compared against the expected sum of muscle loads at the same point in time. Mean of differences and limits of agreement were calculated and included in a Bland & Altman plot.

Kinematic data was analysed with custom Matlab Script (MATLAB 2017b). Absolute changes were calculated for the first 30 seconds of the trial to display the changes in knee rotations due to the loading conditions. Furthermore, all waveforms were plotted to display the full range of motion of the joint.

Chapter 5. Results

5.1 Accuracy, Precision and Validity of the Load Controller

The relationship between each simulated load at the transmission system level and the target load is characterized with a correlation plot. The correlation plot for the medial quadricep transmission system shows all data points simulated are closely related to the corresponding target load (Figure 19).

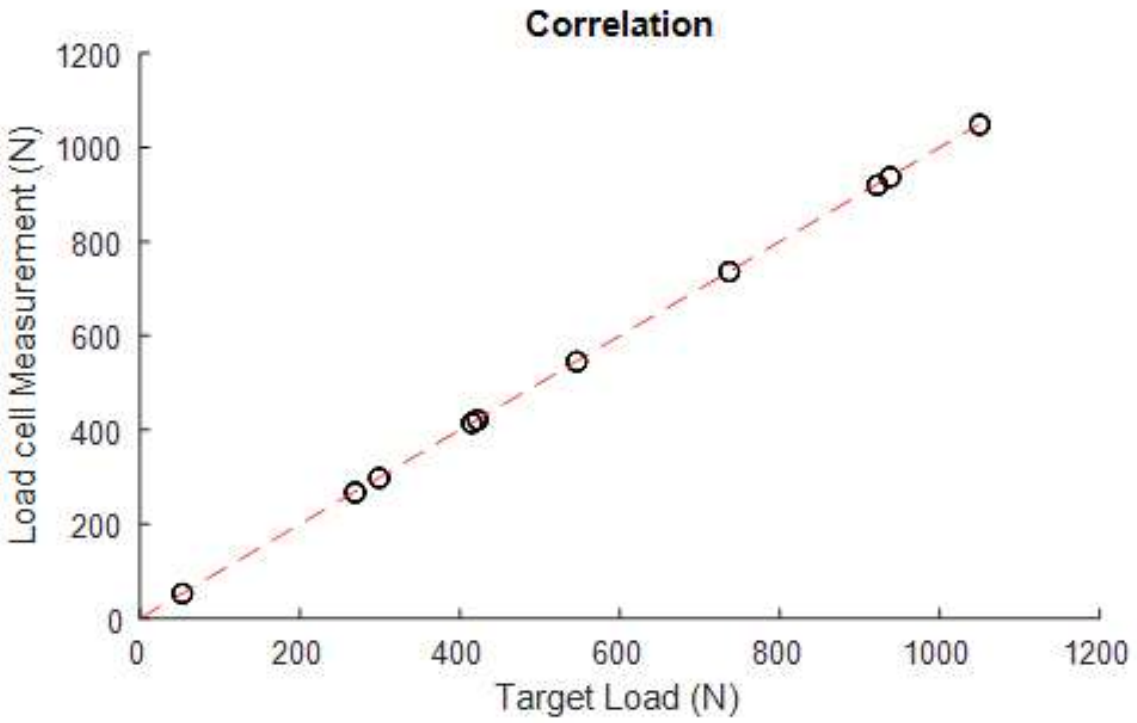

Figure 19. Correlation plot the medial quadriceps transmission. This graph was part of the first analysis of accuracy and precision of the controller. The red dashed line represents the ideal correlation line between the target loads and the loads measured with the load cells

The characterization of differences between the load produced and the target load was plotted using a Bland & Altman agreement method. This shows a mean difference (bias) of -0.98 N with a standard deviation of 0.71N. The limits of agreement are established at +/-1.96 times the standard deviation from the mean difference. These percentage differences show a mean difference -0.0027% with a standard deviation of 0.004%. The limits of agreement are set at 0.005% and -0.01%. The ICC reliability analysis of this muscle was calculated at 0.99.

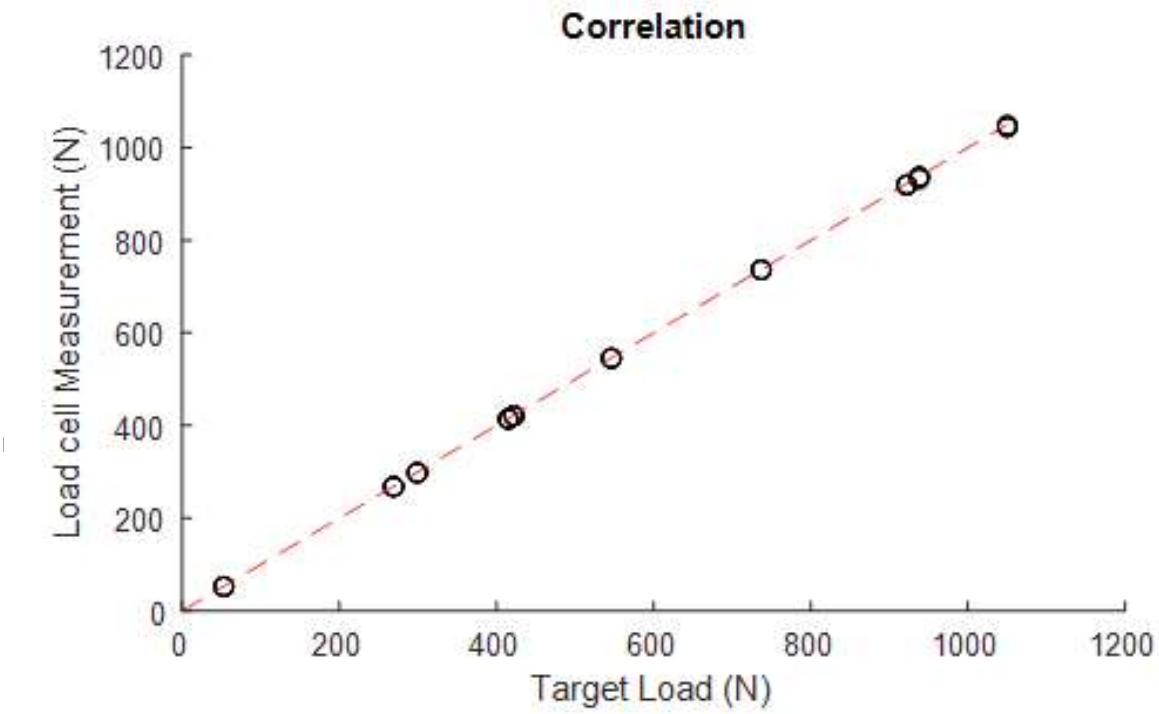

Figure 21. Correlation plot the medial hamstring transmission. This graph was part of the first analysis of accuracy and precision of the controller. The red dashed line represents the ideal correlation line between the target loads and the loads measured with the load cells.

The analysis for the control of the transmission system of the medial hamstring shows a relationship between the load produced and the target load. The scatter plot of these data points shows the measurement of the loads are distributed along the line of an ideal correlation (Figure

21). The absolute difference between the load produced vs the target load shows a mean difference of -1.36N and a standard deviation of 1.44N. The limits of agreement are 1.47N and -4.18N (Figure 22). The percentage difference of the load shows a mean percentage difference of -0.003% with a standard deviation of 0.003%. The limits of agreement are set at 0.004% and -0.01%. The distribution of data points for the highest load, 1050N, is the widest out of all the produced loads. In general, most of the absolute differences are between the 0N and the mean difference line. The biggest difference is found in this absolute difference plot around -7N. Additionally, the percentage difference is less than 0.20% of the target load. Furthermore, the reliability analysis of the medial hamstrings shows an ICC correlation of 0.99 for single measurements.

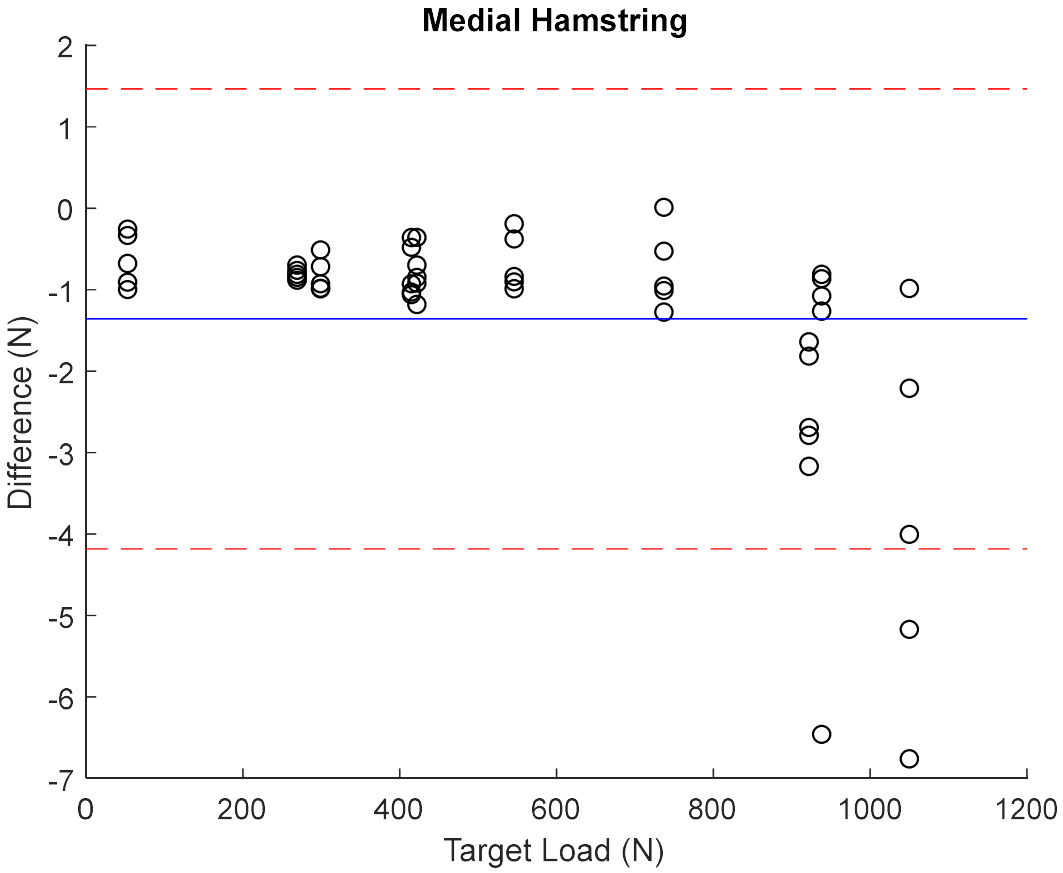

Figure 22. Bland & Altman agreement plot. This plot displays the distribution of differences between the target load and the UOKS loads (used to control the transmissions). The blue line represents the mean difference of the distribution, whereas the dashed red lines are the limits of agreement calculated for this distribution.

The correlation plot for the medial gastrocnemius shows a similar trend that the correlations mentioned above. The distribution of the points fall along the ideal distribution for a perfect correlation between the produced load and the target load. The ICC coefficient for this muscle shows a value of 0.99, reflecting good reliability when compared to the target load. The accuracy and precision analysis show the mean difference to be -1.04N (-0.003%) with a standard deviation of 1.44N (0.004%). The majority of the data points are distributed along the mean

difference with a distribution no larger than 10N for the data points of the two highest loads. This is reflected as a -0.01% difference in a percentage difference distribution plot. However, the largest percentage difference from the bias for these scatter points is just below -0.02% for the 53N load data points, which also falls outside the limits of agreement calculated at 1.78N (0.005%) and -3.87N (-0.012%).

The analysis for the lateral quadriceps shows an ICC correlation with a 0.99 value for single measurements. This is corroborated with the relationship shown on the correlation plot between the load produced and the target load, which shows all the data points aligning with the ideal correlation line. The mean difference describing the bias between the load produced and the target load is -1.12N with a standard deviation of 1.14N. Similarly, the mean percentage difference is -0.003% with a standard deviation of 0.003%. Additionally, the limits of agreement are set at 1.12N (0.004%) and -3.36N (-0.010%). The biggest deviation from the 0N difference is found below 8N for a scatter point of the 1050N load. On the other hand, data points for the 53N load have the widest percentage difference spread for this data set, but still under 0.020% from the ideal 0% difference.

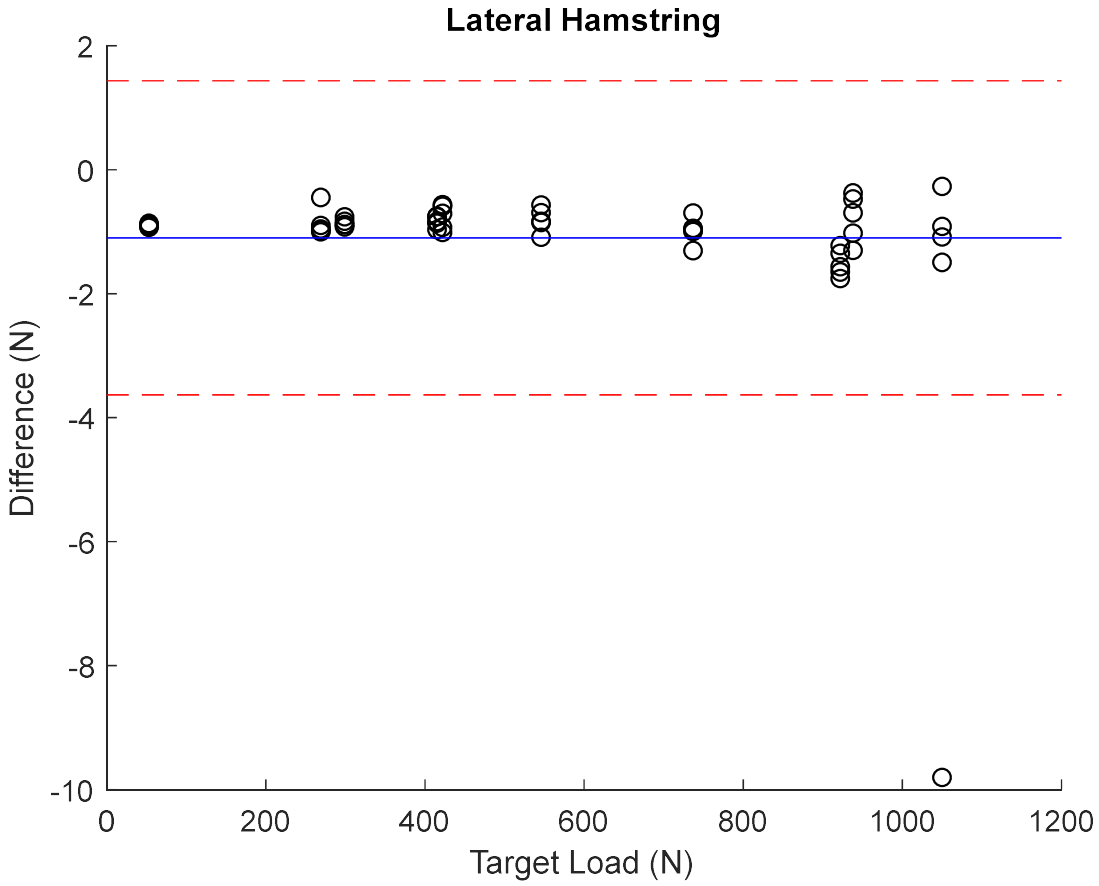

Figure 23. Bland & Altman agreement plot for the lateral hamstring. This plot displays the distribution of differences between the target load and the UOKS loads (used to control the transmissions). The blue line represents the mean difference of the distribution, whereas the dashed red lines are the limits of agreement calculated for this distribution. Mean difference = -1.1 N, upper limit = 1.43 N and lower limit = -3.63N

The ICC coefficient for the lateral hamstring shows a high correlation at 0.99 for single measurements when comparing the produced load with the target load. The distribution of the differences between these paired measurements shows a mean difference of -1.1N and -0.003%, with a standard deviation of 1.29N and 0.0005%. The limits of agreement are 1.43N (0.006%), for the upper limit, where as the lower limit is -3.63N (-0.012%). This distribution displays one

outlier at -10N, but the rest of the points are distributed along the mean difference, reflecting a repeatable fashion (Figure 23). Additionally, the distribution of the points on the percentage difference plot follow a trend to decrease and approximate zero percent as the target load increases.

The lateral gastrocnemius correlation values displays a high correlation between the loads produced and the target loads. The correlation plot shows the data points being distributed along the line representing the ideal correlation. The relationship of these paired measurements is also described by the ICC coefficient calculated at 0.99 for single measurements. The graphical comparison between the measurements display the distribution of the data points to have a mean difference of -0.74N with a standard deviation of 0.49N and limits at 0.22N for the upper limit and -1.71N lower limit. Similarly, the mean percentage difference for these paired measurements is -0.003% with a standard deviation of 0.004 and limits at 0.005% and -0.01%. The distribution of the differences of paired measurements for this muscle show a that the spread of this points is less than 2N above or below the zero newton difference. Finally, the mean bias for all muscles is -1.06N with a 1.1N standard deviation.

5.2 Reliability Analysis of Loading Mechanism

The second subset of data was used to characterize the differences between the loads being produced by the transmissions and the true simulated load after the mechanical components at the front end of the simulator.

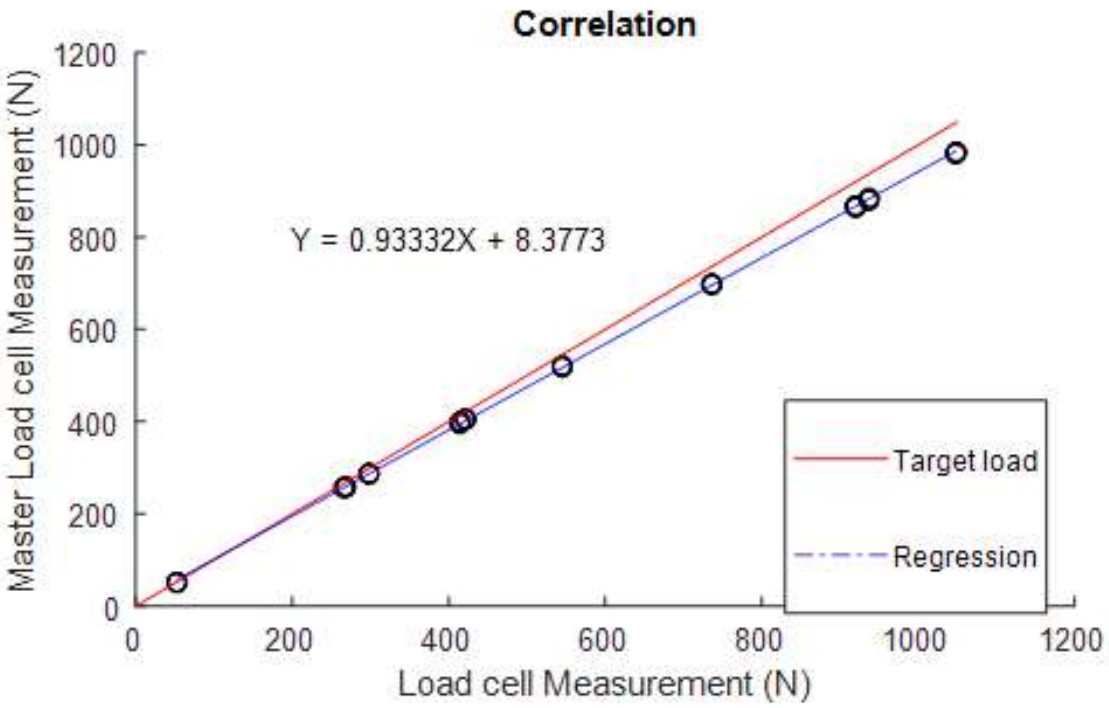

Figure 24. Correlation plot between the UOKS load for the medial quadriceps and the external load cell. The blue line represents the regression of the distributed points. Red line represents the ideal distribution of the correlation.

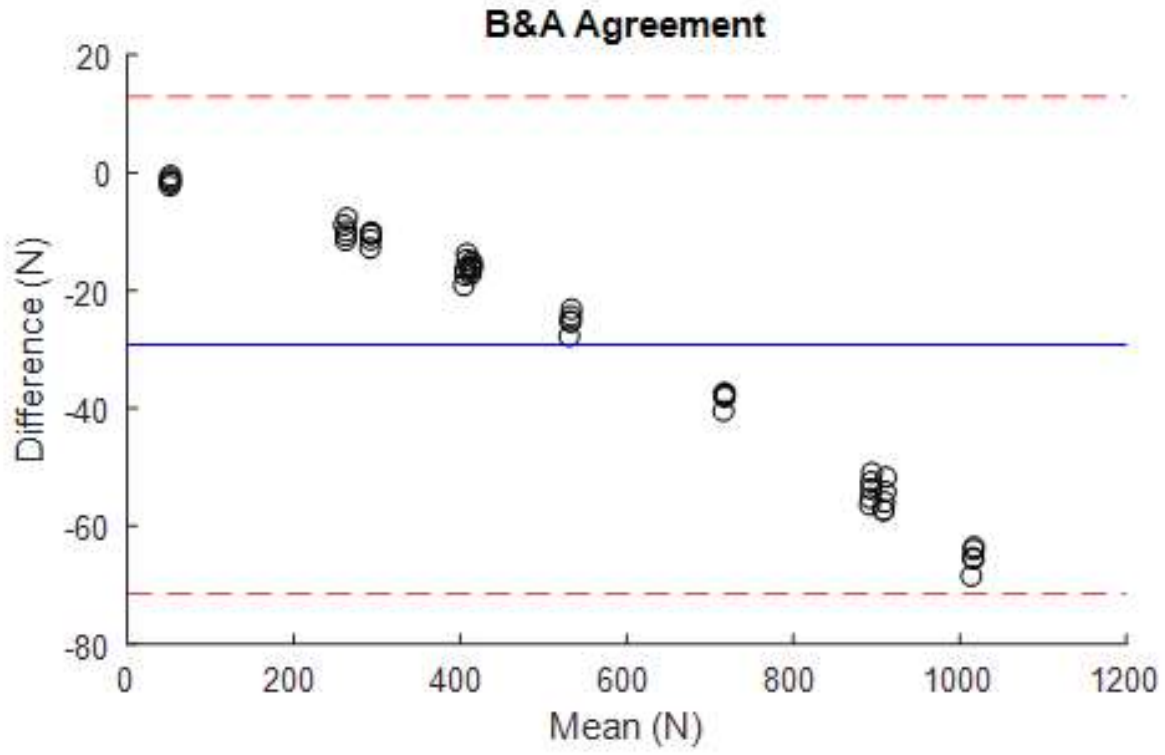

Figure 25. Bland & Altman agreement plot for the quadriceps medial. The distributed points are the differences between paired measurements obtained across all trials for this transmission. Points follow a trend to deviate from the 0N difference as the target load increases. The blue line represents the mean difference and dashed lines are the calculated limits of agreement.

The coefficients obtained from the ICC evaluation show high values for all muscles and the simulated loads, with a minimum value of 0.997 for the medial quadricep transmission and a maximum value of 0.999. The medial quadricep transmission has the largest absolute difference for any individual trial of 70N from the load produced at 1050N, which represents a 7% relative difference with respect to the expected value (Figure 25). The mean difference for this muscle is -29.24N with a standard deviation of 21.50N. The mean percentage difference is -4.67% with a standard deviation of 1.29%. The limits of agreement are 12.91N and -71.38N, whereas the percentage agreements are -2.14% and -7.19%. The distribution of data points is found below

the zero newton difference for the absolute and percentage difference plots, showing that the true simulated load is always below the expected load. The distribution of the differences shows the data points to deviate from the absolute zero difference by a larger value when the produced load increase. A similar trend is observed when the distribution of percentage differences were plotted, as the produced load increases the percentage difference becomes larger. Additionally, the calculation of a linear regression shows the degree of relationship between the paired measurements, which showed the deviation of the true simulated load to be greater when trying to load the front end with this muscle above 500N.

The transmission unit for the medial hamstring do not follow the trend of overestimating results. Even though the ICC coefficient for these paired measurements show a high correlation with 0.99%, the relationship of the measurements displayed that the expected loads are underestimated in comparison to the true simulated load at the front end of the loading mechanism. This trend is noticeable for most of the measurements above 53N. Thus, the absolute mean difference is above the zero on the Y axis at 13.21N with a standard deviation of 9.38N. The absolute difference distribution also shows the difference increases as the expected loads increase in contrast to a distribution of the percentage difference, which decrease as the expected loads increase. On the other hand, these differences show a different trend when being distributed according to the relative difference of the load. The percentage difference approximates zero and close to the mean percentage difference (0.76%) as the expected loads increase for the tested loads above 53N. The only distributed points that do not follow this trend are found outside the limits of agreement (10.99% and -9.46%) and have the largest percentage difference of approximately -15% with respect to the expected load.

The linear best fit was calculated for the distribution of loads between the simulated loads and the front end simulated loads for the transmission of the medial gastrocnemius. The best fit overlaps the distribution of the points showing a good fit. Furthermore, the ICC coefficient for these comparisons displays a similar result, with a value of 0.99 for single measurements. However, the distribution of differences between these paired measurements shows a mean difference of 1.31N below the 0N on the Y axis and a standard deviation of 2.46N with limits of agreement of 3.52 N and -6.14N (Figure 26). Furthermore, the differences between the measurements appear to go from an overestimation to an underestimation (negative to positive difference) as the expected simulated load increases, but none of the points fall outside of the established limits of agreement. The percentage difference distribution of the measurements shows a trend for the points to approximate zero as the expected load increases. This visual representation displays the distribution of the points to be, in most cases, near the mean percentage difference (-1.34%) or above it. The largest percentage difference is -10% for the 53N data points, whereas the rest of the points are located between the mean percentage difference and 1%.

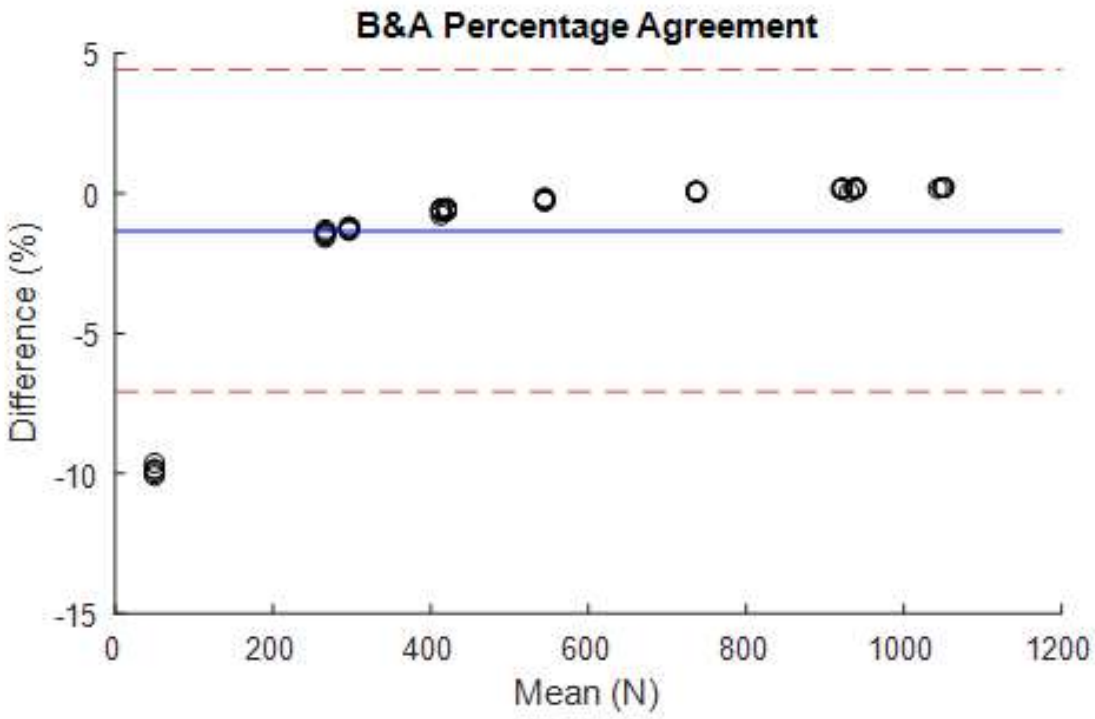

Figure 26. Bland & Altman agreement plot for the reliability analysis of the medial gastrocnemius. The distribution of the percentage difference between the medial gastrocnemius UOKS loads and the external load cell. Points show a trend to approximate zero as the simulated load increases. Blue line represents the mean percentage difference. Red dashed lines represent limits of agreement.

The comparison between the loads for the lateral quadriceps show a relationship with an ICC coefficient for single measurements at 0.99. The distribution of the points in a correlation plot show an overlap between the regression line (measurements shown in blue) and the ideal expected distribution. The deviation of the true simulated measurements shows a change in trend from an underestimation to an overestimation as the expected load increases in value. The largest difference is found at -11N and outside the established limits of agreement for this distribution. The mean difference is -1.12N with a standard deviation of 4.24N and limits of agreement of 7.18N and -9.42N. The true simulated values represent less than +/-2% difference

from the expected value. The trend of the percentage differences between the paired measurements shows a similar pattern of underestimation and overestimation with an increase in percentage deviation as the mean measurement increases. However, the overall trend for this distribution have a mean percentage of 0.12% and a standard deviation of 0.73%.

The paired measurements from the transmission unit that simulated the lateral hamstring has an ICC coefficient of 0.99 showing agreement between the two. Additionally, a correlation graph illustrates this relationship with the overlapping of the expected value and the true simulated value, which displays low difference between the two. Similarly, the difference between these paired measurements is averaged at 3.64N below zero and a standard deviation of 1.83N. The distribution of the points shows that all measurements are located below the 0N difference. This pattern shows an overestimation of the loads for this loading mechanism, meaning that the load applied were below the expected value. Nevertheless, these differences are relatively small for most of the measured loads. The distribution of percentage differences shows an approximation to a 0% difference with a trend of plateauing with a constant value with larger expected loads. This is not the case for the data points of the 53N trials, which present a larger percentage difference of approximately 15% to 17% (or around 8N in absolute value).

Lastly, the loading mechanism for the lateral gastrocnemius displays a good relationship with the expected loads. The regression line for the measured data points shows visual similarities with the expected load and both lines overlapped with each other. This relationship between the paired measurements is corroborated with the ICC coefficient calculated at 0.99. The Bland & Altman agreement plot shows the mean difference to be close to 0 at -0.15N with a

standard deviation of 2.24N. Additionally, the differences follow a pattern of overestimation to underestimation with increased target loads. For this reason, the percentage difference distribution for the data of this muscle shows the data points to approximate zero and distribute around this point, as the difference remains relatively small with larger expected loads.

5.3 In vitro Simulations

The new UOKS was used during the in vitro simulations to provide more insights on the new controller and the automated loading mechanism. The results presented in this section include data for 15 trials of one in vitro simulation. Visual inspection of the data indicate that the pressure inside the compartment was localized inside the medial compartment of the knee for all trials.

The initial results show the sum of applied loads to follow a trend during the initial loading phase of the trials. The slopes for each trial are displayed in (Figure 27) showing the deviations between them trials. The mean of these slopes is 29.33 +/- 2.73 N/s for the first 30 seconds of the trial. The combined representation of these curves shows a clear separation between trials, with retests of same conditions overlapping one another on the phase where the loads had already been applied. On the other hand, the slopes for the loads measured with Tekscan show a similar trend with overlapping of the waveforms for the curves for the first 30 seconds of the trials. The mean slope for all the curves is 35.51 +/- 4.89 N/s. However, the opposite is observed for the load measurements obtained with the Tekscan sensor during the phase when the loads had already been applied. The Tekscan pressure values display the same

value for mean slope of as the Tekscan loads, where as contact area shows a slope of 1.99 +/- .6833 mm/s during the loading phase.

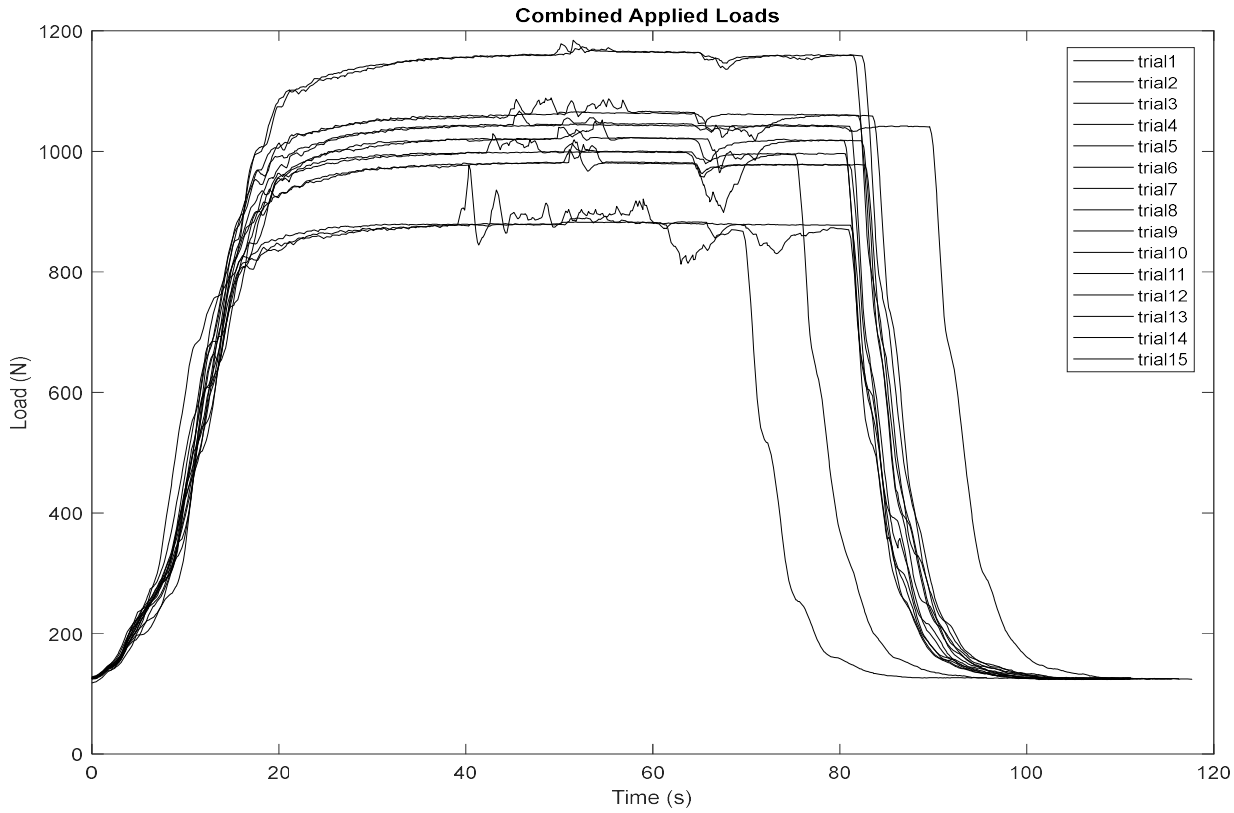

Figure 27. This plot includes the sum of all applied loads for all 15 trials. The initial phase demonstrates the repeatability of the loads in all trials. The mean rate of change of all trials was calculated at 29.33 +/- 2.73 N/s.

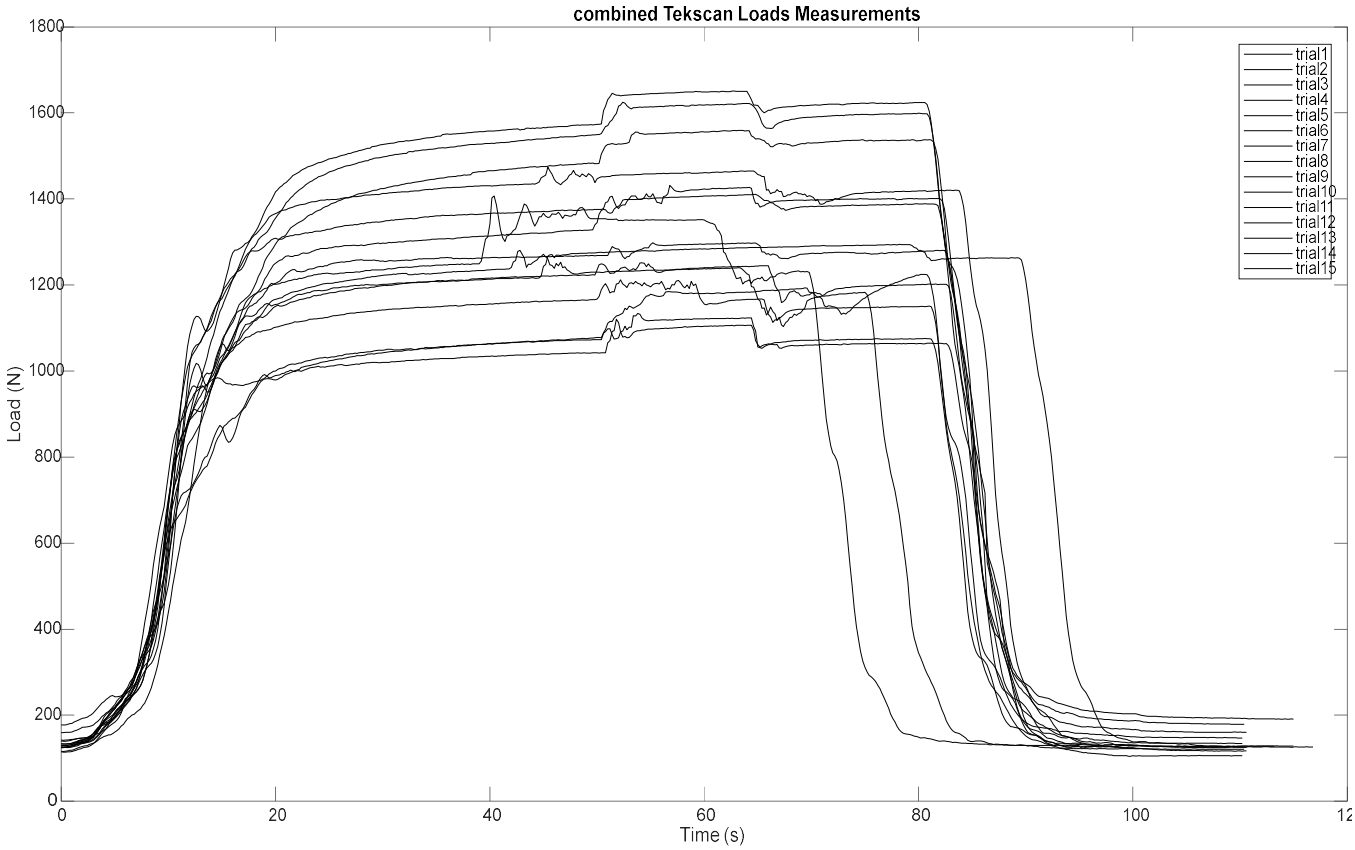

Figure 28. Plot for the load measurements obtained with Tekscan. The mean rate of change of the load applies during the first 30 seconds of the trials was calculated at 35.51 +/- 4.89 N/s. These curves represent the 15 trials of the pilot simulation.

A comparison between of load waveforms show the difference between the two systems. For all trials, Tekscan sensor experienced higher loads after the system had already the applied simulated the loads. The difference between load measurements are shown in Table 3, as well as the mean and standard deviation (Calculated at the 30th second, which is where the load had been applied). The distribution of these differences in comparison to the loads applied by the UOKS show a bias of 257.10N and a standard deviation of 145.21N. The calculated limits of

agreement show the intervals that included 95% of the distribution of these differences. These are set at 541.71N and 27.51N, as shown in Figure 29.

Table 3. Below the difference between the load measurements of the OKS and Tekscan are displayed. The values found below were obtained from the 30th second of each trial for both methods this frame in time represented the frame in which loads were already applied.

	UOKS	Tekscan	
	Load (N)	Load (N)	Difference (N)
Trial 1	869.27	1235.3	366.03
Trial 2	1050.47	1411.1	360.63
Trial 3	991.04	1221.9	230.86
Trial 4	1030.78	1201.1	170.32
Trial 5	1136.61	1255.5	118.89
Trial 6	1007.68	1198.1	190.42
Trial 7	969.98	1019.6	49.62
Trial 8	1051.65	1346.7	295.05
Trial 9	969.77	1048.3	78.53
Trial 10	877.84	1141.6	263.76
Trial 11	1143.82	1296.3	152.48
Trial 12	1031.13	1424	392.87
Trial 13	1013.15	1496.1	482.95
Trial 14	992.43	1526.2	533.77
Trial 15	871.29	1041.7	170.41
		Mean	257.10
		Standard Deviation	145.21

Additionally, waveforms were plotted to show the representation of the baseline condition and the changes from increasing and decreasing the specific muscle loads. These show that similar conditions overlap with each other indicating a similarity between them. This is not the case for any of the measurements obtained with Tekscan for any of the paired measurements, as seen on Figure 28.

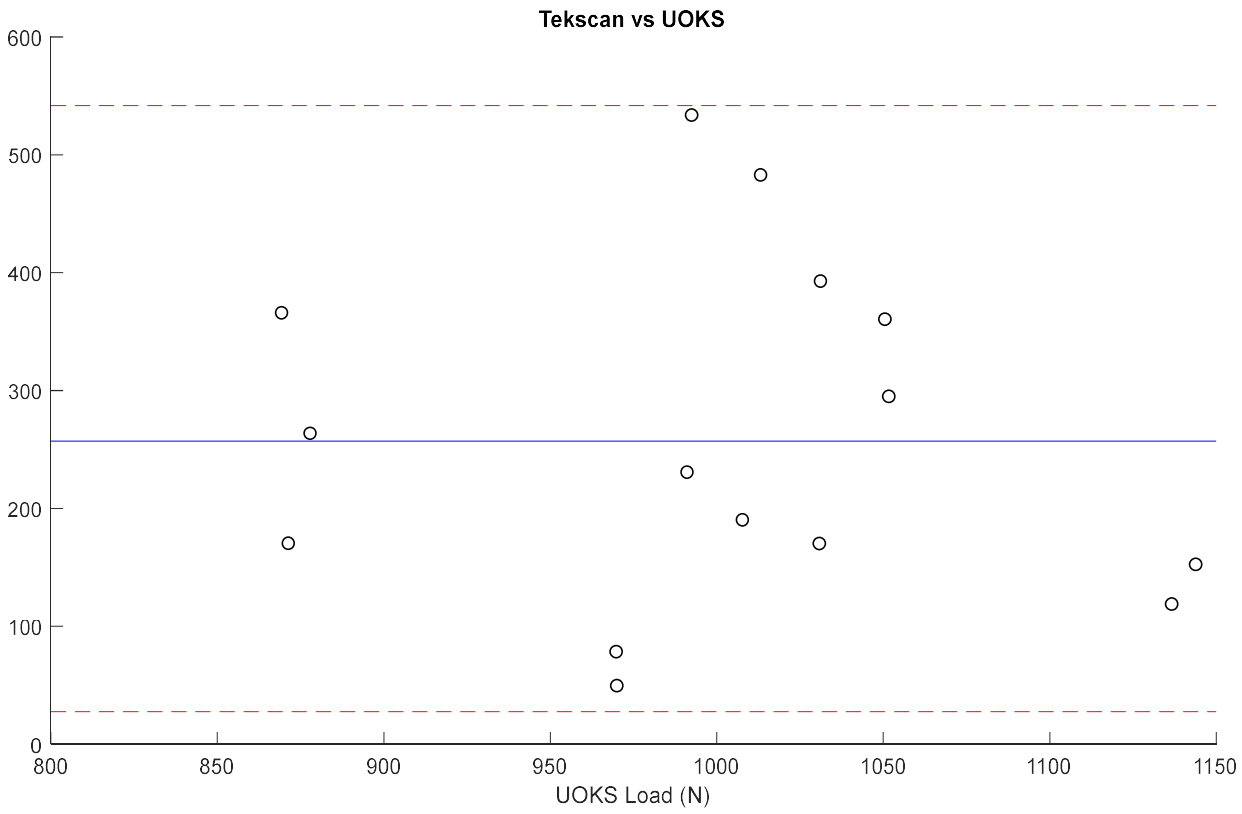

Figure 29. Bland & Altman agreement plot for the differences between the two load measurements obtained with the Tekscan sensor and the UOKS load cells. The blue line represents the mean difference of the distribution and the red dashed line are the limits of agreement for the same distribution.

Pressure measurements as a result of the loading show increased peak pressure values for the medial compartment. Maximum Peak pressure values are higher than 9 MPa in all trials, with a maximum value of 9.6 MPa. On the other hand, contact area changes experience as a response to the increased loading applied to the specimens are shown for each individual trial in Appendix F: Results Values for maximum, minimum and mean contact area are shown on *Table 4*.

Table 4. Table showing the mean contact area, maximum and minimum value for contact area

Tekscan Contact Area (mm^2)			
	Mean Contact Area	Max Contact Area	Min Contact Area
Trial 1	323	359	250
Trial 2	333	374	214
Trial 3	324	374	196
Trial 4	327	363	196
Trial 5	320	374	185
Trial 6	322	370	218
Trial 7	307	367	200
Trial 8	322	363	240
Trial 9	301	363	214
Trial 10	296	348	203
Trial 11	297	352	210
Trial 12	301	301	247
Trial 13	309	309	243
Trial 14	309	348	250
Trial 15	256	301	185

The results obtained for the analysis of kinematic data are summarized below in Figure 31, Figure 30, Figure 32 and in Appendix F: Results Three trials had to be discarded (trials 7,8,9) due to malfunctioning of the sensors that did not provide any data. The waveforms for all rotations show the differences in specimen realignment after unloading. This means that the specimen finished the trial in a different configuration that what it started. Furthermore, maximum changes for each rotation are displayed in Table 5. Maximum absolute changes for the first 30^{th} seconds of the trials were calculated to represent the changes caused by the loading phase of the trials.

Table 5. Maximum change in knee joint rotations obtained with the optotrak motion camera during the first 30 seconds of the trial. These values represent the changes in knee joint orientation as a result of the loads simulated on the specimen. Trials 7, 8 and 9 were discarded due to sensor malfunctioning.

	Maximum change in Degrees (°) for the first 30 seconds		
	Flexion/Extension	Adduction	External/Internal
Trial 1	2.207	1.54	2.33
Trial 2	1.31	1.91	3.60
Trial 3	0.97	1.67	3.22
Trial 4	2.91	2.11	4.56
Trial 5	2.25	1.96	3.96
Trial 6	2.41	1.93	3.95
Trial 7	----	----	----
Trial 8	----	----	----
Trial 9	----	----	----
Trial 10	1.79	1.55	3.35
Trial 11	0.62	1.11	2.21
Trial 12	5.66	2.39	7.01
Trial 13	4.78	1.98	5.99
Trial 14	3.79	1.97	5.35
Trial 15	2.61	2.38	4.65

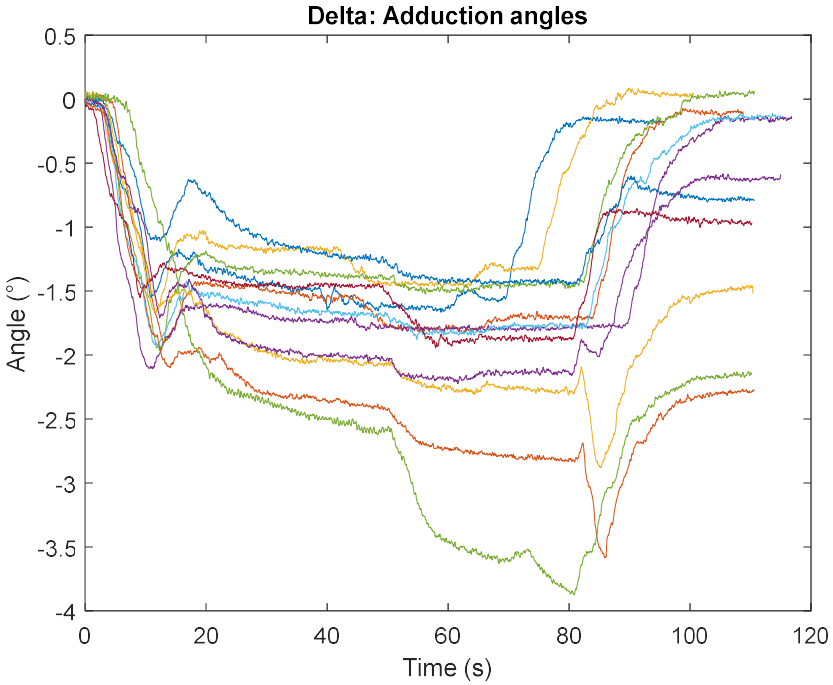

Figure 30. Changes experiences by the knee joint during the loading simulation. The curves represent the change in adduction angles. Negative changes represent an increment in the adduction angle of the joint.

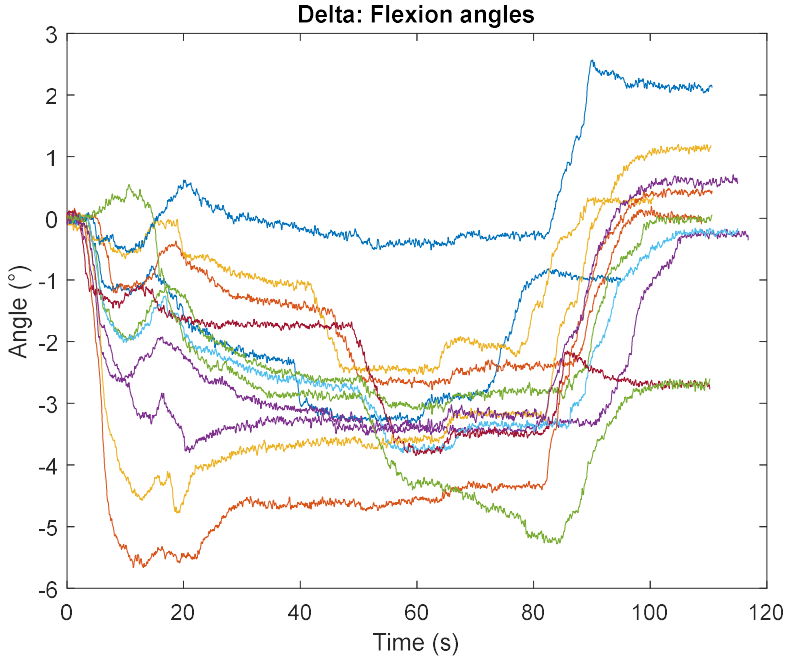

Figure 31. Changes experiences by the knee joint during the loading simulation. The curves represent the change in flexion/extension angles. Positives changes represent extension and negative flexion.

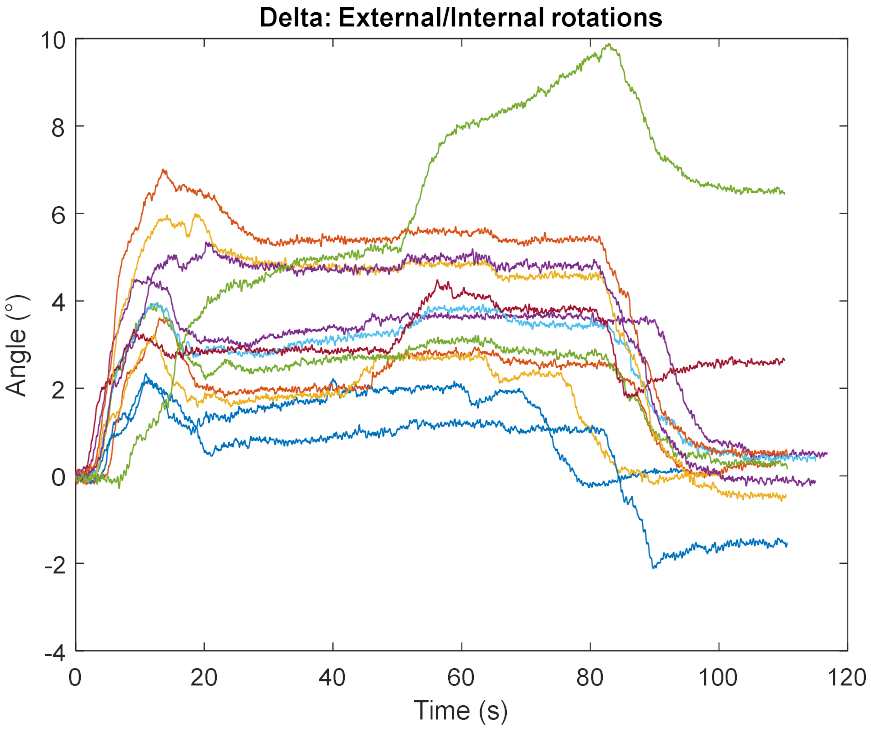

Figure 32. Changes experiences by the knee joint during the loading simulation. The curves represent the change in internal/external rotations for all 15 trials. Positives changes represent exterior rotations and negative describe the internal rotations.

Chapter 6. Discussion

In vitro experiments require repeatable and reliable conditions as a pre-condition for results that can be considered valid, in addition to conditions reflecting physiological interactions. The objective of this research focused on the integration of actuators, load sensors and a GUI to automate the loading mechanism of the UOKS. The integration and testing of electromechanical actuators controlled via a user interface increased the loading capabilities of the UOKS by improving the reliability and accuracy of applied loads, and the modulation of those loads to represent physiological conditions.

6.1 Accuracy, Precision and Validity of the Load Controller

Stepper motors were selected as the actuators in charge of driving the loading capabilities of the system. The capability of precise stepping control and added torque resulted in a reliable loading mechanism as shown by the results. The gearbox increased the resolution of steps for each transmission and added torque to each transmission unit. However, these added capabilities came at the price of limited velocities, as these characteristics are proportionally inverse to each other (Table 6). Each transmission unit was tested during three different settings (calibration, reliability experiment and in vitro simulation), demonstrating the capabilities to create loads and to replace the previous loading system. The load cells were reliable and accurate, with the controller producing these loads in a repeatable fashion. The correlation analyses showed high ICC coefficients (> 0.99) for all applied loads when compared against the respective target loads.

To evaluate the accuracy and precision of the simulator, the differences between the simulated loads and target load for the corresponding trials were evaluated. This evaluation showed that the controller was biased by 1N below the target load. This mean difference corroborated the programmed capabilities of the controller to regulate the loads around the target load by 1N. This feature was implemented to provide a more reliable method to achieve the target load accounting for variation on load cell measurements. Nevertheless, these biases can be improved by implementing proper filtering techniques for the data and a more robust control method. Additionally, the distribution of these differences for all data points against the respective target load showed a pattern of the data points being localized around the bias of 1N (Appendix E). Another pattern was observed when larger target loads were applied during this experiment, the percentage difference between the measured load and the target load decreased, approximating the 0% difference. This showed the difference between the target loads and the simulated loads remained constant, and thus representing a smaller portion of the target load. These patterns also demonstrated the capabilities of the simulator to repeatedly simulate the target loads set by the user with an accuracy of +/-1N.

6.2 Reliability Analysis of Loading Mechanism

The calculated differences between the measurements were below 5% for four of the six transmissions. However, special attention was paid to differences observed on the data from the medial quadriceps and medial hamstring. These two transmission units reported high ICC coefficients, 0.9976 and 0.9996 respectively, nonetheless, the distribution of these differences showed patterns reflected in both the percentage difference distribution and the absolute differences. The transmission assembly used to simulate the medial quadricep force showed the

biggest difference in terms of raw and percentage data. The scatter plot of the percentage difference for transmission showed a trend of the data points to negatively deviate more from the bias as the produced load increased in value (Figure 25). These increasing differences presented a problem when simulating loads above 1200N for this muscle (medial quadriceps), and even though loads above these values were not tested, the trend indicates that higher loads will produce larger differences. An explanation for this difference was related to the mismatch dimensions of the driving and driven pulleys of the mechanical components. The difference in dimensions affected the ratio between the pulleys, this affected the load applied at the front end of the simulator. Mechanical loses in the system also contributed to the difference found for this muscle. Mechanical factors, such as wear, tear and lubrication level of the bearings supporting the shaft affected the outcome of the load transmissions. Moreover, differences found on medial hamstring data showed an increase in absolute difference as the magnitude of the simulated load increased, but the percentage mean difference remained under 0-5%. These differences can present a problem for simulations that look at differences between muscles with load values similar to each other. Future experiments that focus on the effect of small differences between muscle groups, increasing error of the medial hamstring could make two loads overlap and affect the outcome of the experiment. For this reason, special care should be taken when designing a loading protocol and particularly with the muscle load profiles being selected for simulation.

6.3 In vitro simulations

The reported results for the in vitro simulations showed the capabilities of the simulator to apply a set of simulated loads to a cadaveric specimen. The repeatably of the simulated loads

profiles was corroborated by the plots that showed the overlapping of the initial phase of the loading. The initial phase of the curves indicated the start of the simulation and the slopes showed a resemblance between all conditions. The mean slope of this curve reflected the rate of change of the load to have a small variation according to the calculated standard deviation. This small variation was attributed to the initial tension of the wires and the method used to calculate the rate of change for the load. First, with an increased initial tension on the wires, the target loads for any muscle were reached earlier and the opposite for a lower initial tension on the wires. Second, the rates of change were calculated from the start to the 30th second of the trial to include the phase in which the loads were applied and stabilized; and even though the calculation included phases when the loads started to plateau, the standard deviation showed the small variation of the slopes for the sum of simulated loads. This was considered to be a reflection of the repeatability of the loading and the characteristics of the loading capabilities of the simulator. Additionally, this was one of the added advantages of using automated systems to preserve the repeatability of conditions in loading experiments.

Differences were also found between the loads that were applied and the joint loads obtained with the Tekscan sensor. In general, all trials showed a higher load for the Tekscan measurements than those applied by the muscles. The differences between the test and retest trials followed no clear pattern and the waveforms were inconsistent between max values for repeated trials (Table 5). At first, it was believed that the initial vertical force had an effect on the load difference. The initial vertical force was applied at the beginning of each trial to keep the specimen in position, nevertheless, the effect of such force did not affect the joint loads. These initial readings showed consistency with only the sum of pre-simulation muscle loads

programmed to be reached at the end of each simulation at a value of 30 N for each muscle. Additionally, the testing environment and the size of the knee could have affected the readings of the sensor. The size of this knee did not have enough room to fit the sensor inside the joint space, and so part of the sensor could have been damaged during installation without the experimenters knowing about it. Also, the environment of the simulation involved the use of substances such as a saline solution that could have affected the readings of the sensor.

6.4 Limitations

The UOKs is not without limitations. The junction between the stepper motor and the gearbox used a collet to clamp the shaft of the stepper motor. This interface was prone to slippage and eventually caused wear of one element in the junction. This issue was of concern as some of the gearboxes used for the transmission system had to be disassembled and inspected for damaged during calibration. For this reason, the interface is not ideal for high torque transmission, particularly when the gearbox inner system can be driven by the output shaft but is a limitation of using off the shelf components. Additionally, the output of the gearbox used a D-shaft to interface with a shaft coupling to connect to the driving shafts located in the back of the simulator. Torque transmission in this interface was ensured with a setscrew on the coupling that prevented slippage between the D-shaft, however, torque transmission relied entirely upon the flat surface of the setscrew. Another limitation of using set screws is the vibration of the system can eventually loose the screw and potentially affect torque transmission.

The quasi-static nature of the simulator can only provide a limited hindsight of such interactions. Results obtained with this simulator should only be compared to discrete points in time and not as a continuous circumstance for the following reasons. First, the loading

application on loads is not likely to occur in the same fashion on in vivo situations, as some muscles might activate at different times and at a higher velocity. Second, the dynamic simulation of loads might require a more robust control method with more capabilities to load muscles at specific times, specific frequencies and with more sources of feedback. The selected feedback load cells used by the controller are not recommended for dynamic loading and due to their fabrication and physical properties it would be hard to obtain accurate or precise dynamic measurements under fast circumstances

Another limitation of the simulator comes from the integration of other instruments used with the current testing protocols. The current workflow involved three operators to perform a single trial with four different instruments. This potentially affects the time synchrony of trials, making it hard to obtain the relevant data from different sources at the same point in time.

The use of Tekscan can be troublesome as the k-scan sensors do not come in a variety of sizes or with the capabilities of being trimmed to adjust to specimen size. This issue limits the use of these sensors to specimens with considerably larger dimensions to accommodate the sensor without causing any folding onto itself, which can also affect readings with the sensor. Tekscan I-scan pressure sensors do not perform reliably under dynamic conditions and tend to provide better and accurate readings as the load is kept constant on the sensor for a short period of time, however, these sensors can track movement and activation of the sensels overtime. Moreover, the analysis of kinematic changes for the rotations showed that the joint experienced change of a few degrees in all three rotations. The rotations of the joint potentially affected the curvature of the sensor, which is reported to cause overestimations of force values. Another limitation of the sensor was found during a visual inspection of the trials, which showed the saturation of the

sensor during parts of the loading protocol. Furthermore, the use of the motion capture system can be compromised in some instances, where the simulator physical appearance can introduce noise into the readings of the instrument. This became a recurrent issue during in vitro testing, the motion capture camera could not complete a calibration for each segment due to background noise. However, removing the tools from the specimen and blocking the simulator would reduce the surrounding noise, allowing the cameras to pick up the sensors.

Other limitations of the presented protocol encountered during in vitro testing of the simulator regarding alignment and suspension of the specimen inside the loading chamber. The current fixtures do not allow a proper physiological alignment to simulate a heel strike position. Instead, the specimen leans to the side and predisposes the knee joint to experience more pressure on the leaning side. This could be corroborated as the initial Tekscan pressure readings would show considerably higher readings on the leaning side of the joint. Additionally, the unconstrained behaviour of the knee affected the application of vertical loads causing the specimen to flex, move and accidentally reposition the specimen in a different configuration. This was the case for many simulated trials, which changed the alignment of the specimen and affected the directional forces being applied. This issue occurred consistently throughout the all four in vitro simulations, but the appearance of such became more common with smaller specimen sizes.

6.5 Future Work

In vitro testing of the new UOKS showed the reliability of the simulator to create loads in a reliable and accurate fashion. The capabilities of the simulator to be used for in vitro protocol

are dependent on the amount of time invested in the preparation of the specimen. The current simulator design provided numerous challenges when it came to suspend and align the specimen inside the loading chamber. Nevertheless, the novelty of the UOKS relies on the unconstrained response of the simulator due to its custom made fixtures. Proper positioning of the specimen became an arduous task due to the constrained adjustment of the hip joint and ankle concave plate. This highlights the need for further improvement and research on a more flexible and reliable set of fixtures to suspend the specimen. New fixtures can provide a more simple and fast approach to suspend the specimen. Additionally, proper suspension of the specimen can improve the loading protocols by allowing the application of vertical ground reaction forces without the specimen lifting from the concave plate and losing feedback from the load cell of the MTS testing machine.

Chapter 7. Conclusion

The purpose of this thesis was to further increase the capabilities of the UOKS. An automated loading system was built to replace a mechanical loading framework from the previous iteration of the UOKS. The new system was design and built to replace the hanging weight mechanism of the UOKS. A set of six transmissions and load cells were added to the UOKS. A control GUI was programmed to control the motion of the transmission and tested to asses it's accuracy, precision and validity. The analysis showed the capabilities of the fully integrated actuator based loading mechanism to generate loads for simulated conditions in an accurate and reliable manner. Furthermore, the implementation of load cell measurements and computer controlled proved to generate and achieve target loads programmed by the user in a repeatable manner. In vitro simulations showed the capabilities of the simulator to transmit these loads to a cadaveric specimen. For these reasons, it is considered that the new automated UOKS proved to be a reliable load driven simulator capable of reliable performance. Thus, the new capabilities of the UOKS can be used to decrease the knowledge gap on the effect of muscle forces have on knee joint contact mechanics.

References

[1] G. Li, T. W. Rudy, C. Allen, M. Sakane, and S. L.-Y. Woo, “Effect of combined axial compressive and anterior tibial loads onin situ forces in the anterior cruciate ligament: A porcine study,” *J. Orthop. Res.*, vol. 16, no. 1, pp. 122–127, Jan. 1998.

[2] K. L. Markolf, W. L. Bargar, S. C. Shoemaker, and H. C. Amstutz, “The role of joint load in knee stability.,” *J. Bone Joint Surg. Am.*, vol. 63, no. 4, pp. 570–85, Apr. 1981.

[3] K. L. Markolf, J. Mensch, and H. Amstutzm, “Stiffness and Laxity of the Knee - The contributions of the supporting structures,” *J. bone Jt. Surg. Am. Vol.*, vol. 58, 1976.

[4] B. D. Beynnon, P. M. Vacek, M. K. Newell, T. W. Tourville, H. C. Smith, S. J. Shultz, J. R. Slauterbeck, and R. J. Johnson, “The effects of level of competition, sport, and sex on the incidence of first-time noncontact anterior cruciate ligament injury,” *Am. J. Sports Med.*, vol. 42, no. 8, pp. 1806–1812, 2014.

[5] L. Y. Griffin, M. J. Albohm, E. A. Arendt, R. Bahr, B. D. Beynnon, M. DeMaio, R. W. Dick, L. Engebretsen, W. E. Garrett, J. A. Hannafin, T. E. Hewett, L. J. Huston, M. L. Ireland, R. J. Johnson, S. Lephart, B. R. Mandelbaum, B. J. Mann, P. H. Marks, S. W. Marshall, G. Myklebust, F. R. Noyes, C. Powers, C. Shields, S. J. Shultz, H. Silvers, J. Slauterbeck, D. C. Taylor, C. C. Teitz, E. M. Wojtys, and B. Yu, “Understanding and preventing noncontact anterior cruciate ligament injuries: A review of the Hunt Valley II Meeting, January 2005,” *Am. J. Sports Med.*, vol. 34, no. 9, pp. 1512–1532, 2006.

[6] J. C. Buckland-Wright, “Early radiographic features in patients with anterior cruciate ligament rupture,” *Ann. Rheum. Dis.*, vol. 59, no. 8, pp. 641–646, 2000.

[7] D. M. Daniel, M. Lou Stone, B. E. Dobson, D. C. Fithian, D. J. Rossman, and K. R. Kaufman, “Fate of the ACL-injured Patient,” *Am. J. Sports Med.*, vol. 22, no. 5, pp. 632–644, Sep. 1994.

[8] H. Roos, T. Adalberth, L. Dahlberg, and L. S. Lohmander, “Osteoarthritis of the Knee after Injury to the Anterior Cruciate Ligament or Meniscus: The Influence of Time and Age,” *Osteoarthritis Cartilage*, vol. 3, no. 4, pp. 261–267, 1995.

[9] G. Li, T. W. Rudy, M. Sakane, A. Kanamori, C. B. Ma, and S. L. Y. Woo, “The importance of quadriceps and hamstring muscle loading on knee kinematics and in-situ forces in the ACL,” *J. Biomech.*, vol. 32, no. 4, pp. 395–400, 1999.

[10] D. Butler, N. Noyes, and E. Grood, “Ligamentous restraints to anterior drawer in the human knee : a biomechanical study,” *J. Bone Jt. Surg.*, vol. 62, no. November 2015, pp. 259–270, 1980.

[11] C. R. Winby, D. G. Lloyd, T. F. Besier, and T. B. Kirk, “Muscle and external load contribution to knee joint contact loads during normal gait,” *J. Biomech.*, vol. 42, no. 14, pp. 2294–2300, 2009.

[12] D. G. Lloyd and T. S. Buchanan, “Strategies of muscular support of varus and valgus isometric loads at the human knee,” *J. Biomech.*, vol. 34, no. 10, pp. 1257–1267, 2001.

[13] T. E. Flaxman, A. D. Speirs, and D. L. Benoit, “Joint stabilisers or moment actuators: The role of knee joint muscles while weight-bearing,” *J. Biomech.*, vol. 45, no. 15, pp. 2570–2576, 2012.

[14] K. B. Shelburne, M. R. Torry, and M. G. Pandy, “Contributions of muscles, ligaments, and the ground-reaction force to tibiofemoral joint loading during normal gait,” *J. Orthop. Res.*, vol. 24, no. 10, pp. 1983–1990, Oct. 2006.

[15] G. N. Williams, T. Chmielewski, K. Rudolph, T. S. Buchanan, and L. Snyder-Mackler, “Dynamic knee stability: current theory and implications for clinicians and scientists,” *J Orthop Sport. Phys Ther*, vol. 31, no. 10, pp. 546–566, 2001.

[16] G. N. Williams, P. J. Barrance, L. Snyder-Mackler, M. J. Axe, and T. S. Buchanan, “Specificity of muscle action after anterior cruciate ligament injury,” *J. Orthop. Res.*, vol. 21, no. 6, pp. 1131–1137, 2003.

[17] J. Hashemi, R. Breighner, T. H. Jang, N. Chandrashekar, S. Ekwaro-Osire, and J. R. Slauterbeck, “Increasing pre-activation of the quadriceps muscle protects the anterior cruciate ligament during the landing phase of a jump: An in vitro simulation,” *Knee*, vol. 17, no. 3, pp. 235–241, 2010.

[18] P. a Torzilli, X. Deng, and R. F. Warren, “The effect of joint-compressive load and quadriceps muscle force on knee motion in the intact and anterior cruciate ligament-sectioned knee.,” *Am. J. Sports Med.*, vol. 22, no. 1, pp. 105–112, 1994.

[19] S. J. Wall, D. M. Rose, E. G. Sutter, S. M. Belkoff, and B. P. Boden, “The Role of Axial Compressive and Quadriceps Forces in Noncontact Anterior Cruciate Ligament Injury,” *Am. J. Sports Med.*, vol. 40, no. 3, pp. 568–573, 2012.

[20] P. S. Walker, S. Arno, C. Bell, G. Salvadore, I. Borukhov, and C. Oh, “Function of the medial meniscus in force transmission and stability,” *J. Biomech.*, vol. 48, no. 8, pp. 1383–1388, 2015.

[21] J. M. Marzo and J. Gurske-DePerio, “Effects of Medial Meniscus Posterior Horn Avulsion and Repair on Tibiofemoral Contact Area and Peak Contact Pressure With Clinical Implications,” *Am. J. Sports Med.*, vol. 37, no. 1, pp. 124–129, Jan. 2009.

[22] T. G. Tienen, P. Buma, J. G. F. Scholten, A. Van Kampen, R. P. H. Veth, and N. Verdonschot, “Displacement of the medial meniscus within the passive motion characteristics of the

human knee joint: An RSA study in human cadaver knees," *Knee Surgery, Sport. Traumatol. Arthrosc.*, vol. 13, no. 4, pp. 287–292, 2005.

[23] H. Fujie, T. Mae, T. Sekito, and K. Shino, "Mechanical Functions of Human ACL Bundles :," pp. 255–260, 2000.

[24] H. Fujie, H. Otsubo, S. Fukano, T. Suzuki, D. Suzuki, T. Mae, and K. Shino, "Mechanical functions of the three bundles consisting of the human anterior cruciate ligament," *Knee Surgery, Sport. Traumatol. Arthrosc.*, vol. 19, no. SUPPL1, 2011.

[25] M. Wunschel, O. Mller, J. Lo, C. Obloh, and N. Wlker, "The anterior cruciate ligament provides resistance to externally applied anterior tibial force but not to internal rotational torque during simulated weight-bearing flexion," *Arthrosc. - J. Arthrosc. Relat. Surg.*, vol. 26, no. 11, pp. 1520–1527, 2010.

[26] T. J. Withrow, L. J. Huston, E. M. Wojtys, and J. A. Ashton-Miller, "The effect of an impulsive knee valgus moment on in vitro relative ACL strain during a simulated jump landing," *Clin. Biomech.*, vol. 21, no. 9, pp. 977–983, 2006.

[27] H. N. Andersen and P. Dyhre-Poulsen, "The anterior cruciate ligament does play a role in controlling axial rotation in the knee.," *Knee*, vol. 5, no. 3, pp. 145–149, 1997.

[28] S. C. Shoemaker and K. L. Markolf, "Effects of joint load on the stiffness and laxity of ligament-deficient knees. An in vitro study of the anterior cruciate and medial collateral ligaments.," *J. Bone Joint Surg. Am.*, vol. 67, no. 1, pp. 136–46, Jan. 1985.

[29] C. Riegger-Krugh, T. Gerhart, W. Powers, and W. Hayes, "Tibiofemoral contact pressures in degenerative joint disease," *Clin Orthop Relat Res*, vol. 348. pp. 233–245, 1998.

[30] L. Blankevoort, R. Huiskes, and A. de Lange, "Helical axes of passive knee joint motions," *J. Biomech.*, vol. 23, no. 12, pp. 1219–1229, Jan. 1990.

[31] R. Shenoy, P. S. Pastides, and D. Nathwani, "(iii) Biomechanics of the knee and TKR," *Orthop. Trauma*, vol. 27, no. 6, pp. 364–371, 2013.

[32] D. D. Wu, D. B. Burr, R. D. Boyd, and E. L. Radin, "Bone and cartilage changes following experimental varus or valgus tibial angulation," *J. Orthop. Res.*, vol. 8, no. 4, pp. 572–585, Jul. 1990.

[33] L. Sharma, J. Song, D. Felson, and S. Cahue, "The Role of Knee Alignment in Disease Progression and Functional Decline in Knee Osteoarthritis," *J. Am. Med. Assoc.*, vol. 286, no. 2, p. 188, Jul. 2001.

[34] J. Bruns, M. Volkmer, and S. Luessenhop, "Pressure distribution at the knee joint. Influence of varus and valgus deviation without and with ligament dissection.," *Arch. Orthop. Trauma Surg.*, vol. 113, no. 1, pp. 12–9, 1993.

[35] T. Fukubayashi, P. A. Torzilli, M. F. Sherman, and R. F. Warren, “An in vitro biomechanical evaluation of anterior-posterior motion of the knee. Tibial displacement, rotation, and torque,” *J Bone Jt. Surg Am*, vol. 64, no. 2, pp. 258–264, 1982.

[36] M. Sakane, G. A. Livesay, R. J. Fox, T. W. Rudy, T. J. Runco, and S. L. Woo, “Relative contribution of the ACL, MCL, and bony contact to the anterior stability of the knee.,” *Knee Surg. Sports Traumatol. Arthrosc.*, vol. 7, no. 2, pp. 93–97, 1999.

[37] T. W. Rudy, G. A. Livesay, S. L. Y. Woo, and F. H. Fu, “A combined robotic/universal force sensor approach to determine in situ forces of knee ligaments,” *J. Biomech.*, vol. 29, no. 10, pp. 1357–1360, 1996.

[38] J. W. Arner, J. N. Irvine, L. Zheng, T. Gale, E. Thorhauer, M. Hankins, E. Abebe, S. Tashman, X. Zhang, and C. D. Harner, “The Effects of Anterior Cruciate Ligament Deficiency on the Meniscus and Articular Cartilage A Novel Dynamic In Vitro Pilot Study,” *Orthop. J. Sport. Med.*, no. 4, pp. 1–8, 2016.

[39] G. Li, R. Papannagari, L. E. DeFrate, J. D. Yoo, S. E. Park, and T. J. Gill, “The effects of ACL deficiency on mediolateral translation and varus-valgus rotation.,” *Acta Orthop.*, vol. 78, no. 3, pp. 355–60, Jun. 2007.

[40] D. M. Veltri, X. H. Deng, P. A. Torzilli, R. F. Warren, and M. J. Maynard, “The role of the cruciate and posterolateral ligaments in stability of the knee. A biomechanical study.,” *Am. J. Sports Med.*, vol. 23, no. 4, pp. 436–43, Jul. 1995.

[41] N. Diermann, T. Schumacher, S. Schanz, M. J. Raschke, W. Petersen, and T. Zantop, “Rotational instability of the knee: Internal tibial rotation under a simulated pivot shift test,” *Arch. Orthop. Trauma Surg.*, vol. 129, no. 3, pp. 353–358, 2009.

[42] M. E. Baratz, F. H. Fu, and R. Mengato, “Meniscal tears: the effect of meniscectomy and of repair on intraarticular contact areas and stress in the human knee. A preliminary report,” *Am. J. Sports Med.*, vol. 14, no. 4, pp. 270–275, 1986.

[43] Y. K. Oh, J. L. Kreinbrink, J. A. Ashton-Miller, and E. M. Wojtys, “Effect of ACL Transection on Internal Tibial Rotation in an in Vitro Simulated Pivot Landing,” *J. Bone Jt. Surgery-American Vol.*, vol. 93, no. 4, pp. 372–380, Feb. 2011.

[44] T. E. Flaxman, T. AlkjÆr, E. B. Simonsen, M. R. Krogsgaard, and D. L. Benoit, “Predicting the Functional Roles of Knee Joint Muscles from Internal Joint Moments,” *Med. Sci. Sports Exerc.*, vol. 49, no. 3, pp. 527–537, 2017.

[45] T. J. Withrow, L. J. Huston, E. M. Wojtys, and J. A. Ashton-Miller, “Effect of Varying Hamstring Tension on Anterior Cruciate Ligament Strain During in Vitro Impulsive Knee Flexion and Compression Loading,” *J. Bone Jt. Surgery-American Vol.*, vol. 90, no. 4, pp. 815–823, Apr. 2008.

[46] P. Renström, S. W. Arms, T. S. Stanwyck, R. J. Johnson, and M. H. Pope, "Strain within the anterior cruciate ligament during hamstring and quadriceps activity," *Am. J. Sports Med.*, vol. 14, no. 1, pp. 83–87, 1986.

[47] J. D. Yoo, R. Papannagari, S. E. Park, L. E. DeFrate, T. J. Gill, and G. Li, "The Effect of Anterior Cruciate Ligament Reconstruction on Knee Joint Kinematics Under Simulated Muscle Loads," *Am. J. Sports Med.*, vol. 33, no. 2, pp. 240–246, Feb. 2005.

[48] K. B. Shelburne, M. R. Torry, and M. G. Pandy, "Contributions of muscles, ligaments, and the ground-reaction force to tibiofemoral joint loading during normal gait," *J. Orthop. Res.*, vol. 24, no. 10, pp. 1983–1990, Oct. 2006.

[49] D. D. D'Lima, C. Poole, H. Chadha, J. C. Hermida, a Mahar, and C. W. Colwell, "Quadriceps moment arm and quadriceps forces after total knee arthroplasty.," *Clin. Orthop. Relat. Res.*, no. 392, pp. 213–20, 2001.

[50] a K. Aune, P. W. Cawley, and A. Ekeland, "Quadriceps muscle contraction protects the anterior cruciate ligament during anterior tibial translation.," *Am J Sport. Med*, vol. 25, no. 2, pp. 187–90, 1997.

[51] O. D. Schipplein and T. P. Andriacchi, "Interaction between active and passive knee stabilizers during level walking," *J. Orthop. Res.*, vol. 9, no. 1, pp. 113–119, 1991.

[52] J. Victor, L. Labey, P. Wong, B. Innocenti, and J. Bellemans, "The influence of muscle load on tibiofemoral knee kinematics," *J. Orthop. Res.*, vol. 28, no. 4, p. n/a-n/a, 2009.

[53] B. A. MacWilliams, D. R. Wilson, J. D. DesJardins, J. Romero, and E. Y. Chao, "Hamstrings cocontraction reduces internal rotation, anterior translation, and anterior cruciate ligament load in weight-bearing flexion," *J Orthop Res*, vol. 17, no. 6, pp. 817–822, 1999.

[54] A. J. Goldfuss, C. A. Morehaouse, and B. F. LeVeau, "Effect of muscular tension on knee stability," *Med. Sci. Sports Exerc.*, vol. 5, pp. 267–271, 1973.

[55] A. Mündermann, C. O. Dyrby, D. D. D'Lima, C. W. Colwell, and T. P. Andriacchi, "In vivo knee loading characteristics during activities of daily living as measured by an instrumented total knee replacement," *J. Orthop. Res.*, vol. 26, no. 9, pp. 1167–1172, Sep. 2008.

[56] G. Bergmann, A. Bender, F. Graichen, J. Dymke, A. Rohlmann, A. Trepczynski, M. O. Heller, and I. Kutzner, "Standardized Loads Acting in Knee Implants," *PLoS One*, vol. 9, no. 1, p. e86035, Jan. 2014.

[57] D. Kumar, K. T. Manal, and K. S. Rudolph, "Knee joint loading during gait in healthy controls and individuals with knee osteoarthritis," *Osteoarthr. Cartil.*, vol. 21, no. 2, pp. 298–305, 2013.

[58] J. Aaboe, H. Bliddal, S. P. Messier, T. Alkjær, and M. Henriksen, “Effects of an intensive weight loss program on knee joint loading in obese adults with knee osteoarthritis,” *Osteoarthr. Cartil.*, vol. 19, no. 7, pp. 822–828, 2011.

[59] H. J. Yack, L. A. Washco, and T. J. Whieldon, “Compressive Forces as a Limiting Factor of Anterior Tibial Translation in the ACL-Deficient Knee,” *Clin J Sport. Med*, vol. 4, no. 4, pp. 233–239, 1994.

[60] L. Sharma, D. Dunlop, S. Cahue, J. Song, and K. Hayes, “Annals of Internal Medicine Article Quadriceps Strength and Osteoarthritis Progression in Malaligned and,” *Ann. Intern. Med.*, vol. 138, no. 8, pp. 613–620, 2003.

[61] J. Z. Wu, W. Herzog, and M. Epstein, “Effects of inserting a pressensor film into articular joints on the actual contact mechanics.,” *J. Biomech. Eng.*, vol. 120, no. 5, pp. 655–9, 1998.

[62] J. Z. Wu, W. Herzog, and M. Epstein, “Joint contact mechanics in the early stages of osteoarthritis,” *Med. Eng. Phys.*, vol. 22, no. 1, pp. 1–12, Jan. 2000.

[63] T. Fukubayashi and H. Kurosawa, “The contact area and pressure distribution pattern of the knee. A study of normal and osteoarthrotic knee joints.,” *Acta Orthop. Scand.*, vol. 51, no. 6, pp. 871–879, 1980.

[64] H. Kurosawa, T. Fukubayashi, and H. Nakajima, “Load-bearing mode of the knee joint: physical behavior of the knee joint with or without menisci.,” *Clin. Orthop. Relat. Res.*, no. 149, pp. 283–290, 1980.

[65] J. C. Ihn, S. J. Kim, and I. H. Park, “In vitro study of contact area and pressure distribution in the human knee after partial and total meniscectomy.,” *Int. Orthop.*, vol. 17, no. 4, pp. 214–8, 1993.

[66] A. M. Seitz, A. Lubomierski, B. Friemert, A. Ignatius, and L. Dürselen, “Effect of partial meniscectomy at the medial posterior horn on tibiofemoral contact mechanics and meniscal hoop strains in human knees,” *J. Orthop. Res.*, vol. 30, no. 6, pp. 934–942, Jun. 2012.

[67] P. S. Walker and M. J. Erkiuan, “The Role of the Menisci in Force Transmission Across the Knee,” *Clin. Orthop. Relat. Res.*, vol. 109, no. 109, pp. 184–192, Jun. 1975.

[68] C. Imhauser, C. Mauro, D. Choi, E. Rosenberg, S. Mathew, J. Nguyen, Y. Ma, and T. Wickiewicz, “Abnormal tibiofemoral contact stress and its association with altered kinematics after center-center anterior cruciate ligament reconstruction: an in vitro study.,” *Am. J. Sports Med.*, vol. 41, pp. 815–25, 2013.

[69] A. Zeighami, R. Dumas, M. Kanhonou, N. Hagemeister, F. Lavoie, J. A. De Guise, and R. Aissaoui, “Tibio-femoral joint contact in healthy and osteoarthritic knees during quasi-

static squat: A bi-planar X-ray analysis," *J. Biomech.*, pp. 1–7, 2017.

[70] X. Wang, Y. Wang, K. L. Bennell, T. V. Wrigley, F. M. Cicuttini, K. Fortin, D. J. Saxby, A. van Ginckel, A. R. Dempsey, N. Grigg, C. Vertullo, J. A. Feller, T. Whitehead, D. G. Lloyd, and A. L. Bryant, "Cartilage morphology at 2–3 years following anterior cruciate ligament reconstruction with or without concomitant meniscal pathology," *Knee Surgery, Sport. Traumatol. Arthrosc.*, vol. 25, no. 2, pp. 426–436, 2015.

[71] S. Farrokhi, C. A. Voycheck, B. A. Klatt, J. A. Gustafson, S. Tashman, and G. K. Fitzgerald, "Altered tibiofemoral joint contact mechanics and kinematics in patients with knee osteoarthritis and episodic complaints of joint instability," *Clin. Biomech.*, vol. 29, no. 6, pp. 629–635, 2014.

[72] L. S. Lohmander, P. M. Englund, L. L. Dahl, and E. M. Roos, "The Long-term Consequence of Anterior Cruciate Ligament and Meniscus Injuries," *Am. J. Sports Med.*, vol. 35, no. 10, pp. 1756–1769, Oct. 2007.

[73] A. L. Clark, W. Herzog, and T. R. Leonard, "Contact area and pressure distribution in the feline patellofemoral joint under physiologically meaningful loading conditions," *J. Biomech.*, vol. 35, no. 1, pp. 53–60, 2002.

[74] E. M. Hasler, W. Herzog, T. R. Leonard, A. Stano, and H. Nguyen, "In vivo knee joint loading and kinematics before and after ACL transection in an animal model," vol. 31, 1998.

[75] G. Von Lewinski, C. Hurschler, C. Allmann, and C. J. Wirth, "The influence of pre-tensioning of meniscal transplants on the tibiofemoral contact area," *Knee Surgery, Sport. Traumatol. Arthrosc.*, vol. 14, no. 5, pp. 425–436, 2006.

[76] A. Bedi, N. H. Kelly, M. Baad, A. J. Fox, R. H. Brophy, R. F. Warren, and S. A. Maher, "Dynamic contact mechanics of the medial meniscus as a function of radial tear, repair, and partial meniscectomy," *J Bone Jt. Surg Am*, vol. 92, no. 6, pp. 1398–1408, 2010.

[77] D. C. Marchetti, B. M. Phelps, K. D. Dahl, E. L. Slette, J. D. Mikula, G. J. Dornan, G. Bucci, T. L. Turnbull, and S. B. Singleton, "A Contact Pressure Analysis Comparing an All-Inside and Inside-Out Surgical Repair Technique for Bucket-Handle Medial Meniscus Tears," *Arthrosc. - J. Arthrosc. Relat. Surg.*, pp. 1–9, 2017.

[78] S. J. Lee, K. J. Aadalen, P. Malaviya, E. P. Lorenz, J. K. Hayden, J. Farr, R. W. Kang, and B. J. Cole, "Tibiofemoral contact mechanics after serial medial meniscectomies in the human cadaveric knee.," *Am. J. Sports Med.*, vol. 34, no. 8, pp. 1334–44, Aug. 2006.

[79] F. R. Noyes, O. D. Schipplein, T. P. Andriacchi, S. R. Saddemi, and M. Weise, "The anterior cruciate ligament-deficient knee with varus alignment," *Am. J. Sports Med.*, vol. 20, no. 6, pp. 707–716, Nov. 1992.

[80] R. J. de Jong, P. J. C. Heesterbeek, and A. B. Wymenga, "A new measurement technique

for the tibiofemoral contact point in normal knees and knees with TKR," *Knee Surgery, Sport. Traumatol. Arthrosc.*, vol. 18, no. 3, pp. 388–393, 2010.

[81] S.-F. Hsiao, P.-H. Chou, H.-C. Hsu, and Y.-J. Lue, "Changes of muscle mechanics associated with anterior cruciate ligament deficiency and reconstruction.," *J. Strength Cond. Res.*, vol. 28, no. 2, pp. 390–400, 2014.

[82] W. Herzog, D. Longino, and A. Clark, "The role of muscles in joint adaptation and degeneration," *Langenbeck's Arch. Surg.*, vol. 388, no. 5, pp. 305–315, 2003.

[83] A. Rehan Youssef, D. Longino, R. Seerattan, T. Leonard, and W. Herzog, "Muscle weakness causes joint degeneration in rabbits," *Osteoarthr. Cartil.*, vol. 17, no. 9, pp. 1228–1235, 2009.

[84] T. Alkjær, M. Henriksen, and E. B. Simonsen, "Different knee joint loading patterns in ACL deficient copers and non-copers during walking," *Knee Surgery, Sport. Traumatol. Arthrosc.*, vol. 19, no. 4, pp. 615–621, 2011.

[85] C. M. Rodner, "Medial Opening Wedge Tibial Osteotomy and the Sagittal Plane: The Effect of Increasing Tibial Slope on Tibiofemoral Contact Pressure," *Am. J. Sports Med.*, vol. 34, no. 9, pp. 1431–1441, 2006.

[86] A. Shirazi-Adl and W. Mesfar, "Effect of tibial tubercle elevation on biomechanics of the entire knee joint under muscle loads," *Clin. Biomech.*, vol. 22, no. 3, pp. 344–351, 2007.

[87] J. R. Giffin, "Effects of Increasing Tibial Slope on the Biomechanics of the Knee," *Am. J. Sports Med.*, vol. 32, no. 2, pp. 376–382, 2004.

[88] G. Omori, N. Onda, M. Shimura, T. Hayashi, T. Sato, and Y. Koga, "The effect of geometry of the tibial polyethylene insert on the tibiofemoral contact kinematics in Advance Medial Pivot total knee arthroplasty," *J. Orthop. Sci.*, vol. 14, no. 6, pp. 754–760, 2009.

[89] K. N. Bachus, A. L. DeMarco, K. T. Judd, D. S. Horwitz, and D. S. Brodke, "Measuring contact area, force, and pressure for bioengineering applications: using Fuji Film and TekScan systems.," *Med. Eng. Phys.*, vol. 28, no. 5, pp. 483–8, Jun. 2006.

[90] H. J. Agins, V. S. Harder, E. P. Lautenschlager, and J. C. Kudrna, "Effects of sterilization on the Tekscan digital pressure sensor," *Med. Eng. Phys.*, vol. 25, no. 9, pp. 775–780, 2003.

[91] M. L. Harris, P. Morberg, W. J. Bruce, and W. R. Walsh, "An improved method for measuring tibiofemoral contact areas in total knee arthroplasty: a comparison of K-scan sensor and Fuji film.," *J. Biomech.*, vol. 32, no. 9, pp. 951–8, Sep. 1999.

[92] J. Brimacombe, C. Anglin, A. Hodgson, and D. Wilson, "Validation of calibration techniques for tekscan pressure sensors," *Proc. ISB XXth Congr. - ASB 29th Annu. Meet.*, p. 2003, 2005.

[93] J. M. Brimacombe, D. R. Wilson, A. J. Hodgson, K. C. T. Ho, and C. Anglin, “Effect of Calibration Method on Tekscan Sensor Accuracy,” *J. Biomech. Eng.*, vol. 131, no. 3, p. 034503, 2009.

[94] D. B. Kettelkamp and E. Y. Chao, “A method for quantitative analysis of medial and lateral compression forces at the knee during standing.,” *Clin. Orthop. Relat. Res.*, vol. 83, pp. 202–13, 1972.

[95] D. B. Kettelkamp and A. W. Jacobs, “Tibiofemoral contact area--determination and implications.,” *J. Bone Joint Surg. Am.*, vol. 54, no. 2, pp. 349–56, Mar. 1972.

[96] J. M. Scarvell, P. N. Smith, K. M. Refshauge, H. R. Galloway, and K. R. Woods, “Evaluation of a method to map tibiofemoral contact points in the normal knee using MRI,” *J. Orthop. Res.*, vol. 22, no. 4, pp. 788–793, 2004.

[97] L. E. Defrate, H. Sun, T. J. Gill, H. E. Rubash, and G. Li, “In vivo tibiofemoral contact analysis using 3D MRI-based knee models,” *J. Biomech.*, vol. 37, no. 10, pp. 1499–1504, 2004.

[98] J. M. Scarvell, P. N. Smith, K. M. Refshauge, H. R. Galloway, and K. R. Woods, “Comparison of kinematic analysis by mapping tibiofemoral contact with movement of the femoral condylar centres in healthy and anterior cruciate ligament injured knees,” *J. Orthop. Res.*, vol. 22, no. 5, pp. 955–962, 2004.

[99] G. Li, L. E. Defrate, S. E. Park, T. J. Gill, and H. E. Rubash, “In Vivo Articular Cartilage Contact Kinematics of the Knee An Investigation Using Dual-Orthogonal Fluoroscopy and Magnetic Resonance Image–Based Computer Models,” *Am. Orthop. Soc. Sport. Med.*, vol. 33, no. 1, pp. 102–107, 2005.

[100] J. Yao, A. D. Salo, J. Lee, and A. L. Lerner, “Sensitivity of tibio-menisco-femoral joint contact behavior to variations in knee kinematics,” *J. Biomech.*, vol. 41, no. 2, pp. 390–398, 2008.

[101] Z. F. Lerner, M. S. DeMers, S. L. Delp, and R. C. Browning, “How tibiofemoral alignment and contact locations affect predictions of medial and lateral tibiofemoral contact forces,” *J. Biomech.*, vol. 48, no. 4, pp. 644–650, 2015.

[102] P. Damm, I. Kutzner, G. Bergmann, A. Rohlmann, and H. Schmidt, “Comparison of in vivo measured loads in knee, hip and spinal implants during level walking,” *J. Biomech.*, vol. 51, pp. 128–132, 2016.

[103] I. Kutzner, B. Heinlein, F. Graichen, A. Bender, A. Rohlmann, A. Halder, A. Beier, and G. Bergmann, “Loading of the knee joint during activities of daily living measured in vivo in five subjects,” *J. Biomech.*, vol. 43, no. 11, pp. 2164–2173, 2010.

[104] R. Kuroda, H. Kambic, a Valdevit, and J. T. Andrish, “Articular cartilage contact pressure after tibial tuberosity transfer. A cadaveric study.,” *Am. J. Sports Med.*, vol. 29, no. 4, pp. 403–409, 2001.

[105] Y. Morimoto, M. Ferretti, M. Ekdahl, P. Smolinski, and F. H. Fu, "Tibiofemoral Joint Contact Area and Pressure After Single- and Double-Bundle Anterior Cruciate Ligament Reconstruction," *Arthrosc. - J. Arthrosc. Relat. Surg.*, vol. 25, no. 1, pp. 62–69, 2009.

[106] C. M. Powers, J. C. Lilley, and T. Q. Lee, "The effects of axial and multi-plane loading of the extensor mechanism on the patellofemoral joint.," *Clin. Biomech. (Bristol, Avon)*, vol. 13, no. 8, pp. 616–624, Dec. 1998.

[107] G. A. Paletta, T. Manning, E. Snell, R. Parker, and J. Bergfeld, "The Effect of Allograft Meniscal Replacement on Intraarticular Contact Area and Pressures in the Human Knee," *Am. J. Sports Med.*, vol. 25, no. 5, pp. 692–698, Sep. 1997.

[108] E. G. Meyer, T. G. Baumer, J. M. Slade, W. E. Smith, and R. C. Haut, "Tibiofemoral contact pressures and osteochondral microtrauma during anterior cruciate ligament rupture due to excessive compressive loading and internal torque of the human knee.," *Am. J. Sports Med.*, vol. 36, no. 10, pp. 1966–1977, 2008.

[109] S. D. D'Agata, A. W. Pearsall, B. Reider, and L. F. Draganich, "An in vitro analysis of patellofemoral contact areas and pressures following procurement of the central one-third patellar tendon," *Am. J. Sports Med.*, vol. 21, no. 2, pp. 212–219, 1993.

[110] L. F. Draganich, T. P. Andriacchi, and G. B. J. Andersson, "Interaction between intrinic knee mechanics and the knee extensor mechanism," *J. Orthop. Res.*, vol. 5, no. 8, pp. 539–547, 1987.

[111] W. Herzog, S. Diet, E. Suter, P. Mayzus, T. R. Leonard, C. Müller, J. Z. Wu, and M. Epstein, "Material and functional properties of articular cartilage and patellofemoral contact mechanics in an experimental model of osteoarthritis," *J. Biomech.*, vol. 31, no. 12, pp. 1137–1145, 1998.

[112] L. Blankevoort, J. H. Kuiper, R. Huiskes, and H. J. Grootenboer, "Articular contact in a three-dimensional model of the knee," *J. Biomech.*, vol. 24, no. 11, pp. 1019–1031, 1991.

[113] J. K. Hofer, R. Gejo, M. H. McGarry, and T. Q. Lee, "Effects on tibiofemoral biomechanics from kneeling," *Clin. Biomech.*, vol. 26, no. 6, pp. 605–611, 2011.

[114] M. Wünschel, U. Leichtle, C. Obloh, N. Wülker, and O. Müller, "The effect of different quadriceps loading patterns on tibiofemoral joint kinematics and patellofemoral contact pressure during simulated partial weight-bearing knee flexion," *Knee Surgery, Sport. Traumatol. Arthrosc.*, vol. 19, no. 7, pp. 1099–1106, 2011.

[115] S. Y. Poh, K. S. A. Yew, P. L. K. Wong, S. B. J. Koh, S. L. Chia, S. Fook-Chong, and T. Sen Howe, "Role of the anterior intermeniscal ligament in tibiofemoral contact mechanics during axial joint loading," *Knee*, vol. 19, no. 2, pp. 135–139, 2012.

[116] J. D. Agneskirchner, C. Hurschler, C. Stukenborg-Colsman, A. B. Imhoff, and P.

Lobenhoffer, “Effect of high tibial flexion osteotomy on cartilage pressure and joint kinematics: A biomechanical study in human cadaveric knees. Winner of the AGA-DonJoy Award 2004,” *Arch. Orthop. Trauma Surg.*, vol. 124, no. 9, pp. 575–584, 2004.

[117] J. H. Brechter, C. M. Powers, M. R. Terk, S. R. Ward, and T. Q. Lee, “Quantification of patellofemoral joint contact area using magnetic resonance imaging,” *Magn. Reson. Imaging*, vol. 21, no. 9, pp. 955–959, 2003.

[118] J. M. Bach and M. L. Hull, “A new load application system for in vitro study of ligamentous injuries to the human knee joint.,” *J. Biomech. Eng.*, vol. 117, no. 4, pp. 373–382, 1995.

[119] J. Hashemi, N. Chandrashekar, T. Jang, F. Karpat, M. Oseto, and S. Ekwaro-Osire, “An alternative mechanism of non-contact anterior cruciate ligament injury during jump-landing: In-vitro simulation,” *Exp. Mech.*, vol. 47, no. 3, pp. 347–354, 2007.

[120] L. Maletsky and B. M. Hillberry, “Simulating dynamic activities using a five-axis knee simulator.,” *J. Biomech. Eng.*, vol. 127, no. 1, pp. 123–133, 2005.

[121] S. Shalhoub and L. Maletsky, “Variation in patellofemoral kinematics due to changes in quadriceps loading configuration during in vitro testing,” *J. Biomech.*, vol. 47, no. 1, pp. 130–136, 2014.

[122] M. A. Verstraete and J. Victor, “Possibilities and limitations of novel in-vitro knee simulator,” *J. Biomech.*, vol. 48, no. 12, pp. 3377–3382, 2015.

[123] L. A. Whiteside, M. R. Kasselt, and D. W. Haynes, “Varus-valgus and rotational stability in rotationally unconstrained total knee arthroplasty.,” *Clinical orthopaedics and related research*, no. 219. pp. 147–57, 1987.

[124] O. Müller, J. Lo, M. Wünschel, C. Obloh, and N. Wülker, “Simulation of force loaded knee movement in a newly developed in vitro knee simulator / Simulation von belastungsabhängigen Kniebewegungen in einem neuartigen Knie-Simulator für In-vitro-Studien,” *Biomed. Tech. Eng.*, vol. 54, no. 3, pp. 142–149, Jan. 2009.

[125] P. J. Laz, S. Pal, A. Fields, A. J. Petrella, and P. J. Rullkoetter, “Effects of knee simulator loading and alignment variability on predicted implant mechanics: A probabilistic study,” *J. Orthop. Res.*, vol. 24, no. 12, pp. 2212–2221, Dec. 2006.

[126] G. Li, J. Gil, A. Kanamori, and S.-Y. Woo, “A validated three-dimensional computational model of a human knee joint,” vol. 121, pp. 657–662, 1999.

[127] C. A. Van Ee, A. L. Chasse, and B. S. Myers, “Properties in Cadaveric Test Specimens : Effects of Mechanical Loading , Postmortem Time ,” vol. 122, no. February 2000, pp. 9–14, 2014.

[128] J. W. Polderman and Trentelman.H.L., *The mathematics of systems and control: from*

intelligent control to behavioral systems. Eigen beheer, 1999.

[129] R. H. Bishop, "The Mechatronics Handbook," in *Mobile Sensors and Context-Aware Computing*, 2017, pp. 37–83.

[130] O. Vinogradoc, *Fundamentals of Kinematics and Dynamics of Machies and Mechanisms*. 2000.

[131] Bhargav, M. A. Parameshwaran, S. Sivaraj, and N. Venkataram, "Conceptual design of planetary gearbox system for constant generator speed in hydro power plant," *MATEC Web Conf.*, vol. 144, p. 01004, Jan. 2018.

[132] A. O. Bligh, N. A. Ahmed, and Y. Y. Zheng, "Design and Manufacture of a Planetary Gearbox Rig," *Appl. Mech. Mater.*, vol. 397–400, pp. 176–188, Sep. 2013.

[133] H. W. Ott, *Electromagnetic Compatibility Engineering*. 2009.

[134] K. E. Norden, *Handbook of Electronic Weighing*. 1998.

[135] A. Hunt, A. Cross, J. Davis, U. Erdem, A. Herbert, R. Jenkins, A. Knott, S. Maclean, L. March, D. Tame, G. Thompson, D. Viney, J. Webb, and G. Wort, "Guide to the Measurement of Force," 2013.

[136] ASTM International, "Standard Practices for Force Verification of Testing Machines,." 2016.

[137] P. Gauthier and D. L. Benoit, "Tibio-femoral joint contact mechanics: An invitro simulation with a 6 DOF static knee simulator," 2016.

[138] M. D. Lewek, K. S. Rudolph, and L. Snyder-Mackler, "Quadriceps Femoris Muscle Weakness and Activation Failure in Patients with Symptomatic Knee Osteoarthritis," *J Orthop Res*, vol. 22, no. 1, pp. 110–115, 2011.

[139] E. Suter and W. Herzog, "Does muscle inhibition after knee injury increase the risk of osteoarthritis?," *Exercise and sport sciences reviews*, vol. 28. pp. 15–18, 2000.

[140] K. Manal, J. Gardinier, and N. Chimera, "WHAT ARE WE MISSING WHEN USING INVERSE DYNAMICS?," 2006.

[141] S. L. Woo, B. R. Simon, S. C. Kuei, and W. H. Akeson, "Quasi-linear viscoelastic properties of normal articular cartilage.," *J. Biomech. Eng.*, vol. 102, no. 2, pp. 85–90, 1980.

[142] S. Akizuki, V. C. Mow, F. Müller, J. C. Pita, D. S. Howell, and D. H. Manicourt, "Tensile properties of human knee joint cartilage: I. Influence of ionic conditions, weight bearing, and fibrillation on the tensile modulus," *J. Orthop. Res.*, vol. 4, no. 4, pp. 379–392, 1986.

[143] L. Schatzmann, “Effect of cyclic preconditioning on the tensile properties of human quadriceps tendons and patellar ligaments,” *Knee Surgery, Sport. Traumatol. Arthrosc.*, vol. 6, no. 0, pp. S56–S61, 1998.

[144] S. D. Masouros, A. M. J. Bull, and A. A. Amis, “(i) Biomechanics of the knee joint,” *Orthop. Trauma*, vol. 24, no. 2, pp. 84–91, Apr. 2010.

[145] G. Wu, S. Siegler, P. Allard, C. Kirtley, A. Leardini, D. Rosenbaum, M. Whittle, D. D. D’Lima, L. Cristofolini, H. Witte, O. Schmid, I. Stokes, and Standardization and Terminology Committee of the International Society of Biomechanics, “ISB recommendation on definitions of joint coordinate system of various joints for the reporting of human joint motion--part I: ankle, hip, and spine. International Society of Biomechanics.,” *J. Biomech.*, vol. 35, no. 4, pp. 543–8, Apr. 2002.

[146] E. S. Grood and W. J. Suntay, “A joint coordinate system for the clinical description of three-dimensional motions: application to the knee.,” *J. Biomech. Eng.*, vol. 105, no. 2, pp. 136–44, May 1983.

Appendix A: UOKS components

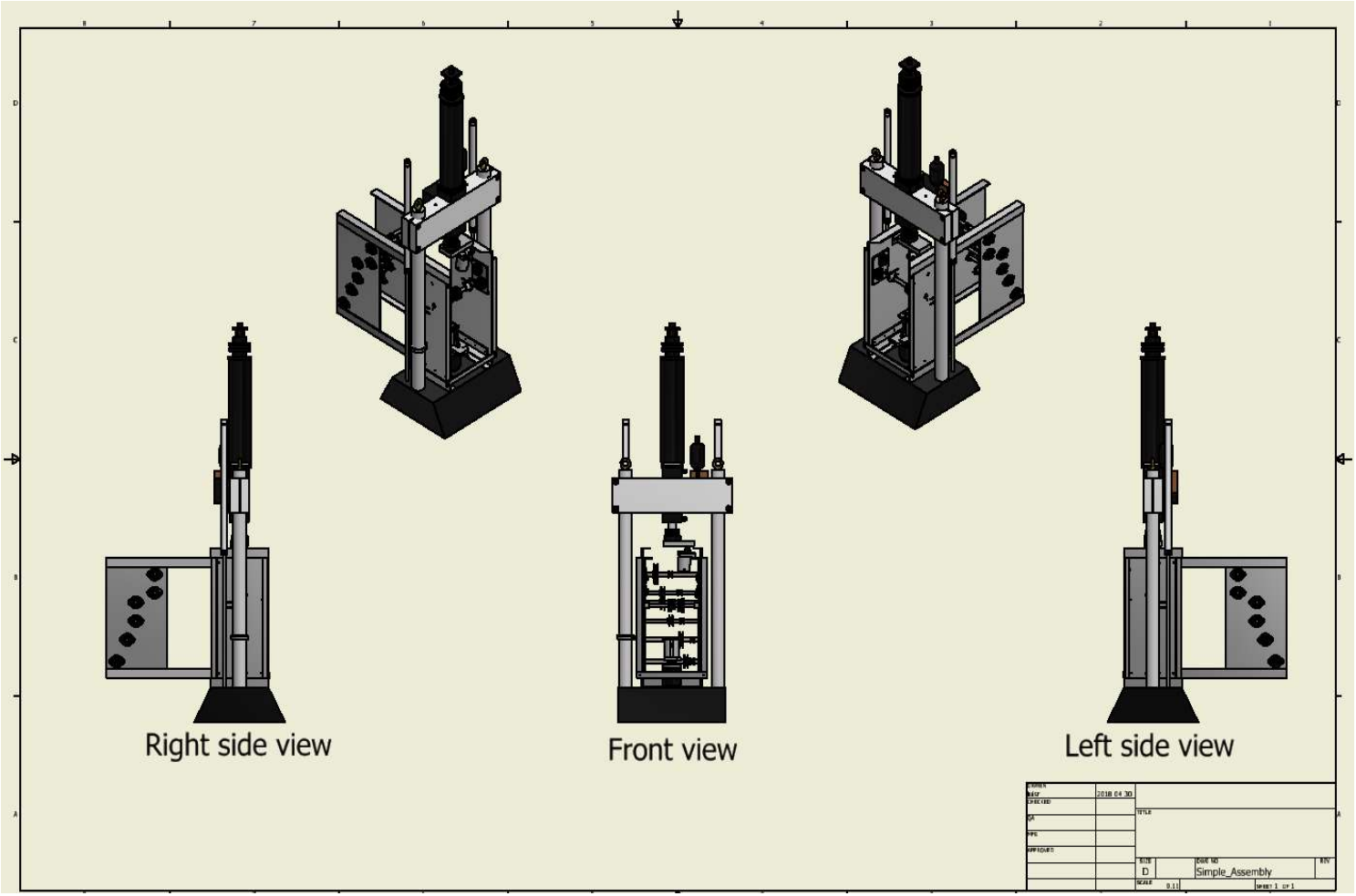

Figure 1. Previous iteration of the UOKS mounted on the MTS machine

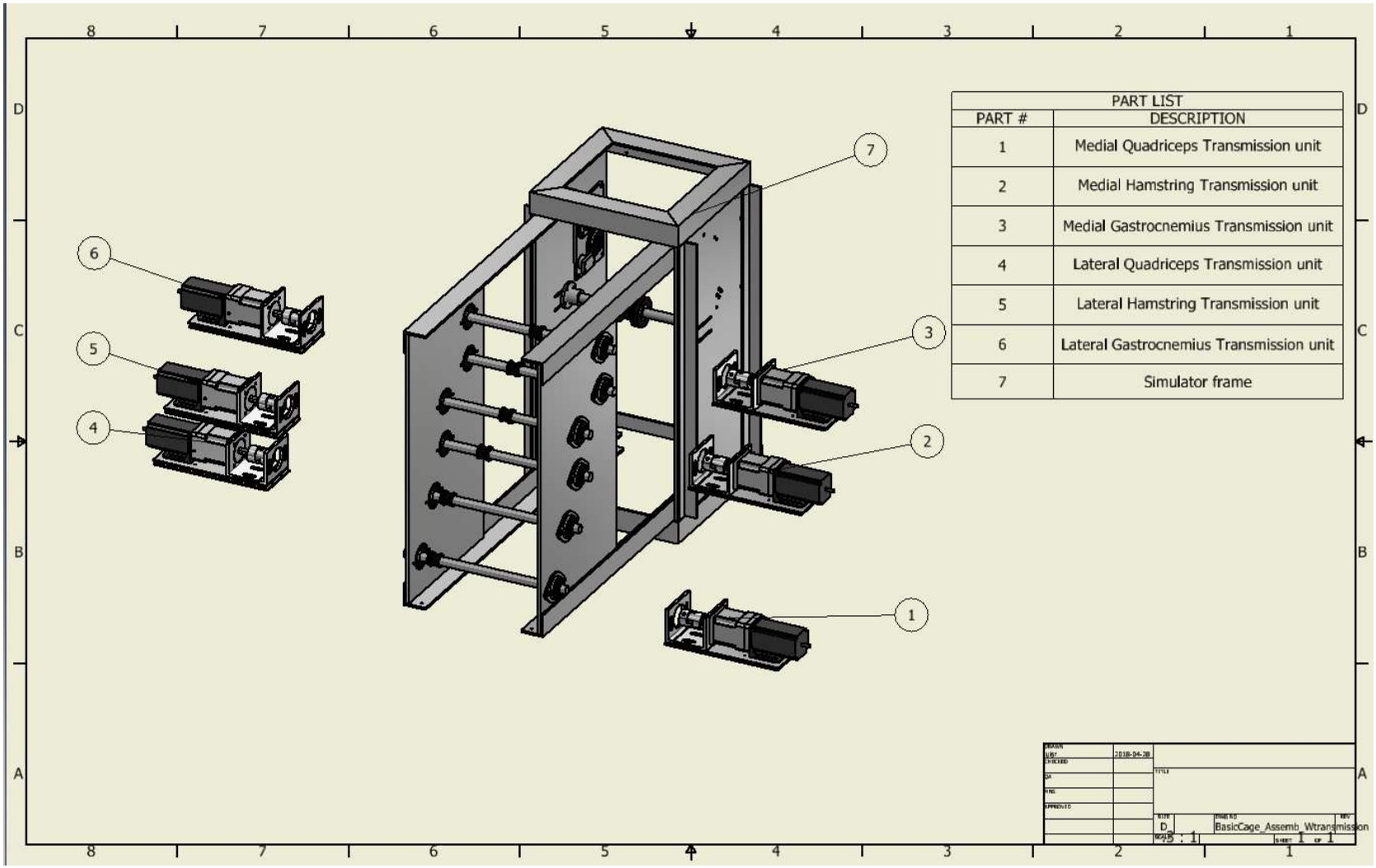

Figure 2. Transmission units distributed to the sides of the simulator to balance the extra weight. Transmissions to the right show the lateral muscles and left side shows the contralateral muscles.

Appendix B: Stepper Motor Driver Specifications

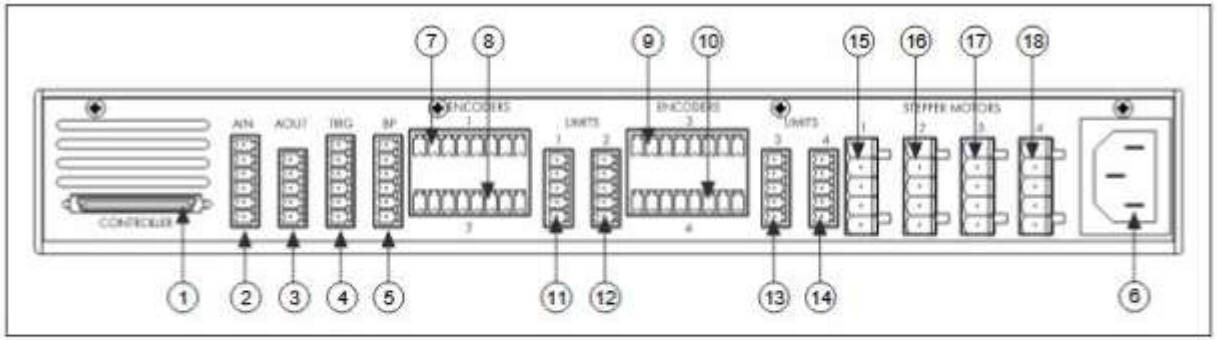

1	Motion Controller Connector	**Encoder Connectors**		**Limit Connectors**		**Motor Connectors**	
2	Analog Input Connector	7	Axis 1	11	Axis 1	15	Axis 1
3	Analog Output Connector	8	Axis 2	12	Axis 2	16	Axis 2
4	Trigger Connector	9	Axis 3	13	Axis 3	17	Axis 3
5	Breakpoint Connector	10	Axis 4	14	Axis 4	18	Axis 4
6	AC Power						

Figure 3. Back panel diagram of the national instruments MID-7604 stepper motor driver. Image retrieved from products datasheet.

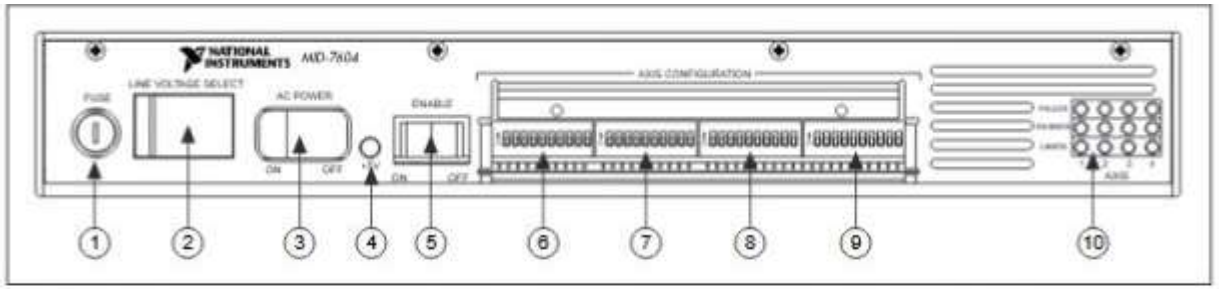

1	Main Input Fuse	5	Enable Switch	8	Axis 3 DIP Switch Bank
2	Line Voltage Select Switch	6	Axis 1 DIP Switch Bank	9	Axis 4 DIP Switch Bank
3	Power Switch	7	Axis 2 DIP Switch Bank	10	LED Status Array
4	Green Power LED				

Figure 4. Front panel of the stepper motor driver. Image retrieved from the products datasheet.

Specifications

The following specifications apply only to the MID-7604/7602. To obtain a complete system specification, you must account for your motion controller. Refer to your controller specifications to determine overall system specifications.
Some signals have compatibility defined as signal pass-through, which means the MID-7604/7602 may have passive filtering on these signals but will not affect the voltage range or current handling capability. Consult your motion controller specifications to determine the allowable voltage range and logic level compatibility of the signal.

Stepper Amplifiers

Type.....IM481H modular hybrid, bipolar chopper
Chopping frequency.....20 kHz
DC-bus motor.....24 VDC nominal
Current per phase .....0.20 to 1.4 A peak (0.14 to 1 A RMS) (factory setting is 0.50 A peak)
Microstepping selections .....2, 4, 8, 16, 32, 64, 128, 256 ?5, 10, 25, 50, 125, 250 (factory default is ?10 microsteps/step)
Continuous power output rating (all axes combined) .....80 W continuous

Motion I/O

Encoder inputs .....Quadrature, incremental
Voltage range
Single ended input threshold.....TTL/CMOS
Noise filter (RC time constant) .....100 ns
Maximum quadrature frequency.....1 MHz
Limit and home switch inputs compatibility .....Signal pass-through
Inhibit inputs
Voltage range .....0 to 12 VDC
Inhibit low voltage .....0.8 V
Inhibit high voltage .....2 V
Inhibit output
Voltage range .....0 to 5 VDC
Output low voltage.....0.5 V at 64 mA
Output high voltage.....2.4 V at 32 mA
Trigger input compatibility .....Signal pass-through
Noise filter (RC time constant) .....100 ns
Breakpoint output compatibility .....Signal pass-through
Analog input compatibility .....Signal pass-through
Noise filter (RC time constant) .....10 ?s

Analog output compatibility .....Signal pass-through
Shutdown input compatibility.....Signal pass-through
+5 V output .....1 A

Included Connectors

Encoders.....8-position mini-combicon 3.81 mm plug (1 per axis)
Limits .....6-position mini-combicon 3.81 mm plug (1 per axis)
Motors .....5-position combicon 5.08 mm plug (1 per axis)
Breakpoints .....6-position mini-combicon 3.81 mm plug (1 total)
Triggers .....6-position mini-combicon 3.81 mm plug (1 total)
Analog input .....6-position mini-combicon 3.81 mm plug (1 total)
Analog output .....5-position mini-combicon 3.81 mm plug (1 total)
AC power .....Detachable AC power cord (IEC standard type)
Motion I/O .....68-pin female high density VHDCI type

Power Supply

Input voltage .....115/230 VAC, 2/1 A, 60/50 Hz
Measurement category II
Fuse
115 VAC input (factory default) .....F3A 250V (Bussmann #GMA-3)
230 VAC input .....F1.5A 250V (Bussmann #GMA-1.5)
Dimensions .....5 mm □ 20 mm

Host Bus Voltage Interlock

Undervoltage threshold.....4 VDC

Physical Characteristics

Dimensions (W □ H □ L) .....25.4 cm □□4.3 cm □□30.7 cm
(10 in. □ 1.7 in. □ 12.1 in.)
Weight .....4.5 kg (10 lb.)

Environment

Operating temperature .....0 ºC to 40 ºC
Storage temperature .....–20 ºC to 70 ºC
Humidity .....10% to 90% RH, noncondensing
Maximum altitude.....2,000 m
Pollution Degree 2

Safety

This product is designed to meet the requirements of the following standards of safety for electrical equipment for measurement, control, and laboratory use:

• EN 61010-1, IEC 61010-1

• UL 508C, UL 61010-1
• CAN/CSA C22.2 No. 61010-1
UL Listed to UL 508C, power conversion equipment.
Note For UL and other safety certifications, refer to the product label or the *Online Product Certification* section.

Electromagnetic Compatibility

This product meets the requirements of the following EMC standards for electrical equipment for measurement, control, and laboratory use:
• Emissions: EN 55011 Class A at 10 m FCC Part 15A above 1 GHz
• Immunity: EN 61326:1997 + A2:2001, Table 1
• CE, C-Tick, and FCC Part 15 (Class A) Compliant
Note For the standards applied to assess the EMC of this product, refer to the *Online Product Certification* section.
Note For EMC compliance, operate this device according to the documentation.

CE Compliance

This product meets the essential requirements of applicable European Directives as follows:
• 73/23/EEC; Low-Voltage Directive (safety)
• 89/336/EEC; Electromagnetic Compatibility Directive (EMC)

General Specifications

- NEMA Size 23
- High Torque at moderate speeds
- Inch standard mounting
- CE cUR and UR compliant
- Unipolar or Bipolar windings
- Features: leadwire connection, flat or smooth shaft
- Options: MS connector, terminal boxes, encoder mounting provisions,
- 200 LPR, 400 LPR encoders with line drivers
- Custom Motors

Phases	2
Full Steps per Revolution	200
Step Angle	1.8°
Step Accuracy (of one full step, no load)	± 2 %
Operating Temperature	-20°C to +40°C
Insulation Class	Class B, 130°C
Insulation Voltage Rating	340 Vdc
Insulation Resistance	100 Megohms

Leadwire Hookup Models

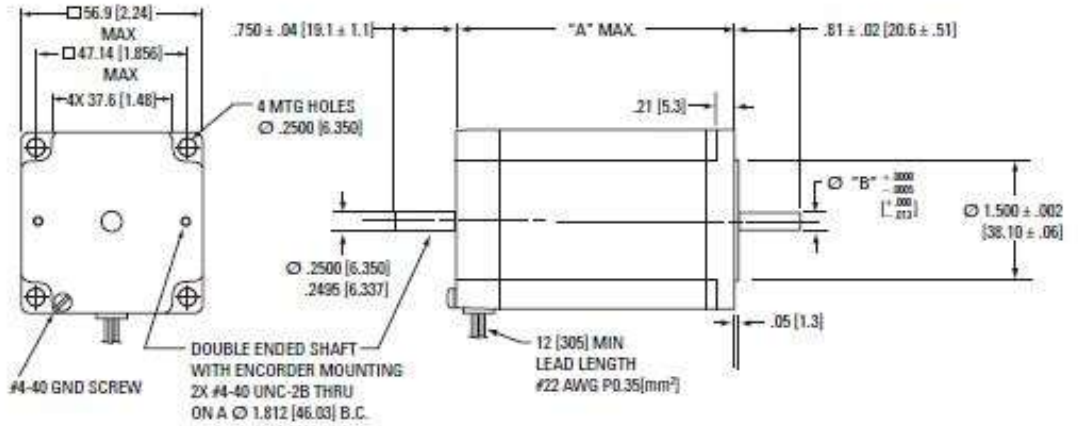

Dimensions in inches [mm]

Model	"A" Max	"B" Max
T2H	1.64 (41.6)	0.2500 (6.35)
T21	2.21 (56.1)	
T22	3.06 (77.7)	
T23	4.06 (103.1)	0.3125 (7.94)

Terminal Box Construction

Model	"A" Max
T2H	2.84 (72.1)
T21	3.41 (86.6)
T22	4.26 (108.2)
T23	5.26 (133.6)

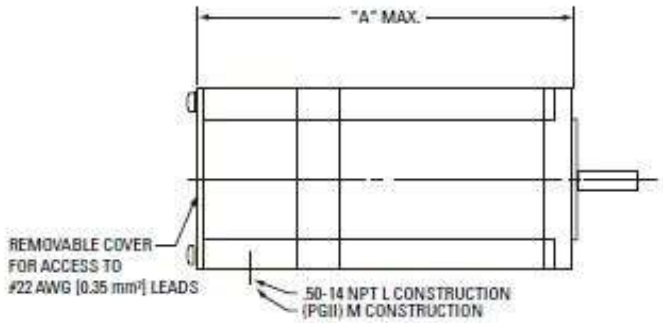

Dimensions in inches [mm]

Table 6.Specific characteristics of the stepper motor used in the simulator

T23xxHK	•		380 (2.68)	6.0	0.28	1.5	7.0 (0.049)	3.04	0.0084 (0.059)	3.3 (1.5)	15 (67)	25 (111)
T23xxHJ	•			3.8	0.64	3.9						
T23xxLC		•		0.67	23.5	136						
T23xxLH		•		3.0	1.0	6.2						
T23xxLF		•		1.8	2.8	17						
T23xxLE		•		1.5	4.1	24						

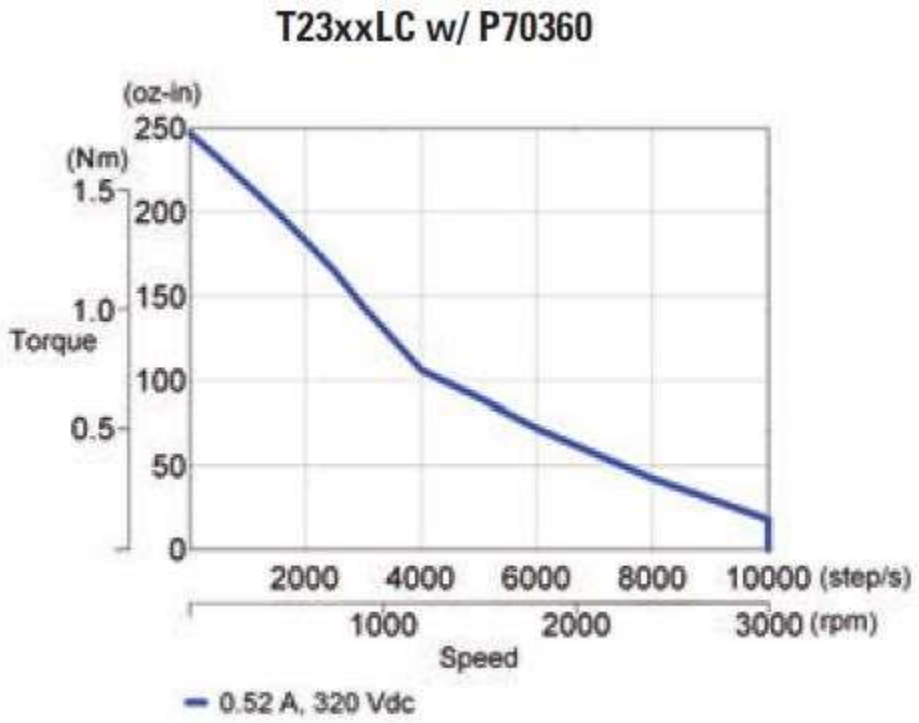

Figure 5. Speed vs Torque curves for the stepper motors

Appendix C: Front Panel and Block Diagram of the UOKS Controller

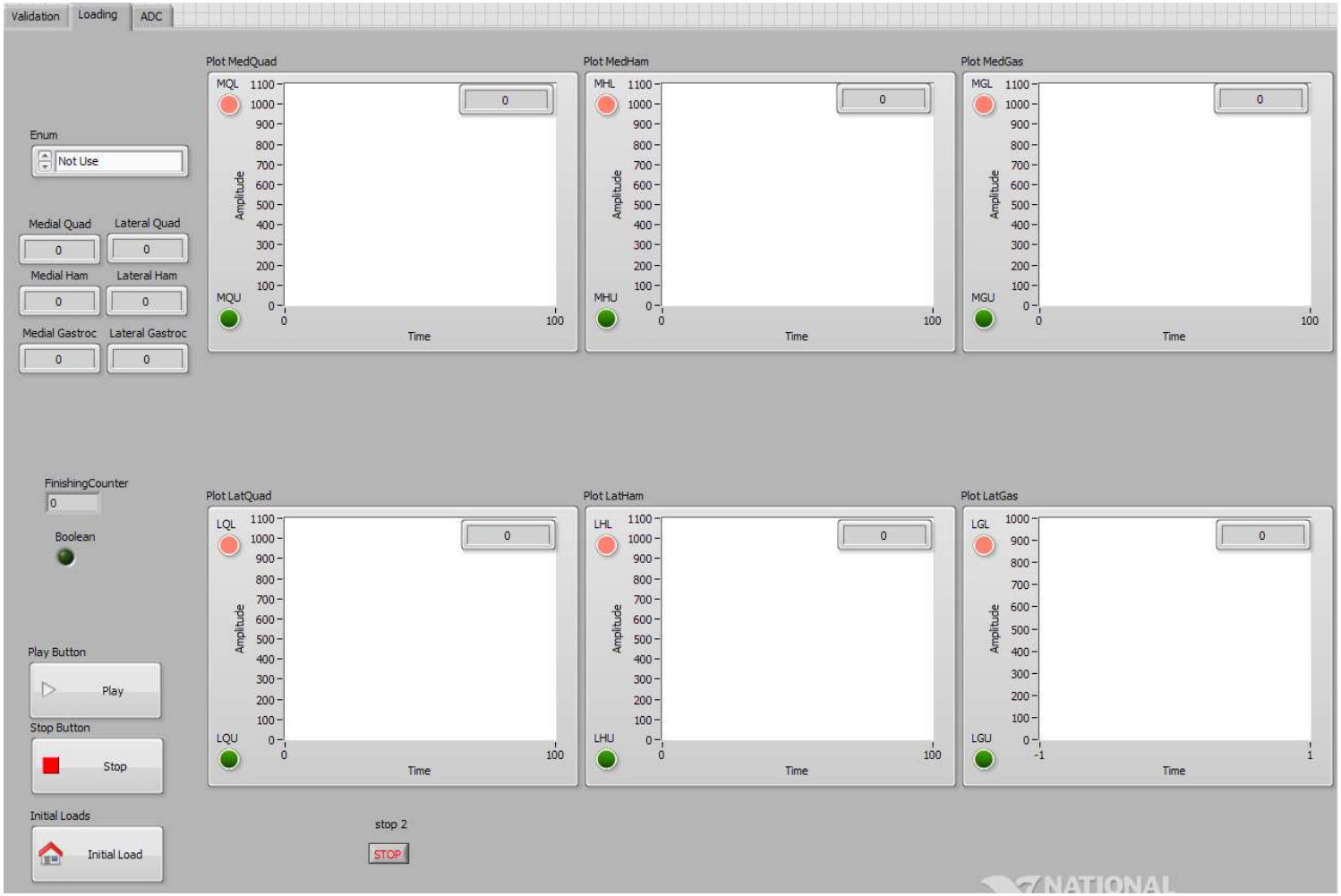

Figure 6. GUI front panel. This front panel can display real time measurements of the load cells for each of the six simulated loads. The user has the option of selecting from 12 default loading profiles. The user can also stop and return the simulation to the initial state.

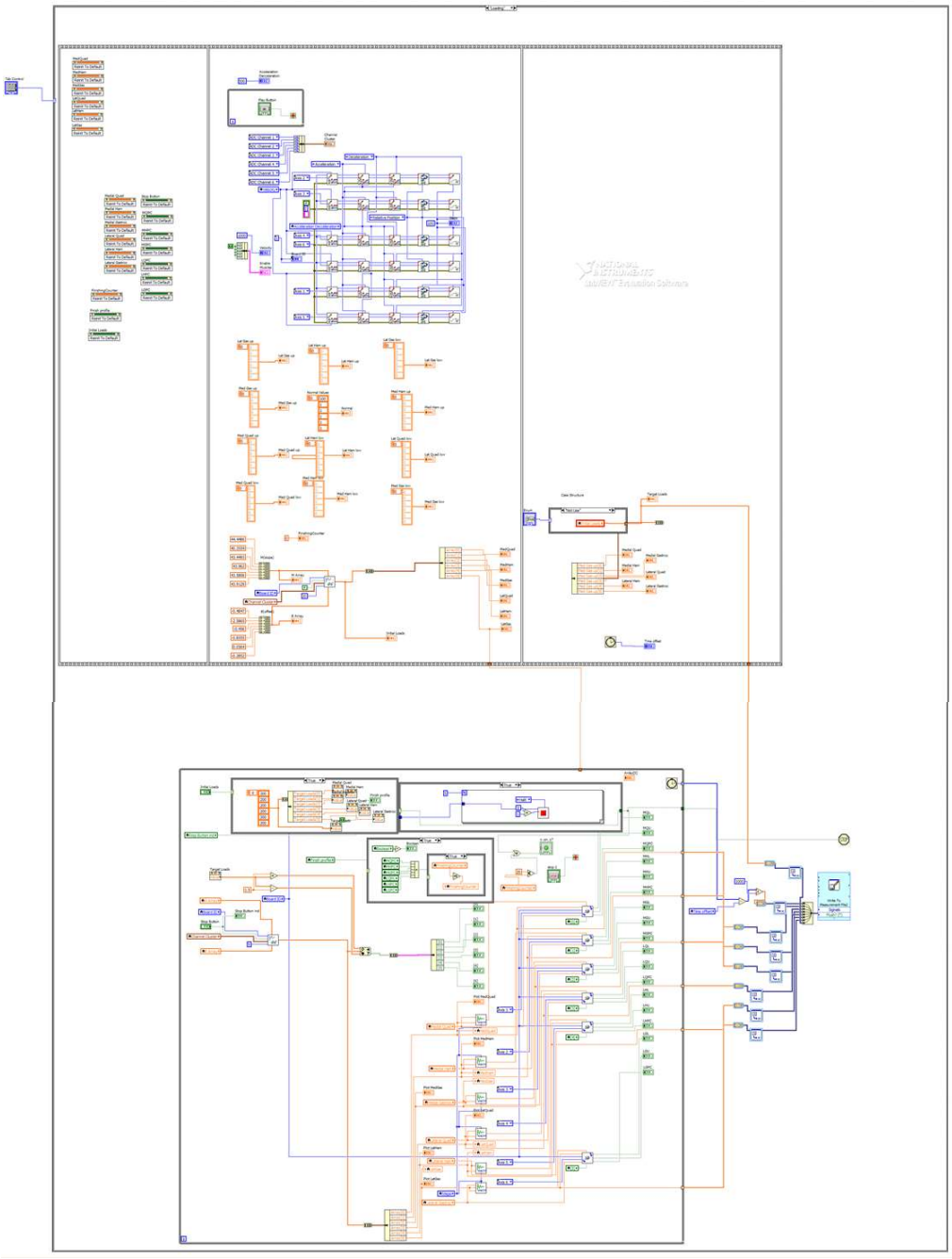

Figure 7. Block diagram of the routine used for experiment 2. This routine initializes the stepper motor drivers and provides real time feedback from the load cells to the user

Appendix D: Tekscan Sensor Technical information

Tekscan® **Medical Sensor 4011**

PRESSURE MAPPING, FORCE MEASUREMENT, AND TACTILE SENSORS

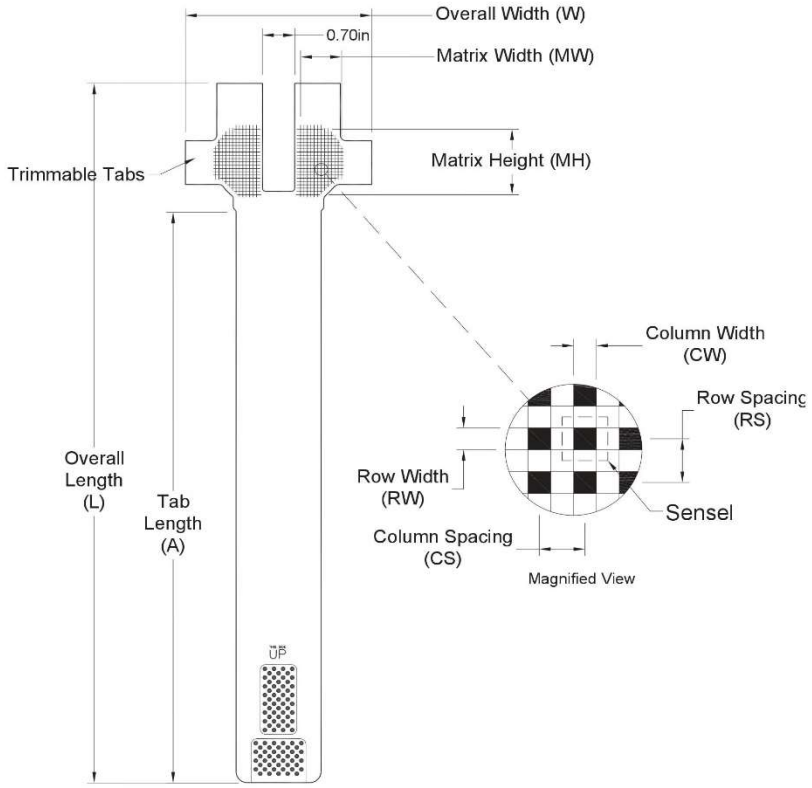

General Dimensions					Sensing Region Dimensions						Summary	
Overall Length *L*	Overall Width *W*	Tab Length *A*	Matrix Width *MW*	Matrix Height *MH*	Columns *CW*	Columns Pitch *CS*	Columns *Qty.*	Rows *RW*	Rows Pitch *RS*	Rows *Qty.*	Total No. of Sensels	Sensel Spatial Resolution
(mm) 406.4	(mm) 104.1	(mm) 330.2	(mm) 24.8	(mm) 40.0	(mm) 1.1	(mm) 1.9	13	(mm) 1.1	(mm) 1.9	21	273	(sensel per sq-cm) 27.6
(in) 16.00	(in) 4.10	(in) 13.00	(in) 0.98	(in) 1.58	(in) 0.045	(in) 0.075	13	(in) 0.045	(in) 0.075	21	273	(sensel per sq-in) 177.8

Pressure Ranges	
kPa	3,448
psi	500

+1.617.464.4281 | 1.800.248.3669 | info@tekscan.com | www.tekscan.com

SD_Rev A_020215 Sensor Datashe

Figure 8. Teksan 4011 pressure sensor data sheet. Image retrieved online from: https://www.tekscan.com/products-solutions/medical-sensors/4011

Appendix E: Statistical Analysis

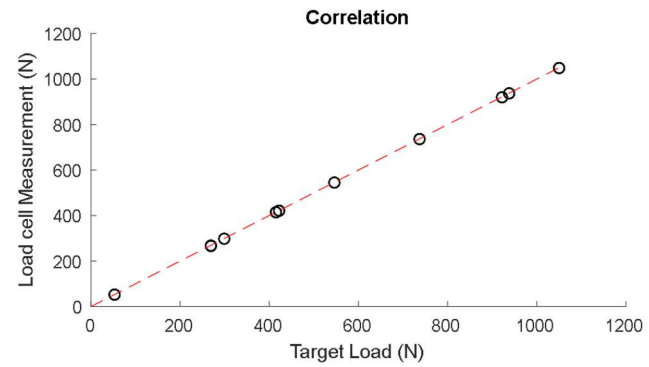

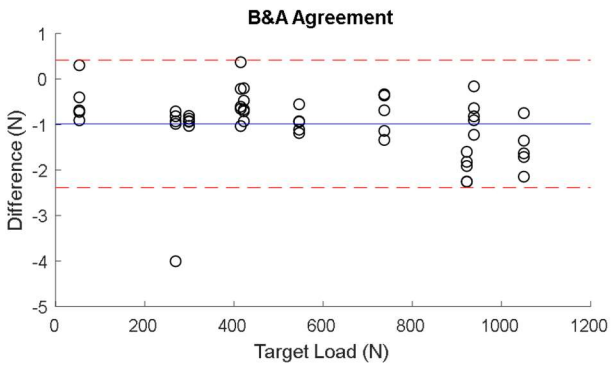

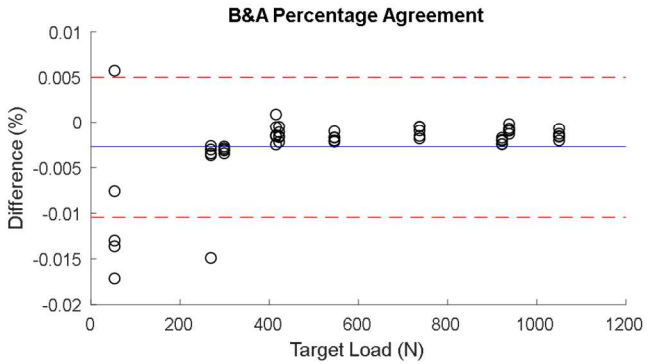

	Single Measurements	Multiple Measurements
ICC	1.0000	1.0000
Lower Bound	1.0000	1.0000
UpperBound	1.0000	1.0000
F	7.9540e+05	7.9540e+05
DoF1	49	49
DoF2	49	49
p-Value	0	0

Figure 9. Results from the analysis for the medial quadriceps controller. Top left plot shows a correlation between paired measurements. Top right plot showing the distribution of differences between the measurements using the bland & altman method of agreement. Bottom left plot shows Bland & Altman in percentage differences. Bottom right shows a table showing the ICC calculations for the paired measurements.

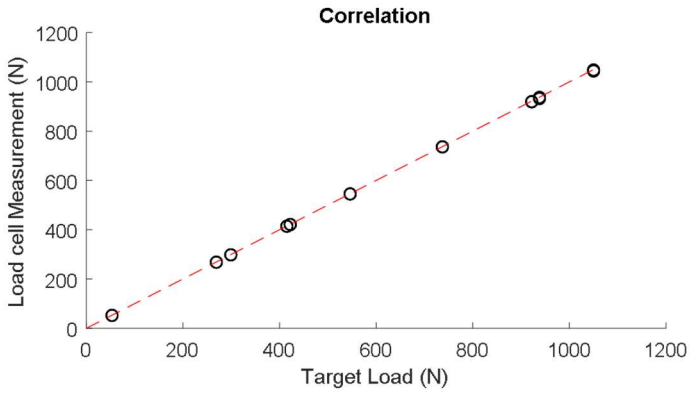

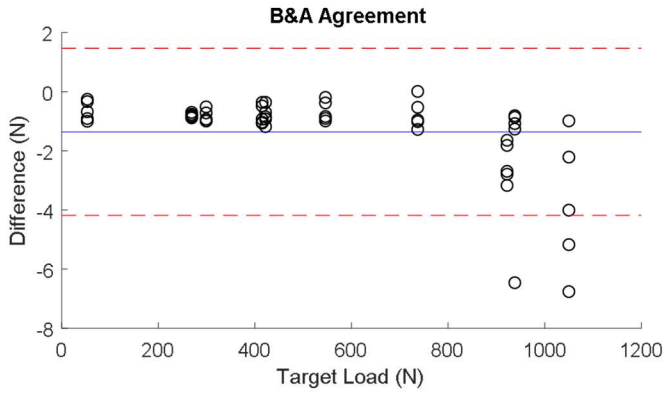

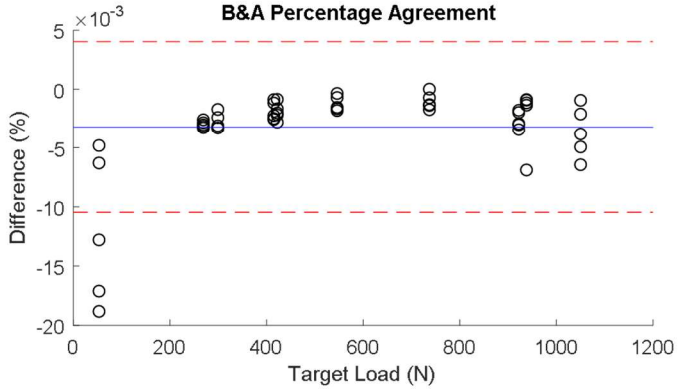

	Single Measurements	Multiple Measurements
ICC	1.0000	1.0000
Lower Bound	1.0000	1.0000
UpperBound	1.0000	1.0000
F	1.9518e+05	1.9518e+05
DoF1	49	49
DoF2	49	49
p-Value	0	0

Figure 10. Results from the analysis for the medial hamstrings controller. Top left plot shows a correlation between paired measurements. Top right plot showing the distribution of differences between the measurements using the bland & altman method of agreement. Bottom left plot shows Bland & Altman in percentage differences. Bottom right shows a table showing the ICC calculations for the paired measurements.

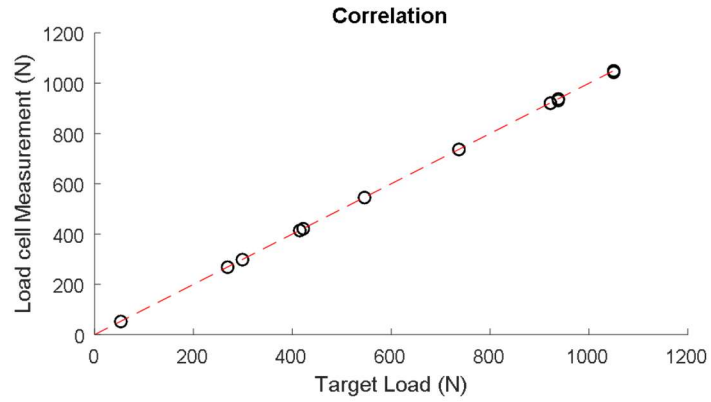

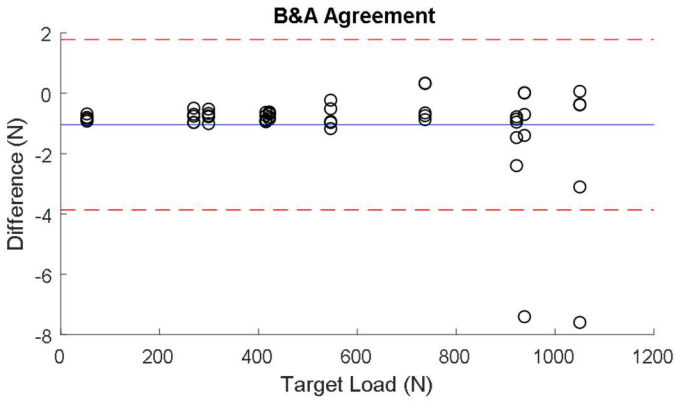

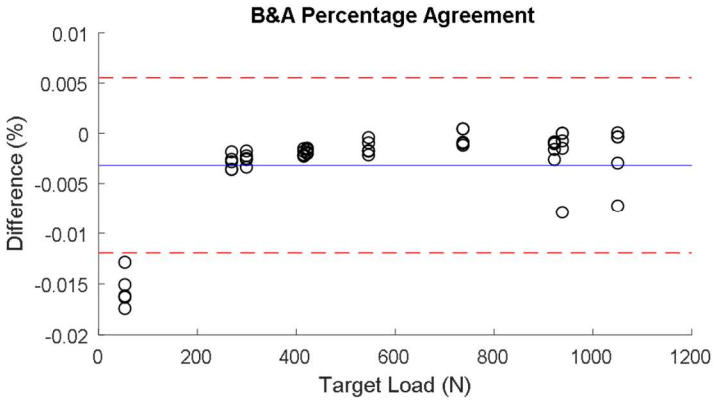

	Single Measurements	Multiple Measurements
ICC	1.0000	1.0000
Lower Bound	1.0000	1.0000
UpperBound	1.0000	1.0000
F	1.9547e+05	1.9547e+05
DoF1	49	49
DoF2	49	49
p-Value	0	0

Figure 11. Results from the analysis for the medial gastrocnemius controller. Top left plot shows a correlation between paired measurements. Top right plot showing the distribution of differences between the measurements using the bland & altman method of agreement. Bottom left plot shows Bland & Altman in percentage differences. Bottom right shows a table showing the ICC calculations for the paired measurements.

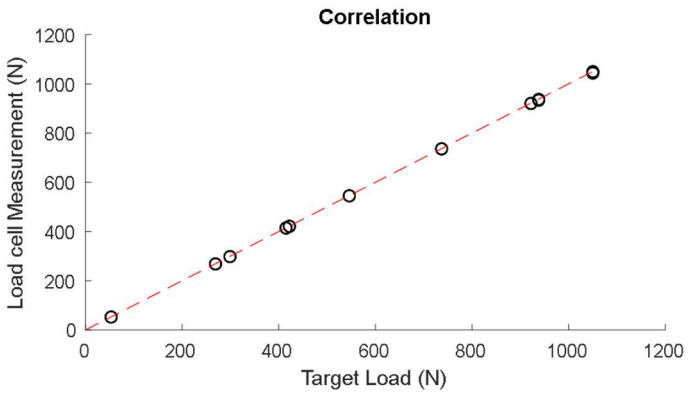

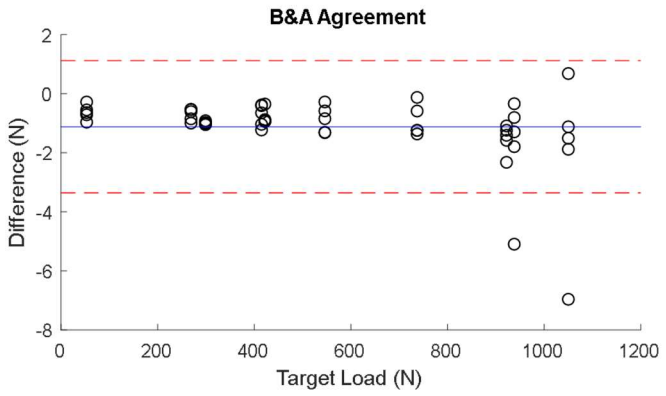

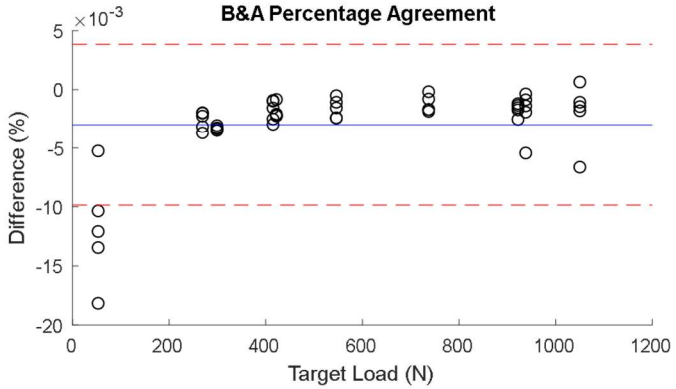

	Single Measurements	Multiple Measurements
ICC	1.0000	1.0000
Lower Bound	1.0000	1.0000
UpperBound	1.0000	1.0000
F	3.1045e+05	3.1045e+05
DoF1	49	49
DoF2	49	49
p-Value	0	0

Figure 12. Results from the analysis for the lateral quadriceps controller. Top left plot shows a correlation between paired measurements. Top right plot showing the distribution of differences between the measurements using the bland & altman method of agreement. Bottom left plot shows Bland & Altman in percentage differences. Bottom right shows a table showing the ICC calculations for the paired measurements.

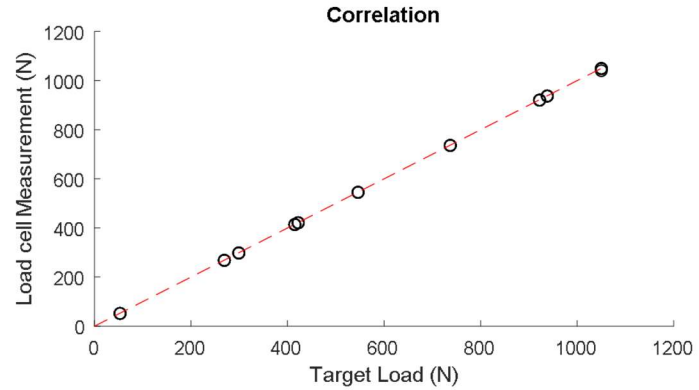

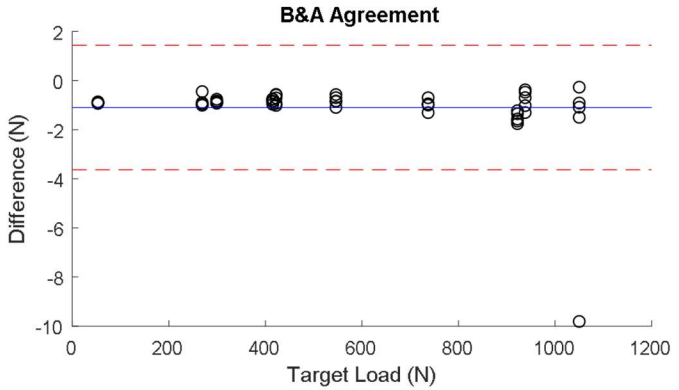

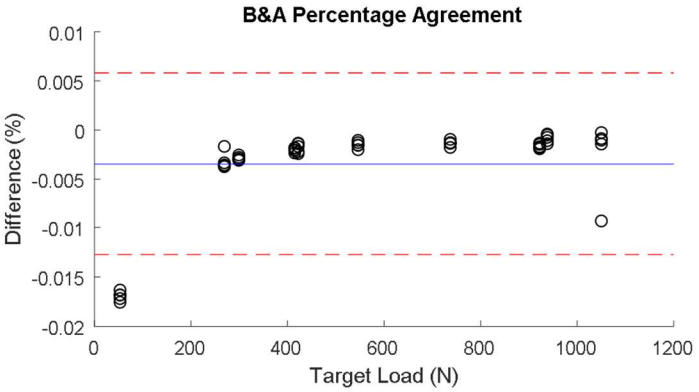

	Single Measurements	Multiple Measurements
ICC	1.0000	1.0000
Lower Bound	1.0000	1.0000
UpperBound	1.0000	1.0000
F	2.4299e+05	2.4299e+05
DoF1	49	49
DoF2	49	49
p-Value	0	0

Figure 13. Results from the analysis for the lateral hamstrings controller. Top left plot shows a correlation between paired measurements. Top right plot showing the distribution of differences between the measurements using the bland & altman method of agreement. Bottom left plot shows Bland & Altman in percentage differences. Bottom right shows a table showing the ICC calculations for the paired measurements.

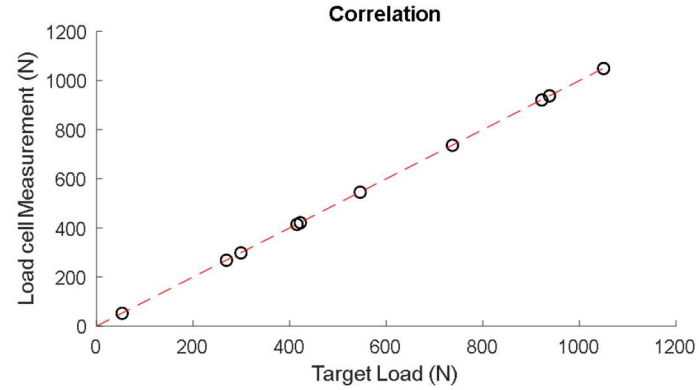

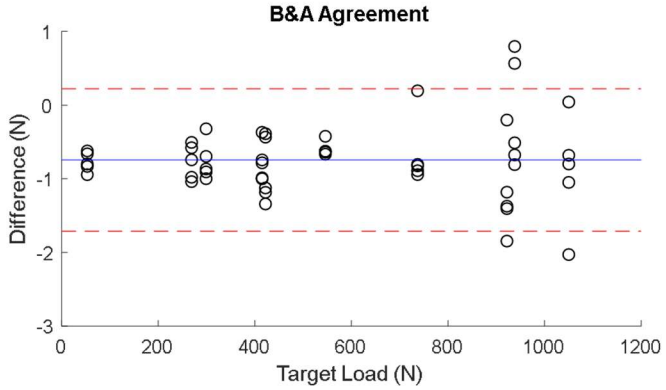

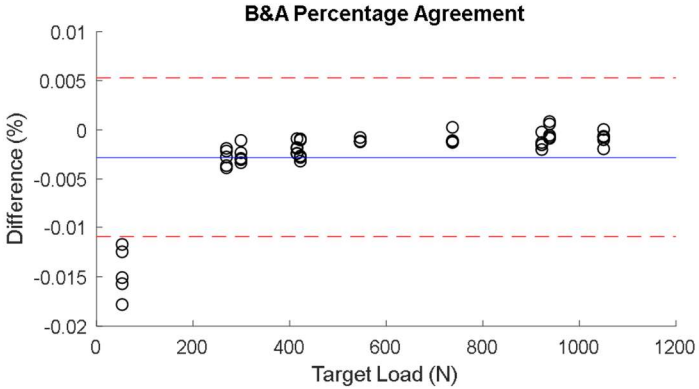

	Single Measurements	Multiple Measurements
ICC	1.0000	1.0000
Lower Bound	1.0000	1.0000
UpperBound	1.0000	1.0000
F	1.6702e+06	1.6702e+06
DoF1	49	49
DoF2	49	49
p-Value	0	0

Figure 14. Results from the analysis for the lateral gastrocnemius controller. Top left plot shows a correlation between paired measurements. Top right plot showing the distribution of differences between the measurements using the bland & altman method of agreement. Bottom left plot shows Bland & Altman in percentage differences. Bottom right shows a table showing the ICC calculations for the paired measurements.

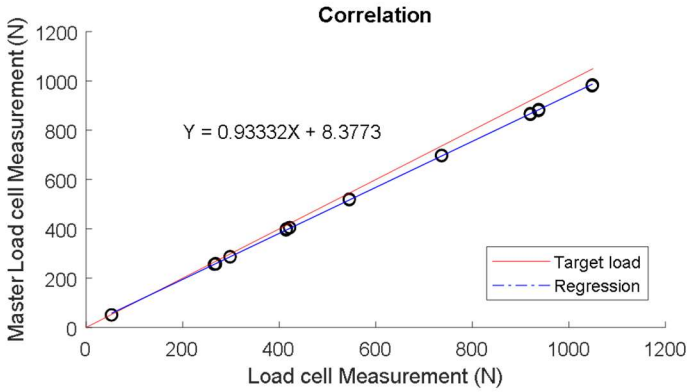

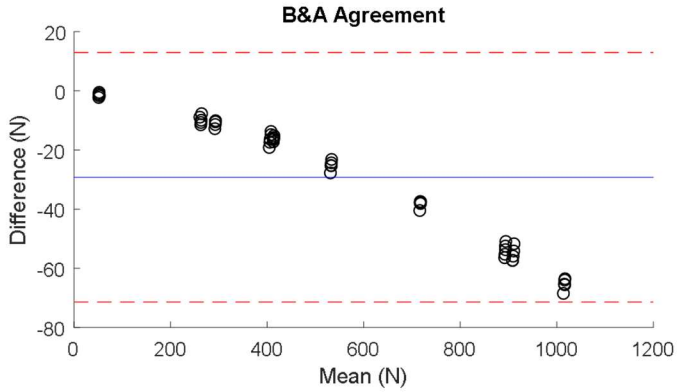

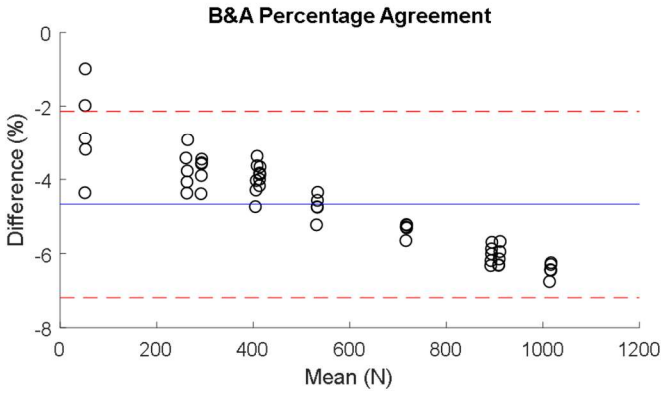

	Single Measurements	Multiple Measurements
ICC	0.9976	0.9978
Lower Bound	0.9957	0.9978
UpperBound	0.9986	0.9993
F	819.6026	819.6026
DoF1	49	49
DoF2	49	49
p-Value	0	0

Figure 15. Results from the analysis for the medial quadriceps loading mechanism. Top left plot shows a correlation between paired measurements. Top right plot showing the distribution of differences between the measurements using the bland & altman method of agreement. Bottom left plot shows Bland & Altman in percentage differences. Bottom right shows a table showing the ICC calculations for the paired measurements.

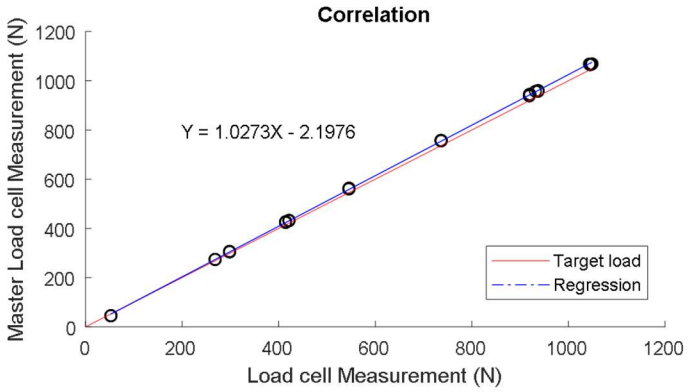

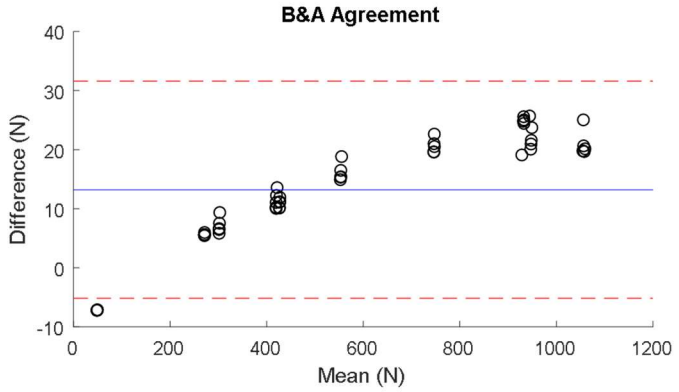

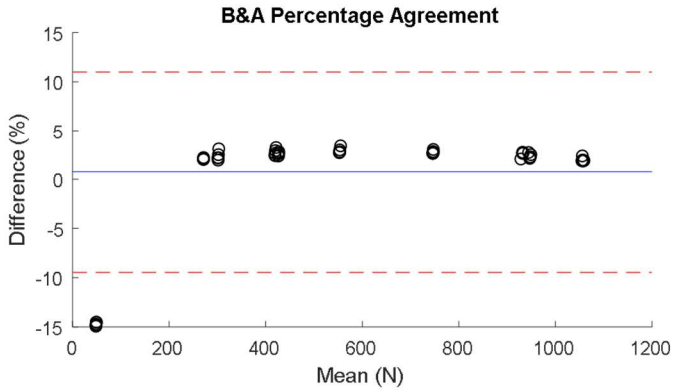

	Single Measurements	Multiple Measurements
ICC	0.9996	0.9996
Lower Bound	0.9993	0.9996
UpperBound	0.9998	0.9999
F	4.7231e+03	4.7231e+03
DoF1	49	49
DoF2	49	49
p-Value	0	0

Figure 16. Results from the analysis for the medial hamstring loading mechanism. Top left plot shows a correlation between paired measurements. Top right plot showing the distribution of differences between the measurements using the bland & altman method of agreement. Bottom left plot shows Bland & Altman in percentage differences. Bottom right shows a table showing the ICC calculations for the paired measurements.

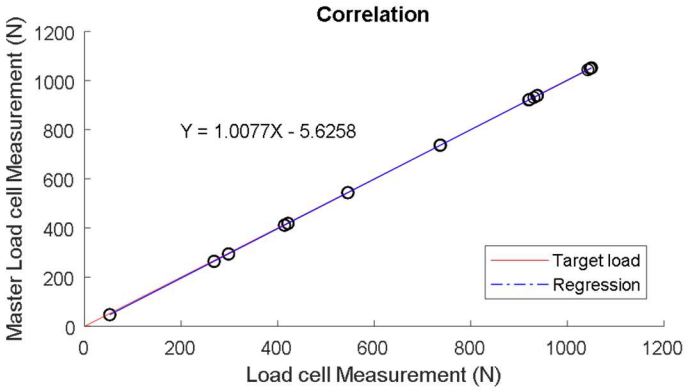

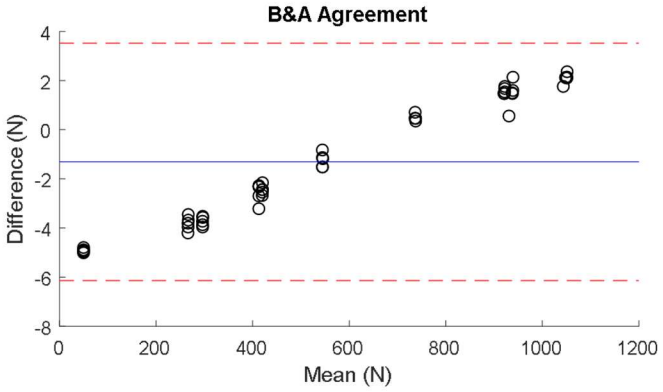

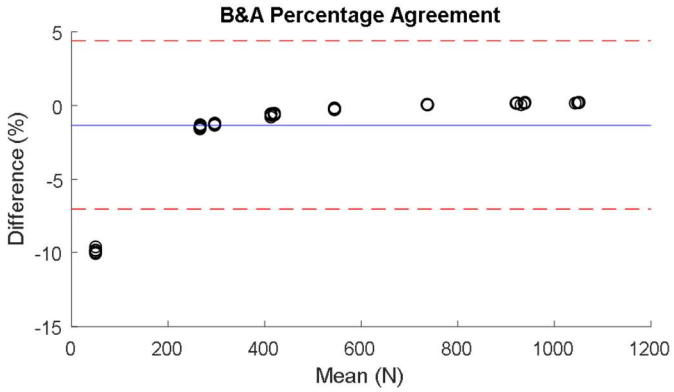

	Single Measurements	Multiple Measurements
ICC	1.0000	1.0000
Lower Bound	0.9999	1.0000
UpperBound	1.0000	1.0000
F	6.7201e+04	6.7201e+04
DoF1	49	49
DoF2	49	49
p-Value	0	0

Figure 17. Results from the analysis for the medial gastrocnemius loading mechanism. Top left plot shows a correlation between paired measurements. Top right plot showing the distribution of differences between the measurements using the bland & altman method of agreement. Bottom left plot shows Bland & Altman in percentage differences. Bottom right shows a table showing the ICC calculations for the paired measurements.

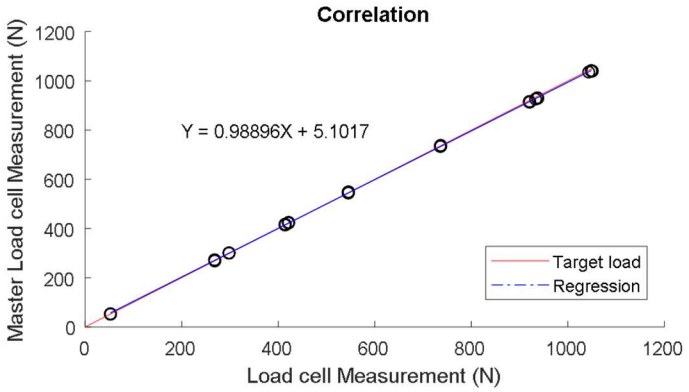

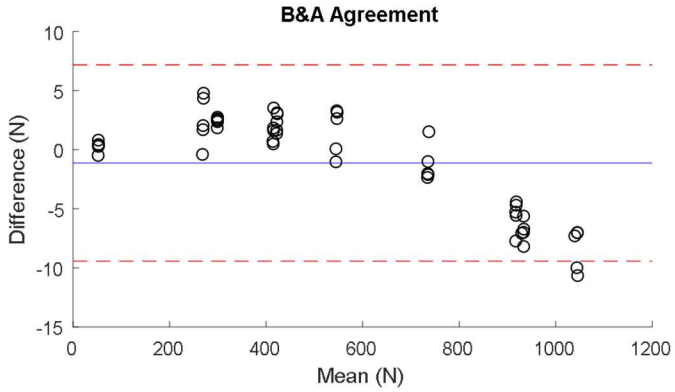

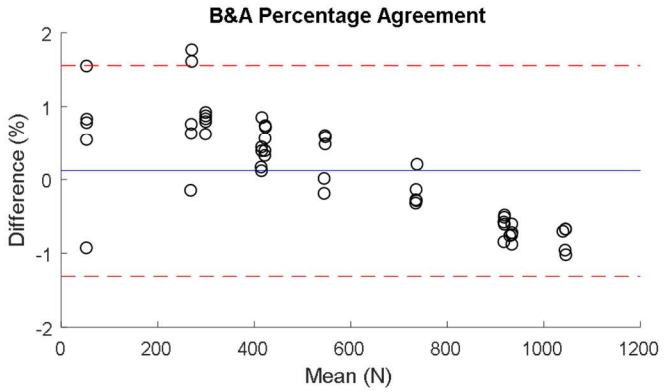

	Single Measurements	Multiple Measurements
ICC	0.9999	0.9999
Lower Bound	0.9998	0.9999
UpperBound	0.9999	1.0000
F	2.2325e+04	2.2325e+04
DoF1	49	49
DoF2	49	49
p-Value	0	0

Figure 18. Results from the analysis for the lateral quadriceps loading mechanism. Top left plot shows a correlation between paired measurements. Top right plot showing the distribution of differences between the measurements using the bland & altman method of agreement. Bottom left plot shows Bland & Altman in percentage differences. Bottom right shows a table showing the ICC calculations for the paired measurements.

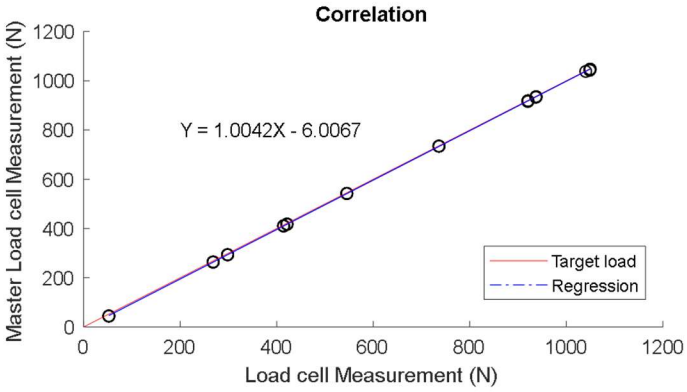

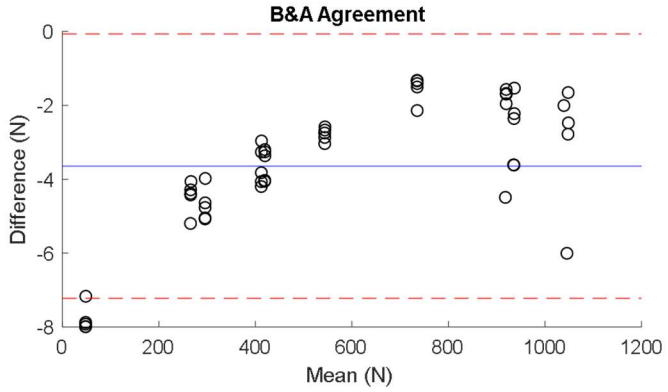

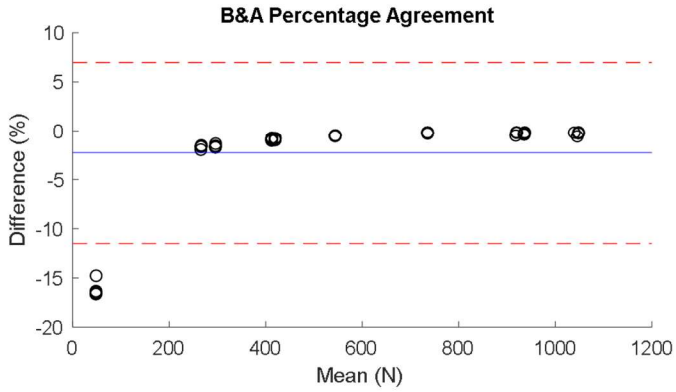

	Single Measurements	Multiple Measurements
ICC	1.0000	1.0000
Lower Bound	1.0000	1.0000
UpperBound	1.0000	1.0000
F	1.2204e+05	1.2204e+05
DoF1	49	49
DoF2	49	49
p-Value	0	0

Figure 19. Results from the analysis for the lateral hamstrings loading mechanism. Top left plot shows a correlation between paired measurements. Top right plot showing the distribution of differences between the measurements using the bland & altman method of agreement. Bottom left plot shows Bland & Altman in percentage differences. Bottom right shows a table showing the ICC calculations for the paired measurements.

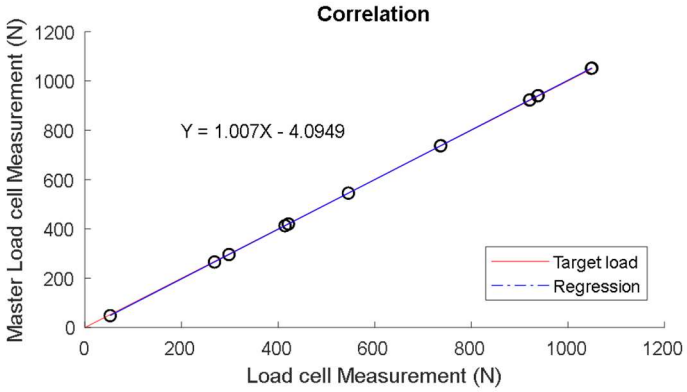

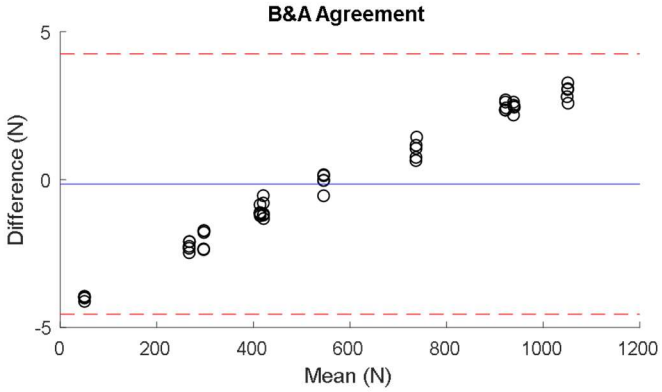

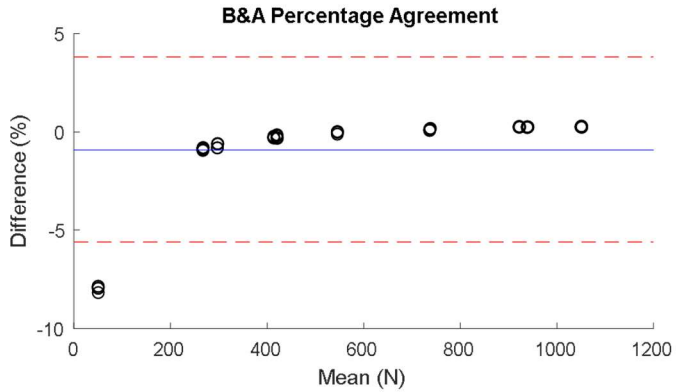

	Single Measurements	Multiple Measurements
ICC	1.0000	1.0000
Lower Bound	1.0000	1.0000
UpperBound	1.0000	1.0000
F	8.1184e+04	8.1184e+04
DoF1	49	49
DoF2	49	49
p-Value	0	0

Figure 20. Results from the analysis for the lateral gastrocnemius loading mechanism. Top left plot shows a correlation between paired measurements. Top right plot showing the distribution of differences between the measurements using the bland & altman method of agreement. Bottom left plot shows Bland & Altman in percentage differences. Bottom right shows a table showing the ICC calculations for the paired measurements.

Appendix F: Results

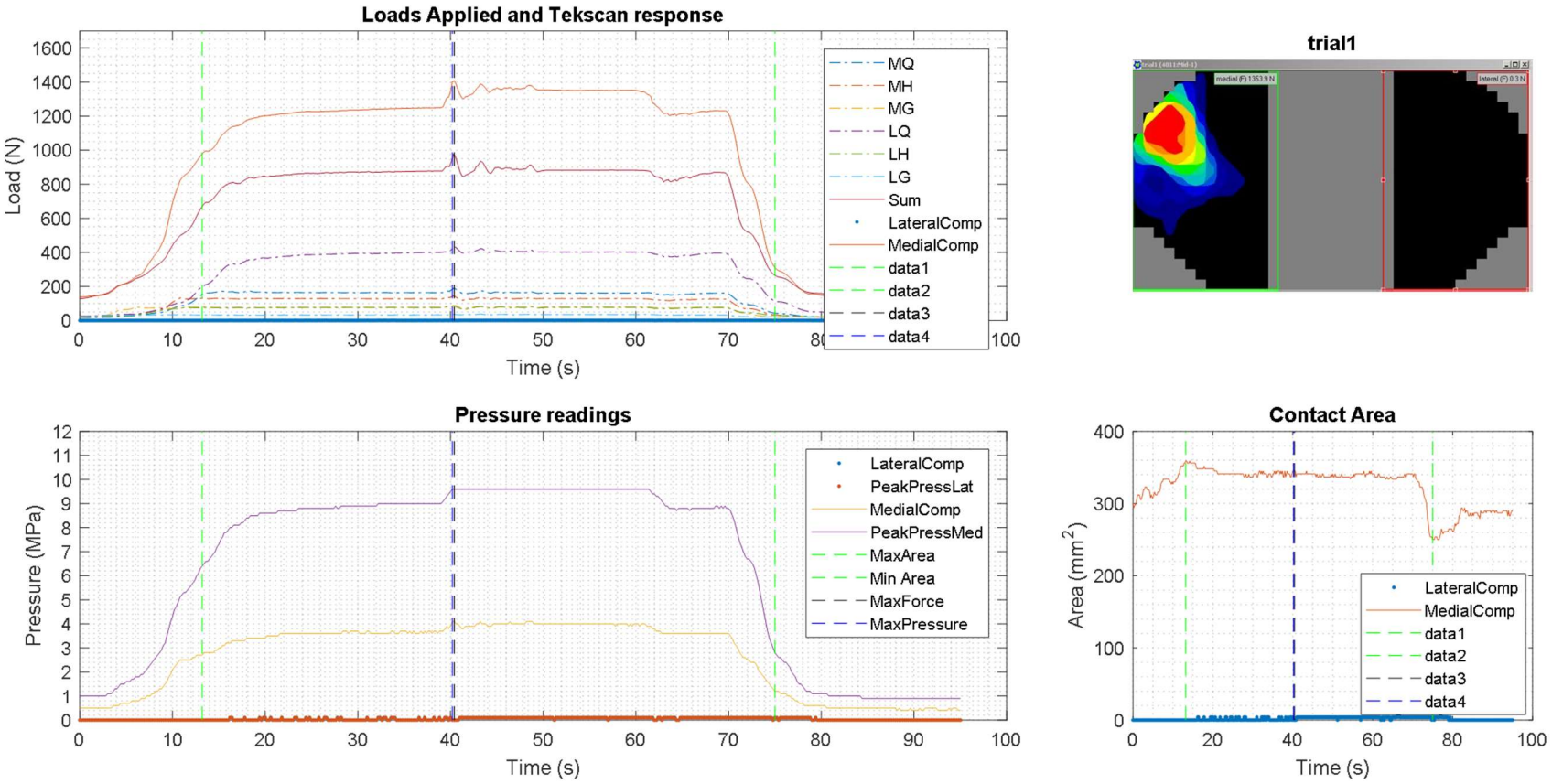

Figure 21. Data obtained with Tekscan for trial 1. Top left plot show the sum of all applied load(red) and the load measurements obtained with Tekscan. Due to biased alignment the medial compartment of the knee was the only sections exited during the trial, as seen in the Top right. The bottom left displays the waveforms for pressure and peak pressures in the knee. Bottom right shows medial compartment contact area distribution during the trial

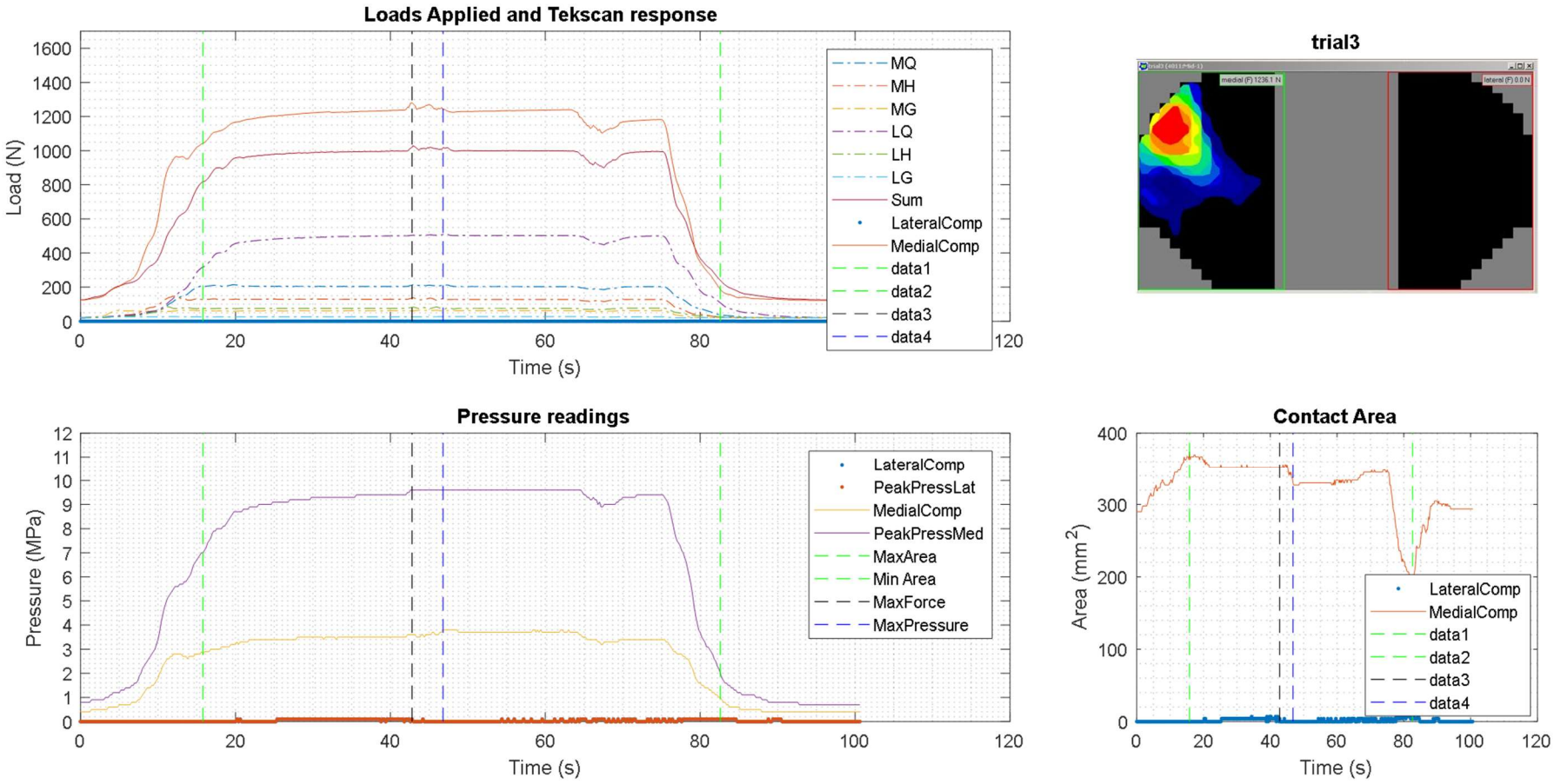

Figure 22. Data obtained with Tekscan for trial 3. Top left plot show the sum of all applied load(red) and the load measurements obtained with Tekscan. Due to biased alignment the medial compartment of the knee was the only sections exited during the trial, as seen in the Top right. The bottom left displays the waveforms for pressure and peak pressures in the knee. Bottom right shows medial compartment contact area distribution during the trial

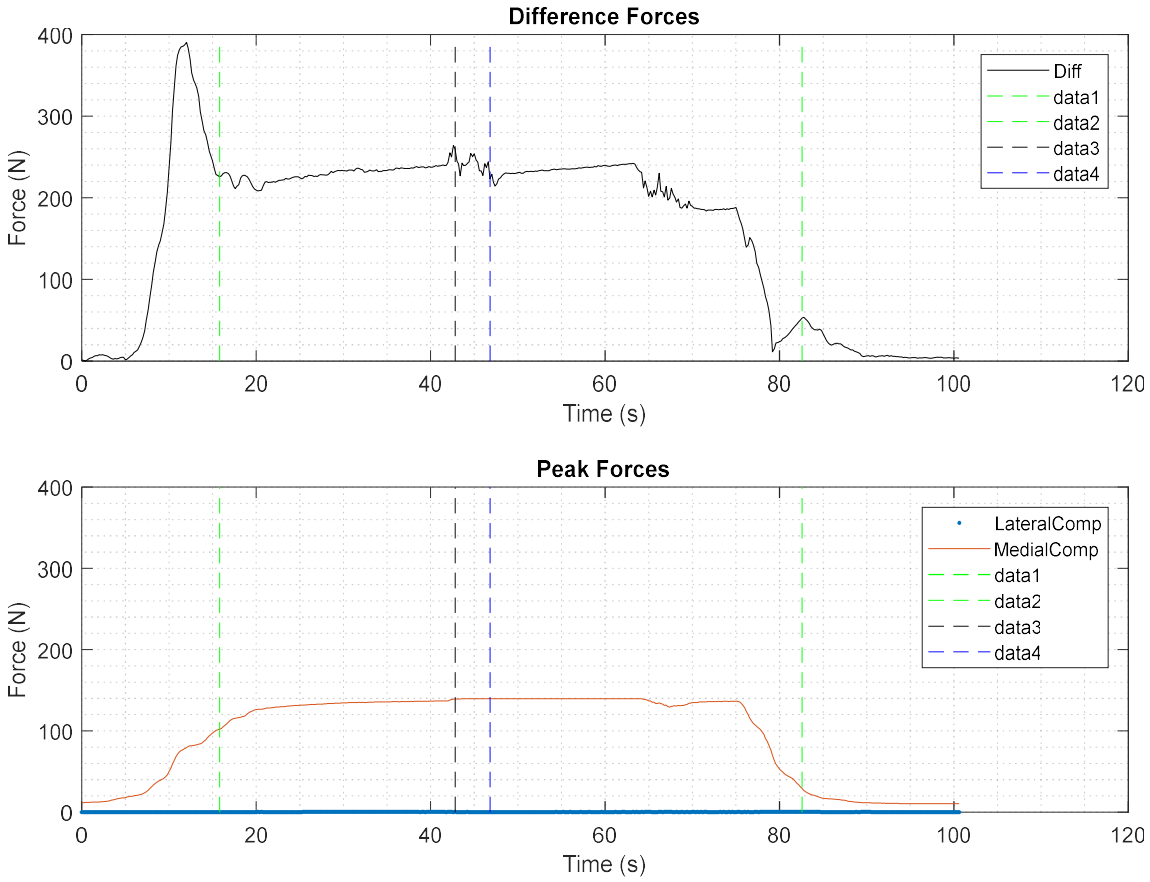

Figure 23. Top graph displays the waveform for the difference between the Load obtained by the Tekscan and the UOKS loads for trial 3. Bottom plot shows Medial compartment peak forces. These peak forces are reported for the sensel with the highest peak pressures for any frame.

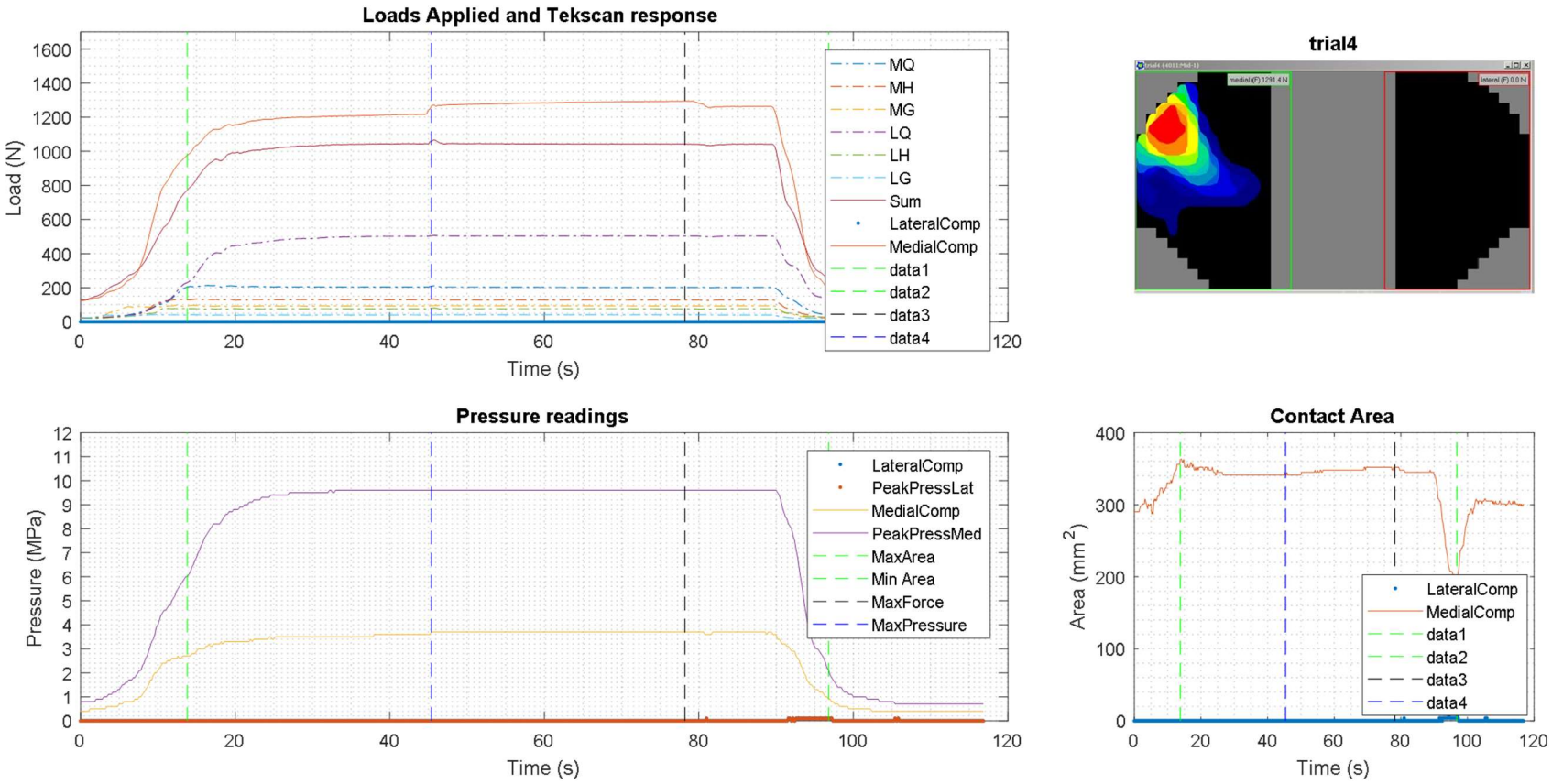

Figure 24. Data obtained with Tekscan for trial 4. Top left plot show the sum of all applied load(red) and the load measurements obtained with Tekscan. Due to biased alignment the medial compartment of the knee was the only sections exited during the trial, as seen in the Top right. The bottom left displays the waveforms for pressure and peak pressures in the knee. Bottom right shows medial compartment contact area distribution during the trial

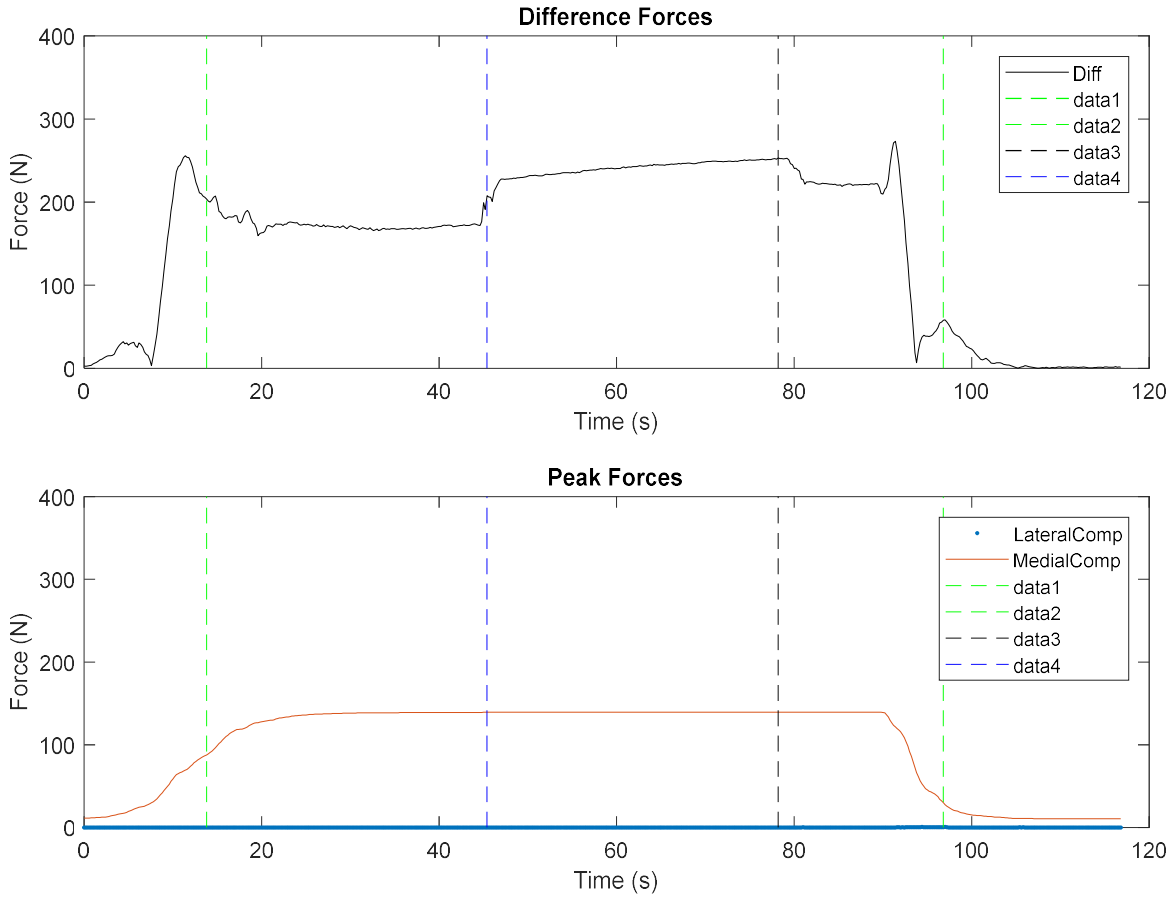

Figure 25. Top graph displays the waveform for the difference between the Load obtained by the Tekscan and the UOKS loads for trial 4. Bottom plot shows Medial compartment peak forces. These peak forces are reported for the sensel with the highest peak pressures for any frame.

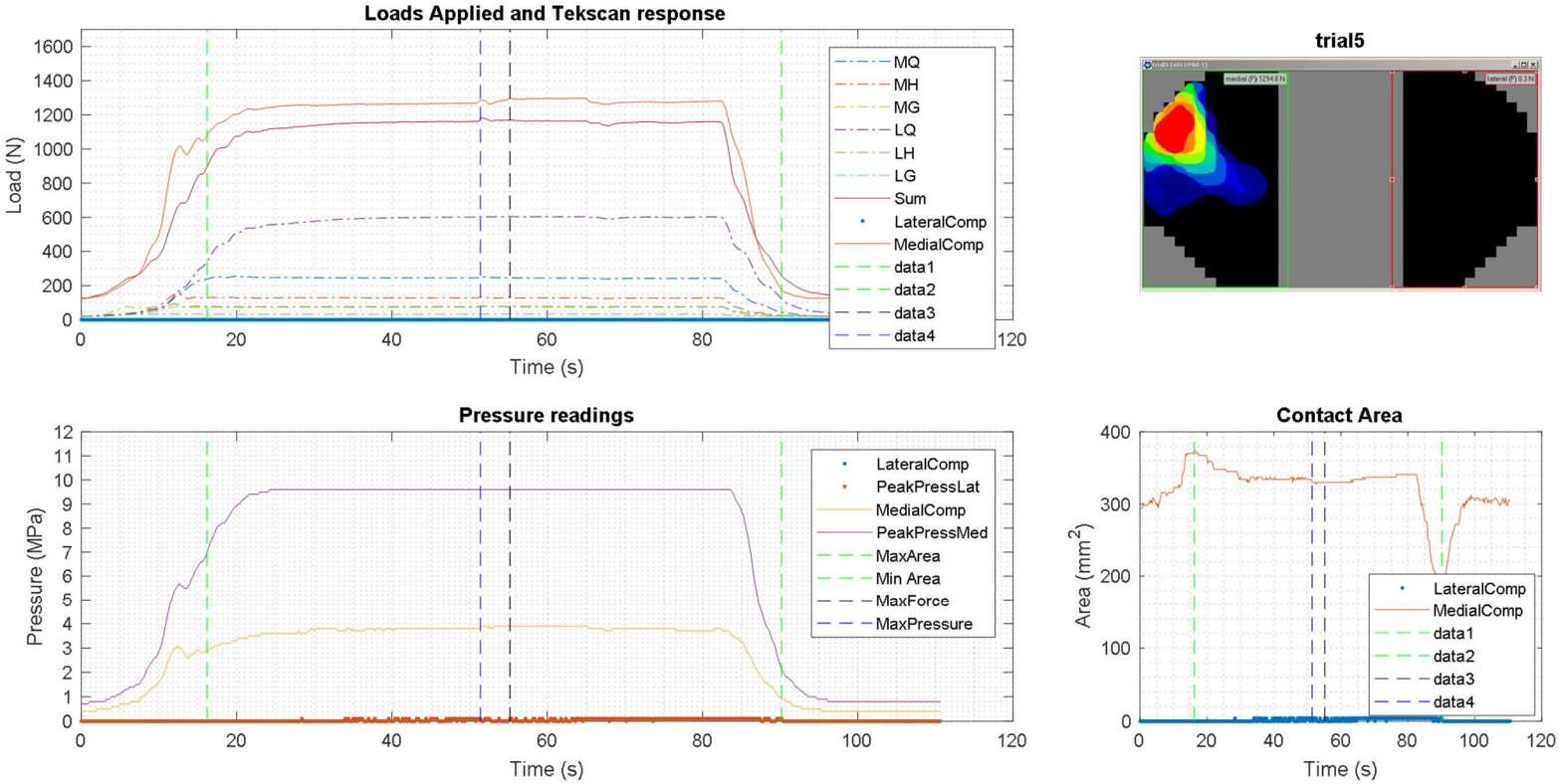

Figure 26. Data obtained with Tekscan for trial 5. Top left plot show the sum of all applied load(red) and the load measurements obtained with Tekscan. Due to biased alignment the medial compartment of the knee was the only sections exited during the trial, as seen in the Top right. The bottom left displays the waveforms for pressure and peak pressures in the knee. Bottom right shows medial compartment contact area distribution during the trial

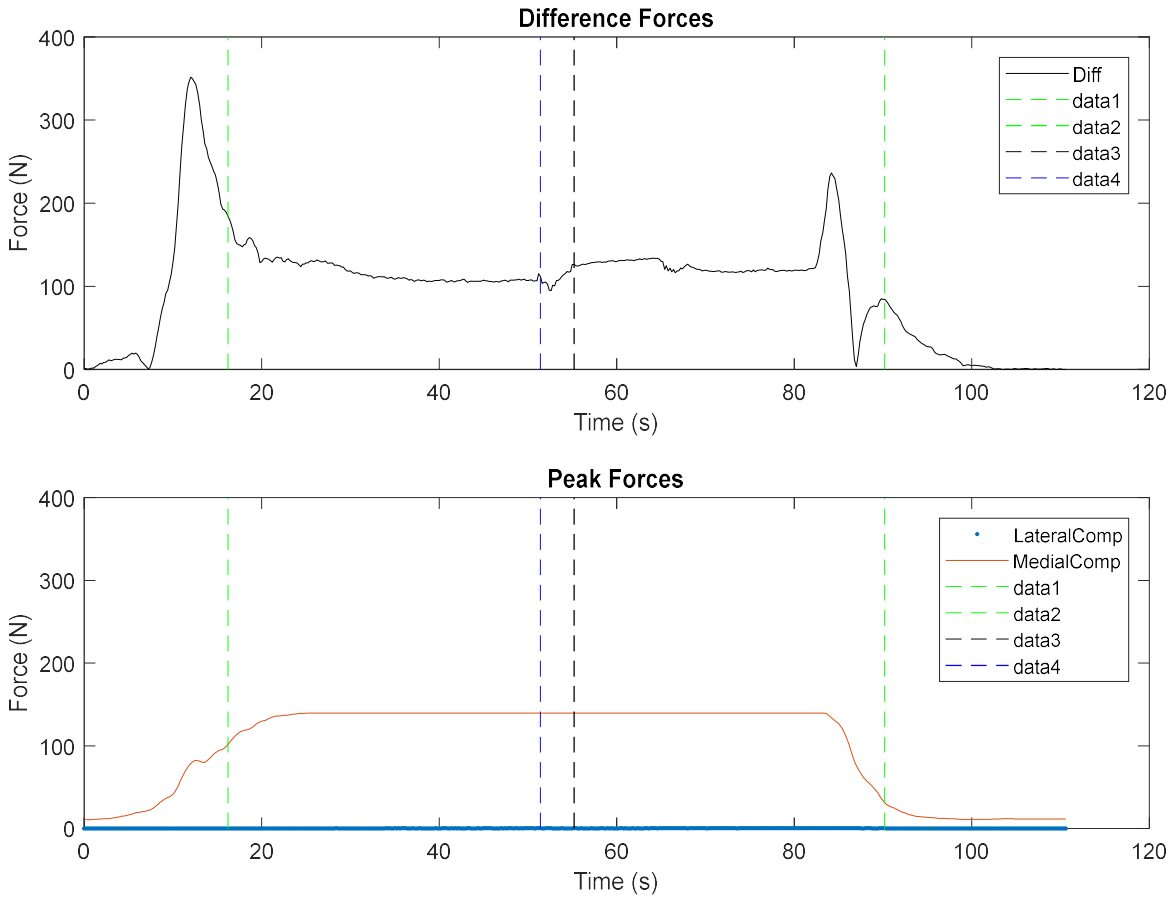

Figure 27. Top graph displays the waveform for the difference between the Load obtained by the Tekscan and the UOKS loads for trial 5. Bottom plot shows Medial compartment peak forces. These peak forces are reported for the sensel with the highest peak pressures for any frame.

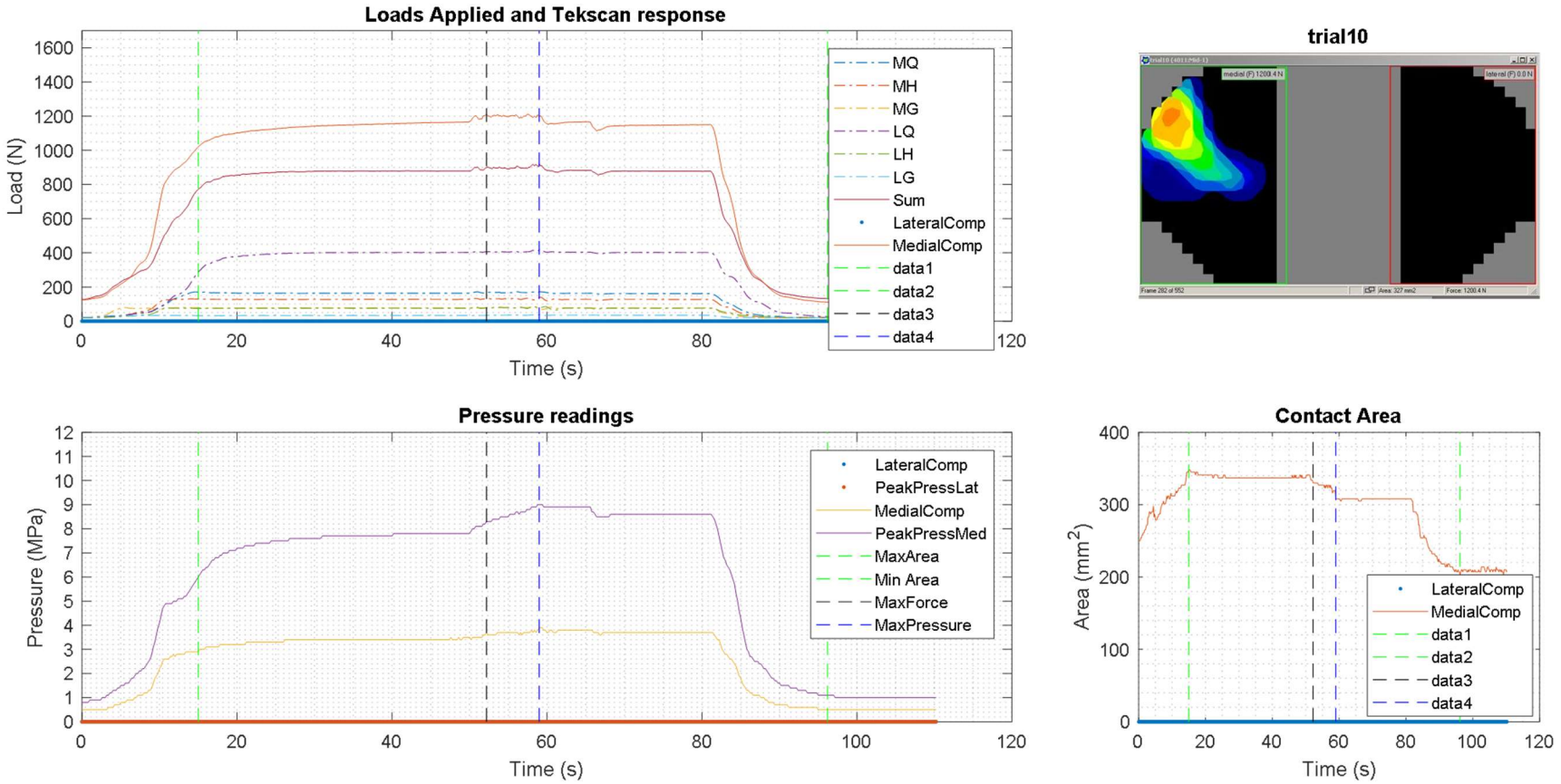

Figure 28. Data obtained with Tekscan for trial 10. Top left plot show the sum of all applied load(red) and the load measurements obtained with Tekscan. Due to biased alignment the medial compartment of the knee was the only sections exited during the trial, as seen in the Top right. The bottom left displays the waveforms for pressure and peak pressures in the knee. Bottom right shows medial compartment contact area distribution during the trial

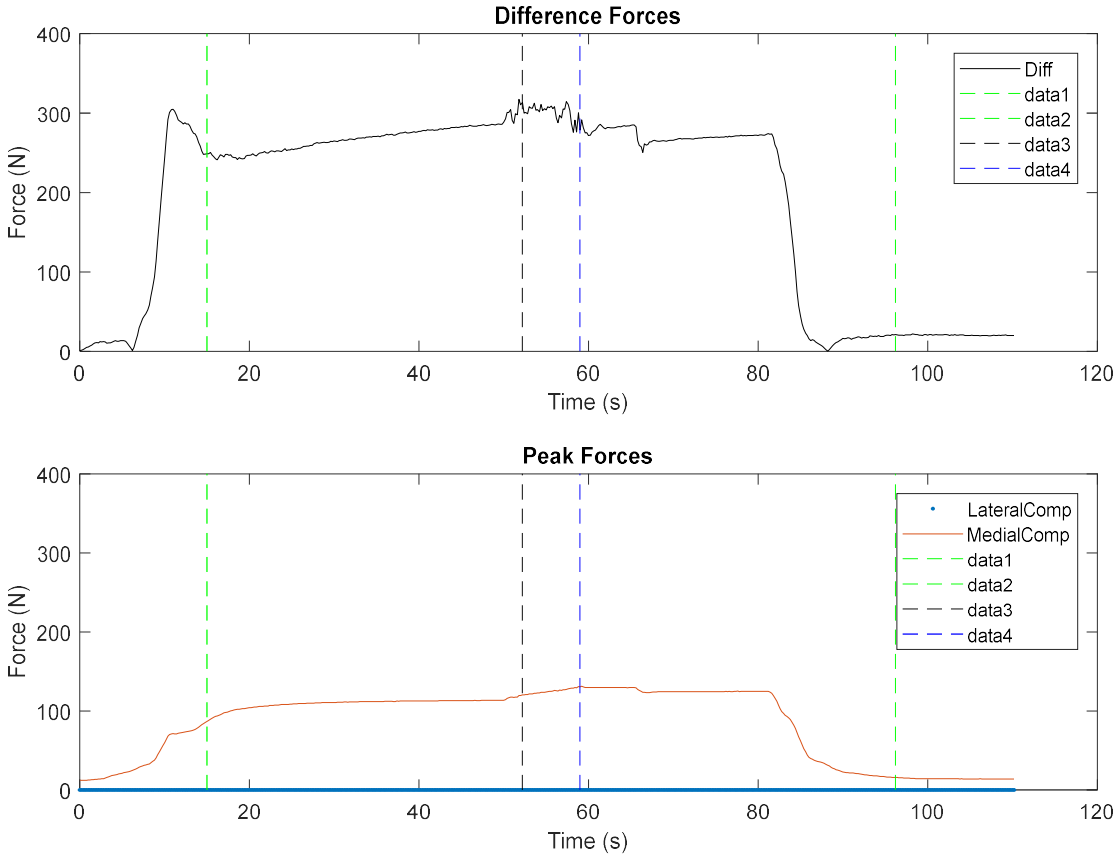

Figure 29. Top graph displays the waveform for the difference between the Load obtained by the Tekscan and the UOKS loads for trial 10. Bottom plot shows Medial compartment peak forces. These peak forces are reported for the sensel with the highest peak pressures for any frame

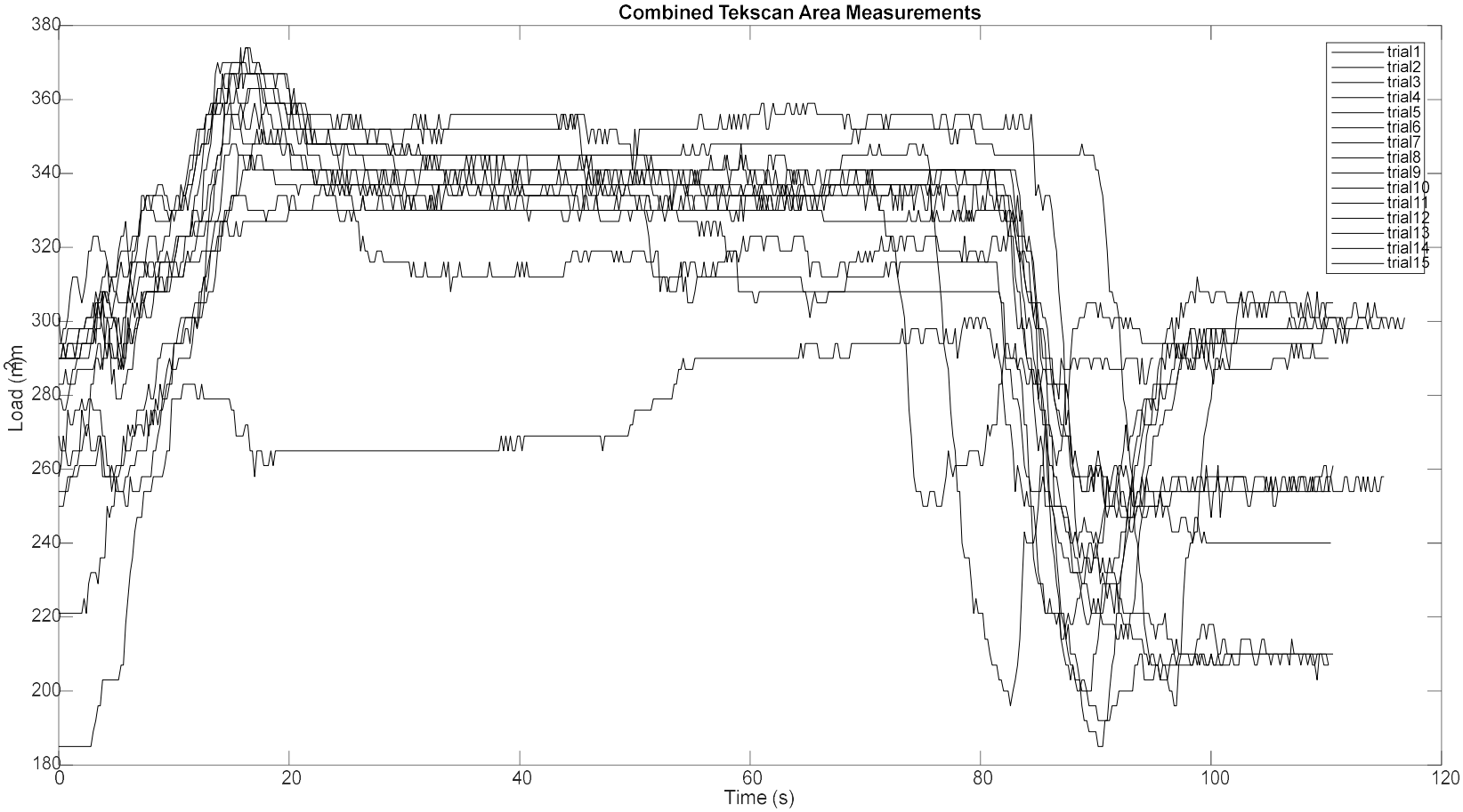

Figure 30. Contact area measurements for al 15 trials.

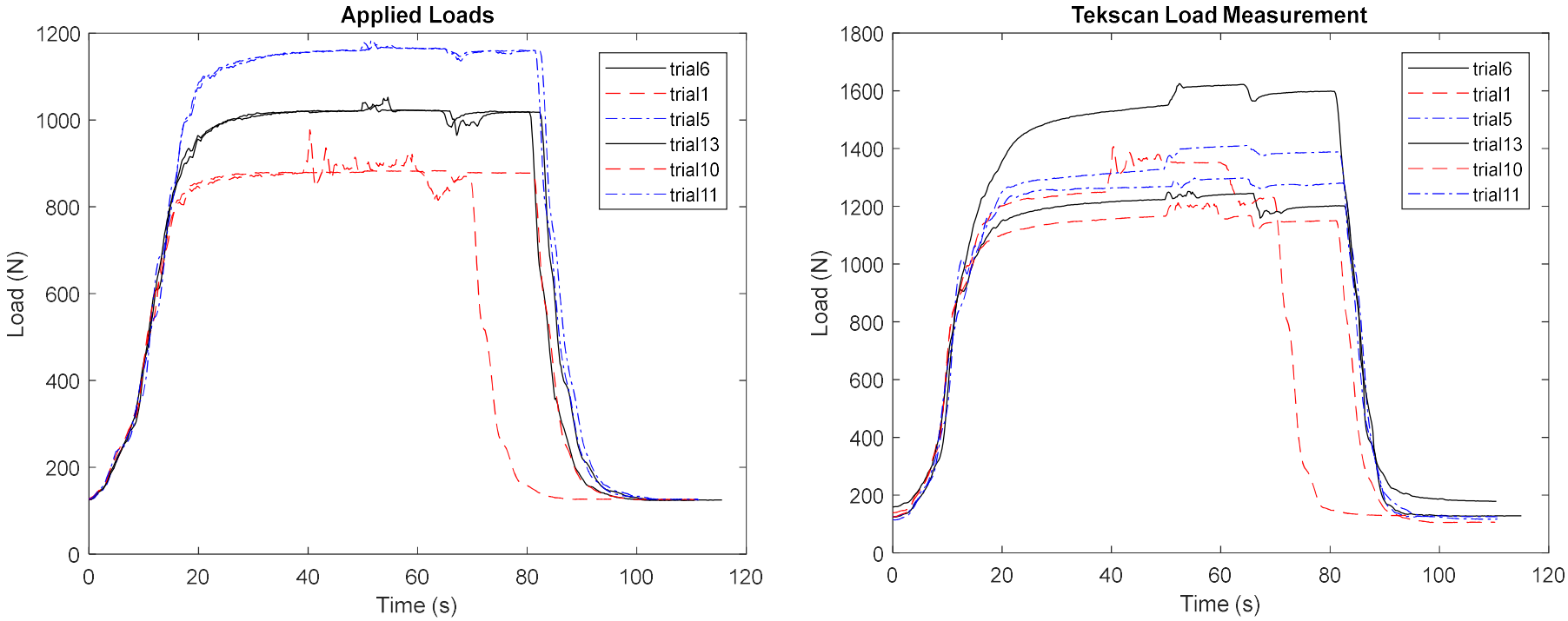

Figure 31. Plot shows the measurement of trials that modulated quadriceps loads. Left plot shows UOKS load measurements, while right shows the loads obtained with Tekscan.

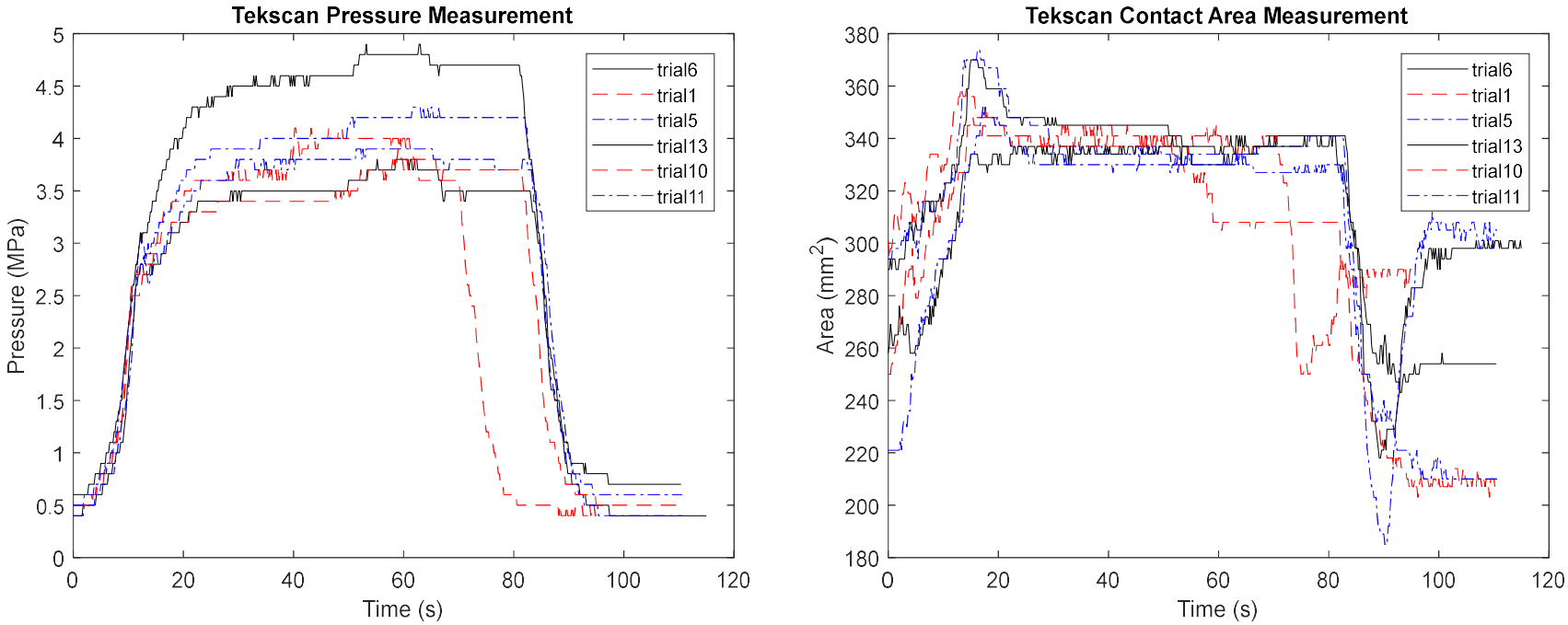

Figure 32. Plot data shows the measurement of trials that modulated quadriceps loads and the resultant effects to pressure and contact area. Left plot shows the pressure, while right shows the change of Contact area over time.

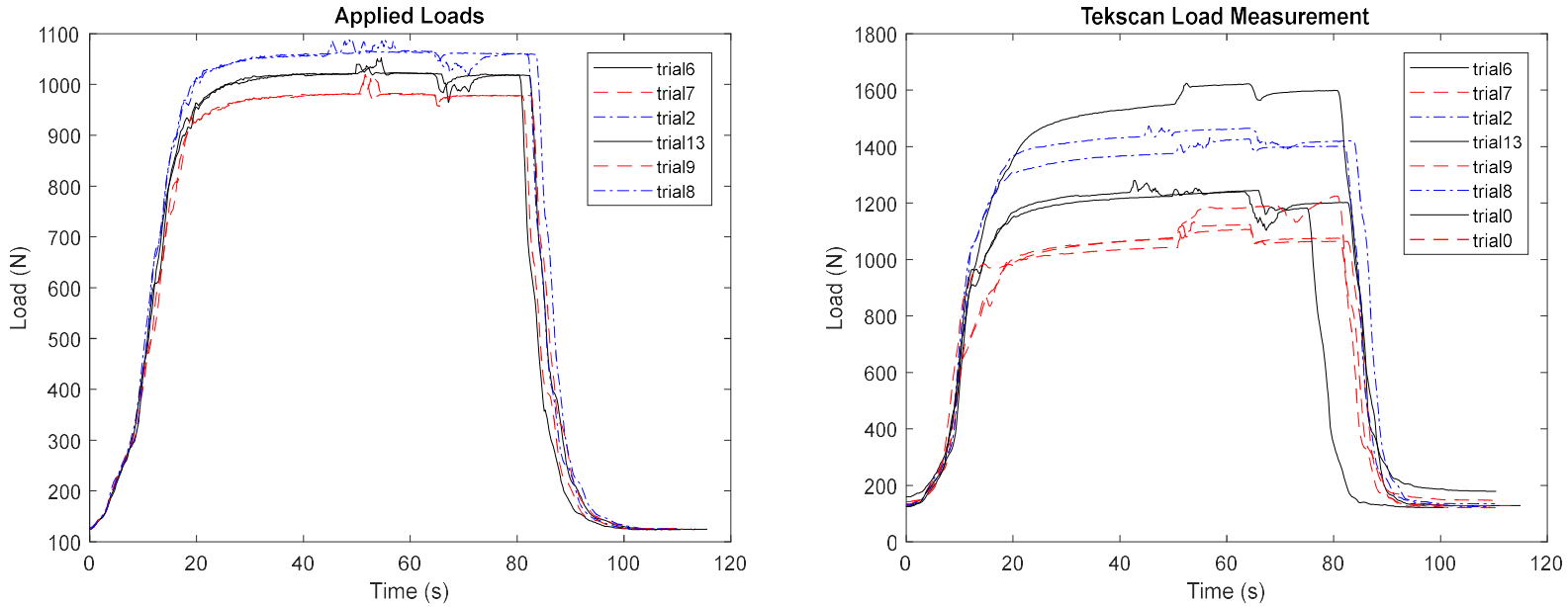

Figure 33. Plot shows the measurement of trials that modulated hamstrings loads. Left plot shows UOKS load measurements, while right shows the loads obtained with Tekscan.

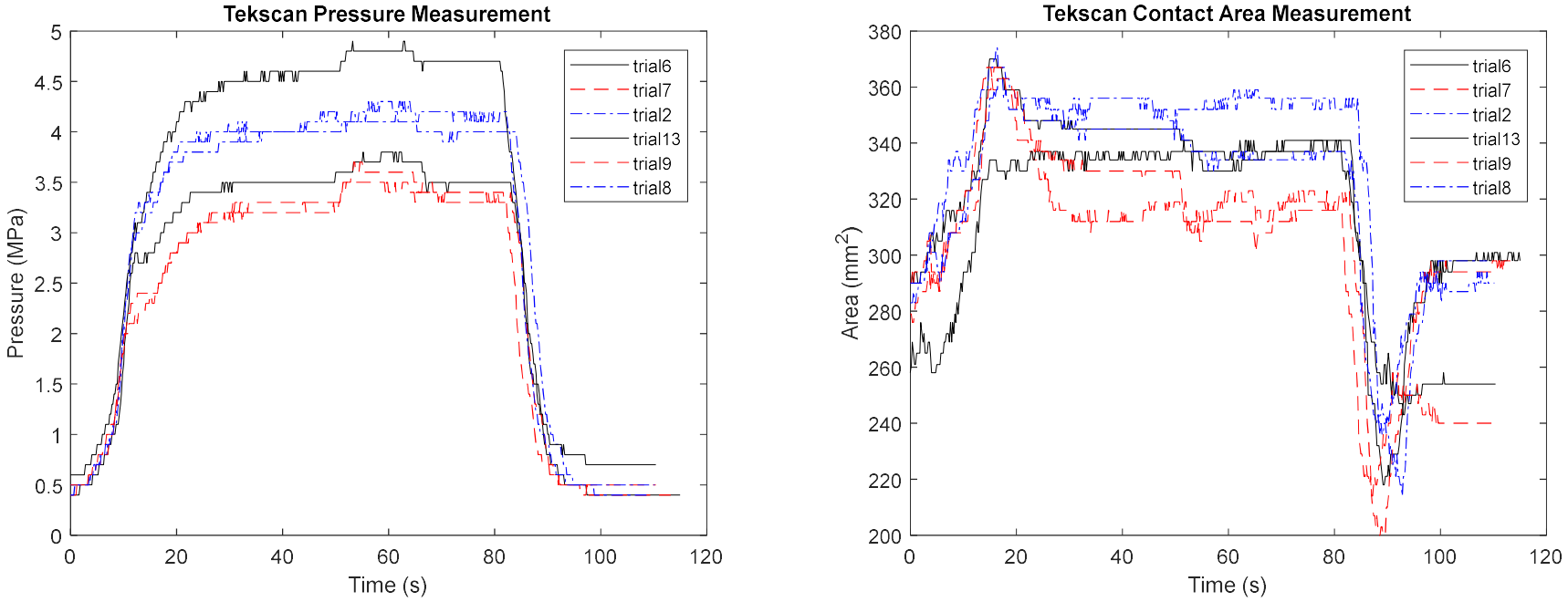

Figure 34. Plot shows the measurement of trials that modulated hamstrings loads and the resultant effects to pressure and contact area. Left plot shows the pressure, while right shows the change of Contact area over time.

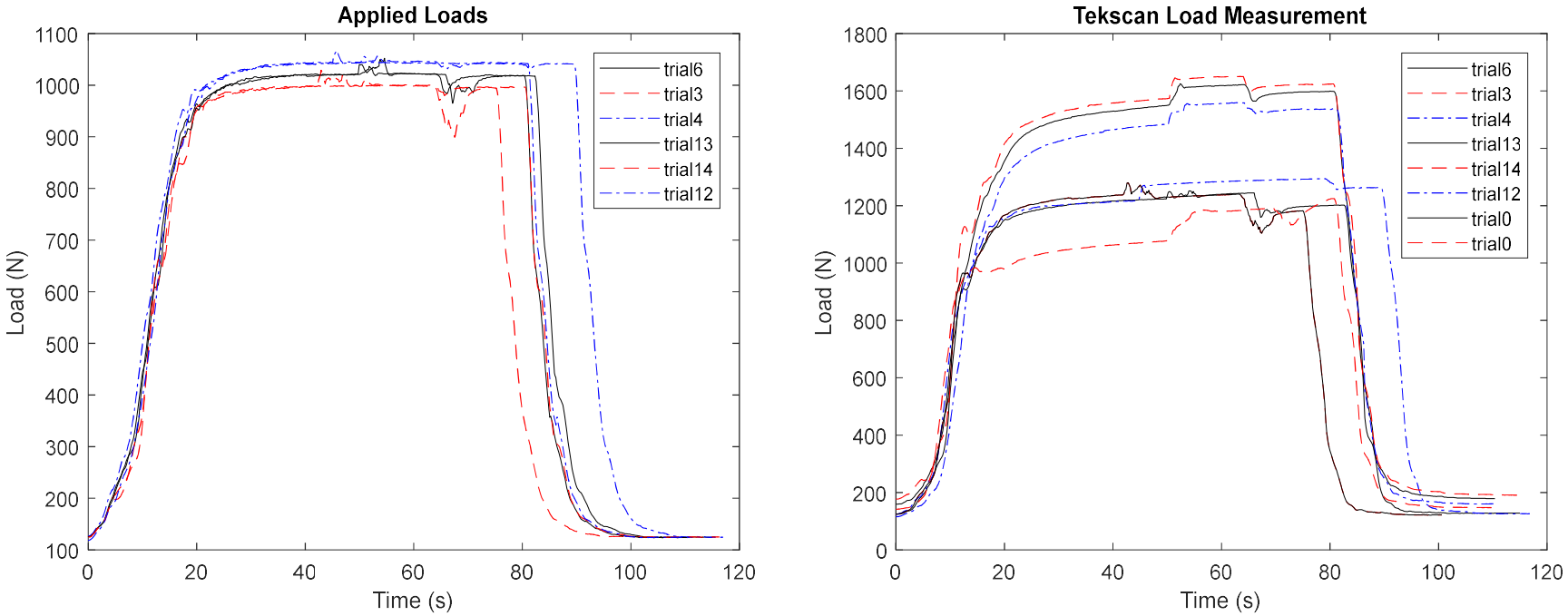

Figure 35. Plot shows the measurement of trials that modulated gastrocnemii loads. Left plot shows UOKS load measurements, while right shows the loads obtained with Tekscan.

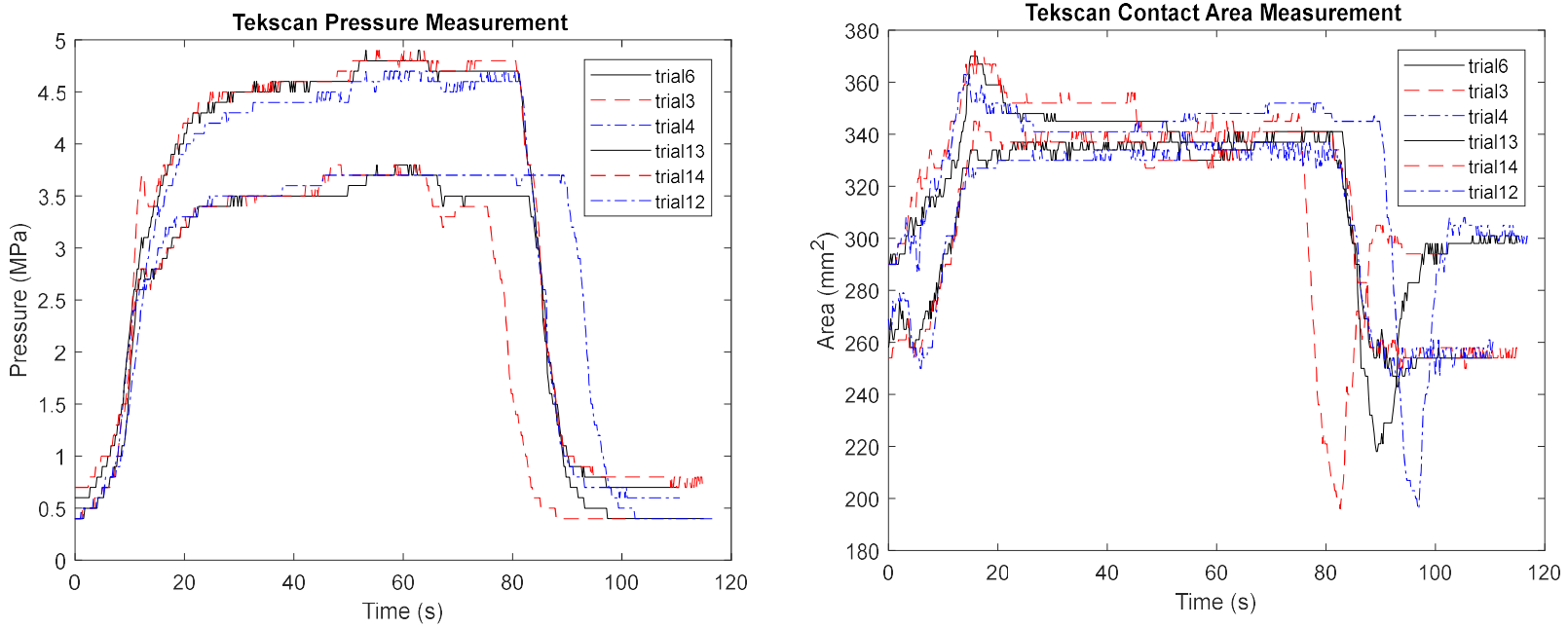

Figure 36. Plot shows the measurement of trials that modulated gastrocnemii loads and the resultant effects to pressure and contact area. Left plot shows the pressure, while right shows the change of Contact area over time.

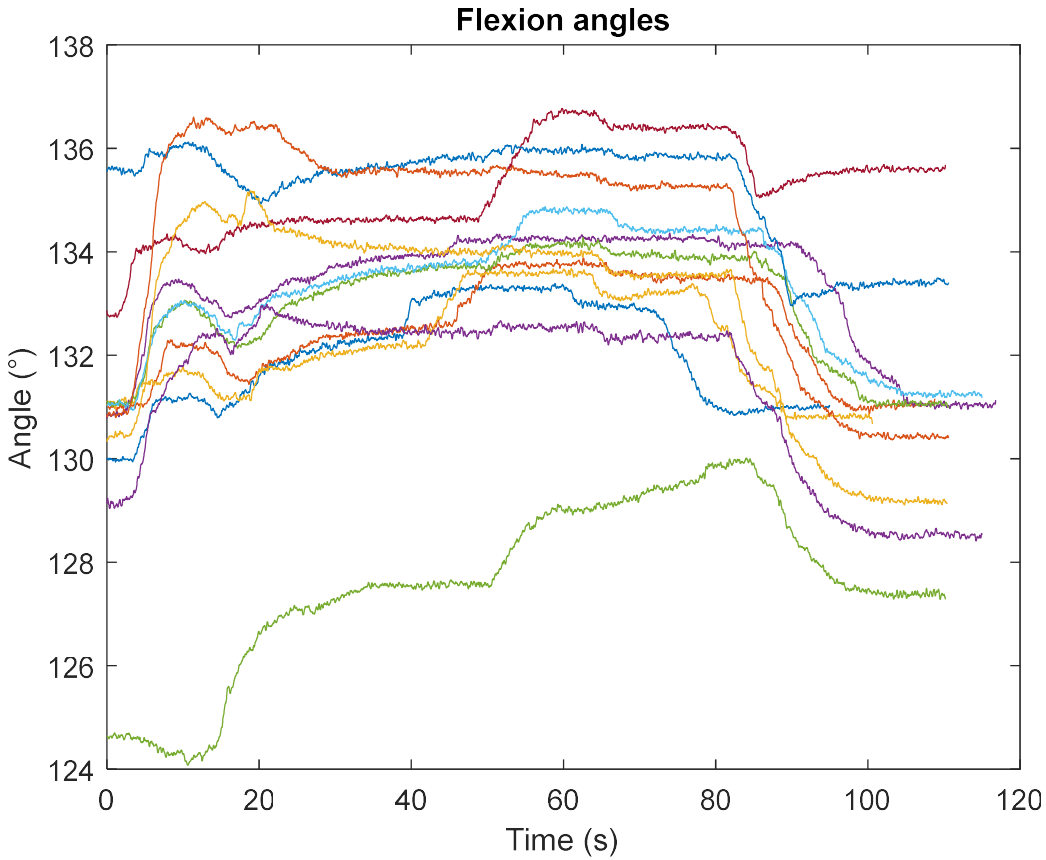

Figure 37. Curves for flexion/extension angles in response to the loads applied by the simulator. Three trials were excluded due to insufficient data. Excluded trials were trials 7,8,9.

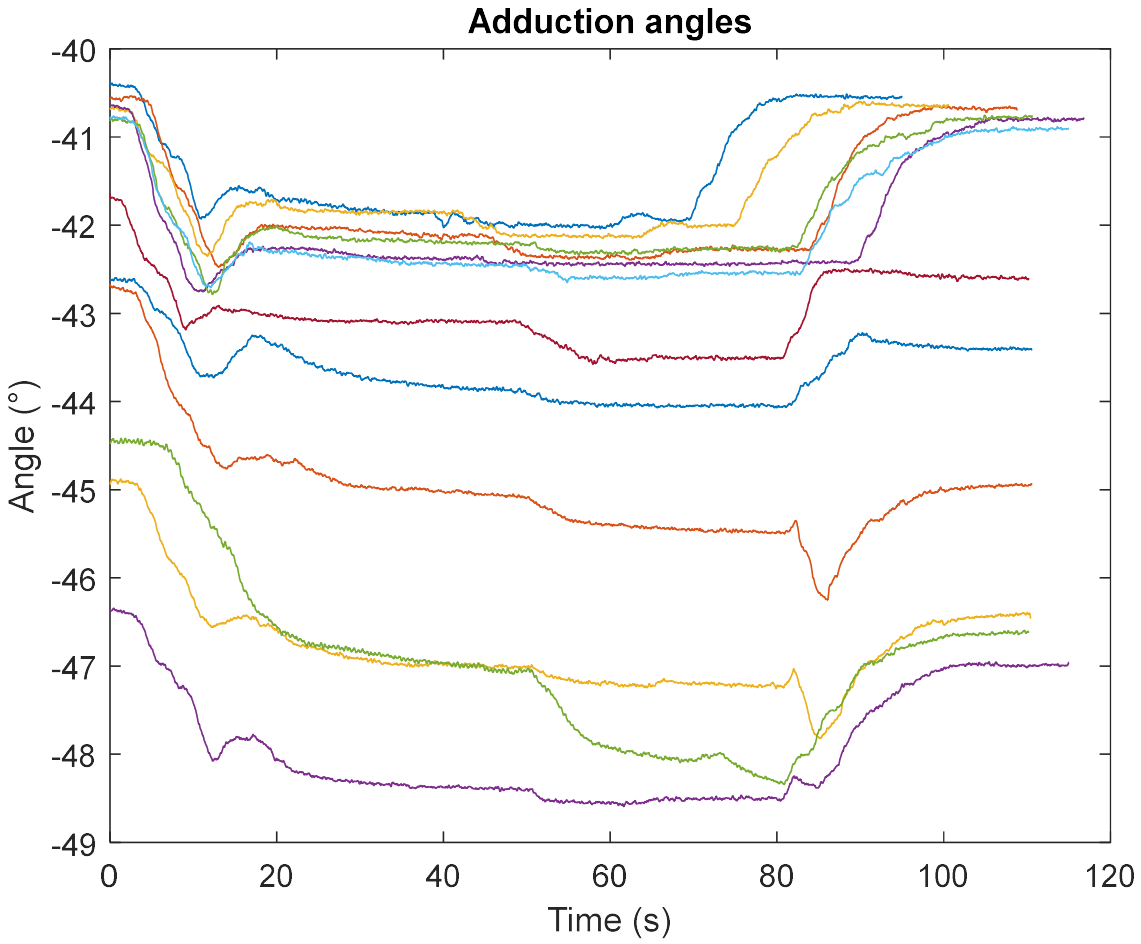

Figure 38. Adduction angles calculated for all trials (with the exception of trials 7,8,9).

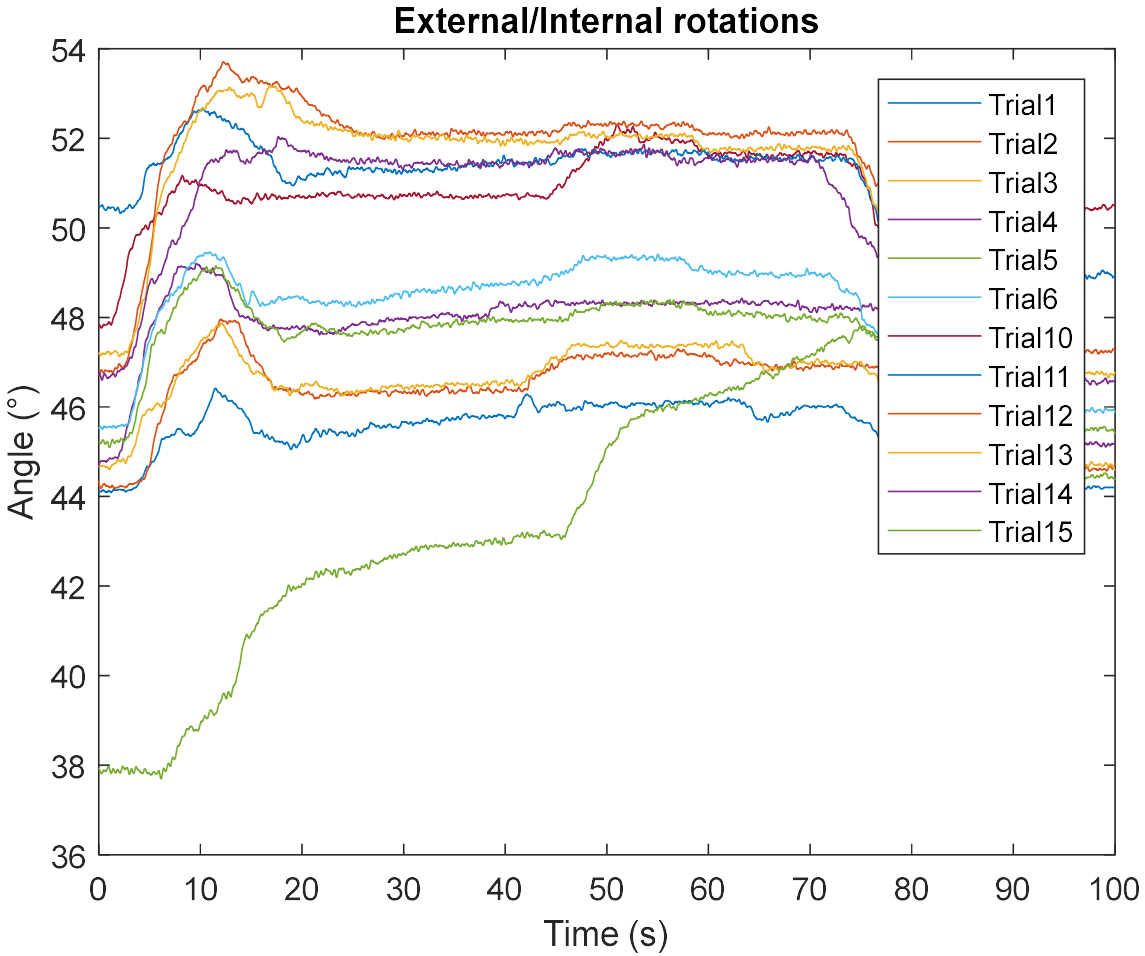

Figure 39. Change sin external/internal rotations. Positive changes refer to external rotations, while negative changes represent internal rotations.

Table 1. Measurements obtained from the Tekscan sensor at the 30th second. The measurements are paired with the sum of loads applied by the simulator.

	UOKS	Tekscan			
	Load (N)	Load (N)	Pressure (MPa)	Peak Pressure (MPa)	Contact Area (mm^2)
Trial 1	869.27	1235.3	3.7	8.9	337
Trial 2	1050.47	1411.1	4.1	9.6	348
Trial 3	991.04	1221.9	3.5	9.3	352
Trial 4	1030.78	1201.1	3.5	9.5	341
Trial 5	1136.61	1255.5	3.8	9.6	334
Trial 6	1007.68	1198.1	3.4	9	348
Trial 7	969.98	1019.6	3.2	8.7	316
Trial 8	1051.65	1346.7	3.9	9.2	345
Trial 9	969.77	1048.3	3.1	8.5	334
Trial 10	877.84	1141.6	3.4	7.6	337
Trial 11	1143.82	1296.3	3.9	9.5	330
Trial 12	1031.13	1424	4.3	8.7	330
Trial 13	1013.15	1496.1	4.5	8.6	330
Trial 14	992.43	1526.2	4.5	8.8	337
Trial 15	871.29	1041.7	3.9	8.5	265

Table 2. Maximum changes experienced by the joint. the table includes the results for all trials.

	Maximum change in Degrees (°)		
	Flexion/Extension	Adduction	External/internal
Trial 1	3.396	1.66	2.60
Trial 2	2.97	1.94	3.80
Trial 3	2.96	1.75	3.42
Trial 4	3.54	2.12	4.56
Trial 5	3.24	2.03	4.11
Trial 6	3.88	1.94	3.98
Trial 7	----	----	----
Trial 8	----	----	----
Trial 9	----	----	----
Trial 10	3.98	1.94	4.58
Trial 11	3.12	1.47	4.33
Trial 12	6.15	3.58	7.01
Trial 13	5.96	2.94	6.57
Trial 14	4.50	2.25	5.58
Trial 15	5.83	3.92	10.17

Table 3. Slopes calculated for all trials from the start to the 30th second.

	UOKS	Tekscan		
	Load(N/s)	Load (N/s)	Pressure (MPa/s)	Contact Area (mm^2/s)
Trial 1	25.70	34.64	34.64	1.35
Trial 2	30.75	40.36	40.36	2.34
Trial 3	27.46	34.67	34.67	1.98
Trial 4	30.69	33.97	33.97	1.60
Trial 5	34.35	35.59	35.59	1.26
Trial 6	29.70	33.91	33.91	1.70
Trial 7	28.08	28.12	28.12	0.80
Trial 8	30.96	38.45	38.45	1.59
Trial 9	28.35	28.81	28.82	1.61
Trial 10	25.54	32.06	32.06	2.74
Trial 11	32.95	37.26	37.26	3.42
Trial 12	31.78	41.44	41.44	1.91
Trial 13	29.91	42.32	42.32	2.44
Trial 14	28.77	42.64	42.64	2.61
Trial 15	24.93	28.43	28.43	2.55
Average	29.33	35.51	35.51	1.99
Standard Deviation	2.37	4.89	4.89	0.68

Appendix G: Matlab scripts

```
Statistics Script for Load cell analysis
%%specify csv reading dimensions, I.E. which columns to extract from the
%%csv file
dataSet = csvread('AllCombined.csv',1,0,[1 0 50 11]);
[dataRow, dataColumn] = size(dataSet);

for i = 1:dataColumn/2
    expID = strcat('LC',num2str(i)); %%Change the first argument of strcat and the
name of the variables
    for j = 1:dataRow
        Experiment.(eval('expID')).MasterLoadcell(j,1) = dataSet(j,i);
        Experiment.(eval('expID')).Loadcell(j,1) = dataSet(j,i+6);
        Experiment.(eval('expID')).Mean(j,1) = (dataSet(j,i+6)+dataSet(j,i))/2;
        Experiment.(eval('expID')).Difference(j,1) =  dataSet(j,i) - dataSet(j,i+6);
        Experiment.(eval('expID')).DifferencePercentage(j,1) = 100*(dataSet(j,i) -
dataSet(j,i+6))/ Experiment.(eval('expID')).Mean(j,1);
        Analysis.(eval('expID')).Loadcell(j,1) =
Experiment.(eval('expID')).Loadcell(j,1);
        Analysis.(eval('expID')).Difference(j,1) =
Experiment.(eval('expID')).Loadcell(j,1) - targetLoad(j,1);
        Analysis.(eval('expID')).DifferencePercentage(j,1) =
Analysis.(eval('expID')).Difference(j,1)/targetLoad(j,1);
    end
    Experiment.(eval('expID')).meanDiff = mean(Experiment.(eval('expID')).Difference);
    Experiment.(eval('expID')).STD = std(Experiment.(eval('expID')).Difference);
    Experiment.(eval('expID')).UpperLimit =Experiment.(eval('expID')).meanDiff +
(Experiment.(eval('expID')).STD * 1.96);
    Experiment.(eval('expID')).LowerLimit =Experiment.(eval('expID')).meanDiff -
(Experiment.(eval('expID')).STD * 1.96);


    Analysis.(eval('expID')).meanDiff = mean(Analysis.(eval('expID')).Difference);
    Analysis.LC_mean(i,1) = mean(Analysis.(eval('expID')).Difference);
    Analysis.(eval('expID')).STD = std(Analysis.(eval('expID')).Difference);
    Analysis.LC_STD(i,1) = std(Analysis.(eval('expID')).Difference);
    Analysis.(eval('expID')).UpperLimit =Analysis.(eval('expID')).meanDiff +
(Analysis.(eval('expID')).STD * 1.96);
    Analysis.(eval('expID')).LowerLimit =Analysis.(eval('expID')).meanDiff -
(Analysis.(eval('expID')).STD * 1.96);


    Experiment.(eval('expID')).meanDiffPercentage =
mean(Experiment.(eval('expID')).DifferencePercentage);
    Experiment.(eval('expID')).STDPercentage =
std(Experiment.(eval('expID')).DifferencePercentage);
    Experiment.(eval('expID')).UpperLimitPercentage
=Experiment.(eval('expID')).meanDiffPercentage +
(Experiment.(eval('expID')).STDPercentage * 1.96);
    Experiment.(eval('expID')).LowerLimitPercentage
=Experiment.(eval('expID')).meanDiffPercentage -
(Experiment.(eval('expID')).STDPercentage * 1.96);


    Experiment.(eval('expID')).RegressionCoefficients =
polyfit(Experiment.(eval('expID')).Loadcell,Experiment.(eval('expID')).MasterLoadcell,
1);
    Experiment.(eval('expID')).Regression =
polyval(Experiment.(eval('expID')).RegressionCoefficients,Experiment.(eval('expID')).L
oadcell);
```

```
    Analysis.(eval('expID')).meanDiffPercentage =
mean(Analysis.(eval('expID')).DifferencePercentage);
    Analysis.(eval('expID')).STDPercentage =
std(Analysis.(eval('expID')).DifferencePercentage);
    Analysis.(eval('expID')).UpperLimitPercentage
=Analysis.(eval('expID')).meanDiffPercentage + (Analysis.(eval('expID')).STDPercentage
* 1.96);
    Analysis.(eval('expID')).LowerLimitPercentage
=Analysis.(eval('expID')).meanDiffPercentage - (Analysis.(eval('expID')).STDPercentage
* 1.96);

    switch i
        case 1
            muscle = 'Medial Quadriceps';
            motor =  'Motor MQ';
        case 2
            muscle = 'Medial Hamstring';
            motor = 'Motor MH';
        case 3
            muscle = 'Medial Gastrocnemius';
            motor = 'Motor MG';
        case 4
            muscle = 'Lateral Quadriceps';
            motor = 'Motor LQ';
        case 5
            muscle = 'Lateral Hamstring';
            motor = 'Motor LH';
        case 6
            muscle = 'Lateral Gastrocnemius';
            motor = 'Motor LG';
            Analysis.OverallmeanDiff =  mean(Analysis.LC_mean);
            Analysis.OverallmeanSTD =  mean(Analysis.LC_STD);
     end

     %ICC calculation loop //this function was download from the Matlab exchange forum
https://www.mathworks.com/matlabcentral/fileexchange/22099-intraclass-correlation-
coefficient-icc
    for loop=1:1
        M =
[Experiment.(eval('expID')).MasterLoadcell,Experiment.(eval('expID')).Loadcell];
        type1 = '3-1';
        typek = '3-k';
        alpha = .05;
        r0 = 0;

        %single measurements
        [ICCoeff.Single.r, ICCoeff.Single.LB, ICCoeff.Single.UB, ICCoeff.Single.F,
ICCoeff.Single.df1, ICCoeff.Single.df2, ICCoeff.Single.p] = ICC(M, type1, alpha, r0);
        %Multiple measurements
        [ICCoeff.Multiple.r, ICCoeff.Multiple.LB, ICCoeff.Multiple.UB,
ICCoeff.Multiple.F, ICCoeff.Multiple.df1, ICCoeff.Multiple.df2, ICCoeff.Multiple.p] =
ICC(M, typek, alpha, r0);

        Experiment.(eval('expID')).ICC = ICCoeff;
        clear vars M ICCoeff
    end

    for loop=1:1
        M =  [targetLoad,Analysis.(eval('expID')).Loadcell];
        type1 = '3-1';
```

```
        typek = '3-k';
        alpha = .05;
        r0 = 0;

        %single measurements
        [ICCoeff.Single.r, ICCoeff.Single.LB, ICCoeff.Single.UB, ICCoeff.Single.F,
ICCoeff.Single.df1, ICCoeff.Single.df2, ICCoeff.Single.p] = ICC(M, type1, alpha, r0);
        %Multiple measurements
        [ICCoeff.Multiple.r, ICCoeff.Multiple.LB, ICCoeff.Multiple.UB,
ICCoeff.Multiple.F, ICCoeff.Multiple.df1, ICCoeff.Multiple.df2, ICCoeff.Multiple.p] =
ICC(M, typek, alpha, r0);

        Analysis.(eval('expID')).ICC = ICCoeff;
        clear vars M ICCoeff
    end
    %%
    %This loop draws the Agreement graphical representations and displays
    %ICC coefficients for each load cell
    for loop=1:1

        Experiment.(eval('expID')).Figure.WindowSize = [50 50 1200 600];
        Experiment.(eval('expID')).Figure.Window =
figure('Name',muscle,'NumberTitle','off');
        Experiment.(eval('expID')).Figure.Window.Position =
Experiment.(eval('expID')).Figure.WindowSize;
        Experiment.(eval('expID')).Figure.Window.Color = 'w';
        Experiment.(eval('expID')).Figure.sp1 = subplot(2,2,1);

scatter(Experiment.(eval('expID')).Loadcell,Experiment.(eval('expID')).MasterLoadcell,
'black');
        l1 = line([0,1050],[0,1050],'Color','red','LineStyle','-');
        l2 =
line(Experiment.(eval('expID')).Loadcell,Experiment.(eval('expID')).Regression,'Color'
,'blue','LineStyle','-.');
        title('Correlation')
        xlabel('Load cell Measurement (N)')
        ylabel('Master Load cell Measurement (N)')
        l=legend([l1 l2],{'Target load', 'Regression'},'Position',[0.3614 0.6153
0.0933 0.0608]);
        if eq(1,sign(Experiment.(eval('expID')).RegressionCoefficients(2)))
            signCoeff = '+';
        elseif  eq(-1,sign(Experiment.(eval('expID')).RegressionCoefficients(2)))
            signCoeff = '-';
        else
            signCoeff = '+';
        end
        txt = strcat('Y = ',{'
'},num2str(Experiment.(eval('expID')).RegressionCoefficients(1)),'X',{'
'},signCoeff,{'
'},num2str(abs(Experiment.(eval('expID')).RegressionCoefficients(2))));
        text(200,800,txt)

        Experiment.(eval('expID')).Figure.sp2 = subplot(2,2,2);

scatter(Experiment.(eval('expID')).Mean,Experiment.(eval('expID')).Difference,'black')
;
        y = Experiment.(eval('expID')).UpperLimit;
        line([0,1200],[y,y],'Color','red','LineStyle','--')
        y = Experiment.(eval('expID')).LowerLimit;
        line([0,1200],[y,y],'Color','red','LineStyle','--')
        y = Experiment.(eval('expID')).meanDiff;
        line([0,1200],[y,y],'Color','blue','LineStyle','-')
```

```
        title('B&A Agreement')
        xlabel('Mean (N)')
        ylabel('Difference (N)')

        Experiment.(eval('expID')).Figure.sp3 = subplot(2,2,3);

scatter(Experiment.(eval('expID')).Mean,Experiment.(eval('expID')).DifferencePercentag
e,'black');
        y = Experiment.(eval('expID')).UpperLimitPercentage;
        line([0,1200],[y,y],'Color','red','LineStyle','--')
        y = Experiment.(eval('expID')).LowerLimitPercentage;
        line([0,1200],[y,y],'Color','red','LineStyle','--')
        y = Experiment.(eval('expID')).meanDiffPercentage;
        line([0,1200],[y,y],'Color','blue','LineStyle','-')
        title('B&A Percentage Agreement')
        xlabel('Mean (N)')
        ylabel('Difference (%)')

        Experiment.(eval('expID')).Figure.sp4 = subplot(2,2,4);
        Experiment.(eval('expID')).Figure.sp4.Visible = 'off';

        Experiment.(eval('expID')).Figure.t =
uitable(Experiment.(eval('expID')).Figure.Window);
        Experiment.(eval('expID')).ICC.dat =  {
Experiment.(eval('expID')).ICC.Single.r,Experiment.(eval('expID')).ICC.Multiple.LB
;...

Experiment.(eval('expID')).ICC.Single.LB,Experiment.(eval('expID')).ICC.Multiple.LB
;...

Experiment.(eval('expID')).ICC.Single.UB,Experiment.(eval('expID')).ICC.Multiple.UB;..
.
                Experiment.(eval('expID')).ICC.Single.F,
Experiment.(eval('expID')).ICC.Multiple.F;...
                Experiment.(eval('expID')).ICC.Single.df1,
Experiment.(eval('expID')).ICC.Multiple.df1;...
                Experiment.(eval('expID')).ICC.Single.df2,
Experiment.(eval('expID')).ICC.Multiple.df2;...

Experiment.(eval('expID')).ICC.Single.p,Experiment.(eval('expID')).ICC.Multiple.p;
            };
         Experiment.(eval('expID')).dat = { 'Mean
difference',Experiment.(eval('expID')).meanDiff;'Standard
Deviation',Experiment.(eval('expID')).STD;...
              'Upper Limit',Experiment.(eval('expID')).UpperLimit;'Lower Limit',
Experiment.(eval('expID')).LowerLimit;'Mean Difference
(%)',Experiment.(eval('expID')).meanDiffPercentage;...
               'Standard Deviation
(%)',Experiment.(eval('expID')).STDPercentage;'Upper Limit
(%)',Experiment.(eval('expID')).UpperLimitPercentage;'Lower Limit
(%)',Experiment.(eval('expID')).LowerLimitPercentage;...
            };

        Experiment.(eval('expID')).Figure.t.ColumnEditable = logical([1,1]);
        Experiment.(eval('expID')).Figure.t.ColumnName = {'Single Measurements',
'Multiple Measurements'};
        Experiment.(eval('expID')).Figure.t.RowName = {'ICC', 'Lower
Bound','UpperBound ','F', 'DoF1', 'DoF2','p-Value'};
        Experiment.(eval('expID')).Figure.t.Data = Experiment.(eval('expID')).ICC.dat;
        Experiment.(eval('expID')).Figure.t.Units = 'normalized';
        pos1 = Experiment.(eval('expID')).Figure.sp4.Position;
        pos2 = [0,0,.3075,.248];
```

```
        pos2(1) = pos1(1)+(pos1(3)/2)-(pos2(3)/2);
        pos2(2) = pos1(2)+(pos1(4)/2)-(pos2(4)/2);
        Experiment.(eval('expID')).Figure.t.Position = pos2;
%         xlsPasteTo('Experiment',(eval('expID')),1200, 1500,'f10')

    end
    % Analysis of Repeatability and Typical error
    for loop=1:1
        Analysis.(eval('expID')).Figure.WindowSize = [50 50 1200 600];
        Analysis.(eval('expID')).Figure.Window =
figure('Name',motor,'NumberTitle','off');
        Analysis.(eval('expID')).Figure.Window.Position =
Analysis.(eval('expID')).Figure.WindowSize;
        Analysis.(eval('expID')).Figure.Window.Color = 'w';
        Analysis.(eval('expID')).Figure.sp1 = subplot(2,2,1);
        scatter(targetLoad,Analysis.(eval('expID')).Loadcell,'black');
        line([0,1050],[0,1050],'Color','red','LineStyle','--');
        title('Correlation')
        xlabel('Target Load (N)')
        ylabel('Load cell Measurement (N)')

        Analysis.(eval('expID')).Figure.sp2 = subplot(2,2,2);
        scatter(targetLoad,Analysis.(eval('expID')).Difference,'black');
        y = Analysis.(eval('expID')).UpperLimit;
        line([0,1200],[y,y],'Color','red','LineStyle','--');
        y = Analysis.(eval('expID')).LowerLimit;
        line([0,1200],[y,y],'Color','red','LineStyle','--');
        y = Analysis.(eval('expID')).meanDiff;
        line([0,1200],[y,y],'Color','blue','LineStyle','-');
        title('B&A Agreement')
        xlabel('Target Load (N)')
        ylabel('Difference (N)')

        Analysis.(eval('expID')).Figure.sp3 = subplot(2,2,3);
        s=scatter(targetLoad,Analysis.(eval('expID')).DifferencePercentage,'black');
        y = Analysis.(eval('expID')).UpperLimitPercentage;
        line([0,1200],[y,y],'Color','red','LineStyle','--');
        y = Analysis.(eval('expID')).LowerLimitPercentage;
        line([0,1200],[y,y],'Color','red','LineStyle','--');
        y = Analysis.(eval('expID')).meanDiffPercentage;
        line([0,1200],[y,y],'Color','blue','LineStyle','-');
        title('B&A Percentage Agreement')
        xlabel('Target Load (N)')
        ylabel('Difference (%)')

        Analysis.(eval('expID')).Figure.sp4 = subplot(2,2,4);
        Analysis.(eval('expID')).Figure.sp4.Visible = 'off';

        Analysis.(eval('expID')).Figure.t =
uitable(Analysis.(eval('expID')).Figure.Window);
        Analysis.(eval('expID')).ICC.dat =  {
Analysis.(eval('expID')).ICC.Single.r,Analysis.(eval('expID')).ICC.Multiple.LB ;...

Analysis.(eval('expID')).ICC.Single.LB,Analysis.(eval('expID')).ICC.Multiple.LB ;...

Analysis.(eval('expID')).ICC.Single.UB,Analysis.(eval('expID')).ICC.Multiple.UB;...
            Analysis.(eval('expID')).ICC.Single.F,
Analysis.(eval('expID')).ICC.Multiple.F;...
             Analysis.(eval('expID')).ICC.Single.df1,
Analysis.(eval('expID')).ICC.Multiple.df1;...
```

```
            Analysis.(eval('expID')).ICC.Single.df2,
Analysis.(eval('expID')).ICC.Multiple.df2;...

Analysis.(eval('expID')).ICC.Single.p,Analysis.(eval('expID')).ICC.Multiple.p;
            };
        Analysis.(eval('expID')).dat = { 'Mean difference',
Analysis.(eval('expID')).meanDiff;'Standard
Deviation',Analysis.(eval('expID')).STD;...
              'Upper Limit',Analysis.(eval('expID')).UpperLimit; 'Lower
Limit',Analysis.(eval('expID')).LowerLimit;'Mean Difference
(%)',Analysis.(eval('expID')).meanDiffPercentage;...
              'Standard Deviation (%)',Analysis.(eval('expID')).STDPercentage;'Upper
Limit (%)',Analysis.(eval('expID')).UpperLimitPercentage;'Lower Limit
(%)',Analysis.(eval('expID')).LowerLimitPercentage;...
            };



        Analysis.(eval('expID')).Figure.t.ColumnEditable = logical([1,1]);
        Analysis.(eval('expID')).Figure.t.ColumnName = {'Single Measurements',
'Multiple Measurements'};
        Analysis.(eval('expID')).Figure.t.RowName = {'ICC', 'Lower Bound','UpperBound
','F', 'DoF1', 'DoF2','p-Value'};
        Analysis.(eval('expID')).Figure.t.Data = Analysis.(eval('expID')).ICC.dat ;
        Analysis.(eval('expID')).Figure.t.Units = 'normalized';
        pos1 = Analysis.(eval('expID')).Figure.sp4.Position;
        pos2 = [0,0,.3075,.248];
        pos2(1) = pos1(1)+(pos1(3)/2)-(pos2(3)/2);
        pos2(2) = pos1(2)+(pos1(4)/2)-(pos2(4)/2);
        Analysis.(eval('expID')).Figure.t.Position = pos2;

    end


end

clearvars -except Experiment Analysis targetLoad

for i = 1:6
       expID = strcat('LC',num2str(i)); %%Change the first argument of strcat and the
name of the variables
 switch i
        case 1
            muscle = 'Medial Quadriceps';
            motor =  'Motor MQ';
        case 2
            muscle = 'Medial Hamstring';
            motor = 'Motor MH';
        case 3
            muscle = 'Medial Gastrocnemius';
            motor = 'Motor MG';
        case 4
            muscle = 'Lateral Quadriceps';
            motor = 'Motor LQ';
        case 5
            muscle = 'Lateral Hamstring';
            motor = 'Motor LH';
        case 6
            muscle = 'Lateral Gastrocnemius';
            motor = 'Motor LG';
```

```
 end

        figure('Name',num2str(i),'NumberTitle','off','Color','w');



        scatter(targetLoad,Analysis.(eval('expID')).Difference,'black','.');
        y = Analysis.(eval('expID')).UpperLimit;
        line([0,1200],[y,y],'Color','red','LineStyle','--');
        y = Analysis.(eval('expID')).LowerLimit;
        line([0,1200],[y,y],'Color','red','LineStyle','--');
        y = Analysis.(eval('expID')).meanDiff;
        line([0,1200],[y,y],'Color','blue','LineStyle','-');
        title(muscle)
        xlabel('Target Load (N)')
        ylabel('Difference (N)')

end

for i = 1:6
       expID = strcat('LC',num2str(i)); %%Change the first argument of strcat and the
name of the variables
 switch i
        case 1
            muscle = 'Medial Quadriceps';
            motor =  'Motor MQ';
        case 2
            muscle = 'Medial Hamstring';
            motor = 'Motor MH';
        case 3
            muscle = 'Medial Gastrocnemius';
            motor = 'Motor MG';
        case 4
            muscle = 'Lateral Quadriceps';
            motor = 'Motor LQ';
        case 5
            muscle = 'Lateral Hamstring';
            motor = 'Motor LH';
        case 6
            muscle = 'Lateral Gastrocnemius';
            motor = 'Motor LG';

 end


figure('Name',strcat("Experiment",num2str(i)),'NumberTitle','off','Color','w');



        scatter(targetLoad,Experiment.(eval('expID')).Difference,'black','o');
        y = Experiment.(eval('expID')).UpperLimit;
        line([0,1200],[y,y],'Color','red','LineStyle','--');
        y = Experiment.(eval('expID')).LowerLimit;
        line([0,1200],[y,y],'Color','red','LineStyle','--');
        y = Experiment.(eval('expID')).meanDiff;
        line([0,1200],[y,y],'Color','blue','LineStyle','-');
        title(muscle)
        xlabel('Target Load (N)')
        ylabel('Difference (N)')
```

```
end



for i = 1:6
    data= xlsread('Load Cell Testing_order.xlsx',i);
  for j = 11:60
     temp(j-10,2) = data(j);

  end
  loads = data(1:10)';
  temp(1:end,1) = vertcat(loads,loads,loads,loads,loads);

   testingOrder{i} = temp;
   clearvars temp data
end

loadcell = {};
for i = 1:6
nextDir = strcat(dirFile,'\','LC',num2str(i));
cd(nextDir);
[temp,~] = size(dir);
numElement = 50;
clear temp
    for j=1:numElement
        xlsxFile = strcat('experiment_',num2str(i),'_',sprintf('%03d',j),'.xlsx');
        dataFiles = xlsread(xlsxFile);
        loadcell{j,i} = dataFiles;
    end
end



error_53 = {}; value_53 = {};error_269 = {}; value_269 = {};error_299 = {}; value_299
= {};error_415 = {}; value_415 = {};...
     error_422 = {}; value_422 = {};   error_546 = {}; value_546 = {};error_737 = {};
value_737 = {};  error_921 = {}; value_921 = {}; ...
      error_938 = {}; value_938 = {}; error_1050 = {}; value_1050 = {};

  for lcCounter=1:6
   lcCounter
   tempOrder = testingOrder{lcCounter};
   counter53 = 0;counter269 = 0;counter299 = 0; counter415 = 0; counter422 = 0;
   counter546 = 0;counter737 = 0;counter921 = 0; counter938 = 0; counter1050 = 0;
   for i=1:50
    load = tempOrder(i);
 switch load

     case 53
         counter53 = counter53+1;
         order53(lcCounter,counter53) = tempOrder(i,2);
     case 269
         counter269 = counter269+1;
         order269(lcCounter,counter269) = tempOrder(i,2);
     case 299
         counter299 = counter299+1;
         order299(lcCounter,counter299) = tempOrder(i,2);
```

```
     case 415
         counter415 = counter415+1;
         order415(lcCounter,counter415) = tempOrder(i,2);
     case 422
         counter422 = counter422+1;
         order422(lcCounter,counter422) = tempOrder(i,2);
     case 546
         counter546 = counter546+1;
         order546(lcCounter,counter546) = tempOrder(i,2);
     case 737
         counter737 = counter737+1;
         order737(lcCounter,counter737) = tempOrder(i,2);
     case 921
         counter921 = counter921+1;
         order921(lcCounter,counter921) = tempOrder(i,2);
     case 938
         counter938 = counter938+1;
         order938(lcCounter,counter938) = tempOrder(i,2);
     case 1050
         counter1050 = counter1050+1;
         order1050(lcCounter,counter1050) = tempOrder(i,2);
 end
end

clearvars load i j dataFiles counter53 counter269 counter299 counter415 counter422 ...
    counter546 counter737 counter921 counter938 counter1050 tempOrder



 %-------------------------------------------------------------------------
    %plotting 53

    figure

    for counter = 1:5

        identifier = order53(lcCounter ,counter);
        tempData = loadcell{identifier,lcCounter};


        plot(tempData(:,1),tempData(:,3))
        error_53{lcCounter,counter} = abs(tempData(:,2)-tempData(:,3));
        hold on
        clearvars tempData

    end
    title('Load 53')
    [x_53,y_53] = ginput(1);
    hold off
    close(gcf)

    for counter = 1:5
        identifier = order53(lcCounter,counter);
        tempData = loadcell{identifier,lcCounter};
        [~,I] = min(abs(x_53-tempData(:,1)));
        value_53{lcCounter,counter} = tempData(I,3);
        singleError_53{lcCounter,counter} = abs(tempData(I,2)- tempData(I,3));
        valueLoading_53{lcCounter,counter} = tempData(I,2);
        clearvars tempData
    end
%-------------------------------------------------------------------------
```

```
    %plotting 269

    figure

    for counter = 1:5

        identifier = order269(lcCounter,counter);
        tempData = loadcell{identifier,lcCounter};

        plot(tempData(:,1),tempData(:,3))
        error_269{lcCounter,counter} = abs(tempData(:,2)-tempData(:,3));
        hold on
        clearvars tempData

    end
    title('Load 269')
    [x_269,y_269] = ginput(1);
    hold off
    close(gcf)

    for counter = 1:5
        identifier = order269(lcCounter,counter);
        tempData = loadcell{identifier,lcCounter};
        [~,I] = min(abs(x_269-tempData(:,1)));
        value_269{lcCounter,counter} = tempData(I,3);
        singleError_269{lcCounter,counter} = abs(tempData(I,2)- tempData(I,3));
        valueLoading_269{lcCounter,counter} = tempData(I,2);
        clearvars tempData
    end
%-------------------------------------------------------------------------
    %plotting 299

    figure

    for counter = 1:5

        identifier = order299(lcCounter,counter);
        tempData = loadcell{identifier,lcCounter};

        plot(tempData(:,1),tempData(:,3))
        error_299{lcCounter,counter} = abs(tempData(:,2)-tempData(:,3));
        hold on
        clearvars tempData

    end
    title('Load 299')
    [x_299,y_299] = ginput(1);
    hold off
    close(gcf)

    for counter = 1:5
        identifier = order299(lcCounter,counter);
        tempData = loadcell{identifier,lcCounter};
        [~,I] = min(abs(x_299-tempData(:,1)));
        value_299{lcCounter,counter} = tempData(I,3);
        singleError_299{lcCounter,counter} = abs(tempData(I,2)- tempData(I,3));
        valueLoading_299{lcCounter,counter} = tempData(I,2);
        clearvars tempData
    end
```

```
%-------------------------------------------------------------------------
    %plotting 415

    figure

    for counter = 1:5

        identifier = order415(lcCounter,counter);
        tempData = loadcell{identifier,lcCounter};

        plot(tempData(:,1),tempData(:,3))
        error_415{lcCounter,counter} = abs(tempData(:,2)-tempData(:,3));
        hold on
        clearvars tempData

    end
    title('Load 415')
    [x_415,y_415] = ginput(1);
    hold off
    close(gcf)

    for counter = 1:5
        identifier = order415(lcCounter,counter);
        tempData = loadcell{identifier,lcCounter};
        [~,I] = min(abs(x_415-tempData(:,1)));
        value_415{lcCounter,counter} = tempData(I,3);
        singleError_415{lcCounter,counter} = abs(tempData(I,2)- tempData(I,3));
        valueLoading_415{lcCounter,counter} = tempData(I,2);
        clearvars tempData
    end

%-------------------------------------------------------------------------
    %plotting 422

    figure

    for counter = 1:5

        identifier = order422(lcCounter,counter);
        tempData = loadcell{identifier,lcCounter};

        plot(tempData(:,1),tempData(:,3))
        error_422{lcCounter,counter} = abs(tempData(:,2)-tempData(:,3));
        hold on
        clearvars tempData

    end
    title('Load 422')
    [x_422,y_422] = ginput(1);
    hold off
    close(gcf)

    for counter = 1:5
        identifier = order422(lcCounter,counter);
        tempData = loadcell{identifier,lcCounter};
        [~,I] = min(abs(x_422-tempData(:,1)));
        value_422{lcCounter,counter} = tempData(I,3);
        singleError_422{lcCounter,counter} = abs(tempData(I,2)- tempData(I,3));
        valueLoading_422{lcCounter,counter} = tempData(I,2);
```

```
        clearvars tempData
    end

%-------------------------------------------------------------------------
    %plotting 546

    figure

    for counter = 1:5

        identifier = order546(lcCounter,counter);
        tempData = loadcell{identifier,lcCounter};

        plot(tempData(:,1),tempData(:,3))
        error_546{lcCounter,counter} = abs(tempData(:,2)-tempData(:,3));
        hold on
        clearvars tempData

    end
    title('Load 546')
    [x_546,y_546] = ginput(1);
    hold off
    close(gcf)

    for counter = 1:5
        identifier = order546(lcCounter,counter);
        tempData = loadcell{identifier,lcCounter};
        [~,I] = min(abs(x_546-tempData(:,1)));
        value_546{lcCounter,counter} = tempData(I,3);
        singleError_546{lcCounter,counter} = abs(tempData(I,2)- tempData(I,3));
        valueLoading_546{lcCounter,counter} = tempData(I,2);
        clearvars tempData
    end

%-------------------------------------------------------------------------
    %plotting 737

    figure

    for counter = 1:5

        identifier = order737(lcCounter,counter);
        tempData = loadcell{identifier,lcCounter};

        plot(tempData(:,1),tempData(:,3))
        error_737{lcCounter,counter} = abs(tempData(:,2)-tempData(:,3));
        hold on
        clearvars tempData

    end
    title('Load 737')
    [x_737,y_737] = ginput(1);
    hold off
    close(gcf)

    for counter = 1:5
        identifier = order737(lcCounter,counter);
        tempData = loadcell{identifier,lcCounter};
```

```
        [~,I] = min(abs(x_737-tempData(:,1)));
        value_737{lcCounter,counter} = tempData(I,3);
        singleError_737{lcCounter,counter} = abs(tempData(I,2)- tempData(I,3));
        valueLoading_737{lcCounter,counter} = tempData(I,2);
        clearvars tempData
    end

%-------------------------------------------------------------------------
    %plotting 921

    figure

    for counter = 1:5

        identifier = order921(lcCounter,counter);
        tempData = loadcell{identifier,lcCounter};

        plot(tempData(:,1),tempData(:,3))
        error_921{lcCounter,counter} = abs(tempData(:,2)-tempData(:,3));
        hold on
        clearvars tempData

    end
    title('Load 921')
    [x_921,y_921] = ginput(1);
    hold off
    close(gcf)

    for counter = 1:5
        identifier = order921(lcCounter,counter);
        tempData = loadcell{identifier,lcCounter};
        [~,I] = min(abs(x_921-tempData(:,1)));
        value_921{lcCounter,counter} = tempData(I,3);
        singleError_921{lcCounter,counter} = abs(tempData(I,2)- tempData(I,3));
        valueLoading_921{lcCounter,counter} = tempData(I,2);
        clearvars tempData
    end


%-------------------------------------------------------------------------
    %plotting 938

    figure

    for counter = 1:5

        identifier = order938(lcCounter,counter);
        tempData = loadcell{identifier,lcCounter};

        plot(tempData(:,1),tempData(:,3))
        error_938{lcCounter,counter} = abs(tempData(:,2)-tempData(:,3));
        hold on
        clearvars tempData

    end
    title('Load 938')
    [x_938,y_938] = ginput(1);
    hold off
```

```
    close(gcf)

    for counter = 1:5
        identifier = order938(lcCounter,counter);
        tempData = loadcell{identifier,lcCounter};
        [~,I] = min(abs(x_938-tempData(:,1)));
        value_938{lcCounter,counter} = tempData(I,3);
        singleError_938{lcCounter,counter} = abs(tempData(I,2)- tempData(I,3));
        valueLoading_938{lcCounter,counter} = tempData(I,2);
        clearvars tempData
    end


%-------------------------------------------------------------------------
    %plotting 1050

    figure

    for counter = 1:5

        identifier = order1050(lcCounter,counter);
        tempData = loadcell{identifier,lcCounter};

        plot(tempData(:,1),tempData(:,3))
        error_1050{lcCounter,counter} = abs(tempData(:,2)-tempData(:,3));
        hold on
        clearvars tempData

    end
    title('Load 1050')
    [x_1050,y_1050] = ginput(1);
    hold off
    close(gcf)

    for counter = 1:5
        identifier = order1050(lcCounter,counter);
        tempData = loadcell{identifier,lcCounter};
        [~,I] = min(abs(x_1050-tempData(:,1)));
        value_1050{lcCounter,counter} = tempData(I,3);
        singleError_1050{lcCounter,counter} = abs(tempData(I,2)- tempData(I,3));
        valueLoading_1050{lcCounter,counter} = tempData(I,2);
        clearvars tempData
    end

end


cd(defaultDir);
%%
for i = 1:6
    loadC = strcat('loadcell',num2str(i));
    for j = 1:5
        %53
        LC.(eval('loadC')).error{1,j} = error_53{i,j};
        LC.(eval('loadC')).value(1,j) = value_53{i,j};
        LC.(eval('loadC')).singleError(1,j) = singleError_53{i,j};
        LC.(eval('loadC')).loading(1,j) = valueLoading_53{i,j};
        %269
        LC.(eval('loadC')).error{2,j} = error_269{i,j};
```

```
        LC.(eval('loadC')).value(2,j) = value_269{i,j};
        LC.(eval('loadC')).singleError(2,j) = singleError_269{i,j};
        LC.(eval('loadC')).loading(2,j) = valueLoading_269{i,j};
        %299
        LC.(eval('loadC')).error{3,j} = error_299{i,j};
        LC.(eval('loadC')).value(3,j) = value_299{i,j};
        LC.(eval('loadC')).singleError(3,j) = singleError_299{i,j};
        LC.(eval('loadC')).loading(3,j) = valueLoading_299{i,j};
        %415
        LC.(eval('loadC')).error{4,j} = error_415{i,j};
        LC.(eval('loadC')).value(4,j) = value_415{i,j};
        LC.(eval('loadC')).singleError(4,j) = singleError_415{i,j};
        LC.(eval('loadC')).loading(4,j) = valueLoading_415{i,j};
        %422
        LC.(eval('loadC')).error{5,j} = error_422{i,j};
        LC.(eval('loadC')).value(5,j) = value_422{i,j};
        LC.(eval('loadC')).singleError(5,j) = singleError_422{i,j};
        LC.(eval('loadC')).loading(5,j) = valueLoading_422{i,j};
        %546
        LC.(eval('loadC')).error{6,j} = error_546{i,j};
        LC.(eval('loadC')).value(6,j) = value_546{i,j};
        LC.(eval('loadC')).singleError(6,j) = singleError_546{i,j};
        LC.(eval('loadC')).loading(6,j) = valueLoading_546{i,j};
        %737
        LC.(eval('loadC')).error{7,j} = error_737{i,j};
        LC.(eval('loadC')).value(7,j) = value_737{i,j};
        LC.(eval('loadC')).singleError(7,j) = singleError_737{i,j};
        LC.(eval('loadC')).loading(7,j) = valueLoading_737{i,j};
        %921
        LC.(eval('loadC')).error{8,j} = error_921{i,j};
        LC.(eval('loadC')).value(8,j) = value_921{i,j};
        LC.(eval('loadC')).singleError(8,j) = singleError_921{i,j};
        LC.(eval('loadC')).loading(8,j) = valueLoading_921{i,j};
        %938
        LC.(eval('loadC')).error{9,j} = error_938{i,j};
        LC.(eval('loadC')).value(9,j) = value_938{i,j};
        LC.(eval('loadC')).singleError(9,j) = singleError_938{i,j};
        LC.(eval('loadC')).loading(9,j) = valueLoading_938{i,j};
        %1050
        LC.(eval('loadC')).error{10,j} = error_1050{i,j};
        LC.(eval('loadC')).value(10,j) = value_1050{i,j};
        LC.(eval('loadC')).singleError(10,j) = singleError_1050{i,j};
        LC.(eval('loadC')).loading(10,j) = valueLoading_1050{i,j};

    end
end
```

Knee Kinematics

```
function [alphas, betas,gammas, translations ] = kneekinem(
tibiaData,femurData,floatingAxis,leg)
% Function that calculates knee orientation and kinematics
%this is uses to calculate instantaneous spatial configuration
%This method is based on the Joint Coordinate System description of Three
%dimensional motions by Grood and Suntay(1983).
%Reference: Grood ES, Suntay WJ. A Joint Coordinate System for the Clinical
%Description of Three-Dimensional Motions: Application to the Knee.
%ASME. J Biomech Eng. 1983;105(2):136-144. doi:10.1115/1.3138397.
%Rotations and Translations
%alpha = Flexion (+ve)  // sin(alpha) = e2*K = cos(pi/2 + alpha)
%beta = Adduction = (pi/2 + beta) right knee //
%     = Adduction  = (pi/2 - beta) left knee // cos(beta) = I*k
%gamma = External rotation(+ve) // sin(gamma) = -e2*i = cos(pi/2 + gamma) (right knee)
%                               // sin(gamma) = e2*i = cos(pi/2 - gamma)(left knee)

%Input data must have the instantaneous coordinate system of each segment
%and of the complete trial after clean up of the data



tibiaX = tibiaData{1,1};
tibiaY = tibiaData{1,2};
tibiaZ = tibiaData{1,3};
femurX = femurData{1,1};
femurY = femurData{1,2};
femurZ = femurData{1,3};

floating_axisN = floatingAxis;
tibia_or = tibiaData{1,4};
femur_or =  femurData{1,4};

[rowsNum,~] = size(tibiaX);

alpha = zeros(rowsNum,1);alphaSign = zeros(rowsNum,1); gammaSign =
zeros(rowsNum,1);gamma = zeros(rowsNum,1);
beta = zeros(rowsNum,1); vectorH = zeros(rowsNum,3);q1 = zeros(rowsNum,3);q2 =
zeros(rowsNum,3); q3 = zeros(rowsNum,3);

for i=1:rowsNum

        %Calculation of flexion/extension---180 deg means full extension

        alpha(i) = acosd(dot(femurY(i,:),floating_axisN(i,:)));
        alphaSign(i) = -asind(dot(floating_axisN(i,:),femurZ(i,:)));
        alphaSign2(i) = acosd(dot(floating_axisN(i,:),femurZ(i,:))) - rad2deg(pi/2);
        %Calculation of internal/external rotation angle

        gamma(i) = acosd(dot(tibiaY(i,:),floating_axisN(i,:)));
        gammaSign(i) = asind(dot(floating_axisN(i,:),tibiaX(i,:)));


        %Calculation of Adduction angles

        beta(i) = acosd(dot(femurX(i,:),tibiaZ(i,:)));

        if leg(1) == 'r'
```

```
          gammaSign(i)= - gammaSign(i);
          gammaSign2(i) = acosd(dot(floating_axisN(i,:),tibiaX(i,:))) - rad2deg(pi/2);
          gammaSigno(i,:) = -sin(gammaSign2);
          beta(i) = beta(i) - rad2deg(pi/2);
         elseif leg(1) =='l'
          beta(i) =  rad2deg(pi/2) - beta(i);
          gammaSign2(i) = acosd(dot(floating_axisN(i,:),tibiaX(i,:))) + rad2deg(pi/2);
          gammaSigno(i,:) = sin(gammaSign2);
         end

         %Calculation for Translations
         vectorH(i,:) = tibia_or(i,:) - femur_or(i,:);
         temp(i) = norm(vectorH(i,:));

         %medial-laterla translation
         q1(i) = dot(vectorH(i,:),femurX(i,:));

         %anterior-posterior translations
         q2(i) = dot(vectorH(i,:), floating_axisN(i,:));

         %distraction-compression
         q3(i) = - dot(vectorH(i,:),tibiaZ(i,:));

end
vectorH(:,4) = temp;
alphas = [alpha, alphaSign,alphaSign2] ;
betas = beta;
gammas = [gamma,gammaSign,gammaSign2,gammaSigno];
translations = {vectorH, q1,q2,q3};
end
```

Polaris CSV open

```
function [pointerData,femurData,tibiaData,headers] = polarisread(csvFile)

F = fopen(csvFile);
dataFile = textscan(F,'%s %s %s %s %s %s %s %s %s %s %s %s %s %s %s %s %s %s %s %s %s
%s %s %s %s %s %s %s %s %s %s %s %s %s %s %s %s','Delimiter',',');
numHeaders = 37;

pointerTool = [3,6,7,8,9,10,11,12];
BrainT = [15,18,19,20,21,22,23,24];
BrainY = [27,30,31,32,33,34,35,36];

%Header Information
for i=1:numHeaders
    headers{i} = dataFile{1,i}{1};
end
clear vars i

%Splitting tool data
for i=1:8
    pointerInfo{1,i} = dataFile{1,pointerTool(i)}(2:end);
    femurInfo{1,i} = dataFile{1,BrainY(i)}(2:end);
    tibiaInfo{1,i} = dataFile{1,BrainT(i)}(2:end);
end
clear vars i
```

```
%Array Sizes
[~,variableNum] = size(femurInfo);
[elementsNum,~] = size(femurInfo{1,1});
%Tool Numerical Arrays
%Headers: "Frame, Q0, Qx, Qy, Qz, Tx, Ty, Tz"
for j = 1:variableNum
    for i=1:elementsNum
         pointerData(i,j)= str2num(pointerInfo{1,j}{i});
         femurData(i,j)= str2num(femurInfo{1,j}{i});
         tibiaData(i,j)= str2num(tibiaInfo{1,j}{i});
    end
end

end
```

Kinematic processing

```
dirFile = uigetdir;
cd(dirFile)

%Static Calibration of anatomical landmarks
[A_pointer, A_TY, ~, headers] = polarisread('A.csv');
[B_pointer, B_TY, ~, ~] = polarisread('B.csv');
[C_pointer, C_TY, ~, ~] = polarisread('C.csv');
[D_pointer, D_TY, ~, ~] = polarisread('D.csv');
[latMal_pointer, latMal_TY, ~, ~] = polarisread('lat mal.csv');
[medMal_pointer, medMal_TY, ~, ~] = polarisread('med mal.csv');
[latPla_pointer, latPla_TY, ~, ~] = polarisread('lat plat.csv');
[medPla_pointer, medPla_TY, ~, ~] = polarisread('med plat.csv');
[toe_pointer, toe_TY, ~, ~] = polarisread('toe.csv');

TY_General = {A_TY, B_TY, C_TY, D_TY,latMal_TY, medMal_TY,
latPla_TY,medPla_TY,toe_TY};

%Average calculation of location tool during calibration trials,

TY_General = [mean(A_TY(:,2:8))', mean(B_TY(:,2:8))', mean(C_TY(:,2:8))',
mean(D_TY(:,2:8))',...
    mean(medMal_TY(:,2:8))', mean(latPla_TY(:,2:8))',...
    mean(medPla_TY(:,2:8))',mean(toe_TY(:,2:8))'];

TY = mean(TY_General,2)';

%Average calculation of static points
A = mean(A_pointer(:,6:8));
B = mean(B_pointer(:,6:8));
C = mean(C_pointer(:,6:8));
D = mean(D_pointer(:,6:8));
latMal = mean(latMal_pointer(:,6:8));
medMal = mean(medMal_pointer(:,6:8));
latPla = mean(latPla_pointer(:,6:8));
medPla = mean(medPla_pointer(:,6:8));
toe = mean(toe_pointer(:,6:8));

clearvars -except A B C D latMal medMal latPla medPla toe TY
```

```
%Calculation of Fix distances between tool and Pointer tool for all the
%digitized points
TYRotM = quat2rotm(TY(1:4));

TY2A = TYRotM' * (A - TY(5:7))';
TY2B = TYRotM' * (B - TY(5:7))';
TY2C = TYRotM' * (C - TY(5:7))';
TY2D = TYRotM' * (D - TY(5:7))';
TY2LM = TYRotM' * (latMal - TY(5:7))';
TY2MM = TYRotM' * (medMal - TY(5:7))';
TY2LP = TYRotM' * (latPla - TY(5:7))';
TY2MP = TYRotM' * (medPla - TY(5:7))';
TY2Toe = TYRotM' * (toe - TY(5:7))';


%Plot points in reference to tool
for i=1:1
figure('Name','Reference Tool Y')
scatter3(TY2A(1), TY2A(2), TY2A(3))
hold on
scatter3(TY2B(1), TY2B(2), TY2B(3))
hold on
scatter3(TY2C(1), TY2C(2), TY2C(3))
hold on
scatter3(TY2D(1), TY2D(2), TY2D(3))
hold on
scatter3(TY2LM(1), TY2LM(2), TY2LM(3))
hold on
scatter3(TY2MM(1), TY2MM(2), TY2MM(3))
hold on
scatter3(TY2LP(1), TY2LP(2), TY2LP(3))
hold on
scatter3(TY2MP(1), TY2MP(2), TY2MP(3))
hold on
scatter3(TY2Toe(1), TY2Toe(2), TY2Toe(3))
hold on
scatter3(0, 0, 0)
hold on
plot3([TY2A(1) TY2B(1)],[TY2A(2) TY2B(2)], [TY2A(3) TY2B(3)],'-')
hold on
plot3([TY2A(1) TY2D(1)],[TY2A(2) TY2D(2)], [TY2A(3) TY2D(3)],'-')
hold on
plot3([TY2C(1) TY2B(1)],[TY2C(2) TY2B(2)], [TY2C(3) TY2B(3)],'-')
hold on
plot3([TY2C(1) TY2D(1)],[TY2C(2) TY2D(2)], [TY2C(3) TY2D(3)],'-')
end

%Re-orientation for visual representation with point D as the origin

xAxis = TY2A - TY2D ;
yAxis = TY2C - TY2D ;
zAxis = cross(xAxis,yAxis);

x = (xAxis/ norm(xAxis))';
y = (yAxis/ norm(yAxis))';
z = (zAxis/ norm(zAxis))';

TransMat = [x;y;z];% this matrix transforms into the nre defined coordinate system
```

```
% A2D = TransMat' * (TY2A - TY2D)
A2D_ = TransMat * (TY2A - TY2D) ;
B2D_ = TransMat * (TY2B - TY2D) ;
C2D_ = TransMat * (TY2C - TY2D) ;
Toe2D_ = TransMat * (TY2Toe - TY2D);
LP2D_ = TransMat * (TY2LP - TY2D);
MP2D_ = TransMat * (TY2MP - TY2D);
LM2D_ = TransMat * (TY2LM - TY2D);
MM2D_ = TransMat * (TY2MM - TY2D);

 %plot tatic points in reference of Corner D
for i=1:1
figure('Name','Reference corner D')
scatter3(A2D_(1), A2D_(2), A2D_(3))
hold on
scatter3(B2D_(1), B2D_(2), B2D_(3))
hold on
scatter3(C2D_(1), C2D_(2), C2D_(3))
hold on
scatter3(Toe2D_(1), Toe2D_(2), Toe2D_(3))
hold on
scatter3(LP2D_(1), LP2D_(2), LP2D_(3))
hold on
scatter3(MP2D_(1), MP2D_(2), MP2D_(3))
hold on
scatter3(LM2D_(1), LM2D_(2), LM2D_(3))
hold on
scatter3(MM2D_(1), MM2D_(2), MM2D_(3))
hold on
scatter3(0,0,0)
hold on
end

%% Controlled kinematic test with two rigid bodies
%Tool Y corresponts to tibia
%Tool T was attached to femur

clear all
close all
clc

dirFile = uigetdir;
cd(dirFile)

%Static calibration. This part extracts data from files. There are a total
%of 13 calibration points. The cornes of the base and  anatomical
%landmarks. There are 4 landmarks per segment
for i = 1:1
%Plate corners
[A_pointer, A_TYtemp, A_TTtemp, headers] = polarisread('CalibrationCornerA.csv');
[B_pointer, B_TYtemp, B_TTtemp, ~] = polarisread('CalibrationCornerB.csv');
[C_pointer, C_TYtemp, C_TTtemp, ~] = polarisread('CalibrationCornerC.csv');
[D_pointer, D_TYtemp, D_TTtemp, ~] = polarisread('CalibrationCornerD.csv');



%Tibia anatomical Landmarks
[latMal_pointer, latMal_TYtemp, ~, ~] = polarisread('CalibrationLateralMaleolus.csv');
[medMal_pointer, medMal_TYtemp, ~, ~] = polarisread('CalibrationMedialMaleolus.csv');
[latPla_pointer, latPla_TYtemp, ~, ~] = polarisread('CalibrationLateralPlateau.csv');
[medPla_pointer, medPla_TYtemp, ~, ~] = polarisread('CalibrationMedialPlateau.csv');
[toe_pointer, toe_TYtemp, ~, ~] = polarisread('CalibrationToe.csv');
```

```
%Femur anatomical landmarks

[latEpi_pointer, ~, latEpi_TTtemp, ~] =
polarisread('CalibrationLateralEpicondile.csv');
[medEpi_pointer, ~,medEpi_TTtemp , ~] =
polarisread('CalibrationMedialEpicondile.csv');
[greTro_pointer, ~, greTro_TTtemp, ~] =
polarisread('CalibrationGreaterTrochanter.csv');
[hipJ_pointer, ~,hipJ_TTtemp, ~] = polarisread('CalibratioHipJointCenter2.csv');
end

%Average calculation for all the extracted static points
for i = 1 :1
    %Plate
    [A,~] = toolaverage(A_pointer);
    [B,~] = toolaverage(B_pointer);
    [C,~] = toolaverage(C_pointer);
    [D,~] = toolaverage(D_pointer);

    [A_TY,~] = toolaverage(A_TYtemp);
    [B_TY,~] = toolaverage(B_TYtemp);
    [C_TY,~] = toolaverage(C_TYtemp);
    [D_TY,~] = toolaverage(D_TYtemp);

    [A_TT,~] = toolaverage(A_TTtemp);
    [B_TT,~] = toolaverage(B_TTtemp);
    [C_TT,~] = toolaverage(C_TTtemp);
    [D_TT,~] = toolaverage(D_TTtemp);

    %Tibia
    [latMal,~] = toolaverage(latMal_pointer);
    [medMal,~] = toolaverage(medMal_pointer);
    [latPla,~] = toolaverage(latPla_pointer);
    [medPla,~] = toolaverage(medPla_pointer);
    [toe,~] = toolaverage(toe_pointer);

    [latMal_TY,~] = toolaverage(latMal_TYtemp);
    [medMal_TY,~] = toolaverage(medMal_TYtemp);
    [latPla_TY,~] = toolaverage(latPla_TYtemp);
    [medPla_TY,~] = toolaverage(medPla_TYtemp);
    [toe_TY,~] = toolaverage(toe_TYtemp);

    %Femur
    [latEpi,~] = toolaverage(latEpi_pointer);
    [medEpi,~] = toolaverage(medEpi_pointer);
    [greTro,~] = toolaverage(greTro_pointer);
    [hipJ,~] = toolaverage(hipJ_pointer);

    [latEpi_TT,~] = toolaverage(latEpi_TTtemp);
    [medEpi_TT,~] = toolaverage(medEpi_TTtemp);
    [greTro_TT,~] = toolaverage(greTro_TTtemp);
    [hipJ_TT,~] = toolaverage(hipJ_TTtemp);

    %Tools Average
    TY_storage = [A_TY;B_TY;C_TY;D_TY;latMal_TY ;medMal_TY;latPla_TY;...
                medPla_TY;toe_TY] ;
    TY = mean(TY_storage);
    TT_storage = [A_TT;B_TT;C_TT;D_TT;latEpi_TT ;medEpi_TT;greTro_TT;...
                hipJ_TT];
```

```
    TT = mean(TT_storage);

    clearvars -except A B C D TT TY toe latEpi medEpi latPla medPla latMal...
                    medMal greTro hipJ

end

%calculation of fix distances
%This is the calibration section
for i = 1 : 1

TYRotM = quat2rotm(TY(1:4));
%Plate with respect to TY
TY2A = TYRotM' * (A(5:7) - TY(5:7))';
TY2B = TYRotM' * (B(5:7) - TY(5:7))';
TY2C = TYRotM' * (C(5:7) - TY(5:7))';
TY2D = TYRotM' * (D(5:7) - TY(5:7))';
%Tibia with respct to the respective tool (Tool-Y)
TY2LM = TYRotM' * (latMal(5:7) - TY(5:7))';
TY2MM = TYRotM' * (medMal(5:7) - TY(5:7))';
TY2LP = TYRotM' * (latPla(5:7) - TY(5:7))';
TY2MP = TYRotM' * (medPla(5:7) - TY(5:7))';
TY2Toe = TYRotM' * (toe(5:7) - TY(5:7))';

%Femur with respct to the respective tool (Tool-Y)
TTRotM = quat2rotm(TT(1:4));
TT2LE = TTRotM' * (latEpi(5:7) - TT(5:7))';
TT2ME = TTRotM' * (medEpi(5:7) - TT(5:7))';
TT2GT = TTRotM' * (greTro(5:7) - TT(5:7))';
TT2HJ = TTRotM' * (hipJ(5:7) - TT(5:7))';

%Setting new coordinate system
xAxis = TY2A - TY2D ;
yAxis = TY2C - TY2D ;
zAxis = cross(xAxis,yAxis);
x = (xAxis/ norm(xAxis))';
y = (yAxis/ norm(yAxis))';
z = (zAxis/ norm(zAxis))';
end

%New Trial

trial_TY = []; trial_TT = []; TT_cd = []; TY_cd = [];
[~, trial_TY,trial_TT, headers] = polarisread('Movement3.csv');
[rows,~] = size(trial_TY);

% [~, I] = toolaverage(trial_TY);
% TT_cd = dataclean(trial_TT,I);
% TY_cd = dataclean(trial_TY,I);
[TT_cd , TY_cd] = cleaner (trial_TT,trial_TY);

[rows, columns] =  size(TT_cd);

digA = [];digB = [];digC = [];digD = [];
digLP = [];digMP = [];digLM = [];digMM = [];
digToe = []; TY_trial = []; digLE = []; digME = [];
digGT = []; digHJ = []; TT_trial = [];

for i = 1: rows
```

```
quatTY = TY_cd(i,1:4);
TYrotM = quat2rotm(quatTY);

quatTT = TT_cd(i,1:4);
TTrotM = quat2rotm(quatTT);

%Reconstruction of Digital markers
digA(i,:) = TY_cd(i,5:7) + (TYrotM * TY2A)';
digB(i,:) = TY_cd(i,5:7) + (TYrotM * TY2B)';
digC(i,:) = TY_cd(i,5:7) + (TYrotM * TY2C)';
digD(i,:) = TY_cd(i,5:7) + (TYrotM * TY2D)';

digLP(i,:) = TY_cd(i,5:7) + (TYrotM * TY2LP)';
digMP(i,:) = TY_cd(i,5:7) + (TYrotM * TY2MP)';
digLM(i,:) = TY_cd(i,5:7) + (TYrotM * TY2LM)';
digMM(i,:) = TY_cd(i,5:7) + (TYrotM * TY2MM)';
digToe(i,:) = TY_cd(i,5:7) + (TYrotM * TY2Toe)';

digLE(i,:) = TT_cd(i,5:7) + (TTrotM * TT2LE)';
digME(i,:) = TT_cd(i,5:7) + (TTrotM * TT2ME)';
digGT(i,:) = TT_cd(i,5:7) + (TTrotM * TT2GT)';
digHJ(i,:) = TT_cd(i,5:7) + (TTrotM * TT2HJ)';


%origin and tibia coordinate system calculation
tibia_or(i,:) = (digLP(i,:)+digMP(i,:)) / 2 ;
tibia_plane(i,:) = (digLM(i,:)+digMM(i,:)) / 2 ;
x_temp = (digMP(i,:)-digLP(i,:));
z_temp = tibia_or(i,:) - tibia_plane(i,:);
y_temp = cross(z_temp,x_temp);
%Normalization
tibiaX(i,:) = (x_temp / norm(x_temp)) ;
tibiaY(i,:) = (y_temp / norm(y_temp)) ;
tibiaZ(i,:) = (z_temp / norm(z_temp)) ;

tibiaData{1,1}(i,:) = (x_temp / norm(x_temp)) ;
tibiaData{1,2}(i,:) = (y_temp / norm(y_temp)) ;
tibiaData{1,3}(i,:) = (z_temp / norm(z_temp)) ;
tibiaData{1,4}(i,:) = tibia_or(i,:);
%origin and femur coordinate system calculation
x_temp=[]; y_temp =[]; z_temp = [];
femur_or(i,:) = (digLE(i,:)+digME(i,:)) / 2 ;
femur_plane(i,:) = (digGT(i,:)+digHJ(i,:)) / 2 ;
x_temp = (digME(i,:)-digLE(i,:));
z_temp = femur_plane(i,:) - femur_or(i,:);
y_temp = cross(x_temp,z_temp);
%Normalization
femurX(i,:) = (x_temp / norm(x_temp));
femurY(i,:) = (y_temp / norm(y_temp));
femurZ(i,:) = (z_temp / norm(z_temp));

femurData{1,1}(i,:) = (x_temp / norm(x_temp)) ;
femurData{1,2}(i,:) = (y_temp / norm(y_temp)) ;
femurData{1,3}(i,:) = (z_temp / norm(z_temp)) ;
femurData{1,4}(i,:) = femur_or(i,:);

floating_axisN(i,:) = cross(tibiaZ(i,:),femurX(i,:)) /
norm(cross(tibiaZ(i,:),femurX(i,:)));
```

```
end

%Use new function!
leg = 'left';
[alphas, betas,gammas, translations ] = kneekinem(
tibiaData,femurData,floating_axisN,leg);
```